Optical Devices for Biochemical Sensing in Flame Hydrolysis Deposited Glass

A thesis Submitted to the Faculty of Engineering of the University of Glasgow for the Degree of Doctor of Philosophy.

by

Jesús M. Ruano-López

A mis padres

Abstract

Previous research in the field of Flame Hydrolysis Deposition (FHD) of glasses has focused on the production of low cost optical devices for the field of telecommunications. The originality of this doctoral research resides in the exploration of this technology in the fabrication of optical bio-chemical sensors, with integrated "Lab-on-a-chip" devices.

To achieve this goal, we have combined and applied different microfabrication processes for the manufacture of sensor platforms using FHD. These structures are unique in that they take advantage of the intrinsic benefits of the microfabrication process, such as, miniaturisation and mass production, and combine them with the properties of FHD glass, namely: low loss optical transducing mechanisms, planar technologies and monolithic integration.

This thesis demonstrates that FHD is a suitable technology for biosensing and Lab-on-a-Chip applications. The objective is to provide future researchers with the necessary tools to accomplish an integrated analytical system based on FHD.

We have designed, fabricated, and successfully tested a FHD miniaturised sensor, which comprised optical and microfluidic circuitry, in the framework of low volume fluorescence assays. For the first time, volumes as low as 570 pL were analysed with a Cyanine-5 fluorophore with a detection limit of 20 pM, or ca. 6000 molecules ($\pm 3\sigma$) for this platform. The fabrication of the sensor generated a compilation of processes that were then utilised to produce other possible optical platforms for bio-chemical sensors in FHD, e.g. arrays and microfluidics. The "catalogue" of methods used included new recipes for reactive ion etching, glass deposition and bonding techniques that enabled the development of the microfluidic circuitry, integrated with an optical circuitry.

Furthermore, we developed techniques to implement new tasks such as optical signal treatment using integrated optical structures, planar arraying of sensors, a

separating element for liquid chromatography, and finally a pumping system for delivering small amounts of liquid along the microfluidic channels.

This thesis comprises six chapters. In Chapter 1, an overview of the topic was presented, offering a review of the various fields addressed, as well as a description of the motivation and originality of this work. Chapter 2 describes the processes developed to fabricate an optical sensor, and Chapter 3 assesses its performance. In Chapter 4, integrated optical circuit designs and their fabrication methods, as well as developing and testing of an array of sensors, are presented. The description of a separating element involved in a liquid chromatography system, and the pumping of liquids in a FHD optical device, were addressed in Chapter 5. Finally, Chapter 6 summarised the conclusions and suggested possible future work. Last but not least, the appendix, contains techniques for hybrid integration; recipes for etching of rare earth glasses; as well as instrumentation designs.

This research has taken Flame Hydrolysis Deposition technique into the world of optical bio-chemical sensors, creating a bridge between analytical assays and FHD glass. In this respect, the demonstrated flexibility of the technology will enable a variety of configurations to be created and implemented, with the prospect of using the techniques for laboratory-on-a-chip technologies. The work has been patented by the University of Glasgow, for future exploitation in analytical biotechnology and Lab-on-a-Chip.

Acknowledgement

I would like to thank both my supervisors, Prof. J. M. Cooper and Prof. J. S. Aitchison, for their encouragement, support and interaction throughout the course of this work. I appreciate all the effort and confidence that they have invested in me, relating to all aspects of my PhD. I would also like to express my gratitude to all of the members of the Optoelectronics and Bioelectronic research groups for their helpful suggestion and comments.

I wish to acknowledge the financial support of my studentship from The Basque Country Education Department (Spain) and from the Engineering and Physical Science Research Council EPSRC (UK).

I would like to extend my gratitude to Jim Bonar and Daniel Ortega for orienting me in the initial phase of my research and Vincent Benoit for doing the same at the end; Andy McLaughlin for his etching expertise and answering many times "one question"; Marcos Vermelho, Duncan Ross and Paolo Marques for their help in the deposition of glasses; Brendan Casey for his anodic bonding knowledge; Mike Jubber for his help with silicon etching; and Claire Troupe for introducing me to PDMS.

I am grateful for the excellent technical support provided by Ian McNicholl for maintaining the Flame Hydrolysis Deposition Facility; Joan Carson for her patient teaching of the cleanroom processes; the dry-etch technicians for his understanding with my "long" etching runs; George Dalgetty and Hugh Moy for enduring my urgent polishing process; Kaz Piechowiak for remaking "the clamp" over and over again; Kenny Mahoney for an excellent job with the fabrication of the filter-amplifier; Mary Robertson and Bill Monaghan for her continual supply of "Jesus" jokes, and Margaret Henderson for her help.

I would like to thank, Michèle Smith, Fermín Reig, Amr Saher, Mary Frances Flynn and David Holmes for helping me edit my thesis, and correcting my "Hispanised" English.

Furthermore, I would like to thank all my friends. They supported and encouraged me day by day, making my stay in Glasgow a wonderful and unforgettable experience.

Finally, my deepest acknowledgement goes out to my family for their support, encouragement, and love given to me during all these years. I am grateful to my sister, Mari Carmen, and brother, Juan Manuel for pushing me and believing in me. They have all made it possible for me to achieve this goal.

Table of Content

List of tables

List of Figures

Chapter 1: INTRODUCTION.

1.1 Introduction.

The development of chemical and biological sensors will play a significant role in improvements of public health, by providing new applications with rapid detection, high sensitivity, portability, and high specificity devices. Nevertheless, the commercialisation of such sensors has continued to lag behind "research" by several years, mainly because these intrinsic advantages can not currently be offered at low cost. The advent of a technology called Micro-Electromechanical Systems (MEMS) has made some advances into this topic, by transferring microfabrication facilities used in electronics areas, into the micro-sensor and micro-actuator industry. In this thesis, Flame Hydrolysis Deposition (FHD) of silica is introduced as a MEMS tool and is used to show how the combination of these microfabrication technologies can be used for the mass fabrication of optical chemical sensor, biosensors and / or a Lab-on-a-Chip technology.

This project approaches this research from the point of view of developing fabrication protocols (sequences of manufacturing steps) and processes for integrated analytical systems, as there is no previous literature that links FHD to a Lab-on-a-Chip or even to a more simple optical devices such as a microfluidic-sensing device. To do this it is, therefore, necessary to explore, improve and / or adapt different techniques associated with FHD for bio-sensing and microfluidic

purposes, such as reactive ion etching (RIE), sealing and bonding techniques and / or packaging issues.

The following chapter provides the reader with a brief overview of the main issues involved in the chemical sensing and biosensor industries. In order to understand what such novel fabrication approach can offer to the optical biochemical field, this chapter presents a review of some of the most exciting past and current achievements in planar optical biosensors. Finally, the principles behind both FHD and RIE are briefly explained. These two main techniques, in combination with "sealing" and "packaging" are investigated in order to fabricate a planar optical biosensor with similar or better performance relative to those presented in the literature review. Finally, the main fabrication problems that this research had to overcome are presented and discussed.

1.2 Chemical Sensors and Biosensors.

A chemical sensor is generally a simple device where the target molecule produces a measurable physical event under controllable circumstances. This occurrence can be a change in the optical, piezoelectric, thermal or electronic properties of a sensor. The task of the "sensor" is simply to transfer this physical event into a measurable electrical signal.

A biosensor is usually a more complex analytical device than a chemical sensor. It is constructed by attaching or retaining biological material (such as enzyme, cells, organelles, DNA, RNA, an antibody, or an antigen) onto a suitable transducing system. When the desired target interacts specifically with the biologically sensitive coating, there is a change in one or more physico-chemical properties at the sensor surface, converting the biochemical response into a quantifiable signal (see Figure 1.1). This change may produce ions, electrons, heat, light or mass, which are converted into an electrical signal by the appropriate transducer [1,2,3,4,5].

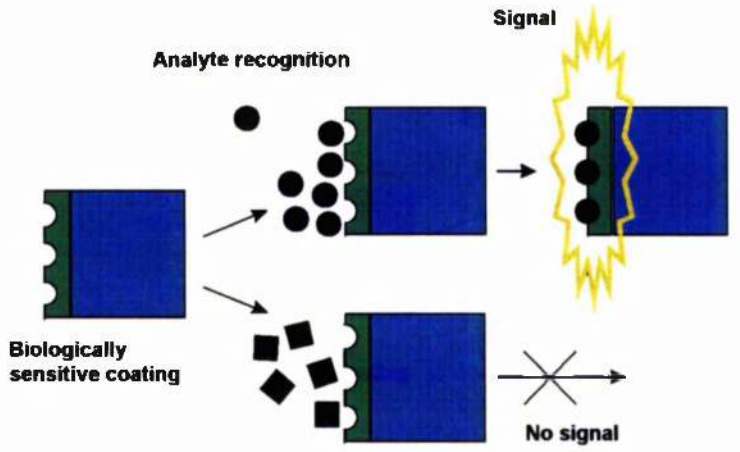

Figure 1.1: Description of the operation of a biosensor showing schematically the role of biological material (green) in functionalising a sensor (blue) [2].

The biosensor mechanism enables a high specificity of biological recognition to provide analytical advantages over more traditional methods. Ideally, it also offers easy sample manipulation, rapid detection, high sensitivity, and portability. Biosensors were first developed as an alternative to conventional laboratories with expensive equipment and highly trained personnel. For example, in the medical field, biosensors are enabling clinical analyses to be performed at the bedside in critical care units, at home, or in doctor's offices. The subsequent results of the test can then be acted upon immediately, thus, avoiding the delays associated with having to send samples to, and wait for results from, centralised laboratories. Glucose biosensors for monitoring diabetes [6,7] and ion-selective electrodes for blood gases and electrolytes [8] are good examples of this biosensor development. Similar advantages are envisaged in other sectors such as environmental analysis and industrial process control.

1.3 A brief History of Biosensors.

The evolution of biosensors has been speeded up by the progress of physical microsensors on silicon. In turn, the physical sensor technology has been encouraged by the development and diversity of silicon processing methods.

During the period of rapid growth of integrated circuits, engineers realised the tremendous potential of using lithographic, etching and other fabrication tools, developed for microelectronics manufacturing, to make mechanical, rather than electronic structures. In the 1950s, for example, mechanical strain gauges were fabricated from silicon wafers and physically glued onto large mechanical components to create pressure sensors. Although these sensors were expensive, because of the complex hand-assembly operations, they were quickly adopted for critical aerospace and industrial application, due to their size and superior performance.

As technology progressed, more effort was made in the area of solid-state microsensors. This has been directed towards developing physical sensors incorporating more sophisticated functions into the silicon chip (pressure transducers [9], fluidic sensors [10], artificial intelligence devices [11], visualisation for robotics [12], actuators and vibrations monitors [13]). Packaging issues have also been improved (wire bonding pads, flip-chip bonding, and stress isolation). All of these features have been built into the chips by using the same parallel processing, and mass production techniques that originally made the integrated circuit so cost-effective.

In 1972, Yellow Spring Instrument Co, shortly followed Beckman instruments, transferred this accumulated sensor knowledge into the biochemical sensors delivering the first commercialised biosensors. Both of these instruments were originally developed for the measurement of glucose. Over the next decade, little advancement was made in the area of commercial biosensing. However, physical microsensors continued providing new devices, such that it was possible to integrate, on a single mass-produced chip, most of the mechanical and electronic elements of a pressure sensor [14,15]. It became feasible to use micromechanical sensors in two key high-volume applications. In the early 1980s, the automotive industry began manufacturing manifold absolute pressure sensors for the newly mandated emission control systems, which soon became indispensable for

automobile pollution control. Today, more than 25 million micro-machined manifold absolute pressure sensors are made worldwide each year [16]. Likewise, earlier models of blood pressure sensors were costly and delicate and required expensive sterilisation between uses. Silicon micro-machining pressure sensors replaced these sensors, providing reusable blood pressure sensors in the operating room where the sensor can be disposed of, instead of being sterilised and reused. More than 20 million micromachined blood pressure sensors are sold world-wide each year [16].

During the mid-80s, there were six biosensor products of note on the market [17]. In the early 90s, this figure rose to approximately 30. Some, such as Medisense's Pen2, Companion2, Pharmacia's Biacore, and Molecular Device's Cytosensor, have delivered useful results. To date, the most successful product is the biosensor from Medisense ^{TM} using British technology and exploited by a U.S. company. This sensor is a glucose meter that uses electrochemical transduction of an enzymatic reaction. However, there has still not been any overwhelmingly successful micro-biosensor product, mainly due to the lack of a fabrication technology that allows mass production of biosensors together with the market potential and clinical needs. The packaging of biosensors has not been fully addressed yet in a mass producible manner, since this area requires more complex functions, such as: movement of fluids, chemical compatibilities (e.g. bonding in the presence of organic solvents), high pressures, and packaging with openings for fluid access [18].

The advent of MEMS has delivered some additional progress in this field. This approach transfers the microfabrication techniques used in microelectronics industry into the micro-sensor and micro-actuator industry such that bio-chemical sensors yearly sales may be improved as much as 25% to 40% [19]. The application of micromachining to chemistry and biotechnology is now being undertaken seriously, although there are as yet, only a few integrated bio-chemical sensors that have been successfully developed. These include ion-selective

electrodes for blood gases and electrolytes, glucose sensors for monitoring diabetes, amperometric sensors for toxic gases, high temperature diode sensors for determination of gases [19], and more recently DNA sensors [20]. However, despite these achievements, their commercialisation is still limited. All these devices ideally should handle a very small amount of liquid, consequently there is much research being done in micro-fluidic machined devices, including valves, micro-pumps, flow channels, restrictors [21], and cell manipulators [22]. Such instruments, using these devices are now known as "micro-total analytical systems" (μTAS) or "Lab-on-a-Chip systems" [23, 24, 25, 26, 27, 28]. To date, only a few of these functions have been integrated into a microscale system, and most chips require a large external instrumentation interface

1.4 Optical Chemical Sensors and Biosensors.

Currently, the most developed application of optoelectronics is in the area of telecommunications. This evolution has led to improved lasers, better waveguides, and cheaper mass-produced "chips". Furthermore, it is also well known that analytical sciences have traditionally relied on numerous kinds of optical information, including absorption and emission spectroscopy, refractometry, and polarimetry. By using optical chip processing technology and analytical chemistry, there is a potential for the mass production of optical biosensors.

The use of fibres for the purpose of chemical sensing was initially limited to the determination of species possessing an intrinsic colour or fluorescence. These included not only certain coloured actinides and transition metals e.g. copper ion, but also many gases with a characteristic absorption in the near infrared, such as methane. In addition, a large field involving fibre-optic chemical sensors has been developed from the combination of fibre-optic technology with traditional methods of indicator chemistry, such as the use of dyes that react with a species of interest and undergo a change in their optical properties. This paved the way for sensing

chemical parameters such as pH [29,30], oxygen partial pressure, carbon dioxide, heavy metal and other pollutants [31].

Complementary to this, planar waveguides (which represent practically the same concept as optical fibres but in microfabricated planar design) have advantages such as miniaturisation, easy deposition and patterning of reagents, increased reliability and reproducibility (a sheet can be used to fabricate many devices), low volumes of reagents used (cheap assays) and a batch fabrication process (low cost) compatible with the IC microelectronic and MEMS technology [32]. A step forward was achieved by combining biochemical and biological recognition elements with waveguide technology to result in so-called optical planar biosensors [33]. In the last decade, practically all important classes of biomolecules (including tissue and whole cells) have been immobilised on waveguide structures [34,35,36]. This has accelerated the evolution of these optical systems and has allowed a commercial availability of some optical biosensors (see Table 1.1).

Manufacturer	Sensor	Optical technique	Application
Pharmacia Biosensor AB	BIAcore™	Surface Plasmon Resonance	Ligand-ligand interactions
Fisons Applied Sensor Technology	IAsys™	Resonant mirror	Ligand-ligand interactions
Biostar Inc.	Optical Immunoassay™	Reflection	Group A Streptococcus antigen detection
Artificial Sensing Instruments	Bios-1™	Integrated optical sensor	Ligand-ligand interactions

Table 1.1: Summary of commercially available optical Biosensor systems [32].

Fluorescence transduction is a specific and stable optical method for biosensing, and this is clearly pointed out by Puyol *et al.* [37]:

"Until now, most of the described miniaturised devices have been based on surface plasmon resonance phenomena or interferometry. However, they present

poor specificity in the response and instabilities due to temperature or pressure variations. More specific optical sensors are those based on measurement principles such as, absorption spectrometry, fluorometry, reflectance, or evanescent wave spectroscopy."

Among all of the optical transducing mechanism mentioned, the most used is that of fluorescence (see Section 3.2). There are three main reasons that fluorescence has become such an important tool for biologist. Firstly, the sensitivity in conventional microscope-based systems can be between 100-1000 fluorescently labelled molecules. This sensitivity allows for an adequate signal from cells using relatively low concentrations of fluorescent probe. Since there is a possibility that any indicator will be toxic, or will significantly perturb the cell, the less indicator used, the better. Moreover, the high sensitivity leads to the use of a fluorescence mechanism in microarrays of wells, where very low amounts of fluorescently labelled molecules need to be detected. Secondly, fluorescence can be sensitive to the molecular environment of the fluorophore and many different kinds of environmental factors, including viscosity [38], quenching by other molecules to measure the pH [39], and solvent polarity [40] can be also measured. And thirdly, there is the ability to sense fast biological events in a parallel way. Fluorophores have fluorescence lifetimes that are short relative to most biological events so that the time response of fluorophore is usually not an issue. As a consequence, this research has focused on the fabrication of an optical biosensor based on fluorescence.

One potential disadvantage is the complex relationship between the amount of signal and the amount of fluorophore present, particularly when it is in a solution in a microstructure or immobilised on a surface.

1.5 State of the art of Planar Optical Biosensors.

This section is organised by the different optical transducing mechanisms and configurations. Critical analyses of these approaches will follow in the next chapters, when an examination of the results obtained in this thesis will be presented.

1.5.1 Sensors based on Evanescent Field.

When a light beam irradiates an interface between two optically transparent media of different refractive indices, total internal reflection occurs within the optically denser medium. An electromagnetic waveform is generated in the optically less dense medium close to the reflecting surface. This evanescent wave is part of the internally reflected light beam, and penetrates a distance equivalent to a fraction of light wavelength into the lower refractive index medium [41]. This "evanescent field" in an optical waveguide can be used to interact with the sample. The evanescent field 'sees' changes in the effective complex refractive index, depending on polarisation (TE or TM), mode number, wavelength and on the properties of the waveguide (refractive indexes, thickness). In an evanescent field biosensor, three different effects can induce the changes of the effective refractive index, namely:

1. The formation of an adlayer of adsorbed or bound molecules on sensor's surface (few nanometers thick), which are transported to the waveguide surface by convection or diffusion from the bulk of the gaseous or liquid sample. The sensor will be working as an affinity sensor.

2. A change of the refractive index of the homogeneous sample covering the waveguide (few micrometers thick). The sensor works as a differential refractometer.

3. Excitation of fluorescence labels in the adlayer. The fluorescence emission will be collected from the optical waveguide.

In affinity sensors, the formation of the bound molecules adlayer is used in evanescent field immunosensors, and very thin high-refractive index films are also necessary to increase its sensitivity. By the same token, in differential refractometers, a low-refractive index is required to enlongate the evanescent field "tale" in the low refractive index film. This higher interaction will increase the sensitivity of the measurement of the refracting index of the whole sample.

Dip-coated SiO_2-TiO_2 waveguides films of only 100-150 nm thickness and high refractive index have been used by Lukosz [42] with sub-nanomolar detection limits of antigen (rabbit-IgG). Similarly, Zhou achieved a detection limit of 20 nM (nanomolar) of fluorescence labelled (fluorescein isothiocyanate, FITC) antibodies using ion-diffused glass waveguides [43]. Femtomolar sensitivity of fluorescence labelled (cyanine, Cy5) protein has been achieved using waveguides of 1 micron thick film of siliconoxynitride (SiON) fabricated by plasma enhanced chemical vapour deposition (PECVD) [44]. The main disadvantage of these sensors is the long optical path length required (several milimiters) and consequently, the relatively high volumes of sample which are necessary (about 0.1 μL) even for capillaries.

An evanescent field sensor can be improved by the integration of an optical reference arm to normalise the signal. This enhanced sensor is named integrated optic interferometer and is described below.

1.5.2 Integrated Optic Interferometric Sensor.

Mach-Zehnder interferometers (MZI), using an evanescent field effect, can be used to compensate for common-mode effects (i.e. temperature or excitation variations) with the normalisation obtained through a reference arm. Immunoreactions have been monitored down to concentration of 50 pM for a 40kDa protein using a

standard integrated interferometer fabricated by enhanced chemical vapour deposition (LPCVD) and PECVD [45]. Duport *et al.* [46] have varied the MZI by ion exchange on a glass substrate. Whereas, the output signal from conventional interferometer is a single light spot with time-varying intensity, their improved device gives a complete spatial interference pattern, enabling the user to distinguish between two evanescent wave interaction effects, namely: (i) light absorption is transformed into a fringe contrast; and (ii) phase variation into a fringe displacement. Luff *et al.* [47] have presented a MZI that incorporates a three-waveguide coupler structure at the output, giving advantages in terms of signal referencing, and in establishing the right operating point in the interference pattern. Its optical path length is 15 mm with an estimated detection limit for protein of 5 pg mm^{-2}.

1.5.3 Surface Plasmon Sensors.

Both evanescent field and surface plasmon sensors are based on a change of the complex refractive index and film thickness. This change is induced by molecules entering or leaving the evanescent field of the guided wave, or by changes in the refractive index of the medium in contact with the evanescent field. However, in comparison with planar waveguide sensors, such as integrated optic interferometer, surface plasmons only propagate as TM electromagnetic waves along the interface between a metal film and a dielectric medium (sample). Surface Plasmon sensors can work either as differential refractometers or as affinity sensors. According to Lukosz, the sensitivities of surface plasmon sensors, as differential refractometers, are about 5-10 times greater than those of the integrated optical sensors. Surface plasmon sensors, with silver films at a wavelength of 632.8 nm and working as a affinity sensors, are about 5 times more sensitive than those with gold films [48], although the silver film is less stable in aqueous environments.

Pharmacia Biosensor AB manufactures a surface plasmon sensor called BIAcore™. This device consists of a gold-coated sensor chip with a polymer

matrix containing ligands and mounted in a cassette that readily interfaces to the fluidic of the system by anti-ligand interactions [49].

1.5.4 Microarrays based on Fluorescence.

As was mentioned, fluorescence assays can be performed using a very low sampling volume. This makes fluorescence suitable as a transducing mechanism in microarrays of cuvettes, where small amounts of sample are necessary. Van den Doel *et al.* [50] have investigated fluorescence detection in subnanolitre microarrays. In contrast to the majority of the research in this field, this work did not focus on applications related to DNA. Their objective was to optimise the fermentation process of human serum albumin, using epi-illumination of an array of chambers (0.5- 1.6 nL) fabricated on silicon and glass. The solution consisted of Rhodamine B in a mixture of glycerol:water (1:1, v/v), in order to avoid evaporation. The detection limit achieved, using a CCD cooled to –42 °C, is 10^8 (0.1 femtomoles) molecules per vial. Further work regarding microarrays and fluorescence was carried out by Wadkins [51]. Wells of 2 mm diameter were formed on glass slides by a photoactivated optical adhesive and antibodies were covalently attached to the wells to form the sensing surface. This glass slide was then interrogated using a 5-mW diode laser with a line generator (635 nm). The line was focussed into one edge of the glass slide. Below the array, a graded index of refraction (GRIN) lenses, an emission filter and a room temperature CCD were placed to image the evanescent wave. Of particular interest to this work were the rectangular wells containing chicken immunoglobulin, which acted as alignment markers, and were used to monitor the non-uniformity of excitation light. Concentrations as low as 5 ng ml^{-1} of staphylococcal enterotoxin B could be measured. Similar work has been done by Rowe *et al.* [52] including a removable flow cell for the introduction of samples and fluorescence antibodies. The detection limits were 10 ng ml^{-1}, reported using a cooled CCD. Narang [53] has also arrived at interesting results regarding high sensitive (TNT and RDX) using two fused silica capillaries combined into a single device. An attractive aspect of

this work was the target analyte, flowing through the capillaries, which displaced the fluorophore-labelled antigen from the binding pocket of the specific antibody. Detection limits as low as 0.5 ng ml^{-1} of RDX or 0.1 ng ml^{-1} of TNT were achieved.

1.5.5 Capillary Electrophoresis.

There are advantages in developing protocols to analyse biological reactions on a much smaller scale than those currently employed. Electrophoresis in a narrow-bore capillary is especially suitable for delivering fluids to structures for such measurements [54, 55].

The essence of capillary electrophoresis is the use of a narrow electrophoresis channel (usually from 10 to 100 μm in inner diameter), which enables rapid dissipation of heat and allows the application of a high field strength. The electrical field produces the movement of the charged particles, which reach a steady state when the electric force balances the frictional drag. This technique shortens the time required for separation, reduces the longitudinal diffusion of analytes, and raises the efficiency of molecular separation. The narrow channel also minimises convection, allowing electrophoresis in free solution. This technique enables control of the direction of fluid flow at the intersection of capillaries, without the need for valves or other moving parts. Separations have been achieved using electrophoretic effects, i.e. differing mobilities of the ions within an electric field result in different migration rates, thus leading to separation. The ratio of the inner surface area to the volume of the inner space where separation takes place is very large, and this emphasises the need for strict control of the adsorption of analytes on the wall of the capillary, particularly if protein are being analysed.

Harrison *et al.* [56] demonstrated that pre-separation mixing of chemical reagents for reaction on-chip and post-separation fluorescent labelling on-chip could be carried out in a microchannel by electrophoresis in glass capillaries. A free space

optical set-up was used for the fluorescence detection. A second approach was carried out by Chen [57], with a detection sensitivity for Cy5 based on capillary electrophoresis and laser-induced fluorescence detection of 100 pM (red semiconductor laser, 2.5 mW and 652 nm). Likewise, Effenhauser [25] performed capillary electrophoresis in an original way, since the micro-capillaries were produced by moulding poly(dimethysiloxane) (PDMS) and by laser-induced fluorescence detection. An electrophoresis-mediated transport of molecules has also been utilised for microscale enzyme assay [58,59].

Currently, there is great interest in single cell analysis and cell manipulation processes such as cell fusing, see Section 1.5.6. A study has been reported involving single-cell injection and successful analysis of cell components by capillary electrophoresis, following cell lysis (cell's membrane rupture) inside a capillary [60].

1.5.6 Cell Screening.

The characterisation of many interesting and important problems in biology and medicine, demands rapid and continuous measurements on a single cell. Currently, there is an interest among pharmaceutical companies to develop micromachined devices, because they offer the prospect of obtaining unique insight into the interactions between cell signals in a manner which is not possible when neighbouring cells are influencing the local environment. Single cell analysis has already demonstrated that it has the potential to deconvolute complex patterns of messenger production with knowledge of the cell's history, in order to indicate an activity related with a disease [61,62,63,64,65,66,67]. Ultimately, these studies seek to understand how molecules inside the cell give rise to observable cell structures and activities that may lead to new developments in biomolecular engineering. The development of fluorescence techniques has greatly aided this effort as its high sensitivity enables low concentrations of fluorescence to be

detected. As stated above, there is a possibility that any fluorescence indicator will be toxic or will significantly perturb the cell.

1.5.7 Liquid Chromatography.

A technique using capillary electrophoresis and denoted as liquid chromatography has taken advantage of the progresses in microfabrication technologies. To date, liquid chromatography has been achieved in columns packed with particles. Currently, the fulfilled requirement for liquid chromatography of deep microchannels of 2 μm or less in width and 12 μm in depth [68], has allowed He *et al.* to develop liquid chromatography through nanocolumns fabricated in quartz [69]. This approach will be explained in Chapter 5, where these results impact upon the research presented in this thesis.

1.5.8 DNA Chip Technology.

In the past five years, a new chemical approach called combinatorial chemistry [20,70] has changed drug discovery technology. High volume gene expression assays can optimise pharmaceutical therapies by targeting genome-based treatment to specific populations, and provide time-efficient methods to study genes involved with cancer growth patterns and tumour suppression. Evaluating the genetic causes of disease may require simultaneous investigation of several genes through the interrogation of the entire fingerprint of genetic information. Traditional gene expressions based on gel assays are time consuming, very expensive, and often restricted to analysing one piece of information at a time (due to resolution of spotting on the gel). A new technology based on "DNA chips" can analyse data much quicker, providing large amounts of genomic information. The nucleic acids are bound to a reusable solid support allowing improvements in automation and data analysis. DNA chips also allow biomedical researchers to study entire genes, and gather information concerning the expression and gene mutation patterns. DNA chip technology requires hybridisation of an unknown nucleotide sequence (target) to an ordered array of known DNA (a probe), immobilised onto a glass

slide or silicon chip. The results are obtained by fluorescence and analysed by pattern recognition. Millions of dollars have been invested to enhance the process. However, the applied technology still requires intense and well-prepared hand-manipulation steps, slowing down the process. Recently, a number of research groups have achieved high and reliable throughput screening using micro-fabrication capabilities borrowed from microelectronic and telecommunication industries [71, 72, 73, 74]. The most remarkable commercial success in DNA chips is an American company called Affymetrix, which commercially introduced in 1996 the GeneChip® technology. This commercial device was based on high density DNA probe arrays, containing DNA sequences as a method to analyse genetic information in the human genome. Integrated sensor systems remain a very attractive choice for the entrepreneurial, innovative biotechnology companies interested in pursuing drug discovery [75]

1.5.9 Lab-on-a-Chip.

The previous review shows that microfabrication techniques used in the microelectronic industry have been adapted for biochemical systems. As a result of this adaptation, microstructures for micro-liquid handling, signal processing, sensors and actuators are being integrated on the same substrate by micromachining, decreasing dramatically the physical size of the biosensor (to the micrometer scale). This miniaturisation decreases fabrication cost, increases reliability through higher reproducibility, reduces power consumption, enables low consumption of costly reagents, and increases the speed of analyses. Naturally, none of these benefits is guaranteed simply by using micromachining, and these technologies must be applied with care, particularly as surface/volume ratio of the structure will increase, and adsorption effects become more significant. Leistiko [76] achieved, on the same substrate, an integration of microfluidic-optical circuitry (by combination of PECVD and RIE), bringing together detectors (Mesa photodiodes) and pigtailing of fibres (with insertion losses 2-5 dB). The sensor was based on absorption or luminescence and its detection limit is not very

practical (10 μM), although, a high degree of integration has been accomplished remarkably well.

Bruno *et al.* [77] approached the Lab-on-a-Chip technology by hybridisation of a six channel, all-solid-state, miniaturised fluorescence sensor array for the determination of blood samples. Their device featured superblue LEDs as light sources, graded index of refraction (GRIN) optics, and photodiodes assembled according to pigtailing procedures [78]. They did not achieve a high degree of uniformity of analyses between the six sensors, probably because the assembly task was not performed in parallel by micromachining techniques.

1.6 Overview of the Fabrication Techniques Employed.

In order to understand the fabrication methods involved in this thesis, this section will introduce the reader to the two main fabrication technologies involved in this work, namely flame hydrolysis deposition (FHD) and reactive ion etching (RIE).

1.6.1 Flame Hydrolysis Deposition.

An explanation of the micro-fabrication technology called FHD will be presented in this section. FHD is a chemical vapour deposition process, where oxides (SiO_2, GeO_2, B_2O_3, and P_2O_5) are synthesised through the hydrolysis of appropriate high vapour pressure precursors. The technique was first conceived by J. Hyde whilst working at Corning Glass in 1934, for the fabrication of transparent articles of silica at low temperatures and with a high degree of purity [79]. It was subsequently applied to the fabrication of optical fibre preforms, and gave birth to the outside vapour deposition method (OVD). The technique was further modified in the vapour axial deposition method (VAD). FHD was subsequently transferred to planar geometries for the fabrication of high-silica content Planar Ligthwave Circuits (PLC) on Si substrates [80].

In this process, metal halides, such as $SiCl_4$, are hydrolysed in an oxy-hydrogen flame to form a low density oxide 'soot'. Each of the gaseous halides ($SiCl_4$, $GeCl_4$, $POCl_3$ and BCl_3) are carried in a separate feedline, so that different planar glass material systems can be produced, either by sequential, or co-deposition of the appropriate soot (see Figure 1.2). Overall, the hydrolysis process is described by the following reactions:

$$SiCl_{4(v)} + 2H_2O_{(v)} \rightarrow SiO_{2(s)} + 4HCl_{(v)} \qquad \text{Equation 1.1}$$

$$GeCl_{4(v)} + 2H_2O_{(v)} \rightarrow GeO_{2(s)} + 4HCl_{(v)} \qquad \text{Equation 1.2}$$

$$2BCl_{3(v)} + 3H_2O_{(v)} \rightarrow B_2O_{3(s)} + 6HCl_{(v)} \qquad \text{Equation 1.3}$$

$$2POCl_{3(v)} + 3H_2O_{(v)} \rightarrow P_2O_{5(s)} + 6HCl_{(v)} \qquad \text{Equation 1.4}$$

Suitable substrates (quartz or thermally oxidised silicon wafer) are placed on the surface of a rotating table with the torch moving radially (see Figure 1.3). The flame in the torch expels the evaporated water leaving submicron particles deposited on the substrates. The 'soot' is then annealed between 1100 °C and 1300°C to form a transparent silica glass. The FHD system is calibrated to obtain approximately one micron of deposited glass per traverse of the torch.

The advantages of this fabrication technique compared with other methods (especially ion-exchange, CVD or RF sputtering) are low optic transmission losses of the materials deposited, the high compatibility with fibre technologies, as well as precise and controllable manipulation of the refractive index of the glass and high refrigence control. Moreover, unlike other methods of depositing cladding material onto silica based waveguides, it is not necessary to have sloping sidewalls to facilitate the filling of the gaps between closely spaced waveguides. This allows

the fabrication of vertical walls and high aspect ratio structures required in optical devices.

The disadvantages of the FHD technology are: the high temperature process involved (over 1100°C); the need for non-commercially available machinery (developed and maintained by the University of Glasgow); the difficulty of integrating microelectrodes and other active optical components; the limitations in the dry etch processing necessary to create deep structures and, the dielectric nature of the materials deposited. The last characteristic may be an advantage if thermal or electrical isolation is needed, or a disadvantage if a process of heat removal is necessary.

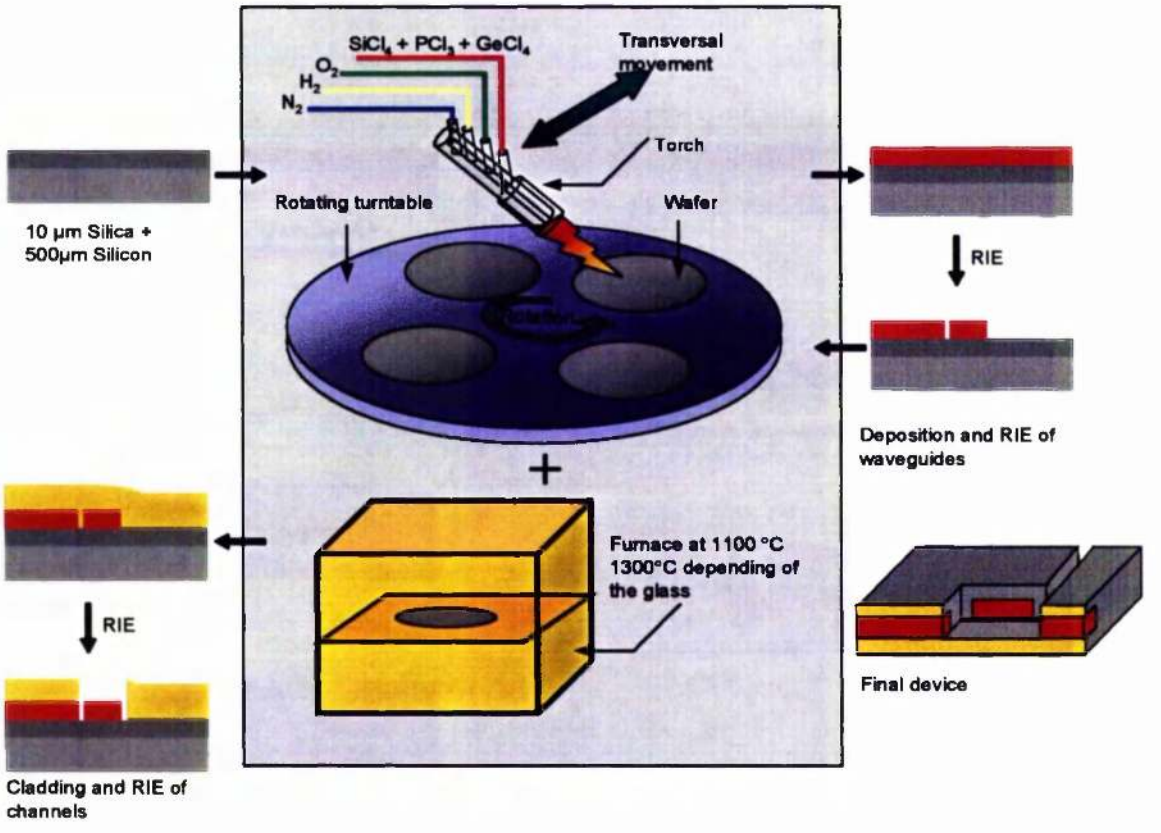

Figure 1.2: Schematic representation of the FHD process used to produce integrated optical sensors. The FHD process consists of hydrolysis and deposition of metal halides on top of a silica on silicon wafer. Subsequently, sintering of the deposited material at high temperature is needed. This useful process is intimately related with reactive ion etching (RIE) which provides a formidable tool to develop an optical circuitry.

FHD silica glass films are already widely used in planar lightwave circuits (PLCs) due to their low optical losses and their inherent compatibility with optical fibres [81]. More information about the FHD process at Glasgow University and its application in optoelectronics can be found in the theses of G. Barbarossa [82], J. R. Bonar [83], A. J. Mclaughlin [84], M.Vermelho [85] and P. Marques [86].

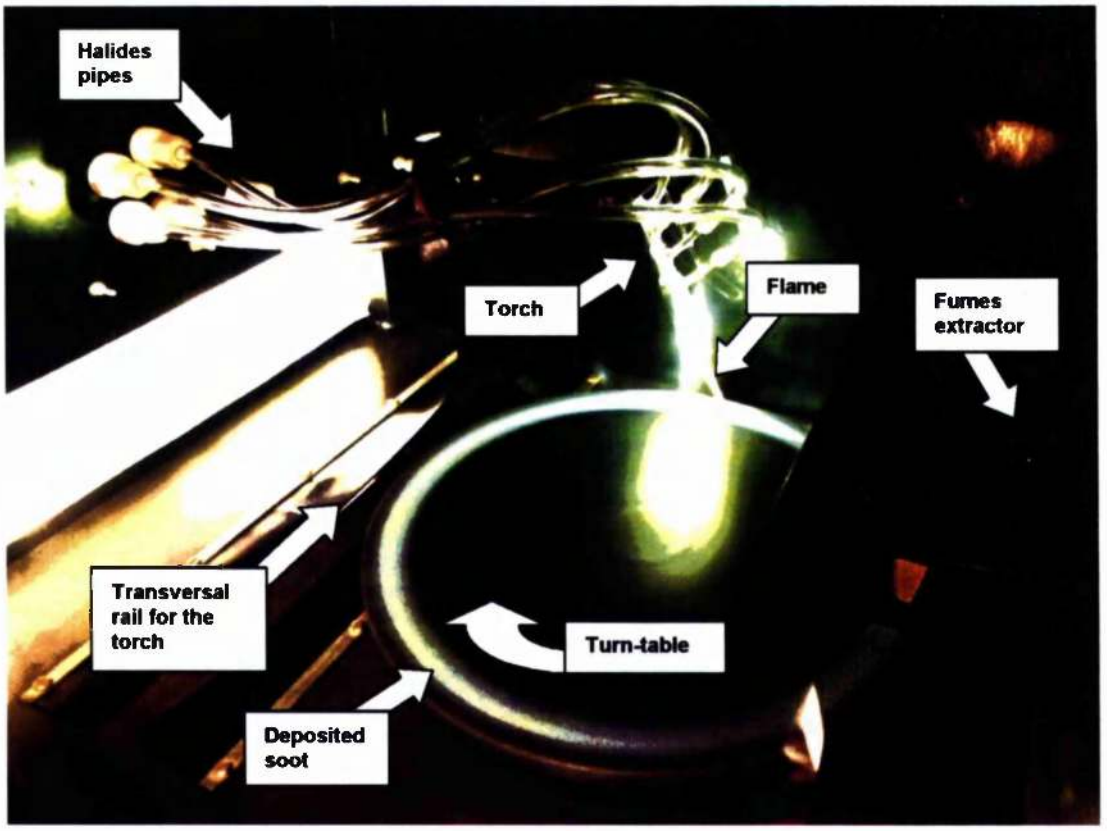

Figure 1.3: Photograph of the machine in operation (the white outer circle on the turntable is the soot deposited so far).

1.6.2 Reactive Ion Etching.

One method of transferring photolithographically defined patterns to the planar silica is to selectively remove unmasked portions of the planar waveguide, using a technique known as etching. A dry etch technique is a plasma based process, characterised by a combination of physical sputtering with the chemical activity of reactive species. Plasma etching has been employed in the microelectronics industry since the early 1970s [87], and offers etch directionality, accurate pattern transfer in a clean process, and good selectivity between the mask and the material being etched. These features are achieved in an automation compatible process, a factor synonymous with mass production [88].

The highly reactive state of matter called "plasma" exists when there are an equal number of positive and negative charged species within the etch chamber. Such a condition occurs when a high-frequency voltage (13.56 MHz) is applied across two parallel electrodes in the presence of appropriate vapours. The feed gas undergoes a number of processes, such as, electron-impact dissociation and ionisation, which creates radicals, positive and negative ions, electrons and neutrals species. The result is known as a glow discharge. As electrons have much higher mobility than the ions, the lower electrode quickly acquires a negative charge, leaving the plasma positive. A boundary region, known as the dark space, occurs between the plasma and the lower electrode, across which there is a potential, commonly referred to as the self-bias voltage. The motion of ions within the plasma is random, and as positive ions drift toward the dark space, they begin to accelerate under the presence of the DC bias. Reactive radicals are adsorbed onto the surface of the material to be etched. This step is followed by a chemical reaction on the surface forming volatile etch products or their precursors. The ongoing ion bombardment of the surface enhances the reaction of the adsorbed radicals, thus, accelerating the etch process. During well-balanced etching, a deposition of polymers on the etched surfaces takes place simultaneously with the etching process. This results in vertically etched walls.

The controllable factors involved in a reactive ion etching are: (i) the flow rate of the etchant gases; (ii) the pressure of the chamber; and (iii) the RF (radio frequency) power applied between the electrodes. The appropriate balance of these parameters permits the desired etching characteristics. For instance, a straightforward way to achieve a high etch rate of glass is to increase the RF power, since the etching is assisted by more rapidly moving ions. However, at the same time, the roughness of the material becomes very high. A compromise between the RF power and the rest of the parameters must be established. These factors and their effects will be briefly explained in the following paragraphs.

Flow Rate: The gas flow rate allows the control of the feed gas, i.e. CHF_3, into the etch chamber. Too low a flow of gas will mean that there is insufficient material to break down and form a glow discharge. Too high flow will mean not enough time to break down the feed gas, thus, there may be a strong dominance of one species over another. The flow rate also places restrictions on the maximum and minimum pressures obtainable in the chamber.

Pressure: The etching pressure determines the level of interaction of the substrate within the plasma. A high pressure will reduce the mean free path for charged particles, thus, encouraging the likelihood of an ionisation event within the plasma, and leading to an increase in the etching rate. Conversely, this increase in residence time of the reacted compounds could increase the production of "polymers", that may be deposited on the sample, slowing down the etching.

A lower pressure can increase the mean free path, and reduce the likelihood of interactions occurring, thereby decreasing the likelihood of etching. The pressure in the chamber has a major effect upon both the size of the sheath between the plasma and the chamber electrode, and the magnitude of the potential (dc bias) across it.

RF Power: This has an effect on the dissociation of the feed gas. A low power would break down the plasma to a lesser extent than at a high power. At high powers, the feed gas would have more kinetic energy, increasing the number of ionisation processes, the sheath potential, as well as, the ion bombardment energy.

INDUSTRY	NECESSITY
The chemical industry	Quantitating and differential analysis of gas and liquids mixtures from chemical processes and products.
The oil and gas industry	Measurement volatile organic compounds.
The paper industry	Monitoring bleaching processes and toxic compounds.
The food industry	Prevention of contaminated foods and beverages from the market. Monitoring product quality by analysis of flavours and odours in the food, beverage, liquor and perfume processes that presently rely on human palates and noses.
The environmental industry	Prevention of environmental contaminants from causing damage to the ecosystem.
Home goods	Acceptable cost for CO, CO_2 and humidity sensors to install into homes and offices.
Clinical diagnostic industry	Improvement and new formats of the patient health due to the availability of easy, fast and cheap diagnostic equipment.
Automotive industry	Some important advances have been made related with physical sensors (acceleration airbag sensors, pressure sensors), although there is a need to discover a method to decrease manufacturing cost for bio-chemical sensors.
Pharmaceutical and agrochemical industries	The use of combinatorial chemistry in these fields requires high throughput screening sensors. Integration, miniaturisation and arraying of these analyses can improve drug discovery, and generate DNA sequence and expression (see Section 1.5.8).
Military industry	Biological and chemical weapons detection and instrumentation to search mines in the battlefield.

Table 1.2: List of some industries and their bio-chemical needs.

1.7 Motivation, Interests and Achievements of this Thesis.

It is important for the chemical and biosensor industry to recognise and then exploit niche markets, where MEMS can provide a unique performance in comparison with competing technologies, such as, DNA analysis with small

volumes of sample or high consumable costs. In Table 1.2 are listed industries that could benefit from this technology with their needs identified.

From Table 1.2, it seems clear that there are many different sectors where chemical sensors and biosensors could be applied. In addition, whatever the technology is, it must offer advantages over existing analytical technologies. An interesting approach is the integration of functionalities with miniaturisation of chemical sensors and biosensors. This method offers two attractive advantages. Miniaturisation provides faster analytical methods and low cost products (see Section 1.7.2), whilst the integration of new funcionalities in the sensor (sample handling, signal processing, calibration) facilitates their use. However, it is very difficult to achieve these requirements at a low cost. The following section explores the problem and proposes a solution.

1.7.1 Research Question Stated in this Thesis.

Previously, Section 1.5 explained the different MEMS approaches used in planar optical biosensing, and their best achievements in order to fulfil the niches explained in Table 1.2. Some of these examples present very low detection limits (femtomolar) with relatively high volumes (evanescent field sensors), and others show high integration level (capillary electrophoresis and detectors within the same chip) but with lower detection limits (about 10 μM). The complexity involved in obtaining low detection limits with high integration levels and low volumes, has the following challenging consequences:

- High cost product: decreased cost would increase market penetration and open new market areas to the technology.

- Poor integration and packaging: this leads to awkward handling of devices. Thus, the market is restricted to situations where well trained personnel are available.

- Stability and sensitivity: reliability over several years is desirable in many applications.

- Real time monitoring: several industries need rapid, high sensitivity and specificity using real-time methods for monitoring processes at low cost.

There are few commercial examples that overcome all these difficulties using MEMS microfabrication techniques (see Table 1.1). It is the purpose of this thesis to demonstrate that FHD can be used to fabricate optical biosensors in large numbers with low detection limits, high integration levels, and low volumes.

The FHD fabrication technique has a main intrinsic advantage, which can help solve some integration and packaging issues. Theoretically, this method permits the fabrication of a microfluidic circuitry integrated within an optical device, in a mass-produced manner, with feasible routes to packaging. FHD of glasses can introduce more functionalities to the sensor, with low cost and low volume. Research that fabricates a laboratory-on-a-chip or even a microfluidic-sensing device using FHD, has not as yet, been reported. Therefore, the major task in this thesis is to demonstrate that FHD glass is a suitable substrate to perform biological or chemical assays

1.7.2 FHD Advantages for Chemical Sensing Applications.

The reasons why FHD can be a successful approach for the fabrication of biosensing devices are described in the following subsections:

1.7.2.1 Based on an optical transducing mechanism.

Turner [1] makes a comparison between electrical and optical biosensors. Some of his conclusions for optical signals are summarised here:

- No reference is required: however, it is a good practise to measure the optical signal of interest to a reference intensity.

- The output signal is not subject to electrical interference. This advantage is particularly important for sensors operated in electrically noisy environments. However, they are subject to background from the ambient light.

- Optical devices are inherently safer than electrical devices when used for in vivo biomedical measurements because there is no danger of electrical shock.

- Amperometric electrochemical sensors are more sensitive to fluctuations in temperature and flow conditions in the sample than are optical sensors.

- Optical sensors can be highly stable with respect to calibration. This is particularly true if the sensor involves the measurement of the ratio of intensity at two different wavelengths.

- Immobilised reagents with different wavelengths responses can be used in optical sensors to respond to more than one analyte.

1.7.2.2 Planar technology.

The FHD technique is a planar technology. Robinson [32] studied the advantages of a planar technology for the fabrication of optical biosensors versus the use of fibres. As the sensing surface in planar optical biosensors is flat, the deposition and patterning of reagents are easier than with fibres. Conventional printing techniques can be adapted to achieve the precise deposition of small quantities of reagent in specific locations on the device surface with relative ease [89]. FHD planar devices can employ the immobilisation of an active chemical as the material is susceptible to simple silane functionalisation [90,91]. Another inherent advantage of a planar technology is that it can lead easily to the production of an array of sensors, in order to increase throughput.

1.7.2.3 Mass production availability.

A planar sheet can be used to fabricate many devices, improving the between-device precision. If a larger number of sensors are reproduced from an individual

sheet of material, there will be greater reproducibility between individual devices when compared with the individual manufacture of large numbers of sensors. This may increase the analytical precision. Manufacturing techniques can also be adapted from other industries, e.g. the microelectronics industry using methods such as, spin coating, evaporation, photolithography, bonding and etching. These batch fabrication processes in FHD glass already allow to industry to fabricate hundreds of devices on a single wafer, for less than 10 euros (6 pounds).

1.7.2.4 Miniaturisation of the assays.

The miniaturisation of a chemical analytical system provides a new perspective on the chemical assays, and allows the biochemist to perform experiments in a manner that was impossible previously (e.g. DNA microarrays, single cell analysis). FHD is a technique that provides a method to fabricate "high silica content" based structures capable of containing very small volumes. For example, structures on FHD glass which contain about ca. 300–500 pL of sample can be fabricated and, avoid the misuse of expensive reagents (e.g. cost of DNA maybe from £100,000 to £1,000,000 per gram). Additionally, the reactions can be measured more quickly because the diffusion times of the analytes in these small amounts of solution are much shorter.

1.7.2.5 Monolithic integration of integrated optics.

To date, most of the optical components have been fabricated in bulk-optic configurations, using micro-lenses and prisms, or in fibre-optic configurations using fused-fibre couplers. This approach appears to have limitations in terms of device stability, productivity and suitability for integration. A possible way to overcoming this problem is to integrate monolithically channel waveguide technologies using FHD to form integrated-optic components.

1.7.2.6 Theoretical microfluidic integration.

The integration of a microfluidic circuitry with the sensing device onto FHD glass will allow a flow of compounds and, therefore, a continuous monitoring of the

sample together with a high level of automation [92]. In addition, silica surfaces are needed to allow the electro-osmotic movement of particles [54,55]. This makes a FHD biosensor an ideal approach for continuous monitoring of analyte concentrations in chemistry and biochemistry.

1.7.2.7 Portability and easy handling.

FHD devices are robust and, therefore, are easier to handle. The physical robustness of a planar sensor may allow the user to handle it effortlessly, making addition of sample to the device and subsequent loading into the instrument much easier. This is the result of the device or ("chip") being multi-functional. Easy handling may, in future, also allow non-expert personnel to perform biochemical assays where the device itself can automatically mix, deliver, and select the compounds to be used.

Additionally, the scale or dimension of a FHD based device may permit the analysis of an isolated cell. It is also important to consider that FHD is theoretically a compatible process with the IC microelectronic industry and it also has a demonstrated high compatibility with fibre optics leading to easy and feasible packaging, which will increase the portability of the device [93,94]. However, an integration of active and passive optical FHD devices on a common substrate has not been achieved, and hybrid integration [95,96,97] is required to connect the light source/detector (III-V semiconductors) to the silica on silicon devices.

1.7.3 Thesis's Objectives and their Associated Problems.

Where there is a problem there is also an objective to overcome it. Therefore, this section will summarise the stated objectives in this thesis and their associated problems. Their achievement will define the performance of the future device.

1.7.3.1 Demonstration of low volume fluorescence-based assays on FHD glass.

The output signal of optical sensors depends, in part, on the amount of reagent present in the optical path. Thus, miniaturising the sensor causes a decrease in the magnitude of measured intensities which in turn complicates their measurement. Therefore, it is essential for this research to demonstrate that FHD is a suitable and convenient platform to perform a miniaturise bioassays, i.e. using molecular fluorescence. Following this initial stage, it is required to establish and fabricate the best optical and microfluidic configuration within the fluorescence sensor.

1.7.3.2 Fabrication objectives.

When considering the microfluidic circuitry, some serious problems are identified. Firstly, etching channels with high aspect ratio, vertical and smooth walls is not currently possible with conventional reactive ion etching recipes. Secondly, a sealing technique of these channels has to be found in order to negate evaporation of fluids along the canals. The dielectric nature and non-flat surface of the deposited glass negates the simple use of bonding techniques, i.e. anodic bonding.

1.7.3.3 Demonstration of the intrinsic advantages of FHD glass for chemical sensing.

The advantages that FHD technique has for chemical sensing (see Section 1.7.2) must be demonstrated. Once a microfluidic circuitry and its sealing is performed, it will be necessary to carry out an expansion and enhancement of the functions that this device could have, e.g. micropumping, arraying a single device, and / or developing an optical treatment of the collected signal.

Regarding the optical circuitry, it is known that FHD technology has been extensively used on optical devices for telecommunications. This well established knowledge simplifies the development of fabrication process for integrated optics. However, the wavelength used in analytical chemistry (and in fluorescence in particular) is often much shorter than for telecommunications, necessitating smaller

structures and very small refractive index differences if monomode guiding is required. Miniaturisation can result in some difficulties in the fabrication process, since the acceptable fabrication tolerances will be much smaller too.

1.7.4 Major Achievements.

This research experimentally demonstrates that FHD technology is suitable for fabricating Lab-on-a-Chip devices. A planar silica device and its arraying have been developed for fluorescence measurements, assuring their future applicability to either biological or chemical assays. Application of these biochips in fluorescence assays have resulted in good performance (experimental detection limit of ca. 20 pM, equivalent to 10 zeptomoles or 6000 molecules of a fluorophore called Cy5) [98, 99, 100]. In addition, this technology can be integrated within a suitable fabrication protocol for mass production, such that optical chips can be made simultaneously with an associated microfluidics circuitry [101]. This capability has been enhanced by the adaptation of two additional bonding techniques to FHD glass. This allows us to seal fluidic channels and negate evaporation, either by using an elastomeric material [102], or by anodic bonding of pyrex™ overlayers [103,104]. Moreover, the enhancement of the fabrication of 'active' waveguides has produced a patent [105]. This patent is further explained in Appendix C. This work can increase the functionality of this device, by introducing active optical tools, such as, optical amplifiers and filters. Regarding FHD devices with single cell screening, a collaboration has been established with a company called New Dimension Research & Instrument, Inc (USA). This company is going to test some FHD devices fabricated through this research.

In conclusion, this research took a technology that allowed us to fabricate low loss waveguides for 1550 nm and now offers the possibility of fabricate optical sensor platforms such as the one shown in Figure 1.4.

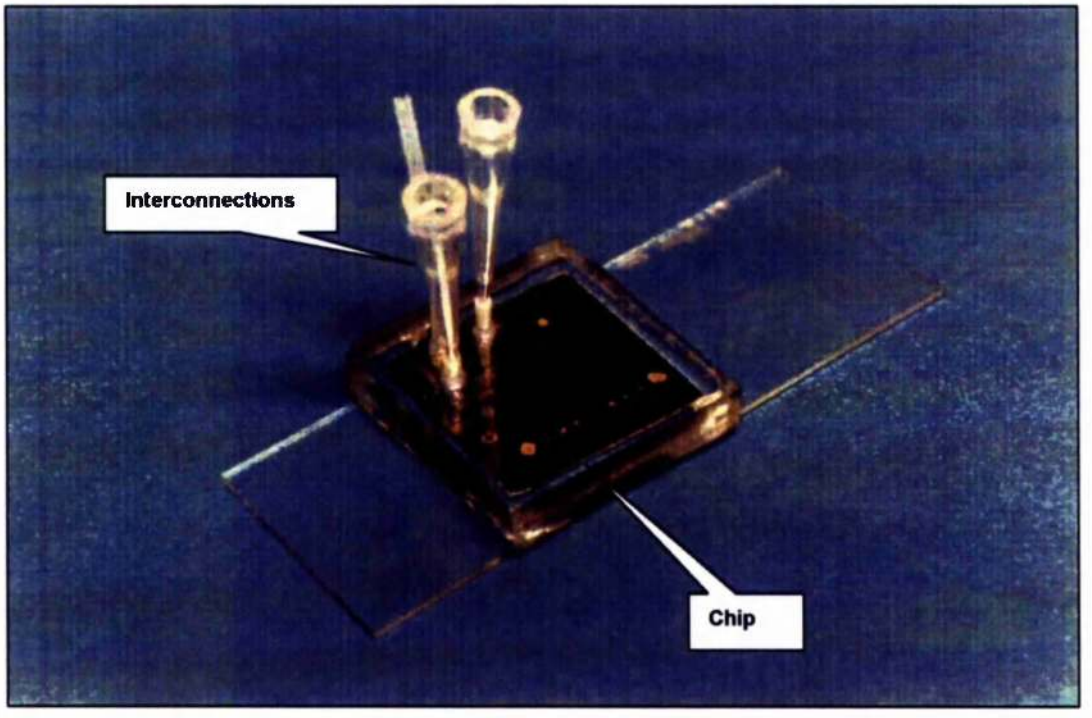

Figure 1.4: Picture of an optical sensor platform based on FHD and fabricated using the "catalogue" of processes developed during this PhD.

1.8 Thesis Outline.

Following this introduction, Chapter 2 describes the processes developed to fabricate a standard optical sensor that comprises sealed microfluidic channels and a buried optical circuitry.

Chapter 3 starts with a brief overview of fluorescence methods used in bioassays. Consequently, an optimisation of a fluorescence sensor design is presented. A FHD fluorescence sensor characterisation is then investigated, and the suitability of FHD glass as a biosensing substrate are discussed.

Chapter 4 presents integrated optical circuit designs and their particular fabrication issues, as well as the developing and testing of a 1x16 power splitter for arraying sensors. The application of integrated optics into the biosensing area is then investigated.

In Chapter 5, the use and flexibility of the techniques explained in Chapter 2 are discussed in order to fabricate more complex systems, such as, a separating element involved in a liquid chromatography system, and the pumping of liquids in a FHD optical device.

A final conclusion of the whole research is provided in Chapter 6 and, at the end, suggestions for future researchers are put forth.

Finally, the appendices offer some fabrication processes that impede the smooth development of the presentation of the thesis but which are also important, such as, techniques for hybrid integration and recipes for etching of rare earth doped glass. This section also includes instrumentation designs of apparatus designed during the thesis.

1.9 References.

1 Turner T.E., Karubc I., and Wilson G., Biosensors, London: Oxford University Press, 1998.

2 Hall E. A. H., Biosensors Cambridge University, Open University Press, 1990.

3 Boisdé G., Harmer A., Chemical and Biochemical Sensing with Optical Fibers and Waveguides, Artech House, Inc, 1996.

4 Wolfeis O. S., Fiber Optic Sensors and Biosensors, Vols. I and II, Boca Raton: CRC Press, 1991.

5 Blum L. J., and P. R. Coulet, Biosensor: Principles and Applications, New York: Marcel Dekker, 1991.

6 Freaney R., McShane A., Keaveny T.V., McKenna M., Rabenstein K., Scheller F.W., Pfeiffer D., Urban G., Moser I., Jobst G., Manz A., Verpoorte E., Widmer M.W., Diamond D., Dempsey E., deViteri F.J.S., Smyth M., Annals Of Clinical Biochemistry, Vol.34, No.Pt3, pp. 291-302, 1997.

7 Shichiri M., Sakakida M., Nishida K., Shimoda S., Artificial Organs, Vol.22, No.1, pp. 32-42, 1998.

8 Wolfbeis O.S., Klimant I., Werner T., Huber C., Kosch U., Krause C., Neurauter G., Durkop A., Sensors And Actuators B-Chemical, Vol.51, No.1-3, pp.17-24, 1998.

9 Chau M.T., Dominguez D., Bonvalot B., Suski J., Sensors And Actuators A-Physical, Vol. 60, No. 1-3, pp.86-89, 1997.

10 Dao R.E., Measurements & Control, No. 163, pp. 128-131, 1994.

11 Rutledge W.C., ISA Transactions, Vol. 31, No. 4, pp. 39-44, 1992.

12 Martinez F., Mitxelena J., Obieta G., Ruano J.M.,VII National Symposium on Pattern Recognition and Image Analysis., Bilbao., Vol. 1, pp. 337-344, 1999.

13 Mason A., Yazdi N., Chavan A.V., Najafi K., Wise K.D., Proceedings Of The IEEE, Vol. 86, No. 8, pp. 1733-1746, 1998.

14 Bryzek J., Peterson K.E., McCulley H.M., IEEE Spectrum, pp. 20-31, 1994.

15 Suzuki K., Ishihara T., Hirata M., Tanigwa H., IEEE International Electron Devices Meeting, Washington DC, Dec. 1-4, pp. 137-140, 1985.

16 Walsh S., Grace R., Micromachine Devices, pp.1, 1999.

17 Wrotnowski C., Biosensors and Chemical sensors, Business Communication Company, 1994.

18 Janata J., Kosowicz M., DeVaney D.M., Chemical sensors Anal. Chem, Vol. 66, 207R-28R, 1994.

19 Weetal H.H., Biosensors & Bioelectronics, 14, pp. 237-242, 1990.

20 Kirkpatrick D.L., Watson S., Ulhaq S., Combinatorial Chemistry & High Throughput Screening, Vol.2, No.4, pp.211-221, 1999.

21 Lammerink I.S., Spiering V.I., Elwenspoek M., Huntam H., and Berg A., IEE-MEMS'96 Workshop, pp. 389-394, 1996.

22 Fuhr G., Shirley S.G., J. Micromech. Microeng., 5, pp. 77-85, 1995.

23 Manz A., Graber N., Widmer H.M., Sensors and Actuators, 62, pp. 978-994, 1990.

24 Van den Berg A., Berfeld, μTAS'96 Conference, 17-22 Nov, pp. 9-15, 1996.

25 Effenhauser C. S., Bruin G. J. M., Paulus A., Ehrat M. Anal. Chem., Vol. 69, pp. 3451-57, 1997.

26 Bratten C. D. T., Cobbold P. H., Cooper J. M., Anal. Chem., Vol. 70, pp. 1164-70, 1998.

27 Dempsey E., Diamond D., Smyth M. R., Urban G., Jobst G., Moser I., Verpoorte E. M. J., Manz A., Widmer H. M., Rabenstein K., Freaney R., Anal. Chim. Acta, 346, pp. 341-49, 1997.

28 Griffith A., Cooper J. M., Anal. Chem., Vol. 70, pp. 2607-12, 1998.

29 Peterson J. L., and Goldstein S. R., U.S. Pat. Appl. 855,384 (1977); U.S. Pat 4,200,110 (1980).

30 Peterson J. L., and Goldstein S. R., U.S. Pat. Appl. 855,397 (1977); U.S. Pat 4,194,877 (1980).

31 Lubbers D. W., and Opitz N., Naturdorsch Z., Vol. 30C, pp. 532-533, 1975.

32 Robinson G., Sensors and Actuators B-Chemical, Vol.29, No.1-3, pp.31-36, 1995.

33 Karube I., Suzuki S., Journal of synthetic organic chemistry, Vol.40, No.3, pp.227-233, 1982.

34 Feast W.J., and Munro H.S., Polymer Surfaces and Interfaces, New York:Wiley,1987.

35 Symour R.B., Mark H.F., Applications of Polymers, New York: Wiley,1988.

36 Nicholson J. M., The chemistry of Polymers, Cambridge: Royal Society of Chemistry,1991.

37 Puyol M., del Valle M., Garces I., Villuendas F., Dominguez C., Alonso J., Anal. Chemistry, 71, pp. 5037-5044, 1999.

38 Petric A., Jacobson A.F., Barrio J.R., Bioorganic & Medicinal Chemistry Letters, Vol. 8., No. 12, pp. 1455-1460, 1998.

39 Werner T., Huber C., Heinl S., Kollmannsberger M., Daub J., Wolfbeis O.S., Fresenius Journal Of Analytical Chemistry, Vol. 359, No.2, pp. 150-154, 1997.

40 Aich S., Basu S., Photochemistry And Photobiology, Vol.70, No. 4, pp. 602-606, 1999.

41 Sethi R.S., Gec Journal of research, Vol. 9, N. 2, 1991.

42 Lukosz W., Abstracts of papers of the American Chemical Society, Vol.213, No.Pt1, pp.210-ANYL, 1997.

43 Zhou Y., Laybourn P.J.R., Magill J.V., Delarue R.M., IEE Proceedings-J Optoelectronics, Vol.139, No.3, pp.223- 227, 1992.

44 Plowman T.E., Reichert W.M., Biosensors & Bioelectronics, Vol. 11, N. 1/2, pp. 149-160, 1996.

45 Heideman R.G., Kooyman P.H., Greve J., Sensors and Actuators B, 10, pp.209-217, 1993.

46 Duport I.S., Helmers H., Greco P., Wagner R., Rimet R., Sensors and Materials, Vol.8, No. 4, pp. 193-198, 1996.

47 Luff B.J., Wilkinson J.S., Piehler J., Hollenbach U., Ingenhoff J., Fabricius N., J. Of Lightwave Technology, 16, N. 4, 1998.

48 Lukosz W., Biosensors & Bioelectronic, 6, pp. 215-225, 1991.

49 Sjoelander S., And Urbaniczky C., Anal. Chem., 63, pp. 2338-2345, 1991.

50 Van den Doel, Part of the SPIE Conf. on Micro- and Nanofabricated Structures and Devices for Biomedical Environmental Applications II, Jan 1999.

51 Wadkins R.M., Golden J.P., Pritsiolas L.M. and Ligler F.S., Biosensors & Bioelectronics, Vol. 13, No. 3-4, pp. 407-415, 1998.

52 Rowe C.A., Anal. Chem., Vol. 71, pp. 3846-3852, 1999.

53 Narang U., Gauger P.R., Kusterbeck A.W., Ligler F.S., Anal. Biochem., 255, pp.13-19, 1998.

54 Manz A., Graber N., Widmer H.M., Sensors And Actuators B-Chemical, Vol. 1, No. 1-6, pp. 244-248, 1990.

55 Manz A., Harrison D.J., Verpoorte E., Widmer H.M., Advances In Chromatography, Vol.33, pp. 1-66, 1993.

56 Harrison D.J., Fluri K., Chiem N., Tang T., Fan Z., Sensors & Actuators B, 33, pp. 105-109, 1996.

57 Chen F.A. *et al*, J. Of Chromatography A, 652, pp.355-360, 1993.

58 Bao J., Regnier F.E., J. Chomatogr. 608, pp. 217-224, 1992.

59 Avila L.Z., and Whitesides G.M., J. Org. Chem., 58, pp. 5508-5512, 1993.

60 Paul C.H., Harrison D.J., Anal. Chem., pp. 1564-1568, 1997.

61 Broach J.R, Thorner J., Nature Suppl., 384, pp. 14-16, 1996.

62 Fodor S., Nature, 364, pp. 555-556, 1993.

63 Allue I., Gandelman O., Dementieva E. Ugarova N., Cobbold P. H., Biochem. J., 319, pp. 463–469, 1996.

64 Takahashi A., Takamatsu T., Calcium Signalling, 9, pp. 617-625, 1997.

65 Cheng L.Z., Fu J., Tsukamoto A., Hawley R.G., Nature Biotechnology, 14, pp. 606-609, 1996.

66 Bratten C. D. T., Cobbold P.H., Cooper J.M., Analytical Chemistry, Vol.70, pp. 1164-1170, 1998.

67 Jiang L., Glidle A., Griffith A., McNeil C.J., Cooper J.M., Bioelectrochemistry And Bioenergetics, Vol.42, No.1, pp. 15-23, 1997.

68 Knox J.H., J. Chromatography Sci., 18, pp. 453-461, 1980.

69 Bing H., Tait N., Regnier F., Anal. Chem., Vol. 70, pp. 4974-4984, 1998.

70 Henry C., Chemical & Engineering News, Vol.77, No.37, p.9, 1999.

71 DeRisi J.L., Iyer V.R., Brown P.O., Science, Vol.278, No.5338, pp.680-686, 1997.

72 Cheung V.G., Nature Genetics, Vol.18, No.3, pp.225-230, 1998.

73 Duggan D.J., Bittner M., Chen Y.D., Meltzer P., Trent J.M., Nature Genetics, Vol.21, No.SS, pp.10-14, 1999.

74 Bowtell D., Nature Genetics, Vol.21, No.2, p.241, 1999.

75 Brown P.O., Botstein D., Nature Genetics Supplement, 21, pp. 33-37, 1999.

76 Leistiko O., Friis P., Part of the SPIE Conf. on Micro- and Nanofabricated Structures and Devices for Biomedical Environmental Applications II, Jan 1999.

77 Bruno A. E., Barnard S., Rouilly M., Walder A., Berger J., Ehrat M., Anal. Chem., Vol. 69, 507-13, 1997.

78 Bruno A.E., Maystre F., Krattinger B., Nussbaum P., Gassmann E., Trends Anal. Chem., 8, pp. 190-198, 1994.

79 Hyde J. F., U. S. Patent, no. 2, 272,342, 1942.

80 Kawachi M., Yasu M., Edahiro T., Electronics Letters, Vol.19, No.15, pp.583-584, 1983.

81 Kawachi M., Opt. Quantum Electron., 22, 391, 1990.

82 Barbarossa G., PhD Thesis, Glasgow University, 1990.

83 Bonar J. R., PhD Thesis, Glasgow University, 1995.

84 Mclaughlin A. J., PhD Thesis, Glasgow University, 1998.

85 Vermelho M., PhD Thesis, Glasgow University, 1999.

86 Marques P.V.S., PhD Thesis, Porto University, 2000.

87 Irving S.R., Solid State Technol., 14, 47, 1997.

88 Coburn J.W., Short Course 23, SPIE, San Jose, 1990.

89 Kimura J., Kawana Y., and Kuriyama T., Biosensors and Bioelectron., 4, pp. 44-48, 1988.

90 Thompson W.R., Cai M., Ho M.K., Pemberton J.E., Langmuir, Vol.13, No.8, pp.2291-2302, 1997.

91 Mukherjeeroy M., Kurihara M., Penn L.S., Journal Of Adhesion Science And Technology, Vol.9, No.7, pp.953-969, 1995.

92 Kovacs G., Petersen K., Albin M., Analytical Chemistry, Vol.68, pp. 407-412, 1996.

93 Yamada Y., Kawachi M., Yasu M., Kobayashi M., Electron. Lett., 20, 589, 1984.

94 Yamada Y., and Kobayashi M., J. Lightwave Technol., 5, 1716, 1987.

95 Jones C.A., Cooper K., IEE Proc.-Optoelectron., Vol. 143,N. 5, 1996.

96 Kawachi M., Yamada Y., Yasu M, Kobayashi M., Electron. Lett., 21, 314, 1985.

97 Kawachi M., Kobayashi M., and Miyashita T., Proc. IGWO'86, FDD5, Atlanta, Feb. 1986.

98 Ruano J.M., Benoit V., Aitchison J.S., Cooper J.M., Anal.Chem., Vol.72, pp. 1093-1097, 2000.

99 Ruano J. M., Ortega D., Bonar J. R., Cooper J. M. and Aitchison J. S., Proc. MNE 98 Conference, 1998.

100 Ruano J. M., Ortega D., Bonar J. R., Cooper J. M., Aitchison J. S., CLEO Europe 98 Proc., 198, 1998.

101 Ruano J.M., Ortega D., Bonar J.R., McLaughlin A.J., Jubber M.G., Cooper J.M., Aitchison J.S., Journal of Microelectronic Engineering, Vol.46, No.1-4, pp.419-422, 1999.

102 Ruano J.M., Benoit V., Aitchison J.S., Cooper J.M., Microengineering in Optics and Optoelectronics, pp.12/1-12/6, 1999.

103 PCT Patent Application, 1999.

104 Ruano J.M., Benoit V., Aitchison J.S., Cooper J.M., Smalltalk 99, San Diego, CA, 1999.

105 Ruano J.M., McLaughlin A.J., Bonar J.R., Jubber M.G., Marques P.V.S., Wilkinson C.D.W., Aitchison J.S., "A reactive ion etching process", 9907302.5, 31st March 1999.

Chapter 2: FABRICATION PROCESSES DEVELOPED FOR BIOCHEMICAL SENSING ON FHD GLASS.

2.1 Introduction.

In this chapter, traditional MEMS techniques such as Reactive Ion Etching (RIE), fuse bonding, anodic bonding, and hybrid integration techniques are adapted and combined with FHD to fabricate biochemical sensing devices. This combination of processes enables the production of very deep etched trenches in FHD glass, and allows these channels to be sealed, producing the necessary microfluidic circuitry together with an optical circuitry. The integration of both circuits in a device avoids the precise alignment requirements and results in a compact and stable device. Moreover, this integration lends itself to the Lab-on-a-Chip concept since the microfluidic circuitry increases the number of functions that can be carried out in a sensing device.

This chapter describes in detail the fabrication protocols used on the FHD glass. The first process is the fabrication of an optical sensor. This sensor consists of an optical circuitry and a set of deep micro-channels. Subsequently, different bonding approaches are described to seal the microfluidic channels.

This set of protocols will be used as a library of processes to develop a variety of more complex functions, such as integrated optical devices, micro-pumping, arraying sensors, or liquid chromatography on FHD glass. To the author's

knowledge, this is the first time that these tasks have been integrated on FHD glass for biosensing purposes. These applications are, therefore, further explained in Chapter 4 and Chapter 5.

2.2 Fabrication Steps for an Optical Sensor on FHD glass.

The fabrication protocol of an optical sensor for bio-chemical sensing involves the fabrication of an optical circuitry, and more importantly, the etching of deep, smooth, and vertical trenches. The optical circuitry consists of integrated optical structures working as a transducing mechanism. The micro-fluidic system contains a micro-analytical chamber and its associated micro-channels. The analyte must be located in the chamber to make the measurement. This optical sensor is the initial and fundamental part of a Lab-on-a-Chip. This simple device is completed by sealing the micro-fluidic system and by a final packaging stage to facilitate its use and commercialisation.

This section describes the fabrication protocol of the optical sensor and the overall fabrication of the micro-channels. The etched trenches need to be deep since they have to reach the optical circuitry that is, in turn, buried deeply to minimise transmission losses. They also need to be smooth and vertical to decrease the scattering losses produced when the light reaches the micro-analytical chamber (see Chapter 3).

The design of the optical system may vary in order to accomplish distinct kinds of transducing mechanisms, including: evanescent field, fluorescence, interferometry or surface plasmon. Nevertheless, the fabrication protocol would always include the same basic steps. The process starts with thermal oxidation of the silicon substrate followed by FHD of silica, photolithography and RIE processes to obtain an optical circuitry (see Figure 2.1.a). Again, the same sequence of events (FHD, photolithography and RIE) is used to fabricate the microfluidic circuitry (See Figure 2.1.b).

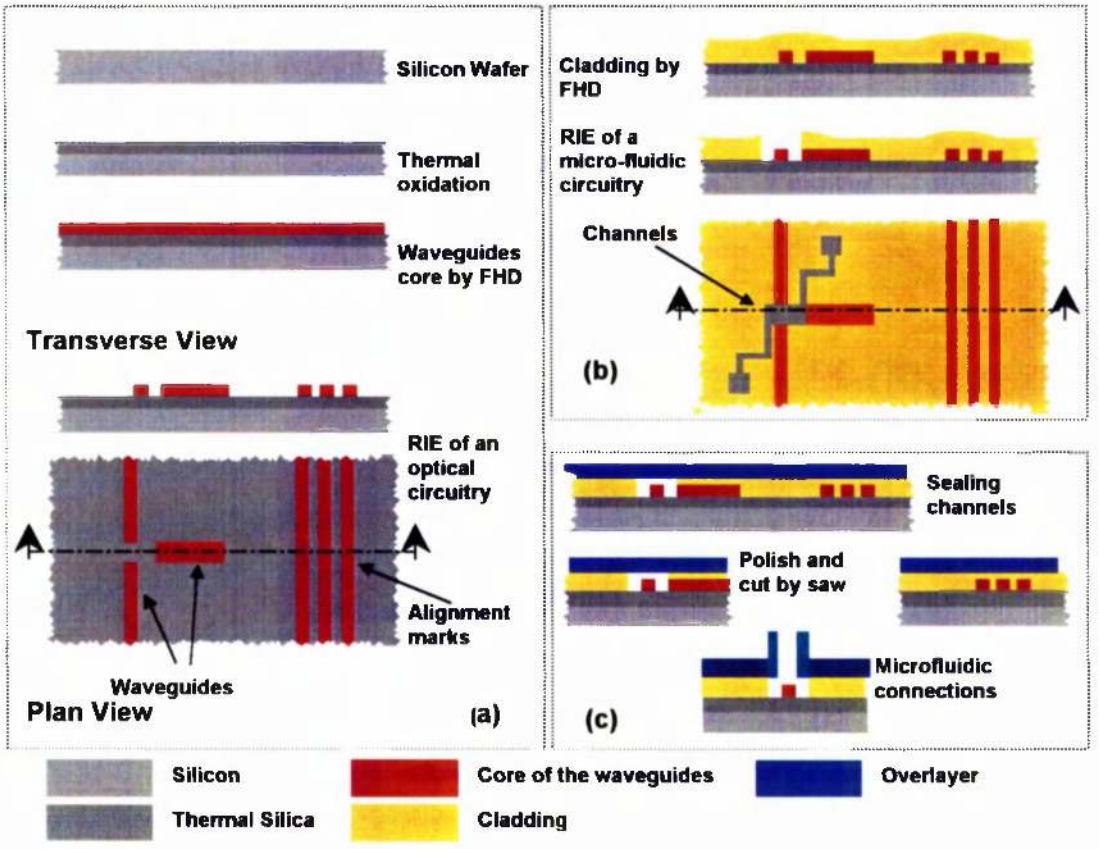

Figure 2.1: Schematic representation of the steps involved in the fabrication of an optical chemical sensor based on FHD glass. (a) Optical circuitry. (b) Cladding and Micro-fluidic circuitry. (c) Packaging issues

This seven-stage procedure was used to fabricate a fluorescence sensor that was successfully tested (see Chapter 3). This work demonstrated that this protocol is an effective method to fabricate a variety of biosensors. It should be noted that some variation in each process is required in order to fabricate different optical or microfluidic configurations. The deposition of layers of glass with different refractive indexes, thicknesses, or the use of different photolithographic masks for the optical and microfluidic circuits provides great flexibility for the fabrication of a range of optical sensors. For example, a "bulk" fluorescence transducing mechanism (analyte in solution) requires three elements: an analytical chamber where the liquid with fluorescently labelled molecules is placed; an excitation

waveguide to pump this sample; and at least one waveguide to collect the fluorescence, generated in the chamber.

Each of the seven fabrication steps are described in the following seven subsections and are summarised in the following points:

1. Thermal oxidation of a silicon wafer to achieve 16 μm (depth) of SiO_2.
2. Deposition of $SiO_2 - GeO_2$ glass by FHD technique.
3. Photolithography step to transfer the waveguide pattern into a photoresist layer.
4. RIE of the $SiO_2 - GeO_2$ glass to obtain the optical circuitry.
5. Deposition of $SiO_2 - P_2O_5$ by FHD technique (the cladding of the waveguides).
6. A photolithography step to transfer the micro-channels pattern into photoresist.
7. RIE of chambers and channels in order to accomplish a microfluidic circuitry.

These seven steps form the nucleus of our Lab-on-a-Chip technology. However, in order to complete the fabrication of this chip some further steps are necessary, such as, the sealing of the etched channels and chambers to avoid evaporation (described in Section 2.3), as well as, some packaging issues (e.g. microfluidic interconnections, or encapsulating) described in Chapter 5. These enhancements allow us to carry out more complex functions regarding mixture, separation or movement of liquids, without hand manipulation.

The layout of the photolithographic masks was designed using the CATS™ software. A Leica 5 electron beam writer (Leica, Cambridge, UK) was used to

write three 2.5 inch x 2.5 inch ferric mask plates for the optical and the microfluidic designs. Two masks were used for defining masks for RIE using photolithography, and an extra photolithographic mask for alignment purposes. The photoresists used were S1818, S1828 and AZ4562 from Shipley. Metals, including Cr and Ni, were from Goodfellows, Cambridge, UK. It is important to point out that is necessary to incorporate alignment marks on the masks if, in the same device, chambers or channels, are integrated with the optical circuitry (see Section 2.2.6.1).

In Figure 2.1 as well as the following illustrations in the thesis, each material has been assigned with a colour, to help the reader fully comprehend the following fabrication steps.

2.2.1 Thermal Oxidation of Silicon Wafers.

The oxidation of the silicon wafer is the starting point of the whole process. The substrates used are 3 inch-diameter silicon wafers, ~500 μm thick. A 16 μm-thick layer of SiO_2 was thermally grown on the surface at 1100°C for 14 hours. This "under-cladding" was used to isolate the waveguides from the silicon substrate because of its non-transparent nature, its high refractive index, and also because FHD soot does not sinter on silicon. British Telecom (BT) laboratories optimised this silicon oxidation process, producing SiO_2 with a resultant refractive index value of 1.4572. at 632.8 nm

2.2.2 FHD of $SiO_2 – GeO_2$ Glass.

FHD is used to deposit a planar, high-silica content film that will form the core of the waveguides. In this process, metal halides such as $SiCl_4$, $GeCl_4$ and BCl_3, are hydrolysed in an oxy-hydrogen flame (see Section 1.6.1) to form a low density oxide 'soot'. The hydrolysis process of these glasses can be described by Equations 1.1-1.4 in Chapter 1.

The SiO_2-B_2O_3-GeO_2 glass is initially deposited as a "soot", which is then sintered at 1350°C for 2 hours. The parameters used in this run are outlined in Table 2.1, and they gave a total thickness of 9 μm, and a refractive index measured by a prism coupling technique [1] of 1.4637 at 632.8 nm.

Warming stage:				
Initial turntable temperature: 150 ° C		Torch warming transversals		
		Number:	2	
		Oxygen:	2 l min^{-1}	
		Hydrogen:	5 l min^{-1}	
		Nitrogen:	3 l min^{-1}	
Deposition stage:				
Halides flows:		Torch flows:		
$SiCl_4$: 150 sccm*		Number:	8	
$GeCl_4$: 62 sccm		Oxygen:	2 l min^{-1}	
BCl_3: 65 sccm		Hydrogen:	5 l min^{-1}	
Master: 638 sccm		Nitrogen:	3 l min^{-1}	
Sintering cycle:				
Initial Temperature	Increasing rate	Sintering time and temperature	Decreasing rate	Final Temperature
1050 °C	15 °C min^{-1}	2 hours at 1350 °C	-10 °C min^{-1}	750 °C
Sintering atmosphere:				
Helium: 0.7 l min^{-1}		Oxygen: 0.1 l min^{-1}		

Table 2.1: Deposition parameters of $SiO_2 - GeO_2$ for the fabrication of an optical circuitry with a resultant refractive index value of 1.4637 and 9 μm-thick. This process is divided in warming stage, deposition stage and sintering cycle. * sccm: standard cubic centimetre gas flow per minute.

Once this process was completed, it was necessary to pattern the optical circuitry onto this new high refractive index glass by photolithography and subsequently

RIE. The next section will explain the former process that transfers a metallic pattern, from a mask to the silica, using photolithography.

2.2.3 Photolithography of the Optical Circuitry.

The starting point for the photolithography step, was a silicon wafer with two silica layers on it (SiO_2, n = 1.4572 ; SiO_2-doped, n = 1.4637 at 633 nm). The cleaning process involved successive immersion in an ultrasonic bath in Opticlear, acetone, and methanol, followed by an acid bath with Piranha solution (90% H_2SO_4 / 10% H_2O_2). After this exhaustive cleaning process, a resistive evaporation of 75 nm of nichrome was performed (NiCr 90 %; 10%), followed by spinning, UV exposure (20 mW cm^{-1}) and the development of S1828 photoresist to transfer the desired metallic pattern on top of the silica.

The polymer was spun for 30 seconds at 4000 rpm, obtaining a thickness of approximately 2.8 μm. The polymer was exposed to ultraviolet light for 12 seconds and developed for 100 seconds in a solution with one part of MF351 and four parts of reverse osmosis water. Before carrying out the nichrome wet etch, a post-bake for 20 minutes at 120 °C was performed in order to harden the photoresist. During the photolithographic process, the substrate was immersed in a NiCr wet etch (8 M ammonium ceric nitrate in 3:1 glacial acetic acid/RO water) in order to remove the non protected metal (See Figure 2.2). This final step left a mask for the next reactive ion etching step (comprising 75 nm thick of NiCr and 2.8 μm of photoresist). Previous experiments had confirmed that S1828 photoresist is appropriated for patterns larger than 1 μm. Nonetheless, due to its thickness, it does not enable very deep structures to be formed in the subsequent RIE process.

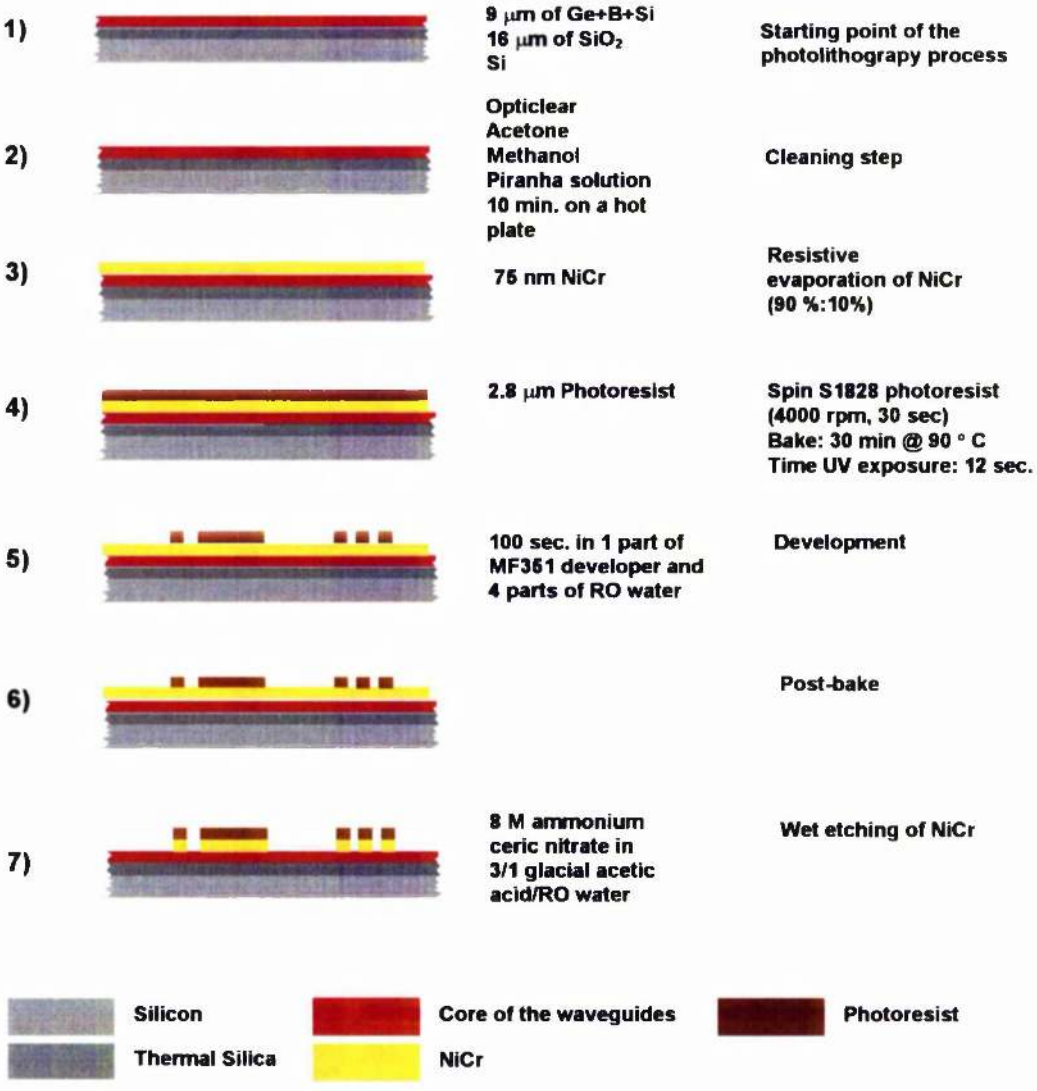

Figure 2.2: Photolithography of an optical circuitry. A NiCr layer is patterned by S1828 and subsequently wet-etched. This process leaves a mask formed by 75 nm thick of NiCr and 2.8 μm of photoresist for the coming RIE of $SiO_2 - GeO_2$ glass.

2.2.4 RIE of the Optical Circuitry.

Once the photolithography has been performed, RIE was used to define the pattern of the silica layer. This RIE process uses an Oxford PlasmaTechnology RIE80 machine, previously cleaned prior to each etch run for 15 minutes with an oxygen plasma.

The RIE technique developed, was inspired by recent work that demonstrated the possibility of making smooth and vertical waveguides with acceptable etching rates using NiCr mask [2,3]. This RIE process of the waveguides was very demanding in terms of verticality and smoothness of the walls in order to keep the optical scattering losses as low as possible. Deep silica etching was not necessary as the waveguides were only 9 μm thick. The samples were initially coated with a bilayered mask. The upper layer of photoresist protects the NiCr layer from the plasma, and reduces sputtering and the subsequent redeposition of NiCr in the bottom of the etched waveguide. The lower NiCr layer increases the smoothness and verticality of the etched walls dramatically. The benefits of using this bilayer mask becomes more evident during the etching of the channels, where a thicker photoresist makes it possible to achieve much deeper structures (see Section 2.2.7). The etch rate was 78 nm min^{-1} using a CHF_3 etch. The flow rate, etching pressure, and RF power were 25 sccm, 60 mT and 190 W, respectively, giving a selectivity of 5.5 to 1 over the photoresist layer. Four runs of 30 minutes were carried out on the sample in order to etch the 9 μm of FHD glass previously deposited. Before each run, a standard oxygen cleaning process was performed in the machine, to keep the chamber free of contamination. To conclude, the substrate was immersed in acetone and then in nichrome wet etchant in order to remove the remaining photoresist and mask respectively (see Figure 2.3).

Shipley S1828 produces better RIE etch results with less undercutting than Shipley S1818 photoresist. The reason could be connected to the fact that S1828 is more resistant and harder than S1818, due to its thicker and more viscous nature. However, the pattern to be transferred to the glass must be larger due to its higher viscosity.

2.2.4.1 Analysis of RIE.

A DekTak surface profiler was used to measure the mask's thickness prior to, and after etching. A Talystep measurement was also used to corroborate the results.

A Hitachi S-800 scanning electron microscope was used to examine and verify the quality of the etch profiles of the samples.

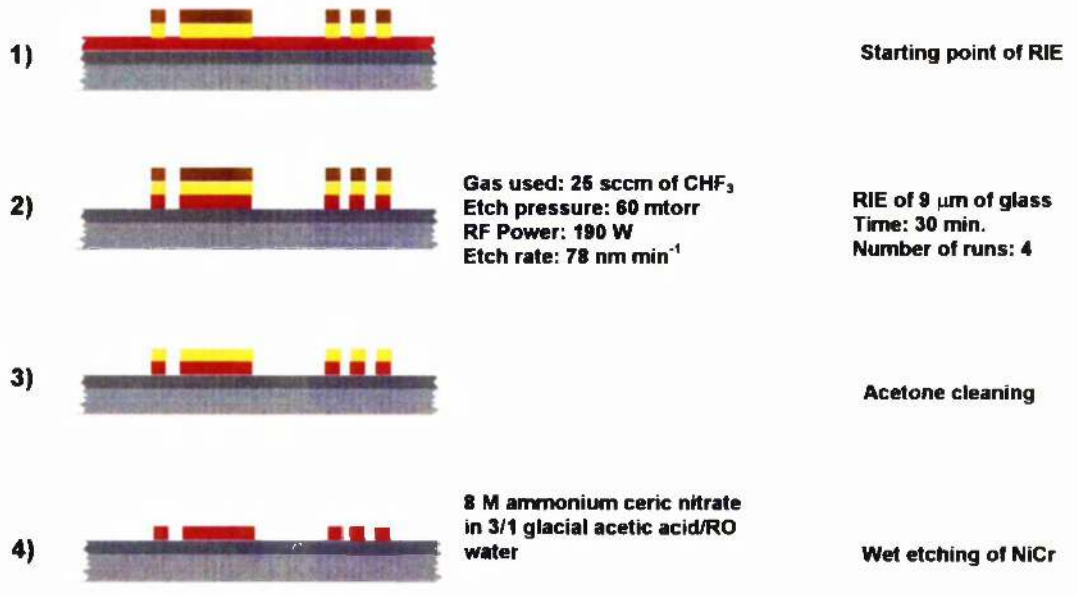

Figure 2.3: RIE of optical circuitry using a bilayer mask comprising nichrome and photoresist.

2.2.5 FHD of $SiO_2 - P_2O_5$ Glass.

Before FHD was used again to deposit a second cladding glass layer, an exhaustive cleaning process was done using an ultrasonic bath in Opticlear W™, acetone, methanol and a final rinse in RO water as described before. Piranha solution (90% H_2SO_4 / 10% H_2O_2) was not used since this solution leaves some material adsorbed on the waveguide's walls, producing artefacts in the following sintering stage. This second glass layer produces a cladding for the waveguides and its refractive index matches that of the thermal oxide underlayer. This equal refractive index was achieved using a mixture of phosphorus (P_2O_5) and boron (B_2O_3) oxide doped glasses. The hydrolysis process of the cladding glass is described by Equations 1.1-1.4 in Chapter 1.

The SiO_2-B_2O_3-P_2O_5 glass was initially deposited as a "soot", which was then sintered at 1150°C for 75 minutes. After this time, glass with a refractive index of 1.4572 was formed (shown schematically as the gold colour in Figure 2.1). It was necessary to engage in three runs of 8 traverses to complete the 24μm layer depth. The parameters used in these runs are outlined in Table 2.2.

Warming stage:				
Initial turntable temperature: 150 ° C		Torch warming transversals		
		Number:	4	
		Oxygen:	2 l min^{-1}	
		Hydrogen:	5 l min^{-1}	
		Nitrogen:	3 l min^{-1}	
Deposition stage:				
Halides flows:		Torch flows:		
$SiCl_4$: 150 sccm		Number of transversals :	8	
PCl_3: 40 sccm		Oxygen:	2 l min^{-1}	
BCl_3: 90 sccm		Hydrogen:	4 l min^{-1}	
Master: 660 sccm		Nitrogen:	3 l min^{-1}	
Sintering cycle:				
Initial Temperature	Increasing rate	Sintering time and temperature	Decreasing rate	Final Temperature
850 °C	20 °C min^{-1}	75 min at 1150 °C	-15 °C min^{-1}	850 °C
Sintering atmosphere:				
Helium: 0.7 l min^{-1}		Oxygen: 0.1 l min^{-1}		

Table 2.2: Deposition parameters of SiO_2 – P_2O_5 for the fabrication of the cladding of the optical circuitry. This process is divided in warming stage, deposition stage and sintering cycle. * sccm: standard cubic centimetre gas flow per minute.

2.2.6 Photolithography of the Microfluidic Circuitry.

The initial photolithographic step was carried out on a silicon wafer with the optical circuitry buried in a 24 μm- thick cladding layer. A RIE mask, formed by deposition of 150 nm of NiCr, and 6 μm of polymer had to be transferred to the

substrate by photolithography. This new pattern (which formed the template for the microfluidic circuitry) was aligned to the buried optical circuitry through alignment marks. This was not a straightforward alignment process, because the NiCr layer used as a RIE mask was opaque. Therefore, a selective deposition of the NiCr masking was needed in order to "see" the alignment marks. This process was carried out by lift-off of the metal covering the alignment marks. This step is explained in detail in the following section.

2.2.6.1 Alignment considerations.

The alignment problem could not be simply solved by written alignment marks both in the optical and in the microfluidic masks. Due to the non-transparency nature of NiCr, an extra photolithographic mask is needed to open a window in this metal layer. Hence, the whole process for the fabrication of a standard optical sensor required three photolithographic masks. Figure 2.4 summarises the process, focusing on the three alignment processes of the patterns. The first mask (top) is a light field mask with waveguides and two alignment marks (broad U shaped). After this photolithographic process (Section 2.2.3), and the RIE and FHD steps (see Section 2.2.4, and 2.2.5 respectively), the second mask (middle) was employed in order to deposit a photoresist window over the alignment marks and their surroundings, in order to facilitate the subsequent selective removing of NiCr by lift-off. Finally, the third mask (bottom of Figure 2.4) consisted of a dark field mask with the microfluidic channels and the alignment marks. To conclude the whole process, a RIE of the channels was carried out as explained in the next section.

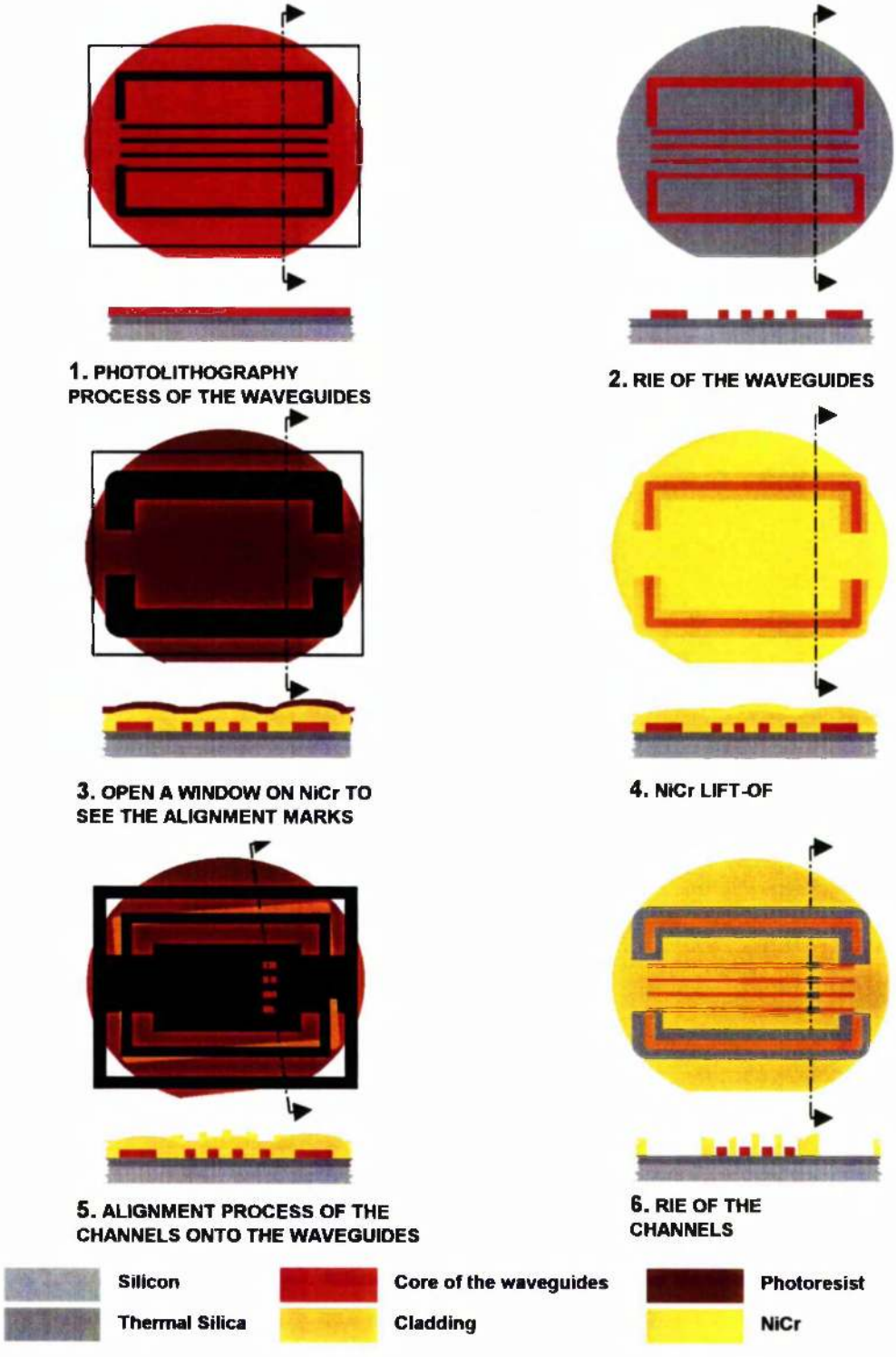

Figure 2.4: Schematic representation of the three alignment processes. The first mask (top) corresponds to a light field mask with waveguides and alignment marks (broad U shaped). Subsequently, the RIE and cladding of the waveguides were carried out. The second mask (middle) was then employed in order to deposit a photoresist window to selectively remove NiCr by lift-off. Finally, the third mask consisted of a dark field mask

with the channels and the alignment marks. Notice that the mis-alignment can be easily seen due to the windows open in the NiCr and the dark field mask.

In the context of the alignment mark pattern, it was found that long strips were more convenient because they minimised the alignment error. Broad U shapes were used because their corners made it possible to align the two axes, vertically and horizontally. The alignment marks were written using a dark field mask (microfluidic circuitry) and were identical to those written using the first photolithographic mask. Therefore, both the channel circuitry and a transparent window with the alignment marks had to be written onto the dark mask to make the substrate visible. Figure 2.4 represents an example of a useful alignment pattern. The mis-alignment could be easily distinguished due to the open windows both on the NiCr and on the dark field mask.

The procedure to open a window in the NiCr (steps 3 and 4 in Figure 2.4) is thoroughly explained in Figure 2.5. The initial step involved a silicon wafer with the optical circuitry buried in a cladding layer of 24 μm- thick. After the cleaning process, spinning, UV exposure, and development of S1818 photoresist (from Shipley, UK) were carried out, using standard protocols. The tolerances involved in this alignment are very large because the only purpose of this process is to deposit photoresist on top of the alignment marks and surrounding them. Subsequently, 150 nm of NiCr was evaporated onto the sample, which was then immersed in acetone to perform the lift-off. This process released the NiCr that was on top of the polymer, leaving the alignment marks visible for the next alignment process.

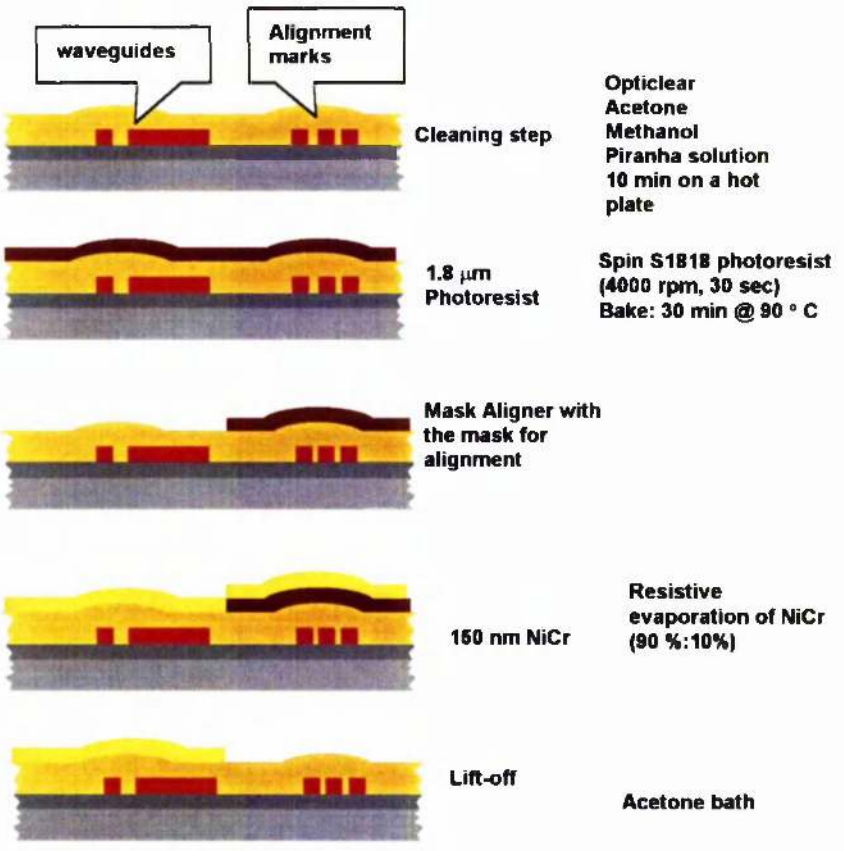

Figure 2.5: This fabrication procedure opened a window on the NiCr layer. This window makes it possible to see the alignment marks used for the next alignment of the microfluidic circuitry mask.

2.2.6.2 Photolithography protocol for RIE of deep channels.

Once the alignment window was opened in the NiCr, the third and final photolithographic process was carried out to transfer the metallic "microfluidic" pattern into the silica (see Figure 2.6). This procedure was more demanding than the one just performed in terms of quality of transferred profiles and alignment between the desired microfluidic patterns and the optical substrate. In order to fulfil the needs of a subsequent deep reactive ion etching, a thick photoresist was used. Shipley AZ4562 photoresist replaced the well known S1818 or S1828 processes. The polymer was spun at standard conditions, namely 30 seconds at 4000 rpm. Experiments confirmed that AZ4562 could only be used for patterns with feature sizes larger than 2 μm.

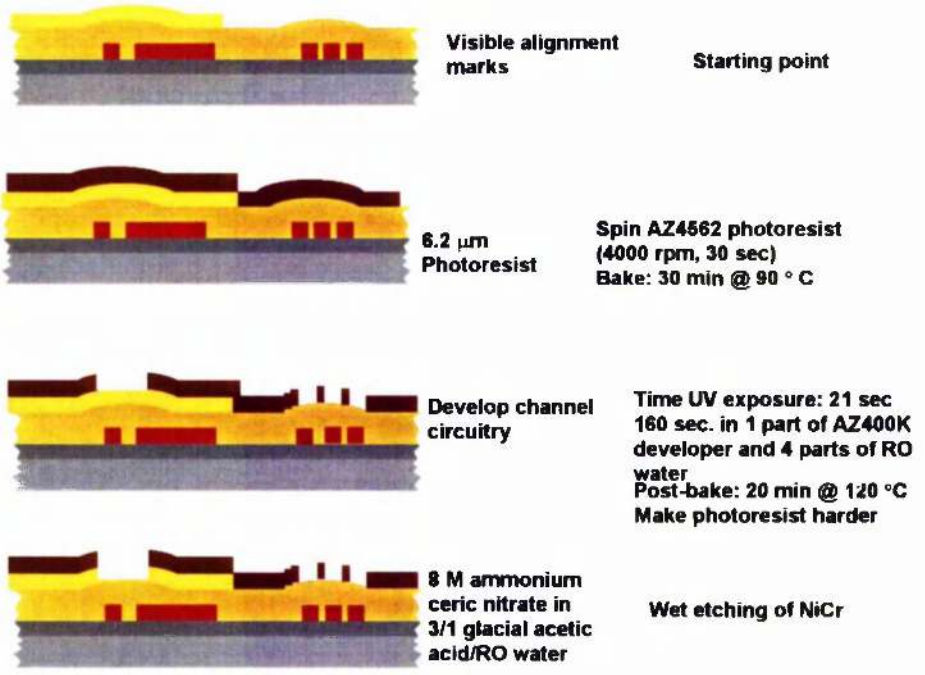

Figure 2.6: Photolithography of a microfluidic circuitry. A NiCr layer was patterned by AZ4562 and subsequently wet-etched. This process left a mask formed by 150 nm thick of NiCr and about 6 μm of photoresist for the coming RIE of $SiO_2 - P_2O_5$ glass.

Although the photolithographic protocol for S1818 and S1828 are well established, consideration must be given to the fact that AZ4562 polymer is very thick, and a uniform thickness of the photoresist covering the entire substrate is more difficult to achieve. The spinning process is described in detail in the following steps:

1. Standard cleaning for photolithography.
2. Fill the syringe with AZ4562 polymer (filtration is not necessary).
3. Cover the sample with the photoresist using the syringe.
4. Leave the photoresist spread out on the sample for 2 minutes.
5. Spin the sample (30 seconds at 4000 rpm).

6. Allow the photoresist to spread out on the sample for 10 minutes.

7. Bake the photoresist for 30 minutes at 90 °C.

After this, the substrate was selectively UV exposed through the ferric mask (20 seconds) and subsequently developed for 160 seconds (1 part of AZ400K developer with 4 parts of RO water). Finally, the photoresist was post-baked for 20 minutes at 120 °C achieving a final photoresist thickness of 6 μm.

During the photolithographic process, the substrate was immersed in a nichrome (NiCr) wet etch (8 M ammonium ceric nitrate in 3/1 glacial acetic acid/RO water) in order to remove the non protected nichrome (See Figure 2.6). This final step left a mask for the subsequent RIE of the FHD silica. This novel mask is formed by 150 nm thick NiCr and 6 μm of photoresist. The reason for the use of this bilayer mask is explained in the next section.

2.2.7 RIE of Channels and Analytical Chambers in FHD glass.

The starting point of this step was a device with an optical circuitry buried in the glass, plus a bilayer mask formed by NiCr and AZ4562 photoresist on top of it. The RIE process was used to etch the analytical chamber through the cladding, reaching the optical circuitry. This etched chamber allowed us to bring the liquid in contact with the optical circuitry. Independently of the optical transducing mechanism used in the optical bio-chemical sensor, the etching has to be deep enough to reach the waveguides, with smooth and vertical walls to minimise the losses in the interface between the liquid and the integrated optics. Channels connected to the analytical chamber were also etched into the device. Once these channels were sealed, the device will offer the possibility to perform not only a measurement of the liquids, but also the free manipulation of the liquid.

The etching process was carried out in the Oxford PlasmaTechnology RIE80 machine. Unlike conventional etching of waveguides, where ridges are simply produced by a NiCr mask [3], this research concentrated on the etching of deep

trenches 4 - 20 μm wide. In this case, the area to be etched is small and there is a lot of metallic masking material to protect the rest of the chip. During the RIE process, the mask will be partially removed and some of the materials will be unavoidably deposited in the trenches. Furthermore, this debris may be trapped in the holes or channels. This has dramatic consequences by causing imperfections in the etched silica trenches. As stated, to produce the needed etching features, a combination of two mask layers were used. The upper layer of photoresist protects the NiCr layer and reduces sputtering, and the subsequent redeposition of NiCr in the bottom of the etched channel, whilst the NiCr layer increased the smoothness and verticality of the etched walls dramatically (see Figure 2.7).

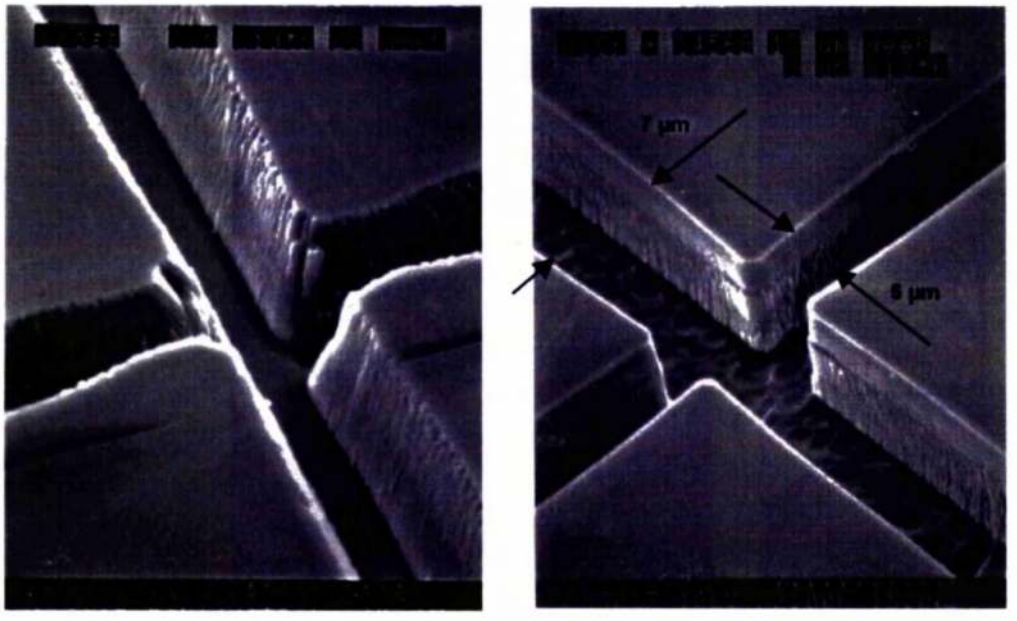

Figure 2.7: SEM pictures of same pattern etched by different masks. a) channels of 5 and 7 μm wide using photoresist mask (verticality of 70°), b) channels of 5 and 7 μm wide using two masks, NiCr plus photoresist (verticality of 89°).

The gas used was CHF_3. The flow rate, etching pressure and RF power were 25 sccm, 60 mT and 190 W, respectively, giving a selectivity of 7.5 to 1 over the photoresist layer and an etch rate of 93 nm min^{-1} was measured by a surface profiler. The sample was etched to a depth of 39 μm using 14 runs of 30 minutes.

Before each run, a standard oxygen cleaning process was performed in the etching machine. To conclude the process, the substrate was immersed in acetone and in nichrome wet etchant in order to remove the remaining photoresist and nichrome respectively (see Figure 2.3).

Using this mask configuration and RIE recipe, it was possible to etch to a depth of ca. 40 μm and produce trenches with vertical and smooth side walls in FHD silica glass [4]. This process fulfils the need for channels widths between 7-20 μm and 4-50 μm in depth required for capillary electrophoresis [5]. The resulting improvement can be seen in the deep trenches shown in Figure 2.8 (up to 39 μm deep). The etching rate is twice the normal rate for standard RIE recipes used at the University of Glasgow.

In conclusion, this step finalises the fabrication of a basic optical sensor. Although this device does not have sealed channels, some fluorescence experiments could be performed under trial conditions. This chapter subsequently shows how these devices can be sealed by different techniques, whilst Chapter 3 demonstrates in detail the viability and high sensitivity of this device for biosensing purposes. Chapter 5 describes how such channels can be packaged with a versatile material called poly(dimethylsiloxane), PDMS.

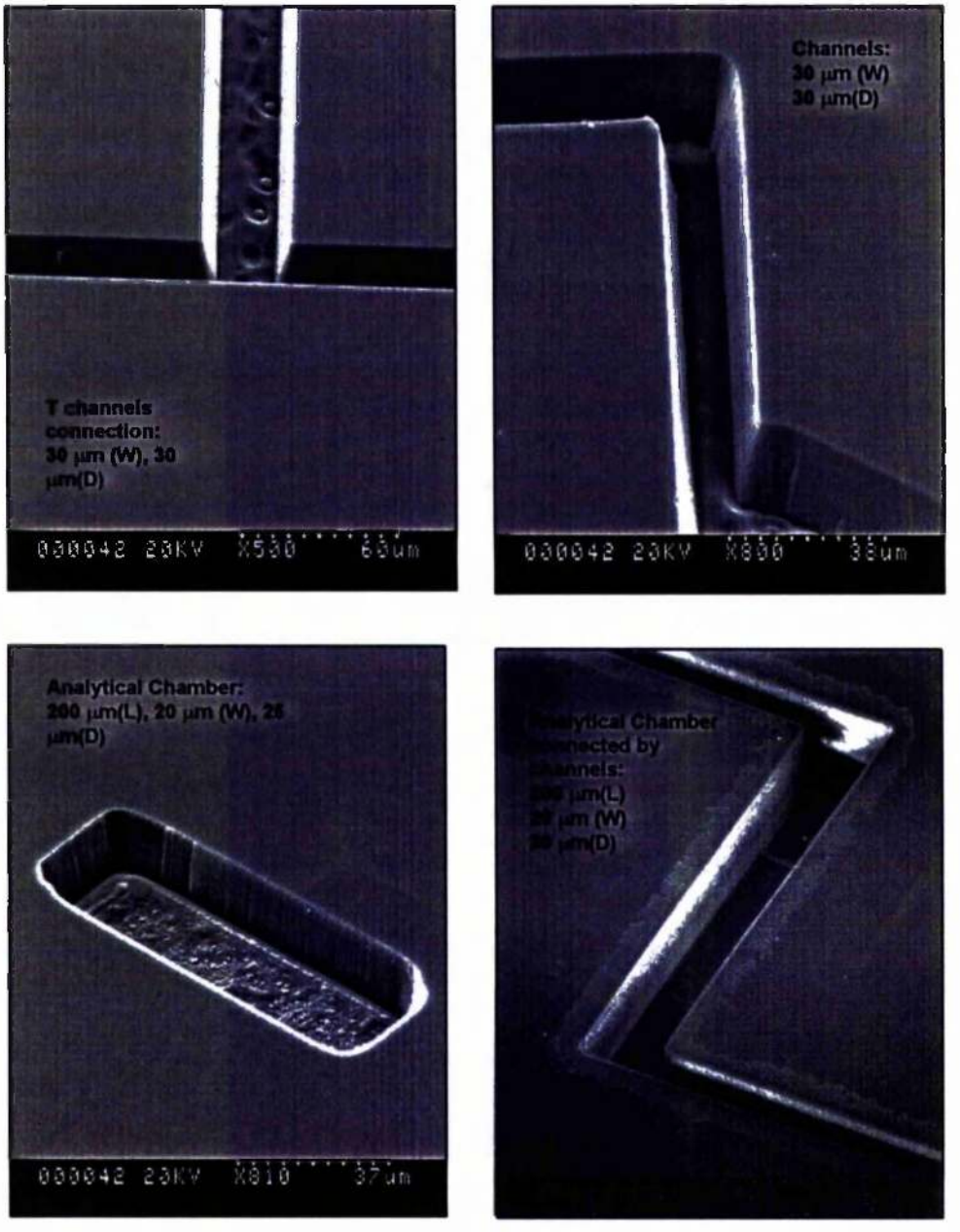

Figure 2.8: SEM images of RIE channels and chambers in silica with different lengths, shapes, and depths. All of the above structures may be addressed by buried waveguides, using the FHD, previously described.

The etching profiles were verified by the DekTak profiler since the electronic microscope can produce some distortion in the acquired images. Fig shows an etched reservoir of 24 μm depth.

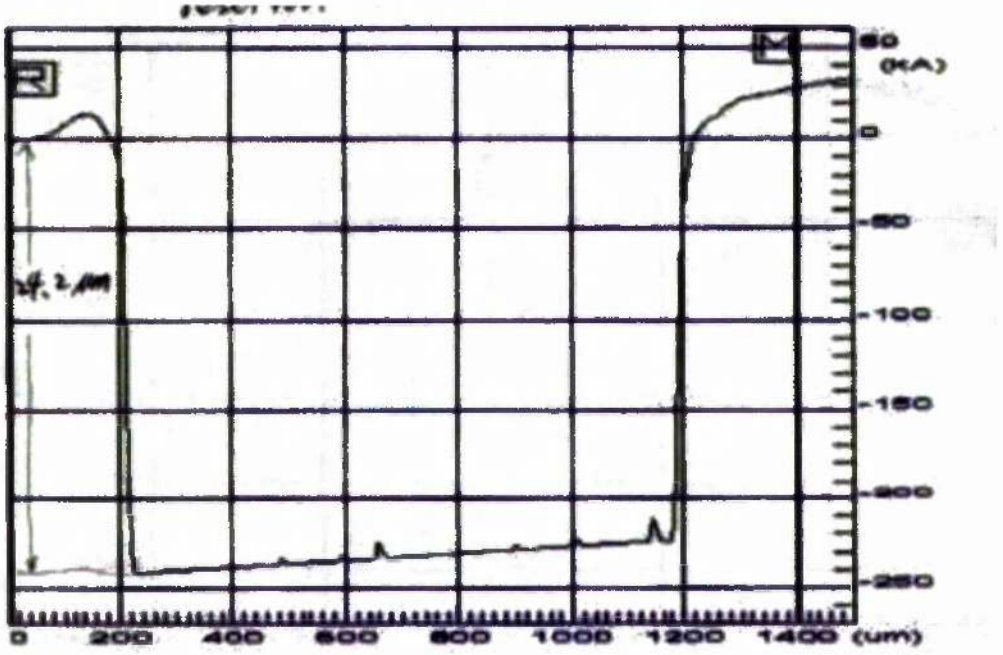

Figure 2.9: DekTak profile of an etched reservoir 24 μm deep.

2.3 Sealing Techniques of a Microfluidic System in FHD.

The micro-channels etched in the optical sensor have to be sealed in order to provide a system that can be employed to manipulate liquids either by pumping, or by electro-kinetic forces [6]. The sealing of the channels is accomplished by bonding an overlayer on top of the optical sensor (see Figure 2.10).

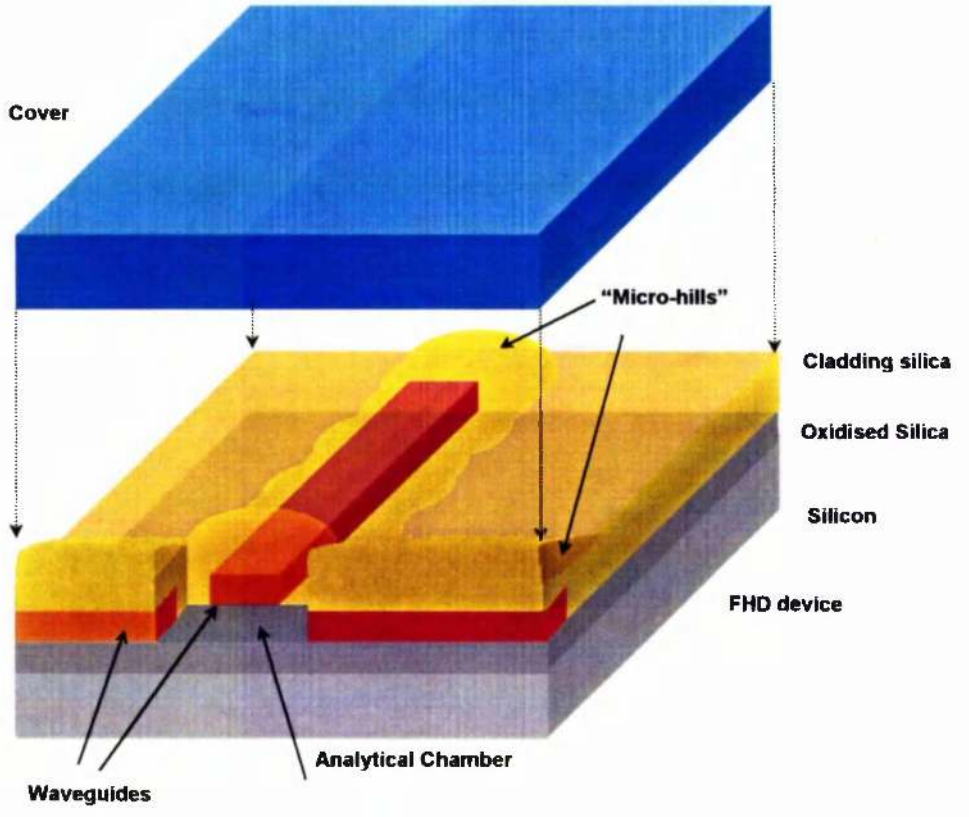

Figure 2.10: Bonding process required to accomplish the sealing of chambers and channels etched in the fluorescence sensor. Note that the FHD device surface is not flat due to the optical circuitry buried in the glass.

Once the microfluidic circuitry and its sealing were completed, it was possible to carry out an expansion and enhancement of the functions that a planar silica sensor offers, such as, movement, mixing or separation of compounds. The insulating characteristic of the silica device does not allow the straightforward use of standard bonding techniques. For example, the well established anodic bonding technique had to be adapted to bond a glass overlayer on top of the optical sensor. Other bonding techniques were developed using: FHD soot as an adhesive when it is sintered at high temperatures, and a polymer called poly(dimethylsiloxane), PDMS.

2.3.1 Adaptation of Anodic Bonding technique for FHD glass.

In 1969, Pomerantz and Wallis first reported this technique, which was referred to as field assisted glass-silicon sealing [7]. It is a process that enables the sealing of sodium-rich glass to either a metal or a semiconductor substrate, on the application of a high voltage and elevated temperature, usually 800 V and 450 °C. The temperature applied is well below the softening point of the glass. The main advantages of this bonding technique are: (i) no adhesives are required (which may otherwise fill or block the channels); (ii) there is a very good sealing of channels (enabling micro-pumping) and; (iii) it is a low temperature process (causing no deformation of the glass). Nevertheless, the dielectric nature and the non-flat surface of a FHD optical device prohibit the use of a standard anodic bonding process.

This research overcame these problems and has achieved, for the first time, an anodic bond of FHD glass on silicon to a Pyrex™ layer. This technique will be patented in the near future, as part of intellect property that will protect the use of FHD in biotechnology [8]. Problems concerning the dielectric nature of the FHD glass were overcome by the evaporation of a thin conductive material on top of the FHD glass. Likewise, the uneven surface of a FHD optical device, which negatively affects the strength of the bond and the sealing of the channels, was overcome by a mechanical polish of the top surface enabling a strong and good seal.

In order to cover a practical range of FHD glass compositions, three cases were analysed: a flat sample with 24 μm of SiO_2 doped with P_2O_5 glass on top of 16 μm of thermal oxidised silica on a silicon wafer; a sample with the same layer formation but with an optical circuitry buried in it (this gave a "non-flat" surface); and finally, the same scenario as the previous sample with its top surface mechanically polished.

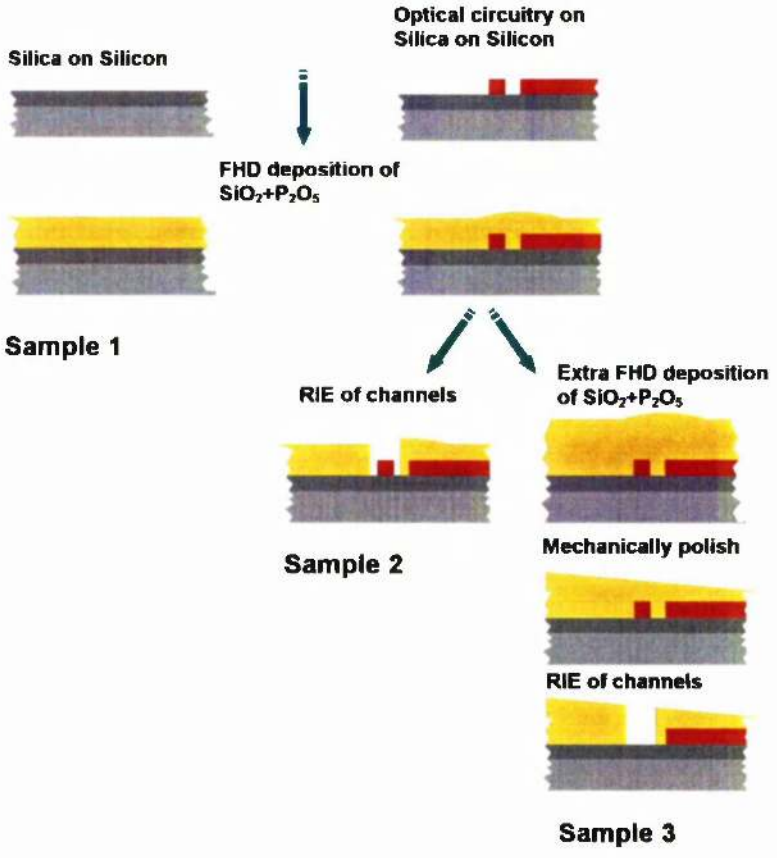

Figure 2.11: Three FHD glass cases analysed for anodic bonding. Firstly, a flat sample with 24 μm of SiO_2 doped with P_2O_5 glass on top of 16 μm of thermal oxidised silica on a silicon wafer. Secondly, a sample with the same layer formation but with an optical circuitry buried in it. This gives a non-flat surface condition. Thirdly, the previous sample with its top surface mechanically polished.

The latter case involves an extra cladding glass layer deposited on the device, which will decrease the tolerances but overcomes difficulties in the non controllable mechanical polish. It should be pointed out that the polished surface can be slightly "tilted" without affecting the optical circuitry. The 24 μm-thick cladding layer is sufficient to clad waveguides of 9 μm depth [2,9]. Hence, it is assumed that if the bond is achieved with this thickness, it will cover a useful and wide enough range of glass thickness employed in FHD "biochip" fabrication. The reason for using SiO_2 and P_2O_5 doped glass and not another FHD composition is

because this is the external layer of the likely optical device, and will always be in contact with the overlayer.

The rich sodium glass sample used in this experiment was borosilicate glass, code 7740 from Corning called Pyrex™. The main composition characteristics of this glass are the high amount of Na_2O (3.8%), and the low amount of impurities that could interference in the bonding process. Initially, flat silicon was bonded to Pyrex, as a control to verify the equipment, and the process worked.

The following sections review and describe the research carried out on the anodic bonding of FHD glasses. This topic starts by giving an intuitive approach. Thereafter, the experimental set-up and the protocol process are described. Finally, the experiments and their results are shown and analysed.

2.3.1.1 Anodic bonding theory.

This section gives a brief description of the theory of anodic bonding. The bond is believed to be governed by ionic flow at the interface between the Pyrex glass and the semiconductor, or metal [10,11,12,13]. Before the Pyrex and its substrate are bonded, they are heated and brought into physical contact. Heating the glass increases its electrical conductivity and creates an electrostatic attraction. A potential is then applied across the elements to be bonded, thereby producing an electric current through the stack and creating an electrostatic field in the gap. This field brings the elements into intimate contact and the bond is accomplished.

The mechanism of the bond can be understood if the conductivity of the Pyrex glass is considered (see Figure 2.12). At a temperature of approximately 450°C the glass contains mobile positive ions and almost immobile negative ions. Thus, when a D.C. voltage is applied across the glass, the positive ions move towards the cathode (ion migration current) and become neutralised. The side adjacent to the cathode becomes depleted of positive ions, and acquires a negative space charge. On the other side, the silicon, or the metal that is in contact with the anode, has a

positive charge. These opposite charges at the interfaces build up an irreversible electrostatic attraction between the Pyrex and the silicon, or metal.

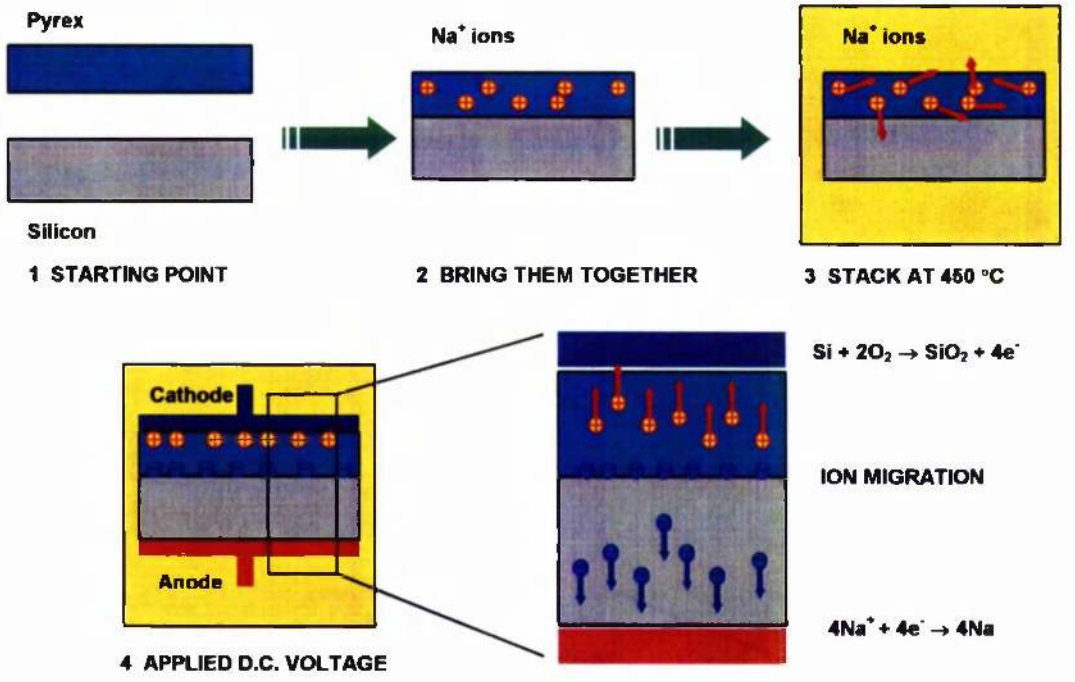

Figure 2.12: Summary of the steps involved in the anodic bonding process of Pyrex and Silicon. At a temperature of approximately 450°C the glass contains mobile positive ions, thus, when a D.C. voltage is applied across the glass the positive ions move towards the cathode (ion migration current) and become neutralised. After this process Pyrex and silicon are brought into irreversible physical contact by electrostatic attraction.

2.3.1.2 Experimental equipment description.

In this section the development of a system to carry out anodic bonding on FHD glass samples will be described. This instrumentation was formed by four elements: a power supply, an ammeter with its protection circuit, a furnace, and a ceramic clamp. This experimental set-up is shown in Figure 2.13. The glass and the silicon were brought into physical contact by a clamp and placed in the furnace. The clamp was made of machinable ceramic called Macor (Goodfellows, Cambridge, UK) which has low thermal conductivity and high dielectric constant (see Appendix A for dimensions). This clamp held together the two substrates inside a furnace, whilst being electrically connected to the power supply by NiCr

wires. The cables were covered with ceramic beads to electrically isolate them in this high temperature condition. Then, a high voltage was applied across the sample with the Pyrex glass at a negative potential relative to the silicon. A high DC power supply (Model M5K2, V.G. Electronics Ltd., Sussex England) and a furnace (Carbolite Furnaces, UK) were used to apply this high voltage at high temperature.

It was necessary to designed and developed a electrical circuit to protect the ammeter from feasible short-circuits created in the clamp and provide a minimum current to the power supply (see Appendix A for circuit design).

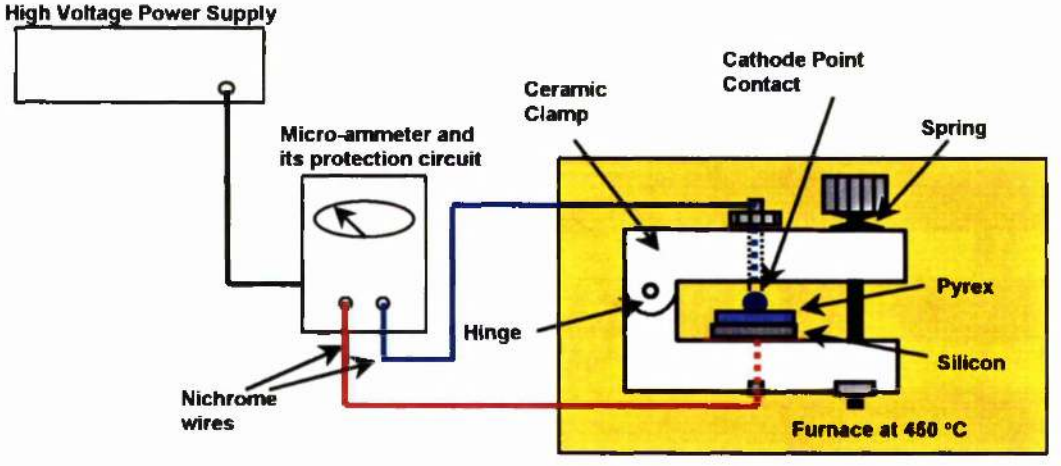

Figure 2.13: Schematic representation of the Anodic Bonding Apparatus. The clamp is made of a machinable ceramic called Macor (low thermal conductivity and high dielectric constant). The wires connecting the clamp's electrodes and the multimeter are of nichrome. A spring is placed in the screw of the clamp to absorb the thermal expansion of its metallic parts.

It is also important to consider the shape of the cathode. A point cathode makes electrical contact to the glass (see Figure 2.13), but also causes anodic bonding to spread out in a radial fashion from a spot beneath the point of contact of the cathode. This radial progression of the bonding front prevents any air bubbles between the surfaces to be bonded [10,11,12].

2.3.1.3 Preparation of the samples.

The Pyrex glass was sliced in squares of 0.5 cm side, and of a thickness of 400 μm. The silicon samples were cut in squares of 1 cm side and about 600 μm thick. The FHD silica on silicon samples required a more elaborate process to obtain the three cases outlined in Figure 2.11. This process consists of the deposition of 24 μm of SiO_2 doped with P_2O_5 glass (see Section 2.2.5) on top of 16 μm of thermal oxidised silica (see Section 2.2.1). Devices with an optical circuitry and channels were used as a "non-flat" test sample. Finally, in order to obtain the third FHD glass condition, the top surface of some of these optical devices was mechanically polished. Afterwards the samples were cut in squares of 1 cm side.

In the context of the mechanical polishing, the process must be as uniform as possible over all the surface of the sample. It was also necessary to polish just a few microns (approximately the thickness of the waveguide depth) to leave a thick enough layer of cladding. In order to minimise the tolerances involved in this non-dimensionally controllable process, it was convenient to introduce some variations in the fabrication of the optical device. A double cladding layer was deposited on top of the optical circuitry, in order to decrease the required tolerances and consequences of a non parallel polishing (see Figure 2.11). Hence, those optical FHD devices, which were anodically bonded to a Pyrex slide, needed to be over-clad. The polishing process was performed in a Logitech polishing machine using a two stage process [14]. A roughing down, employing 3 μm aluminium oxide powder was followed by a final polish in Syton W15 (a colloidal silica solution). In order to achieve a uniform polish, the holder of the sample had to be placed parallel onto the polishing turntable to minimise the non-uniform surface. This was achieved by placing in the holder, four glass samples with identical thickness, surrounding the device. The five samples were bonded up side down onto the holder using wax. The FHD samples were polished one by one to decrease the surface roughness as much as possible, because with the same mis-parallelism, a larger surface to polish, will provoke higher error.

An unavoidable preliminary step before bonding, was the cleaning process. This was for all the samples and consisted of a standard photolithographic cleaning process as previously described. The following section describes the steps to accomplish an anodic bonding of FHD devices.

2.3.1.4 Steps of an anodic bonding process for FHD glass.

The FHD silica on silicon and the Pyrex samples were cleaned and brought into contact by a ceramic clamp forming a trapped stack. The clamp must not apply too much force to the stack (due to the fact that metal electrodes expand at the temperatures involved in the bonding step and may crush the sample).

The clamp's electrodes were connected to the power supply (the cathode must be in contact with the sodium rich glass) and introduced in the furnace. The furnace was switched on and the stack was preheated for 2 hours in order to increase the mobility of the sodium anions of the Pyrex glass. A high D.C. voltage was then applied (typically 800V-1200V) through the stack, giving an ionic current of between 70 μA – 90 μA per cm^{-2}. The migration current starts to flow and is dependent on the bonded surface size, the thickness of the Pyrex, the temperature, and the metallic layer. For instance, the thicker the metal layer was, the higher the peak current (i.e. 200 nm of deposited aluminium gave 70 μA, whereas 1000 nm gave 80 μA). An ammeter read the current through the stack and, as expected, the current fell with an exponential transient as the depletion layer grew (see Figure 2.14). After approximately 5 minutes, the ionic migration stopped and the current reached a steady-state value, see Figure 2.14. The profile of the current decay was usually a good indication that bonding was taking place place.

Subsequently, the power supply and the furnace were switched off. The different expansion coefficients of the glass, silicon, and the metals could damage the stack if the clamp was removed from the furnace at high temperature, thus, the device was left in the furnace for 3 hours, cooling down at –8 °C min^{-1}. Once the clamp was removed from the furnace, the stack was released. When the bond has

formed, strength tests were applied, consisting of a cutting and a polishing of the stack. In a batch production of a FHD optical sensor, the anodic bond process would be carried out to several devices at the same time. Therefore, the bond should be strong enough to withstand slicing and polishing.

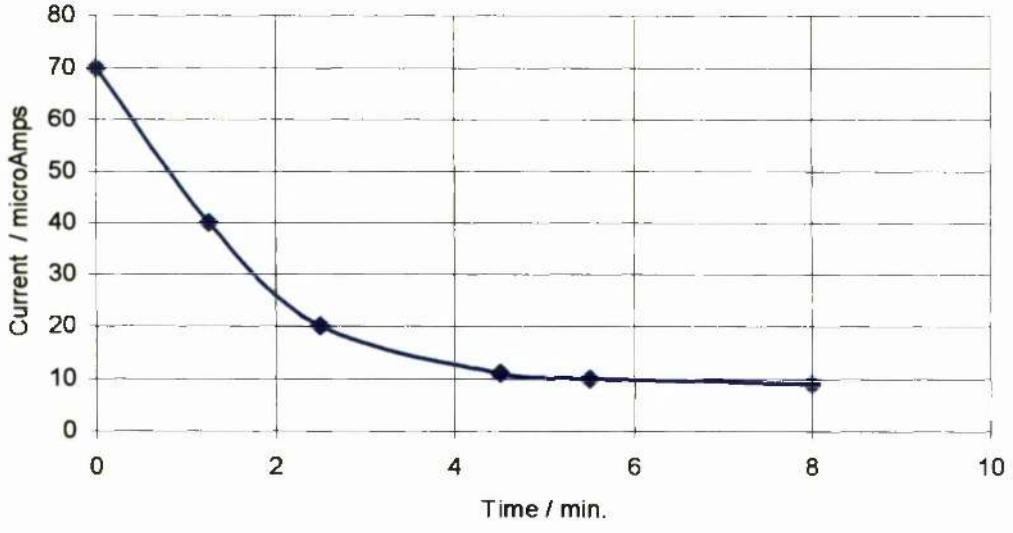

Figure 2.14: Current decay against time for Pyrex and Silicon Stack (0.25 cm^2) in an anodic bonding process. The final steady-state current value (9 μA) usually indicated that the ion migration current finished and the bond was achieved.

2.3.1.5 Experimentation and results of an anodic bonding process for FHD glass.

Table 2.3 summarises all the experiments carried out on anodic bonding. As expected, the Pyrex and Silicon samples bond very strongly, verifying that the equipment was correctly set-up.

EXPERIMENT		SAMPLE FEATURES			PROCESS PARAMETERS					Bond
Cathode	Anode	Surface finish	Metal Layer		T° °C	V KV	St min	l_D µm	i_r µm	
Pyrex 400 µm	Silicon: 600 µm	Flat	No metal layer		450	1	8	70	9	YES
	FHD Silica on silicon: 26 µm	Flat	Metal layer	Al 200 nm	450	1	9	70	10	YES
				Al 1000 nm	450	1	5	80	10	YES
				Gold 100 nm	450	1.2	10	64	6	NO
				NiCr 200 nm	450	0.8	9	95	5	YES
				Ti 180 nm	450	0.8	9	115	2	YES
		Not flat and uniform	Metal layer	Al 200 nm	600	1	9	70	10	YES
		Not flat and not uniform	Metal layer	Al 200 nm	600	1	9	70	10	Not firm

Table 2.3: Summary of the anodic bonding results using different materials and parameters. Flat silicon, micromachined silicon, thermal oxidised silica, different FHD glasses, and some alloys of metals were used to run the experiments to bond to Pyrex.

The flat FHD glass does not bond to Pyrex, due to the fact that the thick silica layer acts as insulator. Therefore, no migration current occurs in the bonding process. This research found that flat FHD samples covered with a layer of evaporated aluminium bonds successfully to the Pyrex. This metallic layer overcomes the insulating effect of silica by improving its conductivity. Different thicknesses of aluminium (from 1000 nm to 200 nm) were successfully bonded. Although the aluminium works very well, it can not be used in Lab-on-a-Chip applications for sensing biological assays since it is not bio-compatible due to corrosion. Thus, other metallic layers were tried: e.g. evaporated nichrome, titanium, and sputtered gold.

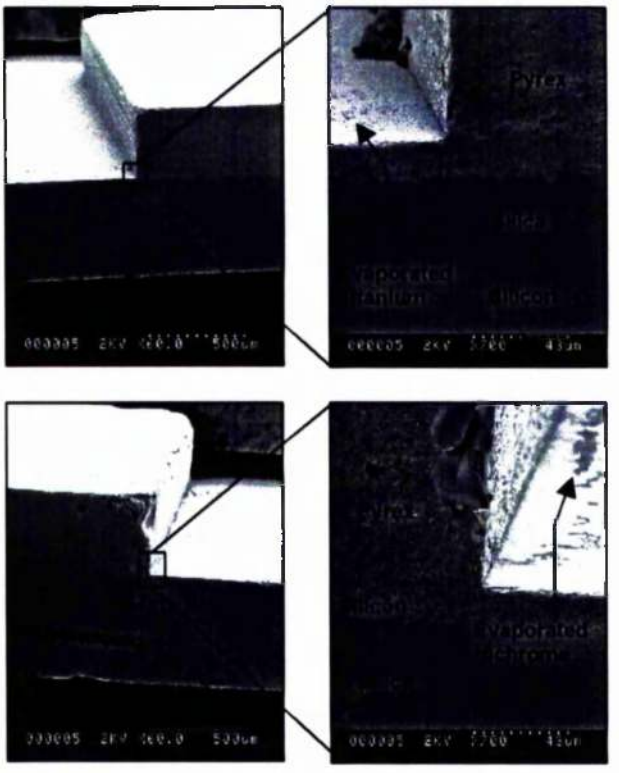

Figure 2.15: SEM pictures of anodic boning results of flat FHD glass and Pyrex using a metallic layer, top figure using titanium, bottom using nichrome.

The NiCr and Ti layer (200 nm thick) on silica, both give a strong bond (see Figure 2.15). One important condition must be taken into account: the anodic bonding has to be performed immediately after the metal evaporation, since these layers are easily oxidised. This oxidation creates an insulating layer that prevents the ion current flow. It is also important to recall the bio-compatibility nature of the titanium [15], in order to be able to apply this anodic bonding approach to FHD glass in biological purposes.

Gold does not work as an adhesion layer. This is the only case for which a decreasing current does not subsequently form a bond. This result has no straightforward explanation, although one of the possible reasons could be deduced from the fact that both the Ti and NiCr (in contrast to Au) layers change

their colour after the bond, indicating that a chemical reaction takes place on their surface.

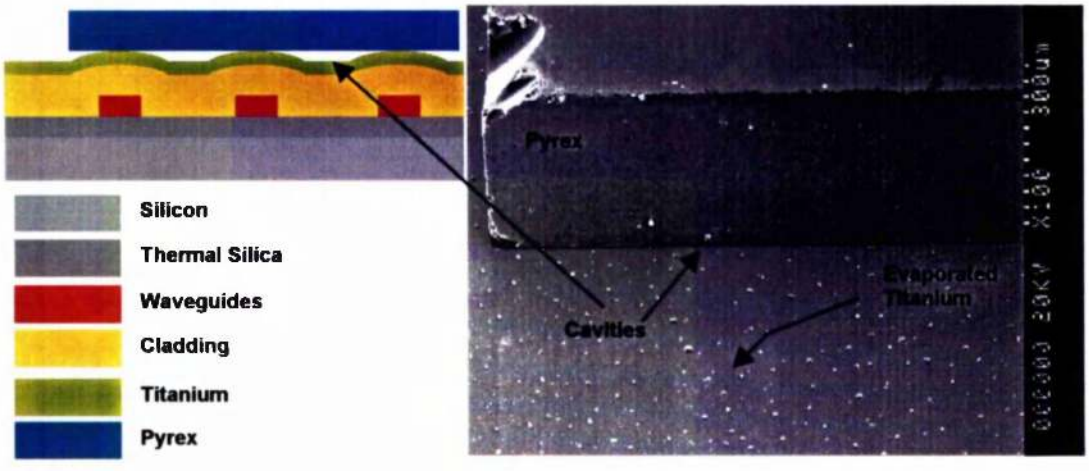

Figure 2.16: Right) SEM picture of anodic boning result of a hilly FHD optical device and Pyrex; Left) Schematic representation using a Titanium layer.

Concerning the non-flat surface condition, it was observed that this feature is crucial in anodic bonding [12]. Different uneven pattern surfaces, covered with a metal layer were tried. An increased bonding temperature (600 °C) was applied in order to try to deform and bend the Pyrex glass by reaching close to its glass softening point. Some of the bonding processes worked and others did not. The randomness of the results suggests that the non-flat pattern played an important role in the bond, as it depended on how many, and how regular the micro-hills were distributed on the FHD device's surface. Hence, a device with many rows of micro-ridges caused by the buried waveguides, establishes a strong bond (see Figure 2.16). Too few micro-ridges on a device's surface did not give a significant number of contact points with the Pyrex glass and, therefore, the bond did not form. This was the case for the optical sensor schematically represented in Figure 2.10. This device with 3 buried waveguides, and with 3 micro-ridges on its surface, did not have enough surface contact points with the overlayer to establish a strong contact. Therefore, a mechanical polish was required prior to bonding. This polishing process is explained in Section 2.3.1.3. A second point to consider

is the sealing established between non flat FHD samples bonded to Pyrex. Because the surface is not flat, micro-cavities are formed at the interface between the two pieces of glass (see Figure 2.16). These holes can produce undesirable effects in the sealing of the channels, and they must be considered in the design stage of the microfluidic circuitry.

In conclusion, this research has found a method to anodically bond FHD optical devices to Pyrex glass. The evaporated metallic layer is always necessary, and a top mechanical polish helps to establish a stronger and more efficient sealing of the FHD optical device. In the case of applied high voltages for electro-kinetic pumping, a further step should be added, because the metallic layer will create a short circuit. It would be necessary to isolate this metallic layer from the electrical potential. This task was not achieved because the tolerances involved in the process (tens of nanometers) make it very difficult, but may involve e.g. the electro-deposition of an insulating layer, such as polyphenol [16].

2.3.2 FHD soot as Adhesive in Bonding Process.

FHD soot was deposited on one substrate, and then was sintered whilst being mechanically clamped with a second sample. This strategy worked well in creating a strong bond. Two different approaches were carried out. The first one consisted of depositing FHD soot onto a quartz sample and bonding it to a non-flat FHD device with an optical and microfluidic circuitry on it (see Section 2.3.2.1). The second method was simpler and bonded two FHD silica glasses (see Section 2.3.2.2)

The deposition soot recipe was the same in both cases. The SiO_2-B_2O_3-P_2O_5 glass was initially deposited as a "soot" onto the sample, which was then sintered at 1100°C for 75 minutes and mechanically clamped to a second piece. A high amount of phosphorous was used because this decreased the sintering temperature in the fusing process (see phosphorous halide flow in Table 2.4) by 50°C. One run

was performed to complete 6.5 μm depth for trials to test bonding. The parameters are described in Table 2.4.

<table>
<tr><td colspan="6">Warming stage:</td></tr>
<tr><td colspan="3">Initial turntable temperature: 150 ° C</td><td colspan="3">Torch warming transversals</td></tr>
<tr><td colspan="3"></td><td>Number:</td><td colspan="2">4</td></tr>
<tr><td colspan="3"></td><td>Oxygen:</td><td colspan="2">2 l min^{-1}</td></tr>
<tr><td colspan="3"></td><td>Hydrogen:</td><td colspan="2">5 l min^{-1}</td></tr>
<tr><td colspan="3"></td><td>Nitrogen:</td><td colspan="2">3 l min^{-1}</td></tr>
<tr><td colspan="6">Deposition stage:</td></tr>
<tr><td colspan="3">Halides flows:</td><td colspan="3">Torch flows:</td></tr>
<tr><td colspan="3">$SiCl_4$: 150 sccm</td><td>Number of transversals :</td><td colspan="2">6</td></tr>
<tr><td>PCl_3: 200 sccm</td><td colspan="2">$POCl_4$: 300 sccm</td><td>Oxygen:</td><td colspan="2">2 l min^{-1}</td></tr>
<tr><td colspan="3">BCl_3: 90 sccm</td><td>Hydrogen:</td><td colspan="2">4 l min^{-1}</td></tr>
<tr><td colspan="3">Master: 200 sccm</td><td>Nitrogen:</td><td colspan="2">3 l min^{-1}</td></tr>
<tr><td colspan="6">Sintering cycle:</td></tr>
<tr><td>Initial Temperature</td><td>Increasing rate</td><td>Sintering time and temperature</td><td>Decreasing rate</td><td colspan="2">Final Temperature</td></tr>
<tr><td>850 °C</td><td>20 °C min^{-1}</td><td>75 min at 1100 °C</td><td>-15 °C min^{-1}</td><td colspan="2">850 °C</td></tr>
<tr><td colspan="6">Sintering atmosphere:</td></tr>
<tr><td colspan="3">Helium: 0.7 l min^{-1}</td><td colspan="3">Oxygen: 0.1 l min^{-1}</td></tr>
</table>

Table 2.4: Deposition parameters of SiO_2 – P_2O_5 - $POCl_4$ soot for bonding purposes. This process is divided in warming stage, deposition stage and sintering cycle. * sccm: standard cubic centimetre gas flow per minute.

2.3.2.1 Bonding non-flat FHD surfaces to quartz.

FHD soot was deposited on a quartz substrate and then sintered in contact with a non-flat FHD optical device creating a strong bond. The stack was mechanically clamped to allow an intimate contact during the sintering process. Figure 2.17 shows a schematic for the bonding protocol for a device that had an optical, and a microfluidic circuitry fabricated by the process explained in Section 2.2. The device consists of two waveguides buried in glass and interrupted by two holes

(100 μm diameter and 24 μm deep). Due to the high temperatures involved in the bonding process, the study of these holes is essential to understand how this process affects the quality of a possible microfluidic circuitry. The recipe involved depositing FHD soot onto a quartz substrate, as described in Table 2.4. Subsequently, this substrate was turned up-side down, clamped to the FHD device, and sintered in a furnace (75 min. at 1100 °C). A final stage involving a slow cooling process was performed to avoid damage of the stack due to the different expansion coefficients of the quartz and the silica on silicon. The stack was then cooled from 850 °C to 250 °C in 5 hours.

A successful bond, and more importantly a good seal, were attained because the soot conforms to the uneven surface of the device. The etched holes were not blocked but their walls were slightly altered (verticality decreased from 90° to ~70°), see final step in Figure 2.17. This lack of verticality affected the optical properties of the devices, because the analytical chamber wall was slightly inclined and the collection efficiency of light from the chamber decreased. In conclusion, this technique makes it possible to seal FHD devices, and in the future, provides a structure which can be used into electro-kinetic pumping (there is not a metallic interface forming a short-circuit).

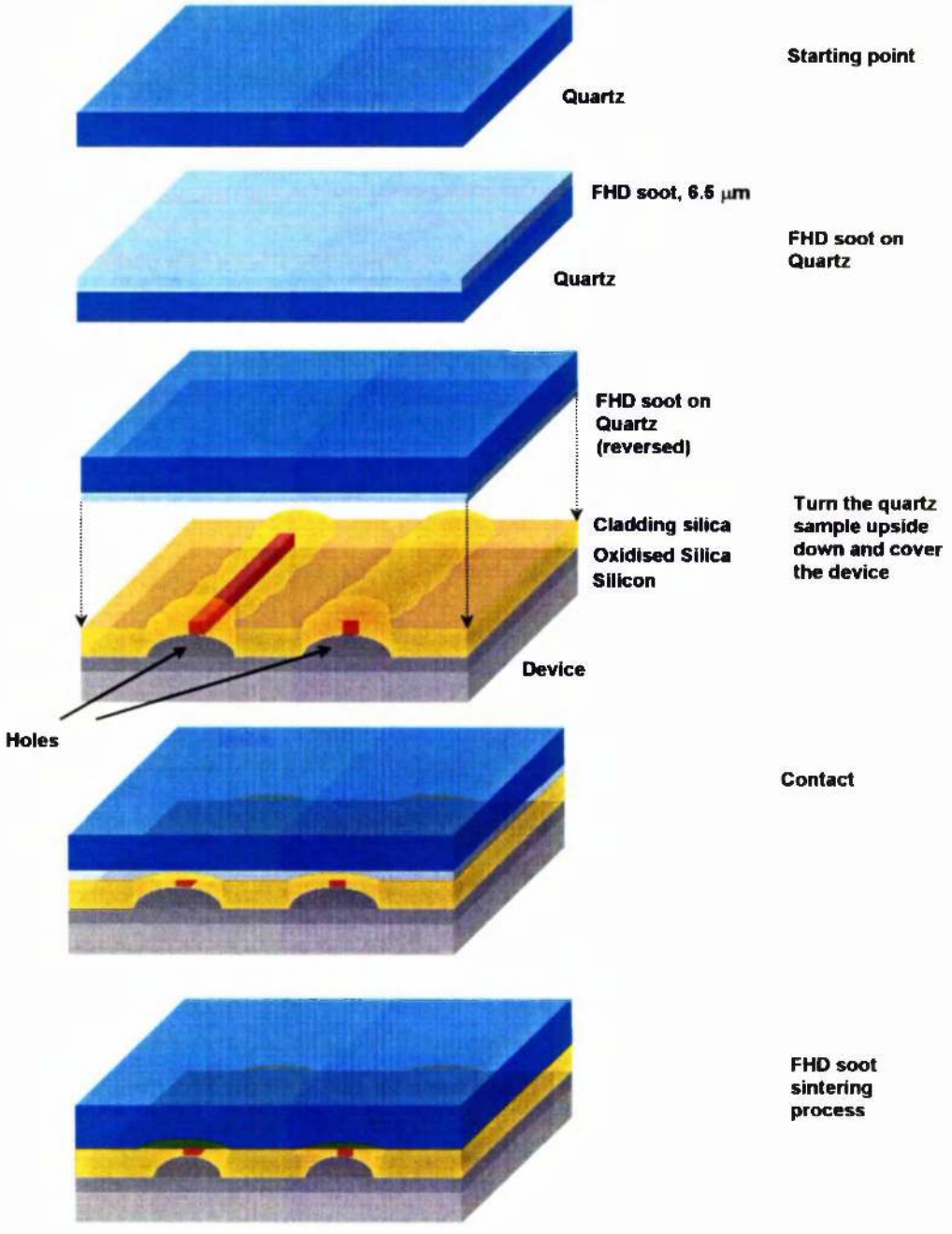

Figure 2.17: This scheme shows the bonding protocol followed to package a device that has an optical and a microfluidic circuitry, fabricated by the process explained in Section 2.2. The device consisted of two waveguides buried in glass and interrupted by two holes (100 μm diameter and 24 μm deep). The bonding was started by depositing FHD soot onto a quartz substrate following the recipe in Table 2.4. Subsequently, this substrate was turned up-side down, clamped, and sintered with the FHD device in a furnace. Notice that the sintered soot adapts to the non-flat surface of the device

2.3.2.2 Bonding between two FHD silica samples.

In this case, the bond is formed by clamping and sintering two silica on silicon samples both of which have been covered with FHD soot. The FHD recipe is described in Table 2.4. The stack was mechanically clamped to allow close contact during the sintering process. This bonding process was not very demanding, due the fact that samples did not have any etched patterns on their surfaces, which could be damaged by the sintering process. Furthermore, there were less problems with the cooling process, since both samples had the same expansion coefficients and, there was not a differential thermal shock when the samples were removed from the high temperature. The results of this bonding are shown in Figure 2.18. One of the problems with this technique is, however, that "bubbles" may become trapped in the stack. This technique can not be used for pumping purposes, when transparency of the cover is required, but can fulfil other hybrid integration purposes, such as, a simple bonding of two FHD optical devices.

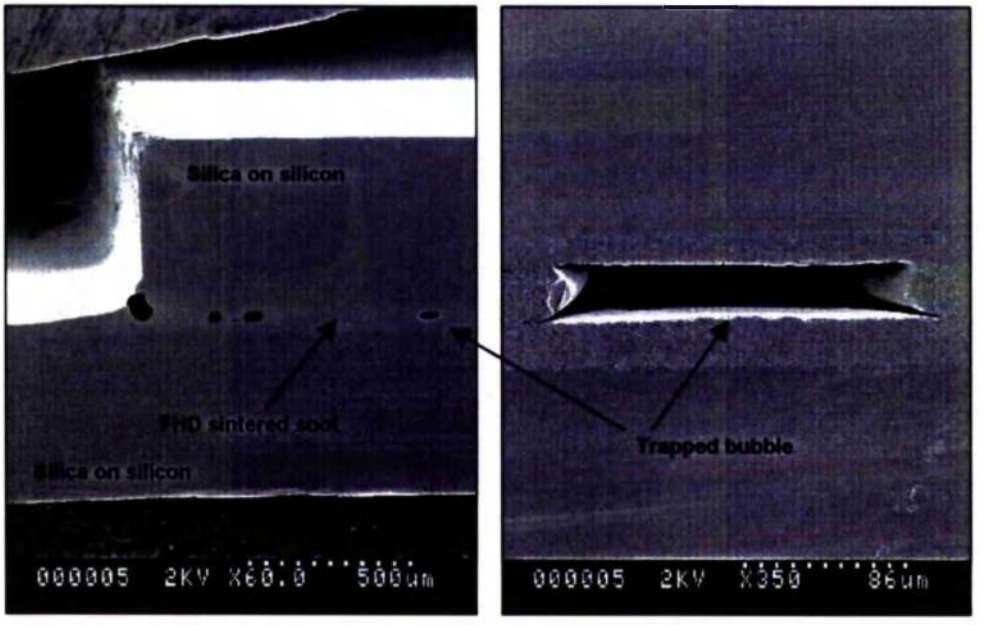

Figure 2.18: SEM pictures of polished cross sections of the bonding between two silica-on-silicon samples by FHD soot. Left picture shows a bubble trapped in the stack.

2.3.3 PDMS Polymer for Bonding and Sealing Purposes.

A third bonding technique investigated in this dissertation used a versatile material called poly(dimethylsiloxane), PDMS. This bonding material enables a straightforward sealing of FHD glass. There are several reports of microfluidic systems based on PDMS [17,18,19,20]. For example, Effenhauser *et al.* [21], created channels in PDMS by casting them against a silicon master. He also sealed (reversibly) a silicon substrate with micromachined channels using a flat piece of PDMS, without any fluidic leakage. The samples were not treated after curing the polymer, and the walls of the channels were hydrophobic. Since the walls of the channels were uncharged, they did not support electrosmotic flow. A different approach, particularly relevant to this section, was carried out by Duffy *et al.* [22]. They fabricated a capillary electrophoresis system based on moulding PDMS against a master, created by rapid prototyping of photoresist (a combination of high-resolution printing and photolithography). An interesting aspect of their work was that before bonding, they oxidised the surfaces to be bonded, both making sealing straightforward and supporting electrosmotic flow. They sealed PDMS irreversibly to another piece of PDMS, or more importantly, to other materials typically used in microfluidic system, such as, glass, silicon, silicon oxide, and oxidised polystyrene. The next experimental section describes the adaptations performed in order to bond this polymer to a device made of FHD glass.

2.3.3.1 Steps to bond PDMS to FHD glass.

The sealing of a microfluidic system made from FHD glass with PDMS involved two main steps: "curing" and "sealing". The first step produced the flat and thick (3 mm) piece of PDMS, and the second one consisted of a modification of the properties of both surfaces, and a subsequent bonding and sealing of the channels (see Figure 2.19).

For the curing process, a 10:1 mixture of PDMS pre-polymer and curing agent (Sylgard 184, Dow Corning, Midland, MI) were thoroughly stirred and poured onto a gold surface on a flat silicon master. This layer of gold (75 nm) was

sputtered on silicon in order to facilitate the removal of the PDMS after curing. Notice that moulding of the PDMS could also have been very easily carried out, if the silicon master had had micromachined features in it. The mixture was settled for 5 hours to remove the bubbles formed in the previous stirring stage. This process can be enhanced by degassing the sample under vacuum. A cure process was then performed for 15 minutes at 90 °C. It is important to point out that the PDMS must be degassed if it is going to be exposed to low pressures in future fabrication steps. This avoids bubble formation inside the polymeric material. The curing process finished with the removal of the PDMS from the gold surface (see Figure 2.19.a).

For surface modification, the FHD device was cleaned in heptane. Subsequently, both the device and the PDMS were rinsed in ethanol and exposed in 20 sccm oxygen plasma flow for 1 minute, 100 W and 13 mT, using an Oxford PlasmaTechnology RIE80 machine. Immediately after removal from the oxygen plasma, the substrates were brought into contact. This process created an irreversible seal of the channels (see Figure 2.19.b).

2.3.3.2 Results of PDMS bonding technique.

Plasma oxidation of the two samples to be bonded has two effects. It makes any bond formed strong, and it changes the nature of oxidised PDMS and silica surfaces. When the two surfaces are brought into contact, an irreversible bond is formed between them. The seal is sufficiently strong that the two substrates can not be peeled apart without failure in cohesion of the bulk PDMS. The reason for such a strong bond is not well understood and may become the subject of future spectroscopic study. Duffy *et al.* [22] suggested that oxidising PDMS in a plasma discharge converts $-OSi(CH_3)_2O-$ groups at the surface to $-O_nSi(OH)_{4-n}$. This would facilitate the formation of covalent siloxane (Si-O-Si) bonds by the condensation reaction between the two substrates. There is a second consequence of the oxidisation of PDMS and silica: silanol (SiOH) groups, introduced onto the surface of the polymer / silica, deprotonate in neutral or basic aqueous solutions

producing SiO^-, creating a hydrophilic layer which wets extremely well, and which can support electrosmotic flow in the channels.

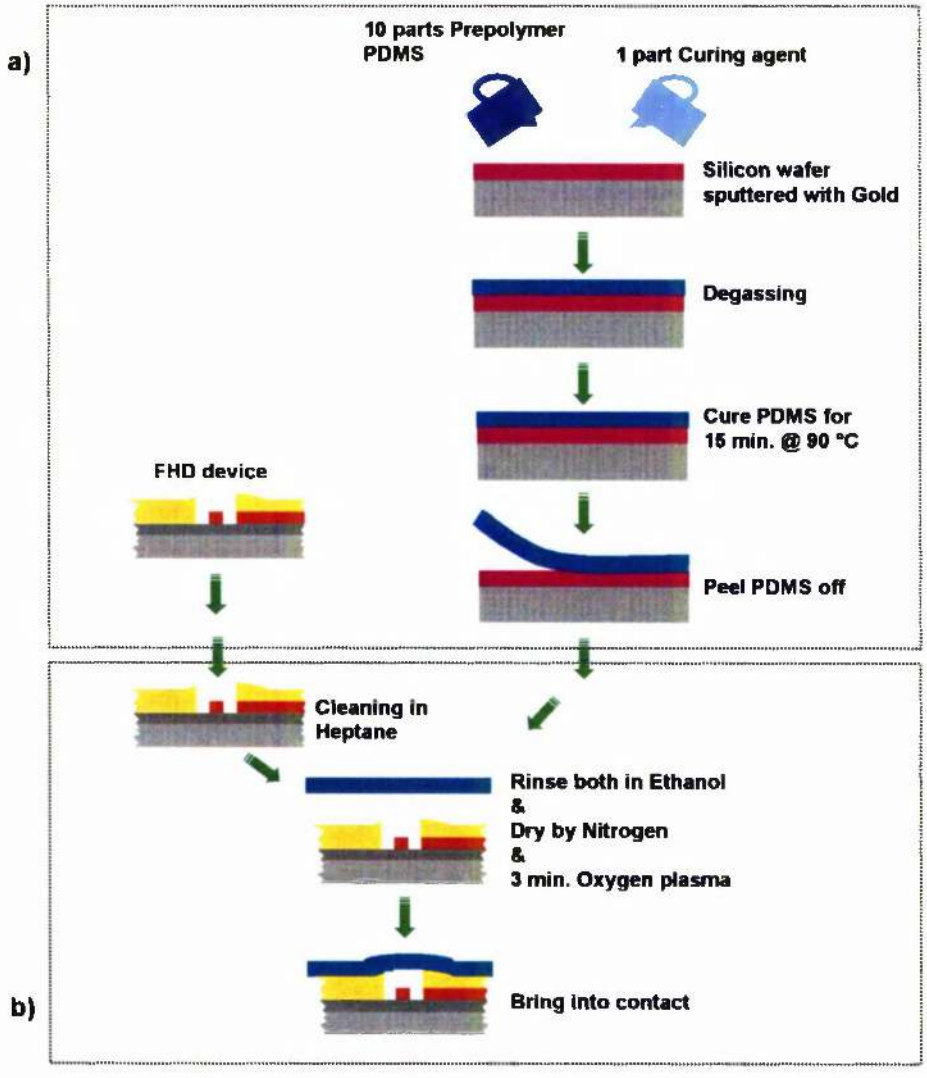

Figure 2.19: Scheme describing the fabrication of enclosed microscopic channels in oxidized PDMS. (a) A pre-polymer of PDMS is cast on a silicon wafer with sputtered gold. (b) The FHD sample is previously rinsed in heptane and then both samples are rinsed in ethanol, dry by nitrogen and then oxidised in oxygen plasma. Both samples are brought into contact obtaining a irreversible bond and strong sealing of the channels.

This sealing technique is the simplest and most convenient process developed so far to facilitate electrokinetic pumping in a FHD device. The properties of this material, i.e. the capability to deform and bend, have enabled the sealing of etched channels on the FHD device, with a non-flat surface. The bonding process is

performed at room temperature and no voltages are required. PDMS also allows the moulding of channels in the bonding layer. This technique is suitable for fluorescence assays due to the low auto-fluorescence of PDMS at most visible wavelengths. Section 5.3 describes further work carried out on this sealing technique to transport liquid from one reservoir to another along a microchannel.

2.4 Conclusions.

The use of flame hydrolysis deposition (FHD) to form integrated Lab-on-a-Chip structures involving silica-on-silicon for biosensing purposes has been examined in this chapter. The FHD process allows buried optical waveguide structures to be produced. They are isolated from the surface using a glass overlayer, or cladding. This arrangement enables sensing regions, such as microanalytical chambers and capillary channels for microfluidics, to be defined by etching through the upper cladding. During the etching, it was necessary to develop a process which produced microstructures with low surface roughness, whilst simultaneously providing deep, high aspect ratio features, as is appropriate for microfluidic structures. Using a nichrome mask, smooth and vertical walls were guaranteed. In this case, the surface to be etched represented only about 0.01% of the total surface. Consequently, the amount of exposed nichrome is extremely high and the environment in the etching chamber becomes contaminated, resulting in redeposition on the etched surfaces. Likewise, a fabrication process using a mask of photoresist alone provides a cleaner process, although the verticality and the depth of the etching are less satisfactory. However, the use of a bi-layer mask (a thick layer of photoresist over nichrome) made it possible to etch deep and vertical channels with no redeposition of contaminants. This gave depths of at least 39 μm.

Using these methods, a planar silica device can be developed by a combination of FHD and RIE in a form that is suitable for fluorescence measurements. This device can be enhanced by the development of additional bonding techniques, as

described in this chapter, such as anodic bonding, FHD soot, or PDMS sealing. The combination of all of these techniques enables the development of *in situ* microfluidic pumping, in order to carry out total analysis functions, such as, treatment or transport of the sample. In this respect, the flexibility of these technologies offers a variety of configurations to be conceived and implemented, with the prospect of using the techniques for the Lab-on-a-Chip concept.

2.5 References.

1 Ulrich R., Torgue R., Applied Optics, Vol. 12, No. 12, 1973.

2 McLaughlin A.J., PhD Thesis, University of Glasgow, 1998.

3 McLaughlin A.J., Bonar J.R., Jubber M.G., Marques P.V.S., Hicks S.E., Wilkinson. C.D.W., Aitchison J.S., Journal of Vacuum Science & Technology B, Vol.16, No.4, pp.1860-1863, 1998.

4 Ruano J.M., Ortega D., Bonar J.R., McLaughlin A.J., Jubber M.G., Cooper J.M., Aitchison J.S., Journal of Microelectronic Engineering, Vol.46, No.1-4, pp.419-422, 1999.

5 Duveneck G. L., Verpoorte E., Oroszlan P., Pawlak M., Erbacher C., Spielmann A., Neuschäfer D., Ehrat M., Anal. Methods & Inst. Special Issue μTAS'96, 158, 1996.

6 Harrison D. J., Li P. C. H., Anal. Chem., Vol. 69, pp. 1564-1568, 1997.

7 Wallis G., Pomerantz D.I., J. Appl. Phys. 40, 3946, 1969.

8 PCT Patent Application, 1999.

9 Marques P.V.S., PhD Thesis, University of Porto, 2000.

10 Denee P.B., J. Appl. Phys. 40, 5396, 1969.

11 Borom M.P., J. Ame. Ceram. Soc., 56, 563, 1970.

12 Anthony T.R., J. Appl. Phys., 54, pp. 2419-2428, 1993.

13 Casey B., PhD Thesis, University of Glasgow, 1999.

14 Bonar J. R., PhD Thesis, University of Glasgow, 1995.

15 Kaciulis S., Mattogno G., Napoli A., Bemporad E., Ferrari F., Montenero A., Gnappi G., Journal of Electron Spectroscopy and Related Phenomena, Vol.95, No.1, pp.61-69, 1998.

16 Lyons M.E.G., Electroactive Polymer Electrochemistry, Ed. Plenum, ISNB. 0-306-45158-1, 1996.

17 Martynova L., Locascio L.E., Gaitan M., Kramer G.W., Christensen R.G., MacCrehan W., Anal. Chem., Vol. 69, pp. 4783-9, 1997.

18 McCormick R.M., Nelson R.J., Alonson-Amigo M.G., Benvegnu D.J., Hooper H.H., Anal. Chem., Vol. 69, pp. 2626-30, 1997.

19 Delamarche E., Bernard A., Schmid H., Michel B., Biebuyck H.A., Network Science, 276, pp. 779-81, 1997.

20 Schueller O.J., Duffy D.C., Rogers J.A., Brittain S.T., Whitesides G.M., Sensors and Actuators A, Vol.78, No.2-3, pp.149- 159, 1999.

21 Effenhauser C. S., Bruin G. J. M., Paulus A., Ehrat M., Anal. Chem., Vol. 69, pp. 3451-57, 1997.

22 Duffy C.D., McDonald J.C., Schueller J.A., Whitesides G.M., Anal. Chem., Vol. 70, N. 23, pp 4974-4984, 1998.

Chapter 3: LOW VOLUME FLUORESCENCE ASSAY IN FHD GLASS

3.1 Introduction.

In this chapter, FHD glass is assessed in the framework of low volume fluorescence-based assays. This approach requires the fabrication of a device in FHD glass with three essential elements: an analytical chamber where the liquid with fluorescence properties is placed; an excitation waveguide to excite the sample; and at least one collection waveguide to collect the fluorescence created in the chamber. Afterwards, both the detector and the excitation source can be added to the device either by hybrid integration [1] or by pigtailing [2].

The fluorescence method, used in bioassays, is reviewed at the beginning of this chapter. Subsequently, both chamber geometry and waveguides configuration of a fluorescence sensor, are studied in detail by computer simulations and experiments with fibres on V-grooves. This micromachined V-groove fibre positioner allowed us to analyse and compare the dimensions of the devices, including, the size and the relative position between the excitation and collection waveguide (in-line and orthogonal arrangement, see Figure 3.1), as well as the width and length of the chamber.

Subsequently, FHD planar silica devices were designed and fabricated following the protocol explained in Section 2.2. These devices consisted of low loss

waveguides with deep and vertical analytical chambers. Using these devices, the properties of FHD glass, as a biosensing substrate, were qualitatively and quantitatively studied (including adsorption of chemicals, scattering from the glass, autofluorescence and transmission losses).

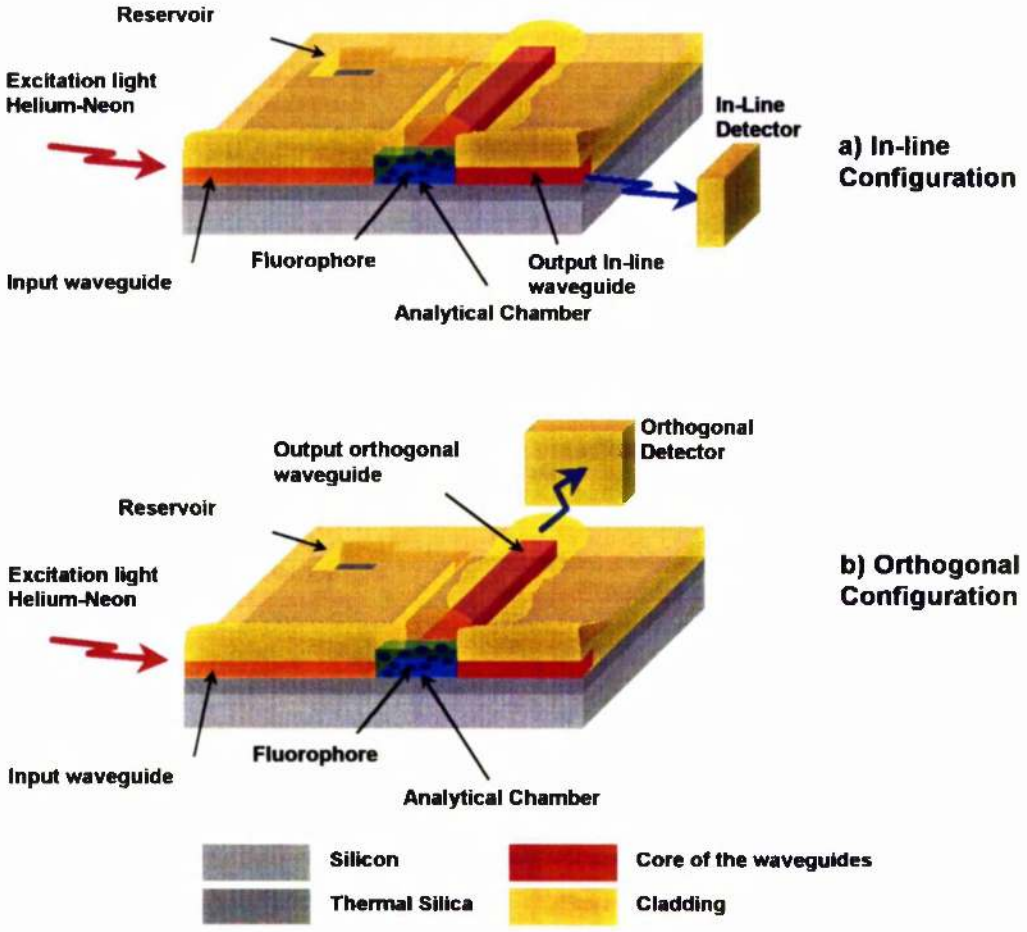

Figure 3.1: Schematic representation of the two different configurations and the basic structure of a fluorescence sensor based on FHD glass. The In-line analysis is represented at the top, and the orthogonal one at the bottom.

These devices were enhanced by the fabrication of etched channels and analytical chambers with different chamber lengths (200μm and 500μm) giving volumes of 230 pl and 570 pl, respectively. The trenches can be sealed to obtain an integrated microfluidic system that enabled transport of fluids and particles in solution, towards the analytical chamber (see Chapter 5). Using the fluorophore dissolved

in buffer, and/or reverse osmosis water, it was possible to obtain the analytical figures of merit of a fluorescence assay fabricated on a FHD glass. The experimental results indicated that these devices had very low detection limits, comparable with other optical techniques and materials [3,4,5,6,7]. The applicability of the device to the miniaturisation of bioassays was illustrated by analytical measurements on fluorescently-labelled oligodeoxynucleotides. Therefore, the work described in this chapter demonstrates that FHD glass is a very competitive substrate for biosensing assays, one of the main objectives of this research. This result validates also the fabrication protocol described in Section 2.2 as an appropriate method to be followed to develop a bio-chemical sensor on FHD. This research left aside immobilisation issues and instead, focused on the optimisation of a fluorescence optical sensor using a soluble fluorophore, named cyanine 5, Cy5. Nevertheless, these devices, in the future could be used for the immobilisation of an active bio-chemical. In this respect, FHD is a silica rich substrate and, as such, lends itself on silica by silane chemistries [8,9].

3.2 Fluorescence Bioassays Theory.

Fluorescence is the emission of light of one wavelength as a consequence of the fluorophore being irradiated with light at shorter wavelength (due to the emitted light the electrons go to higher energy levels and then they fall irradiating light). Using this method, it is possible to measure the intrinsic fluorescence properties of a variety of compounds, including natural molecules such as chlorophyll and porphyrins. The general strategy is most often the indirect detection of analytes by labelling molecules with a fluorophore. More information about the fluorescence principle is described elsewhere [10,11,12,13,14]. Its main features are its high selectivity (very specific detection), and high sensitivity (at low concentrations) as well as the possibility of making parallel measurements (i.e. DNA microarrays [15, 16]). Fluorescence detection can be implemented in bulk assays (analyte in solution) or by imaging immobilised analyte for parallel / multiplex assays (e.g. using an epifluorescence microscope). The fluorophore's sensitivity to the

molecular environment also could provide a means of measuring viscosity [17], pH [18], solvent polarity [19] or other molecules through the fluorophore quenching (i.e. O_2[20], NO_2[21,], SO_2[22]). Finally, fluorophores have fluorescence lifetimes that are short relative to most biological events, so the time response of a fluorophore is usually not a limiting factor in the assay.

Three different measured approaches of the emitted light can be used: its intensity [23]; its polarisability [24,25,26]; or its lifetime [27]. The light intensity emitted by the fluorophore depends on its quantum yield (ratio of the number of fluorescent photons emitted to the number of photons of light absorbed), its absorption (more precisely its molar extinction coefficient), excitation intensity, and the concentration of the fluorophore. Regarding the polarisability and lifetime response of the fluorophore, these are often used to distinguish different compounds in solution because the fluorescence polarisation and lifetime depend on molecular composition of fluorophore. Therefore, fluorescence has enabled a variety of optical biosensing possibilities such as, single cell analysis [28,29], gas detection [30], drug discovery [31] and blood tests [32].

This research used a fluorophore to characterise a FHD based sensor, since this label mechanism is most often used in analytical biochemistry. For example, an antibody, labelled with a fluorophore, reacts with very high selectivity to its immobilised antigen as is quantified through a competitive assay (with labelled and unlabelled ligands, both competing for a fixed number of antigen binding sites) [33,34,35,36,37,38,39]. The labelled antibody can also be attached to an enzyme and react with its immobilised antigen (ELISA, Enzyme-linked immunosorbent assay [40,41]). Similar types of assays can be also described for DNA measurements [15,16]. The immobilisation of the antigen has important advantages: one step process; no reagent is used (dry chemistries); the reaction is volume independent; and often relatively quick. The disadvantage of immobilisation is that the assays are non-repeatable due to the irreversible nature of

the antibody-antigen binding. This obstacle has led to the miniaturisation and mass production of these biosensors, making them cheap and disposable.

Fluorescence Figure	Description
Output (O):	Detector signal with the fluorophore in the chamber.
Dark signal (Dk):	Detector signal with the excitation light off.
Blank signal (Bk):	Detector signal with the chamber filled with the solvent only.
Noise (N):	Noise of the output (RMS).
Analytical Signal (S):	Output signal – Blank signal.
Background (B):	Blank signal – Dark signal.
Signal–Noise ratio (S/N):	Analytical signal / Noise.
Signal–Background (S/B):	Analytical signal / (Blank signal – Dark signal).
Detection limit (Dl):	Concentration when $S = 3\sigma$.

Table 3.1: Description of the figures of merit of a fluorescence experiment.

Figure 3.2 explains some practical figures of merit for a fluorescence or absorbency assay. Starting with the dark signal (Dk), as a specific parameter of the detector, which is measured when the excitation light is off (see Figure 3.2.a). A low value is convenient to obtain low detection limits and increase the dynamic range. When the excitation source (e.g. a laser) is switched on, the blank signal (Bk) is obtained once the analytical chamber is filled with the solvent e.g. buffer (see Figure 3.2.b). When the chamber is filled with the fluorophore, the detector signal is measured and is called output signal (O) (see Figure 3.2.c). Hence, the analytical signal (S) is obtained from the subtraction between the output and the blank signal.

Another important figure of merit is the background signal (B). It is deduced from the subtraction between the blank and dark signal, and its value indicates how well the excitation light is filtered (the lower the better). It is also important to consider the noise in all the previous signals (Dk, Bk, O), particularly the noise of the output signal. The experimental detection limit (Dl) indicates the minimum amount of fluorophore detected by the sensor, and it corresponds to the fluorophore concentration obtained when the standard deviation of the analytical signal is 3 times greater than that for the blank signal. There are also additional figures of

merit that consist of ratios between the signal and noise and between the signal and the background. These figures are summarised in Table 3.1 and Figure 3.2.

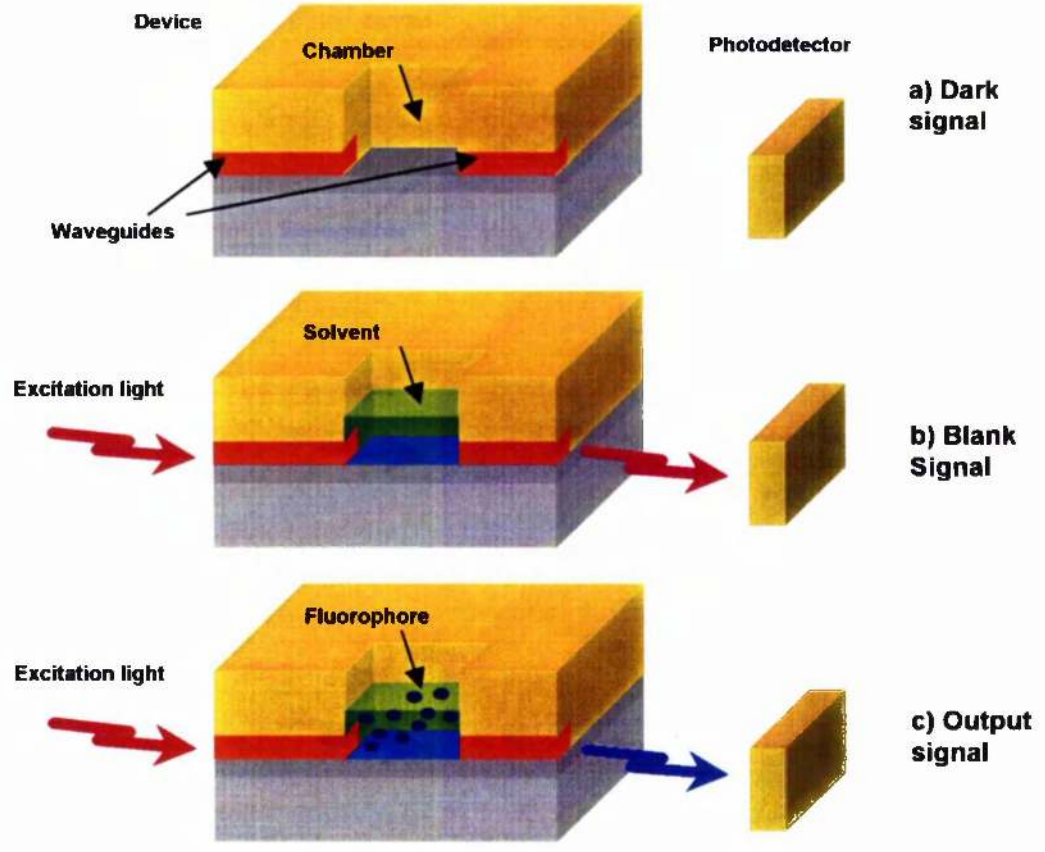

Figure 3.2: Fluorescence process measurement. The dark signal (Dk) is a specific parameter of the used detector, and is obtained when the excitation light is off. The blank signal (Bk) is obtained when the analytical chamber is filled with the solvent and the excitation light is on. In the same vein, when the chamber is filled with the fluorophore the detector signal is measured and is called output signal (O).

3.3 Optimisation of the Waveguides and Chamber dimensions of Low Volume Fluorescence Assays.

As was previously mentioned, the basic structure of a FHD based fluorescence sensor consisted of three main elements: a micro-chamber to hold or immobilise the fluorophore, an input waveguide to excite the fluorophore, and an output waveguide to collect its emission. This approach had to be optimised in order to

maximise the collection of the fluorescence emitted by a fluorophore. A commercial software called 2D BPM (Optiwave Corporation, Canada), based on a beam propagation method (BPM), was used to optimise the dimensions of the waveguides. Subsequently, a prototype, based on V-grooves and fibres, was micro-fabricated to study the best waveguide arrangement. Two types of configurations were investigated, where the waveguides were either "in-line" or orthogonal to each other, as was described previously in Figure 3.1.

3.3.1 Simulation of Fluorescence Assays in FHD glass using BPM.

This section offers a brief review of the fundamentals of the BPM simulation software, followed by an explanation of the optimisation of the in-line waveguides of a fluorescence sensor.

3.3.1.1 2D BPM Software Theory.

2D BPM models the propagation of the light in a waveguide where the cross-section changes along the direction of the propagation. The simulation procedure begins with a known initial electromagnetic field. The role of "time" is then played by the propagation distance. The light propagation is simulated by performing a step-by-step numerical solutions along the propagation direction. The numerical approach is built in the framework of the Finite-Difference Beam-Propagation Method (FDBPM) [42,43,44].

The FDBPM is a numerical solution of equations which governs light propagation in a dielectric media. The BPM-CAD solves the Helmholtz equation that is an approximation of a vectorial wave equation resulting from Maxwell equations [45]. The Helmholtz wave equation is solved, in turn, by another approximation based on the Fresnel equation, called Paraxial Propagation [46]. As a consequence of this complexity, the BPM only considers monochromatic signals. The entry modeling data consists of the refractive index distribution, the starting propagation field, and a set of numerical parameters. The index distribution is provided by the waveguide structure laid out in the Device Layout Designer of the BPM software.

The starting field can be a waveguide mode, a Gaussian field, a rectangular field, or a user field, supplied by file. Below are some of the simulation output data used in this research:

Field Amplitude vs. Distance: the complex field amplitude versus the distance of propagation.

Complex field: This data is the complex field amplitude at the end of propagation.

Power in output waveguides: This is the power in output waveguides, at the end of propagation. The power in each waveguide is specified as the intensity integral limited to the waveguides boundaries.

3.3.1.2 Waveguide Optimisation for the in-line configuration of Fluorescence Assays.

In order to simulate fluorescence in-line collection with 2D BPM software, it was assumed that with a given gap between two waveguides, the more excitation signal measured, the more fluorescence signal would be collected (subsequently this assessment was experimentally verified).

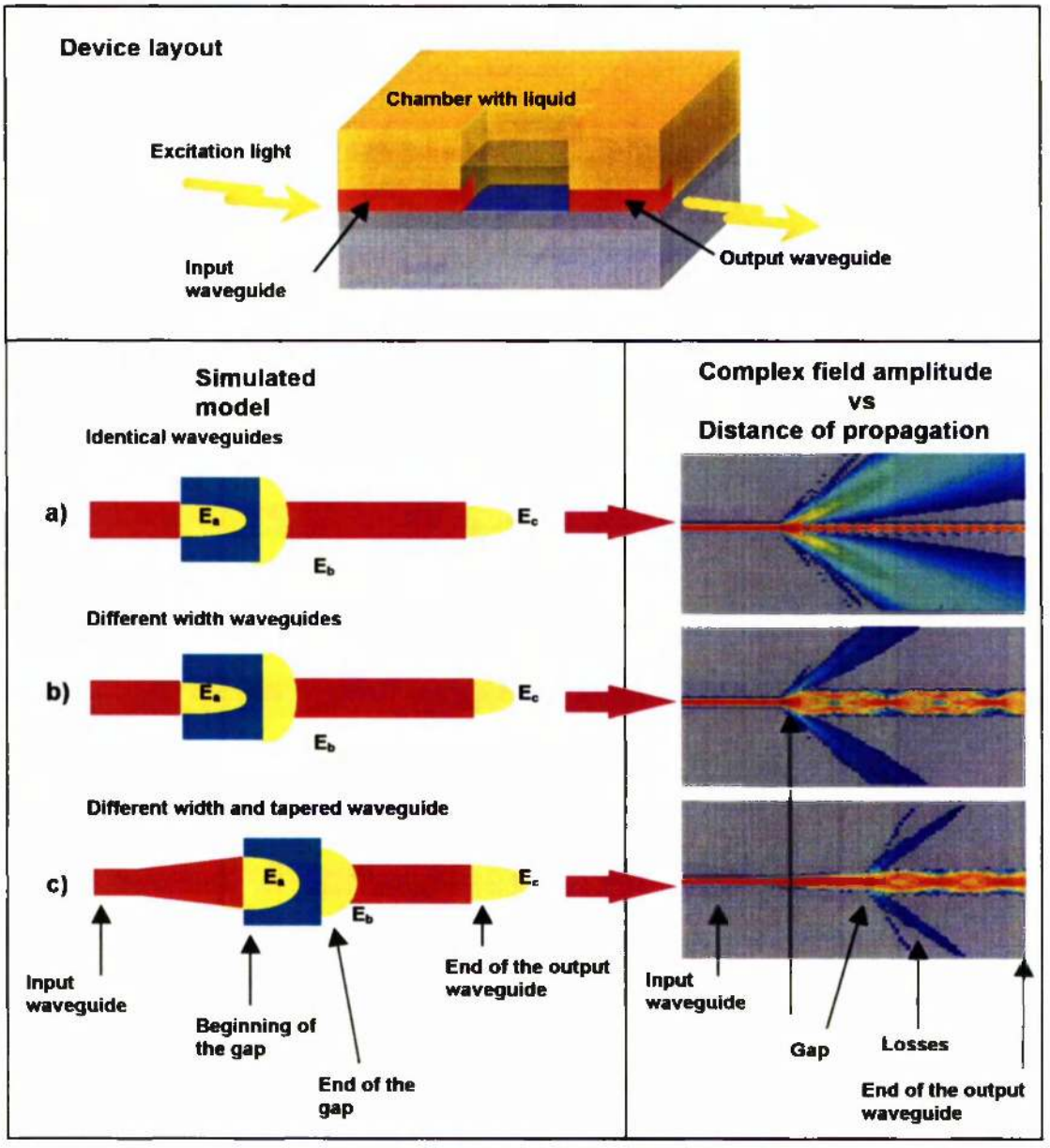

Figure 3.3: Top) Schematic representation of the simulated device. The structure comprises an input and an output waveguide, as well as a chamber (100μm square) filled with water (n = 1.333). Left) Representation of the three different simulation cases depending on the width of the waveguides. Right) simulated result of the three previous cases. It is represented the complex field amplitude versus distance of propagation. The red color indicated highest amplitude and the blue one the lowest. As apparent in the third case, when a taper is introduced, the transmission losses are reduced.

The simulations consisted of two waveguides separated by a gap (chamber) of 1.333 refractive index (water) and 100μm length (see top of Figure 3.3). The purpose of these simulations was to maximise the transmitted power in the

waveguide at the chamber interface. There were three different in-line simulated cases, depending on the width of the waveguides: a) waveguides which had the same width, b) the output waveguide was wider than the input, c) different width and a tapered waveguide (see Chapter 4 for further details) was introduced before the gap (see left side of Figure 3.3). The narrower waveguides width was 9 μm and the wider one was 18 μm. The electromagnetic field shape (represented in the left side of Figure 3.3 by E) is also drawn at the beginning and at the end of the waveguides. From the 2D BPM simulation, the complex amplitude of the transmitted light versus distance for each of the three cases were obtained (see right side of Figure 3.3).

In Figure 3.3.b, the transmission losses in a given gap decrease if the collection waveguide is thicker than the input. In addition, it was noted that, if a taper was introduced in the input waveguide, the electromagnetic field (E_b) after crossing a gap of 100 μm length, had a larger overlap with the first mode of the second waveguide (see Figure 3.3.c). This higher overlapping increased the transmitted light through the gap (95 %) and increases the fluorescence collection signal. As a conclusion, a tapered waveguide together with a wider output waveguide should increase the collection of fluorescence in the in-line arrangement in a fluorescence sensor in FHD glass.

3.3.2 Simulation of Fluorescence Assays in FHD glass using V-Grooves and Fibres.

In the previous section, the BPM software simulated the in-line waveguide arrangements. However, this software could not simulate the orthogonal configuration. As mentioned, the BPM method is based on the paraxial approximations, where simulation of propagation angles larger than 30° are not feasible. In order to analyse the 90° arrangement, a prototype had to be fabricated following the process described in Appendix B.1. The experiments were carried out using the set-up and the procedure explained above.

3.3.2.1 Experimental procedure.

This section starts by giving details about the experimental set-up, such as, reagents used in the experiments, V-groove positioner layout, and its optical set-up. Subsequently, the optimisation of the waveguides and chamber configuration of a FHD based fluorescence sensor is explained.

Reagent used in the experiments.

Reagent grade H_2O_2, H_2SO_4, chlorobenzene, diethyl ether, and acetone (Aldrich, Gillingham, UK) were used for standard cleaning purposes. An aqueous solution of Cy5 fluorophore (Amersham, UK) was prepared in reverse osmosis (R.O.) water (80 μM).

The V-Groove Positioner Layout.

The fabricated prototype to measure orthogonal collection consisted of V-grooves in silicon, perpendicular to each other, where optical fibres were placed and separated by a gap. The whole structure was sealed by a cover slide using an anodic bond (see Section 2.3.1 and Figure B2.3) (see Section B.1 for fabrication details). The gap between the fibres worked as an analytical chamber. The fibres can be placed perpendicular to each other, simulating the orthogonal set-up, or placed in the same V-groove, simulating the in-line configuration. The versatility came from the fact that these fibres were not fixed or glued, and a movement of the fibres along the V-grooves was possible (see Figure 3.4), so changing the apparent volume of the chamber, between the two fibres.

Experimental Procedure for Fluorescence Measurements using the V-groove Positioner.

The device was cleaned by an acid bath with Piranha solution (90% H_2SO_4 / 10% H_2O_2). The aqueous solution of Cy5 fluorophore (80 μM in reverse osmosis water) was introduced in the V-groove by capillary action formed between the cover and the V-groove. The fluorophore was then excited by a 633-nm Helium-Neon. Due to the rather high concentration of fluorophore (80 μM), the

fluorescence could be measured by connecting the output fibres to an optical spectrum analyser (see Section 3.3.2.2).

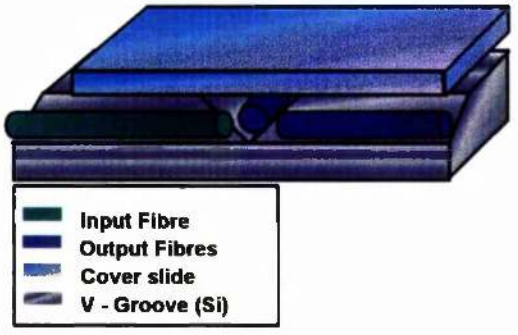

Figure 3.4: Schematic representation of the fabricated prototype consisted of V-grooves in silicon and two optical fibres separated by a gap and topped by a cover slide (see Section B.1 for fabrication details). The gap between the fibres worked as an analytical chamber. The slide was bound onto the silicon by an anodic bond (see Section 2.3.1 and Figure B2.3). The versatility came from the fact that these fibres were not fixed or glued, and a movement of the fibres along the V-grooves was possible.

Optical set-up for Fluorescence Experiments using the V-Groove Positioner.

Two optical configurations were used to collect the fluorescence emitted by the fluorophore placed between the fibres. The input and output fibres were either in in-line illumination, or orthogonal to each other, as described in Figure 3.5. The detector used was an optical spectrum analyser (Model Q8381, Advantest). A 633 nm HeNe laser (1.8mW, Coherent Inc., UK) was used as the excitation source. The coupling of light from the laser to the input fibre (9 μm core diameter) was achieved using a lens (N.A. 0.17 X10, Nikon, UK). Furthermore, the emission light from the fluorophore was measured by the spectrum analyser through the output fibres (100 μm core diameter). The reason for using different core diameters will be examined later in more detail. The narrow band excitation (633NB3.0) filter used in the set-up was part of an Omega Optical XF46 filter set (Glen Spectra, UK).

Initially, the fibres were placed perpendicular to each other, providing an "orthogonal" set-up, and afterwards they were placed in the same V-groove simulating the in-line configuration. The spectrum analyser detector was not able

to measure any fluorescence using a 9-μm core diameter output fibre. However, a 100-μm core diameter fibre was used successfully, confirming previous simulations for the in-line detection, using BPM. As expected, both the orthogonal and the in-line configuration collected more fluorescence when a wider output fibre was used. This conclusion resided in the fact that a high overlap between the emission and collection fields increased the collection efficiency

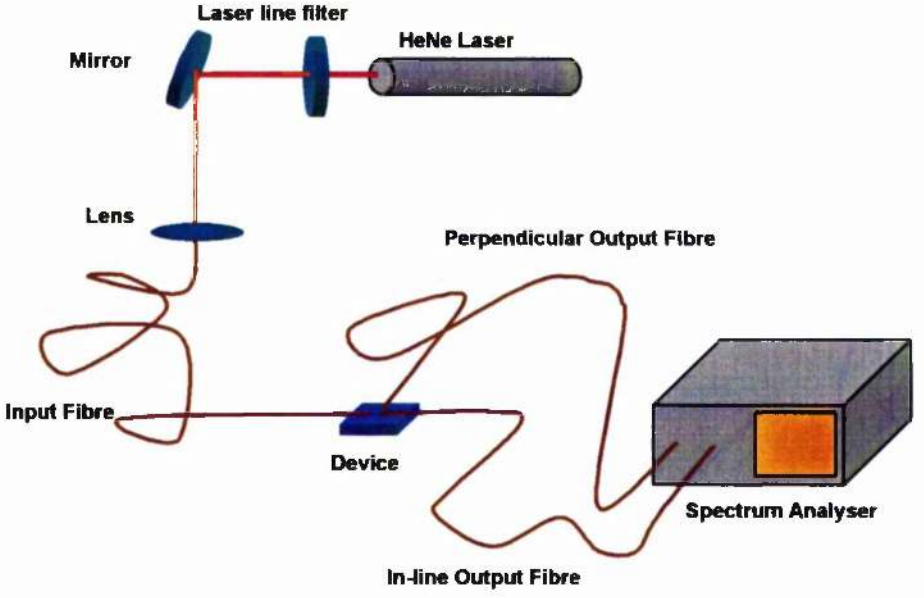

Figure 3.5: Schematic representation of the optical set-up used to collect the fluorescence emitted by the fluorophore using fibres placed on V-grooves.

3.3.2.2 Experiments using the V-groove positioner.

An initial experiment consisted of obtaining the fluorescence spectrum for orthogonal and in-line configuration (see Figure 3.6 and Figure 3.7). Notice that in the spectrum obtained, in the orthogonal configuration (Figure 3.6), there is no light at the excitation wavelength (633 nm). However, in Figure 3.7 there are two peaks. The first peak corresponds to the excitation laser and the second one corresponds to the fluorescence. The peak excitation value is almost five orders of magnitude bigger than the fluorescence peak value. This excitation light creates a

high background signal that must be removed by filters. Therefore, these graphs indicated that the best fluorescence device would be the one involving the collection of the fluorescence in orthogonal configuration.

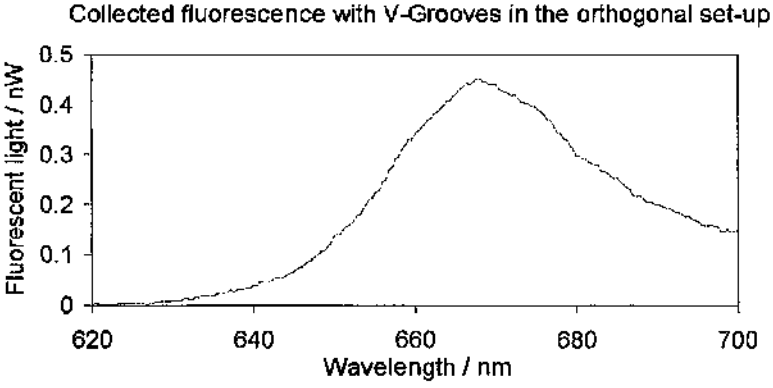

Figure 3.6: Fluorescence spectrum obtained using a V-groove and two fibres perpendicular each other. The fluorophore (80μM) was introduced through the V-groove. The input fibre (excitation one) and the output fibre (collection one) were placed on the V-grooves. The collection fibre was connected to the spectrum analyser obtaining the blue line in the graph.

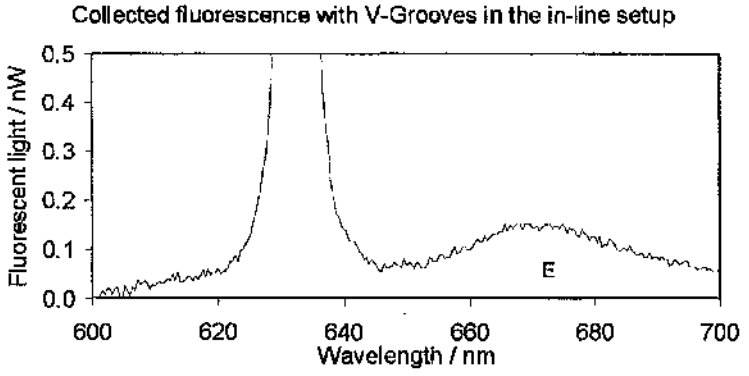

Figure 3.7: Fluorescence spectrum obtained using a V-groove and two fibres at in-line configuration. The fluorophore (80μM) was introduced through the V-groove. The input fibre (excitation one) and the output fibre (collection one) were placed on the same V-groove. The first peak corresponds to the excitation laser and the second one corresponds to the fluorescence. The peak value is almost five orders of magnitude bigger than the fluorescence peak value.

Consequently, a second experiment was carried out starting with the input and output fibres placed orthogonal to each other, and as close as possible. From that initial position, the collection fibre was moved away, increasing the width of the detection volume and obtaining the blue line in the graph in Figure 3.8. Similarly, the green line corresponds to collections of fluorescence moving away from the emission fibre, increasing the length of the detection volume. Both lines were alike, indicating that the fluorescence decayed equally in all directions. Figure 3.8 also reveals that the closer the fibres were to each other, the higher amount of fluorescence light was collected. This meant that the chamber of a fluorescence sensor in FHD glass, working in the orthogonal configuration, should be as narrow as possible to keep the waveguides close each other.

It was also noted that when the emission fibre is at 200 μm away from the collection fibre, there was still a fluorescence collection of about 80 % of the maximum. Therefore, the length of the chamber should be at least 200 μm long because there was still fluorescence created at that distance. When the emission fibre is at 400 μm away from the collection fibre, the fluorescence decreased. This fluorescence decay indicates that there is no reason to make the chamber longer than 500 μm (at that distance, no fluorescence is created).

This experiment was carried out for the in-line configuration as well (two fibres in the same groove). When they were moved apart, the same decay was observed in terms of the collected fluorescence, therefore, shorter chamber lengths should be more convenient for in-line fluorescence.

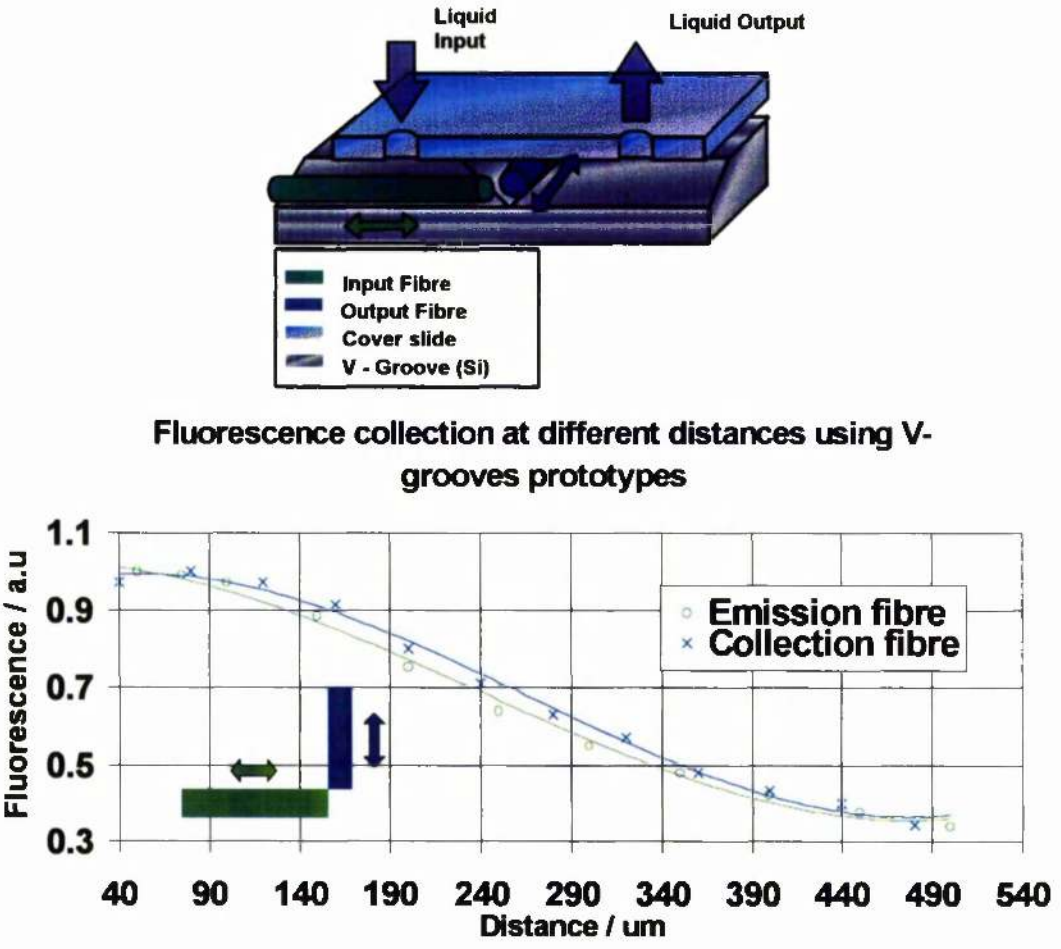

Figure 3.8: Top: Schematic representation of the prototype. The fluorophore was introduced through the V-groove. The input fibre (emission one) and the output fibre (collection one) were placed perpendicularly to each other. The collection fibre was perpendicularly moved away from the input one obtaining the blue line in the graph. Similarly, the green line corresponds to collection of fluorescence moving away from the emission fibre. The distance can be converted into a equivalent volume.

3.3.3 Discussion of the Optimisation Experiments.

These experiments, as well as the simulations with BPM software, led to the design and fabrication of an optical fluorescence device in FHD, optimised for orthogonal fluorescence collection due to its better features [47].

The optimal length of the chamber was, between 200 μm and 500 μm. This conclusion also affects the width of the orthogonal waveguide. The previous section concluded that broad orthogonal collection waveguides collect more fluorescence. Therefore, the width of the collection waveguide in a fluorescence sensor in FHD glass should be as long as the chamber is. This broad waveguide increases the overlap between the emission and collection fields created in the chamber.

Regarding the optimal width of the chamber, this should be as narrow as possible, in order to keep the waveguides as close to each other as possible. The constraint if that fluid needs to flow along the channel.

3.4 Description of the Fluorescence Assays in FHD glass.

Subsequently, FHD planar silica devices were designed using the models provided by BPM and V-groove prototypes. Sensing systems were fabricated following the protocol explained in Section 2.2. These devices consisted of low loss waveguides with deep and vertical analytical chambers (see Figure 3.9). The biochips were enhanced by the fabrication of etched channels and analytical chambers with different chamber lengths (200μm and 500μm). This section describes the properties of FHD glass as a biosensing substrate (adsorption of chemicals, scattering from the glass, autofluorescence, and transmission losses). Using a fluorophore dissolved in aqueous solution, it was possible to collect the figures of merit of a fluorescence assay fabricated on a FHD glass.

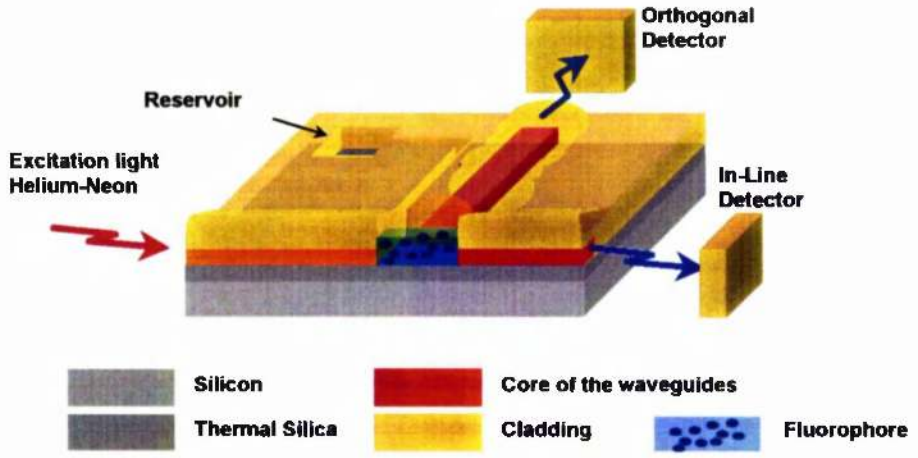

Figure 3.9: Schematic representation of the fluorescence sensor based on FHD glass

3.4.1 Reagents used in the Experiments.

Reagent grade H_2O_2, H_2SO_4, chlorobenzene, diethyl ether, and acetone were from Aldrich, Gillingham (UK). Aqueous solutions of Cy5 (Amersham, UK) with concentrations ranging from 2 pM to 24 nM were prepared by successive dilutions in reverse osmosis water. Cy5-labelled oligodeoxynucleotide (ODN) was obtained as a lyophilised powder from Cruachem (Glasgow, UK). The ODN was labelled through standard phosphoramidite chemistry.

3.4.2 FHD Device Layout.

The layout of the chip is shown in Figure 3.10. Figure 3.10.(a) describes the overall schematic representation of the optical and microfluidic circuitry. Figure 3.10.(b) shows the analytical chamber and its waveguides, whilst Figure 3.10.(c) and (d) are SEM pictures of the microfluidic circuitry and the analytical chamber respectively. In addition to the buried waveguides, the chip comprises a micro-analytical chamber connected to two reservoirs through 15 µm wide and 38 µm deep micro-channels (red objects in Figure 3.10). The overall size of the chip is 2.5 cm x 1.0 cm. Two types of chambers were produced, with dimensions of 200

(L) x 30 (W) x 38 (D) μm- and 500 x 30 x 38 μm, yielding sub-nanolitre volume structures of ca. 230 pL and 570 pL, respectively.

Each device featured one input waveguide and two output waveguides, such that both trans- and orthogonal illumination could be performed, as described. Since the diameter of the core of a standard fibre is 9 μm, the input and the in-line output waveguides width and height were chosen as 9 μm. The waveguides also had a taper-shaped width in order to improve the collection/dispersion efficiency at the chamber interface, as explained in Section 3.3.

The orthogonal waveguides had a starting width equal to the length of the chamber (either 200 μm or 500 μm) and a final width of 90 μm (in order to obtain fibre compatibility with 100 μm core diameter fibres). The "in-line" waveguides have widths that varied between 9 μm and 15 μm.

A set of waveguides were fabricated within the optical chip, in order to characterise the levels of both autofluorescence and the losses within the FHD glass for 633 nm. In addition, an optical Y-branch (see Section 4.4.4 for more details), featuring a narrow "neck" (to minimise the variations of the splitting ratio versus the lateral beam displacement [48]) was incorporated, in order to allow reference measurements of the excitation power (Figure 3.12.a).

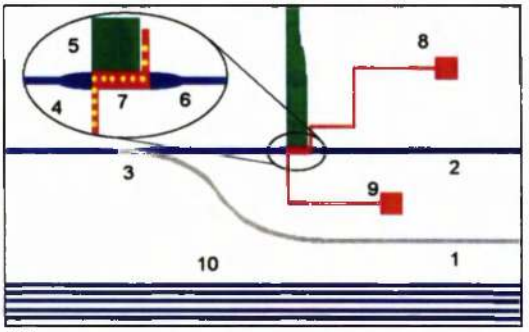

Figure a

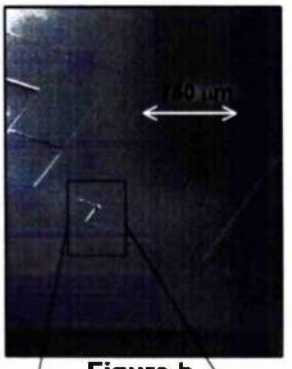

Figure b

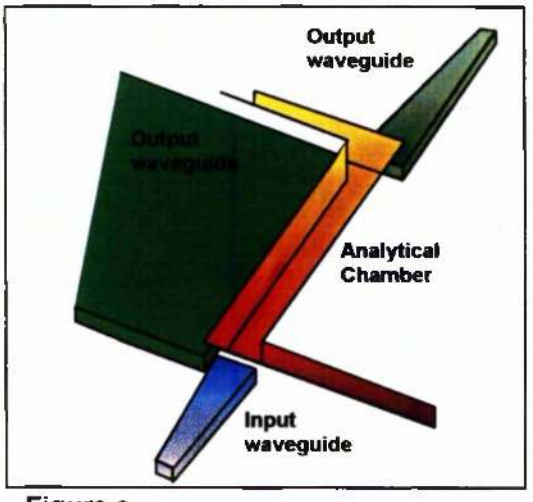

Figure c

Figure d

Figure 3.10: (a) Schematic representation of the fluorescence sensor: (1) reference waveguide (2) In-line output waveguide, (3) Y-branch, (4) input tapered waveguide, (5) orthogonal output waveguide, (6) In-line output tapered waveguide, (7) analytical chamber, (8,9) Reservoirs, (10) straight waveguides. (b) SEM picture of the channels integrated in the optical sensor. (c) Schematic representation of the analytical chamber and its waveguides. (d) SEM picture of 200 µm chamber.

3.4.3 Optical Set-ups for the Experiments using FHD Devices.

Four optical configurations were used in order to study the adsorption that takes place on the channel walls, the absorption of the excitation light by the fluorophore, and finally the fluorescence experiments to characterise the FHD devices.

3.4.3.1 Set-up for adsorption measurements.

The device was placed under an epifluorescence microscope (Nikon Microphot Microscope, Nikon, UK). Thus, the fluorescence could be excited and collected directly within the channels and chamber from the top, without using the waveguides. The device was imaged with a CCD camera (PixelVision Spectra Video SV10K) that was coupled to the photo port of the microscope.

3.4.3.2 Set-up for absorption and scattering measurements.

The absorption and scattering losses taking place in the analytical chamber were analysed using the configuration described in Figure 3.11. This set-up excited the fluorophore using the input waveguide and collected the output signal from above of the chamber. The collected fluorescence was imaged on a CCD camera (CoolSNAP, RS Photometrics) and comprised a narrow band excitation (633NB3.0) filter and one emission (670DF40) filter. Excitation light was coupled to the input waveguide using free space optics (i.e. a x 5 lens with an N.A. 0.12 , Nikon, UK). Fluorescence emission light from the chambers was collected on the CCD detector using microscope objective lens (N.A. 0.4, 16 mm, Ealing). The silicon photodetector E-835 was from Arintsu (Japan).

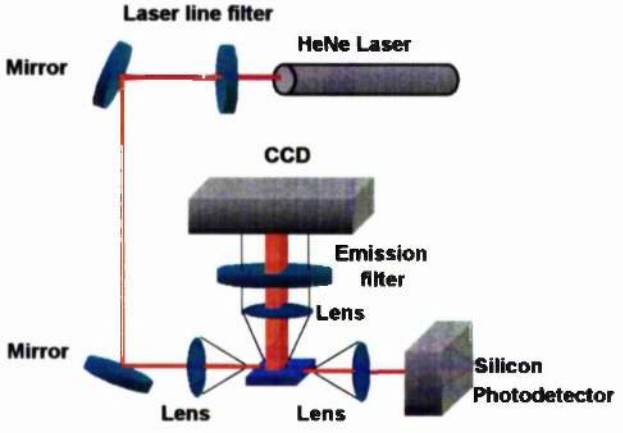

Figure 3.11: Set-up representation of the on-top configuration for absorption and scattering analysis.

3.4.3.3 Set-up for the fluorescence measurements.

In order to characterise the FHD devices as fluorescence sensors, two types of configurations were tested (in-line and orthogonal), as described in Figure 3.12 and Figure 3.13. The coupling of light from the laser to the input waveguide was achieved by a microscope objective lens x5 with N.A. of 0.12 (Nikon, UK), and from the output waveguide to the detector using a x10 lens of N.A. equal to 0.30, Nikon, UK. Although the FHD glass waveguides readily lend themselves to coupling with fibre optics by fibre pigtailing [2], the latter were not used due to the observed high autofluorescence of the standard fibre cladding (polycarbonate) at the analytical wavelengths used.

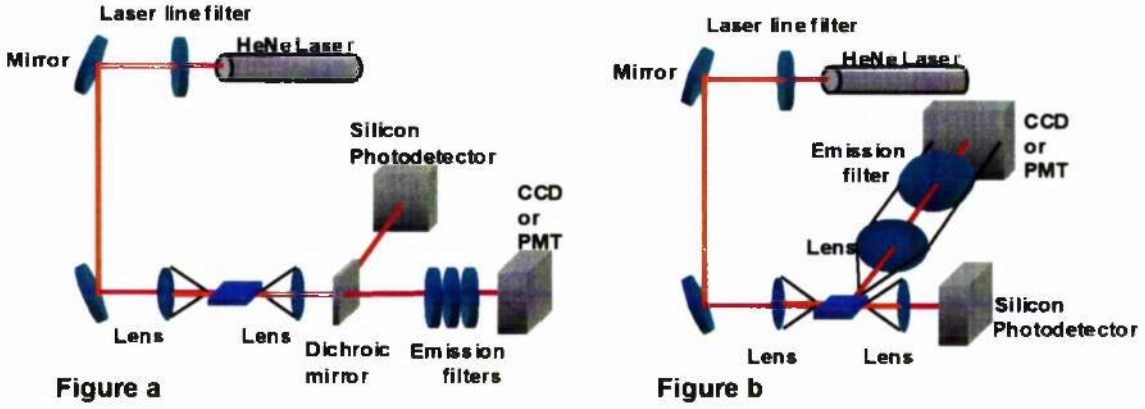

Figure 3.12: Setup representation of the two different configurations. On the left (a) is represented the In-line analysis, and in the right (b), the orthogonal analysis.

Either a CCD (PixelVision Spectra Video SV10K) or a photo-multiplier tube PMT (Hamamatsu, model H5700) were used as fluorescence detectors. In the former case, the CCD was cooled to 255 °K, which was the minimal temperature achievable with the built-in water peltier cooling system, in order to minimise the dark current. The PMT operated at a fixed voltage of 1.2 V. It was enhanced with the development of an electronically shield amplification-filter circuit fed by batteries in order to minimise the noise source coming from the power network

(see Appendix D). The optical filters used were part of an Omega Optical XF46 filter set (Glen Spectra, UK), comprising a narrow band excitation (633NB3.0) filter and emission (670DF40) filters. The silicon photodetector was used to measure the variations of the laser emission and the coupling between the beam and the waveguide.

In the fluorescence measurements, the HeNe excitation laser power was set at 2 mW. For the trans-illumination optical configuration, three emission filters were positioned between the chip and the detector (due to the high throughput of excitation), see Figure 3.12.(a), whilst for the orthogonal set up, only one filter was required (Figure 3.12.b), due to greatly improved signal : noise ratio, see Table 3.2.

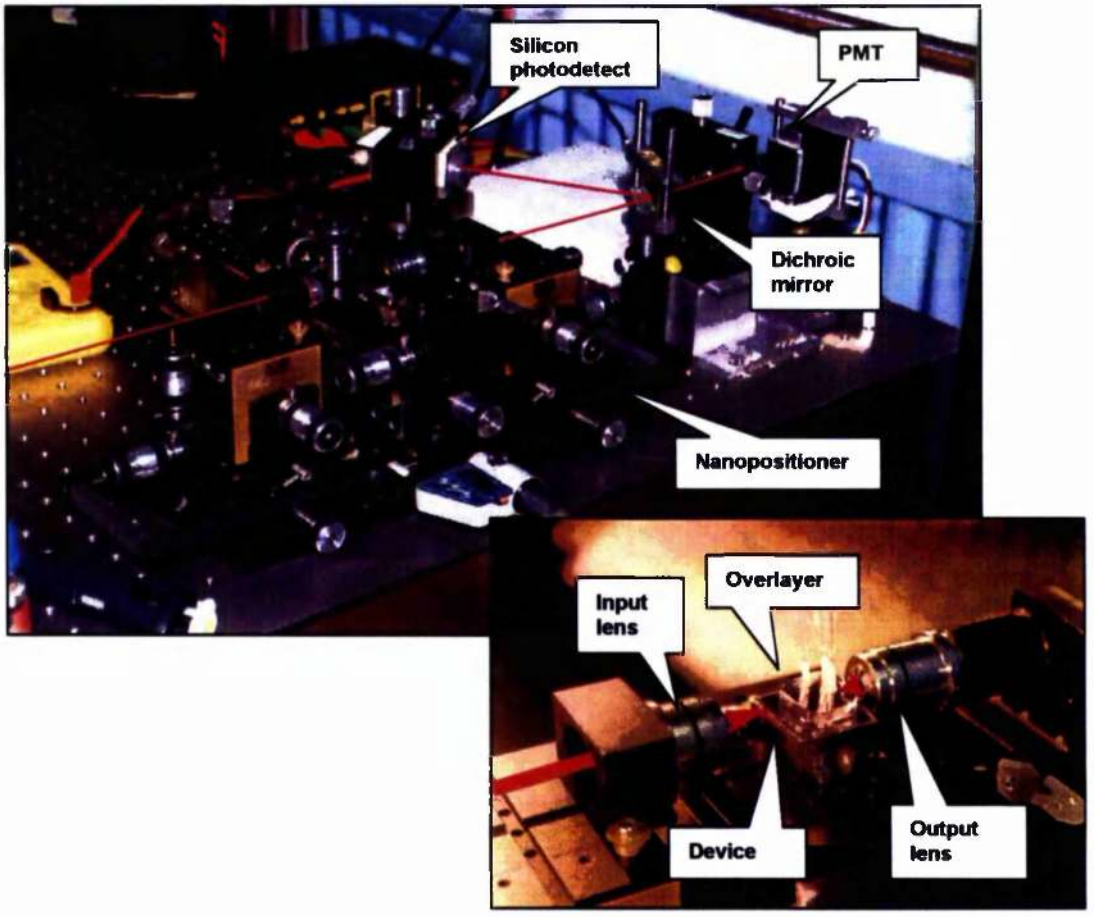

Figure 3.13: Picture of the set-up used for the experiments. The bottom picture shows in detail the device with the lenses.

3.4.3.4 Set-up for the propagation losses measurements.

The waveguides fabricated within the optical chip were used to measure the losses within the FHD glass for 633 nm (see Figure 3.10.a). The optical set-up used the same components as in the previous section, but the arrangement was according to Figure 3.14. Instead of coupling the beam into the waveguide with the chamber, it was coupled into the straight waveguide. The first silicon photodetector intercepted and measured the beam at the input of the lens. Subsequently, the alignment between the beam and the waveguide was maximised by hand and the second detector measured the light transmitted. Waveguides of 2.5 cm of length

were used to obtain an accurate measure of losses (in practice the integrated circuit in the biochip is much smaller).

The previous measurement included the losses in the lens plus the losses in the device. Consequently, the losses in each lens were also measured using the same configuration, i.e. measuring the power before and after the lens. The input lens (x5 with N.A. of 0.12) had 3% losses (Nikon, UK), and the output lens (x10 with N.A. of 0.30) had 7% losses. The lens losses were subtracted from the first measurement giving the losses in 2.5 cm of waveguides.

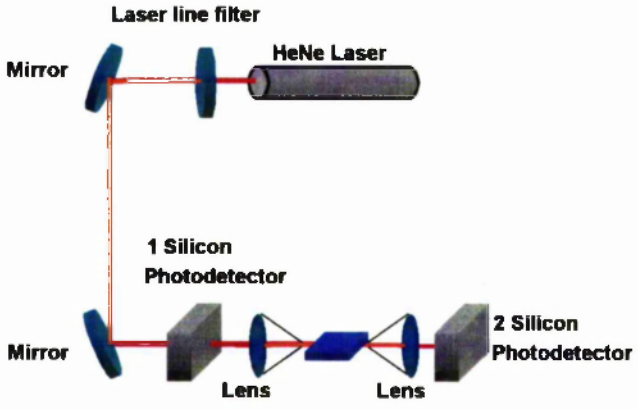

Figure 3.14: Set-up for the transmission losses measurements. The in-line waveguides fabricated within the optical chip were used to measure the losses within the FHD glass for 633 nm. The first silicon photodetector intercepted and measured the beam at the input of the lens. Subsequently, the alignment between the beam and the waveguide was maximised and the second detector measured the light transmitted along a 2.5 cm long waveguide.

3.4.4 Procedure for Fluorescence Measurements and FHD device Characterisation.

The optical set-up used for this purpose is the same as the one explained in the previous section. Prior to use, the devices were cleaned in Pirhana solution (90 % of H_2SO_4 / 10% of H_2O_2). In addition to removing any dirt, this cleaning routine increased the hydrophilicity of the glass surface, which facilitated the subsequent filling of the channels and chamber by capillary action. In order to eliminate

evaporation, a cover slide was firmly bonded onto the device. Since the channels were not sealed, a droplet placed in the edge of the cover slide, spread out into the device. It was demonstrated that this procedure did not interfere with the measured signal.

Upon injection of a droplet of analyte into the reservoir, an increase in the power measured from the in-line output waveguide was observed, indicating that the chamber was filled. In order to allow for a complete signal to noise analysis to be carried out, the blank (Bk) level was measured, in each optical configuration, by filling the analytical chamber with water. The total signal (sum of the blank signal and analytical signal, S) was then measured for increasing concentrations of the analyte. The dark (Dk) current and associated noise of the detectors were also measured in the conditions of the analysis.

3.4.5 Experimental Results.

3.4.5.1 Non-Specific Adsorption and Memory Effects.

The device was set-up in a microscope, as explained in 3.4.3.1. Thus, the fluorescence could be excited and collected directly within the channels and chamber from the top, without using the waveguides. The device was imaged with a CCD camera that was coupled to the photo port of the microscope. Figure 3.15 represents two images of two filling processes with an associated cleaning step between them. After the cleaning, a dark image was obtained, indicating that all the fluorophore was washed away. These pictures show that the filling is reproducible and that no significant memory effects, due to non specific adsorption of the sample molecules onto the walls of the channels and chamber, took place.

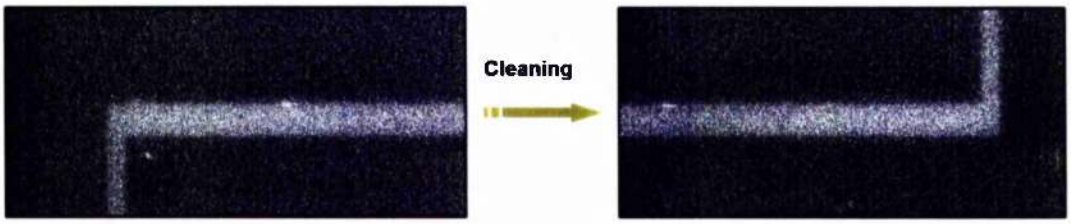

Figure 3.15: Images of two filling processes with its associated cleaning step between them. After the cleaning, a dark image was obtained indicating that all the fluorophore was washed away. The fluorescence was excited and collected directly within the channels and chamber from the top, without using the waveguides. The device was imaged with a CCD camera that was coupled to the photo port of the microscope.

3.4.5.2 Absorption and Scattering losses.

The absorption and scattering losses taking place in the analytical chamber were analysed using the optical arrangement described in Section 3.4.3.2. A 500 μm-length chamber device was placed underneath the detector. The fluorescence could be collected directly within chamber from the top, using the waveguides for the excitation. The concentration of Cy5 used was 24 μM. A cover slide was bonded onto the device and a droplet was introduced by capillary action into the device. The chambers could be filled and emptied uniformly. The device was imaged with the CCD camera obtaining the image in Figure 3.16.(b). Image processing software (IPLab for Windows, Scananalytics, Inc., U.S.A) was used to obtain the fluorescence profile (See Figure 3.16.c). Most of the fluorescence was created at the beginning of the chamber with a peak in the first 50-100 μm. After that maximum, a decay profile was always observed. This corroborated the work previously done with V-grooves and fibres where this decay was also observed (see Figure 3.8).

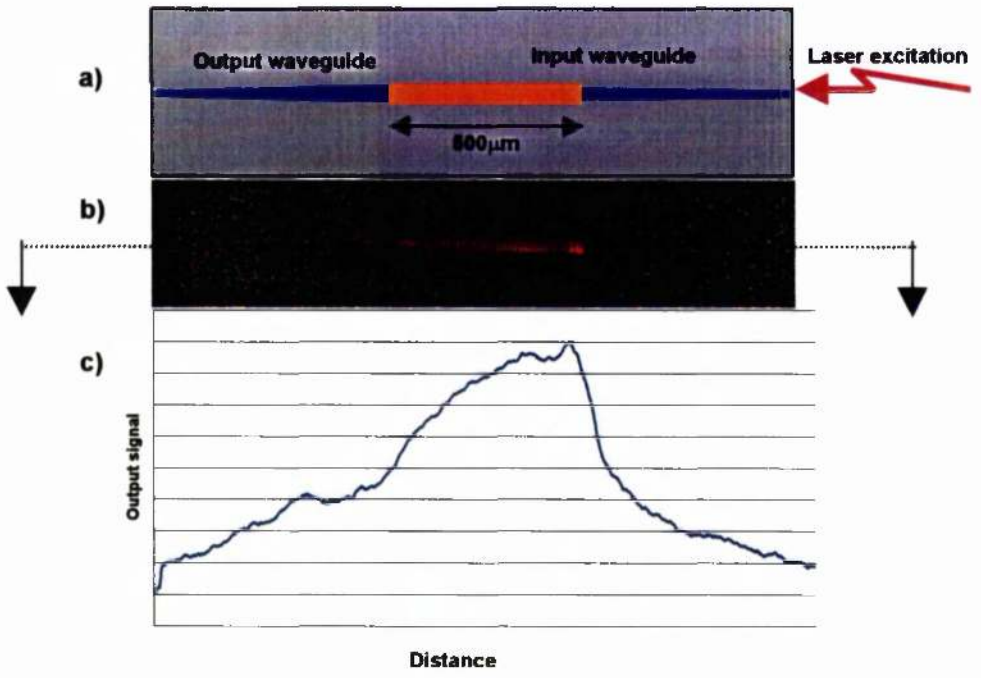

Figure 3.16: Schematic representation (a), CCD image (b), and profile analysis plot (c) of an illuminated chamber of 500-μm length. This device was placed underneath the detector so that fluorescence could be collected directly within chamber from the top, using the waveguides for the excitation.

3.4.5.3 Optical Waveguiding Performance.

The in-line waveguides fabricated within the optical chip were used to measure the losses within the FHD glass for λ=633 nm. The optical set-up and procedure was explained in Section 3.4.3.4. Propagation losses were measured as 0.5 dB cm^{-1} at 633 nm. As expected, this level of loss is higher than that observed at longer telecommunications wavelength, as a consequence of the increased level of Rayleigh scattering at shorter wavelengths. These losses were very competitive for FHD glass [3] and also comparable to glasses deposited using other fabrication techniques. Leistiko *et al.* used also germanosilicate waveguides fabricated by PECVD with losses of 0.5 dB cm^{-1}. However they did not specify the wavelength used and they had higher insertion losses 2-5 dB (typical FHD insertion losses are about 1.4 dB [49]). Puyol *et al.* [4] fabricated waveguides using complementary metal oxide deposition (CMOS) and surprisingly no propagation losses were given.

Plowman *et al.* [5] used siliconoxynitride (SiON) waveguides by PECVD with propagation losses measured at λ=633 nm, being 0.76 dB cm^{-1}.

The level of autofluorescence of the optical circuitry was characterised using the PMT. The transference curves of the PMT between the radiant sensitivity versus the output voltage were used to deduce the power of the autofluorescence emission. The level of autofluorescence of the FHD glasses at 633 nm was estimated to be as low as 0.150 pW cm^{-1}, for an excitation power of 500 μW. FHD glass presented lower autofluorescence values than PDMS [50].

3.4.5.4 Fluorescence Measurements.

Calibration curves for aqueous solutions of Cy5 were experimentally determined for both the in-line and the orthogonal configurations (see optical set-up in Figure 3.12) and for the two different sized chambers (200 μm and 500 μm length). Typical data were obtained using a PMT as the detector in the orthogonal configuration (Figure 3.17.a) and a CCD in the in-line one (Figure 3.17.b). The differences between this set of circumstances are based on the different extents of overlap of the excitation and collection volumes in the different sized chambers. Note that absorption effects had a linear behaviour over the range of Cy5 concentrations used, as indicated by the linearity of the calibration curves.

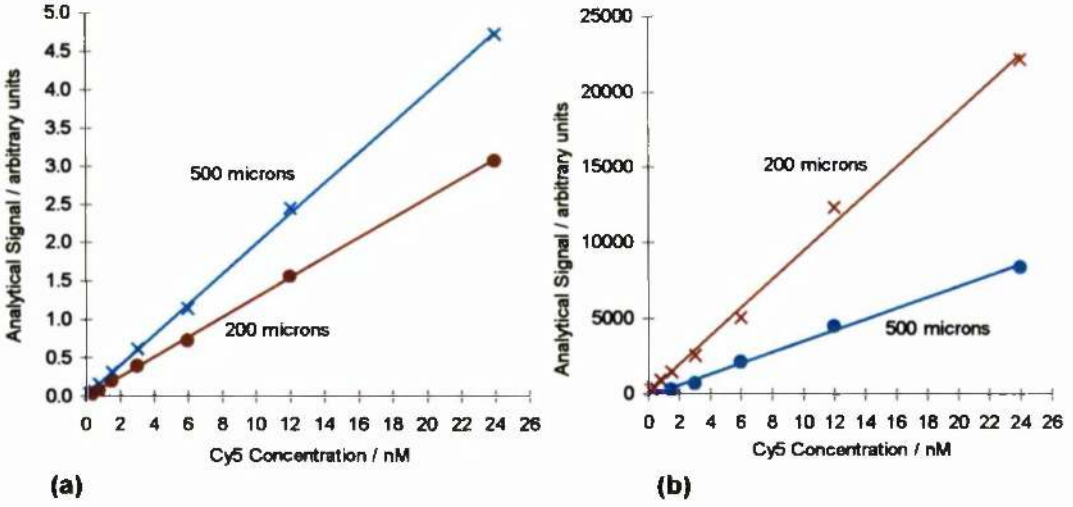

Figure 3.17: Concentration of Cy5 in water versus fluorescence comparing different lengths and configurations: a) A comparison for orthogonal collection using a PMT; b) A comparison for In-line collection using a CCD.

Two different model devices were tested, in which, the chambers were different sizes, and the orthogonal waveguide was adapted accordingly. When an orthogonal waveguide was used for collection, more signal was obtained in the longer chamber, as the waveguide was also wider. However in the in-line configuration, the smaller (230 pL) chamber was characterised by a ~3.5 time increase in the levels of blank signal, as well as total signal, when compared to the bigger chamber (570 pL). This is in agreement with the difference in the levels of power transmitted through the different lengths of chambers obtained using the models provided by BPM and V-groove prototypes.

The two optical configurations were compared using the same detector (PMT) and the same size of the chamber (230 pL). As expected, the orthogonal response was more sensitive (the slope of the calibration curve is 20 times greater) and had higher signal to noise (S/N) and signal to background (S/B) ratio, see Figure 3.17.(a). Once more, as expected, the PMT is more sensitive than the CCD (with better signal: blank ratios, see Table 3.2), although its sensitivity is lower (lower

signal / noise). The same trend, in terms of sensitivity and resolution, was observed within the 570 pL chamber.

Table 3.2 shows a comparison of the analytical figures of merit for the different optical set-ups used in fluorescence measurements with the same concentration of Cy5 in water (3nM, equivalent to either 0.6 attomoles for 230 pl-chamber or 1.7 attomoles of fluorophore for 570 pl-chamber). As expected, for each chamber size, the orthogonal response was characterised by a lower level of background, and higher signal to noise (S/N) and signal to background (S/B) ratios. Accordingly, the experimental detection limit (at 3σ) was found to be lower in the orthogonal configuration, and measured as 20 pM (equivalent to 10 zeptomoles) of material. This absolute value is comparable to that previously obtained using other integrated optical (evanescent) systems, such as those developed in silicon by Effenhauser *et al.* [6] or in SiON by Plowman *et al.* [5]. It also similar to the detection limit reported by Vo-Dinh *et al.* [7] using a membrane immobilised system.

Chamber Length	Detector Optical set-up	Blank (Bk)	Dark (Dk)	Noise (N)	Output (O)	Signal (S)	S/N	S/B	Dt. Lim (DL)
200 μm	CCD In-line	7278	1100	150	9803	2525	16.83	0.41	188 pM
	CCD Ortho.	1550	1100	150	5500	3950	26.33	8.78	95 pM
500 μm	CCD In-line	1930	1100	150	2670	740	4.93	0.89	1.5 nM
	CCD Ortho.	1550	1100	150	7840	6290	41.93	13.98	20 pM
200 μm	PMT In-line	35	25	60	118	58	0.96	5.8	6 nM
	PMT Ortho.	25	25	60	425	400	6.67	NA	375 pM
500 μm	PMT In-line	35	25	60	35	0	0.00	0.00	12 nM
	PMT Ortho.	25	25	60	550	525	8.75	NA	188 pM

Table 3.2: Analytical figures of merit for the different optical and analytical setups used in the experiments measured with the same concentration of Cy5 in water (3nM). Abbreviations are as follows: Dk, dark signal; Bk, blank signal; S, analytical signal; S/N, signal to noise ratio; S/B, signal to background ratio, where B=Bk-Dk; DL, experimentally determined detection limit, defined as the analyte concentration at which S/N=3.

Likewise, Figure 3.18 (a) and (b) show CCD images of the output waveguide for both the trans and orthogonal setup, respectively. As expected, it is seen that the latter configuration provides higher signal to noise (S/N) and signal to blank (S/Bk) measurements than for in-line illumination. In both cases, the scattering losses are higher when the fluorophore is in the chamber because, in addition of the excitation light transmitted in the cladding, some of the emission light that has not been collected in the core waveguide, has also been transmitted in that cladding.

Fluorescence measurements from aqueous solutions of the Cy5-labelled 53-mer ODN were also carried out in the 570 pL chamber, with the orthogonal configuration and PMT detector. At the lowest concentration used, namely 1.25 nM, the limiting noise is that from the dark current, i.e. from the detector. This suggests that, at this level of concentration, the S/N of the measurement could be improved by increasing the laser power. Doing this may result in unwanted effects, such as heating and fluorophore photobleaching, which would alter the validity of the analysis.

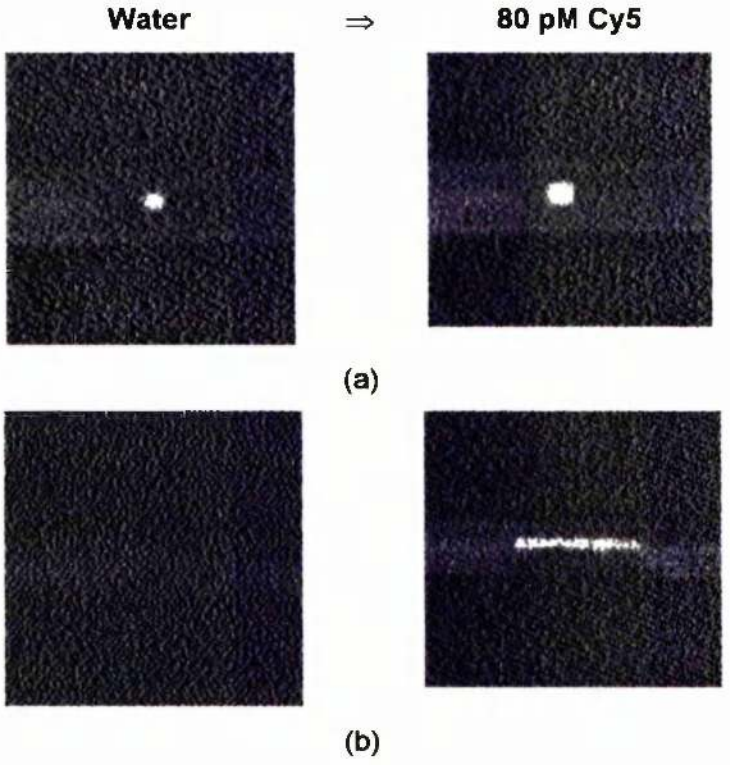

Figure 3.18: (A) CCD image of the In-line output waveguide with water (left), and with a 1.5 nM concentration of Cy5. (B) CCD image of the Orthogonal output waveguide with water (left), and with an 80 pM concentration of Cy5.

3.4.5.5 Noise due to scattered light.

The same optical arrangement as in the previous Section (3.4.3.3) was used to determine elastic scattering noise. Solutions of Cy5-labelled ODN (big molecules) and Cy5 (smaller molecules) were used to analyse the relationship between the scattering noise and the size of the molecules involved in the fluorescence assay. The scattering noise was found 3 times higher as the size of the molecules increased. This is an expected result due to the scattering of light from the molecules in solution [51], demonstrating that the analytical noise is the limiting source of noise. This study could, in future, be extended by using ODN's of different lengths

Further, as expected, the scattering increases for increased concentrations of fluorophore [52] (as the absolute number of molecules in the pico-litre chamber

increases), see Figure 3.19. As the concentration of ODN was increased (up to 180 nM), the analytical noise was found to increase by more than two orders of magnitude, owing to Rayleigh scattering of radiation by the ODN molecules

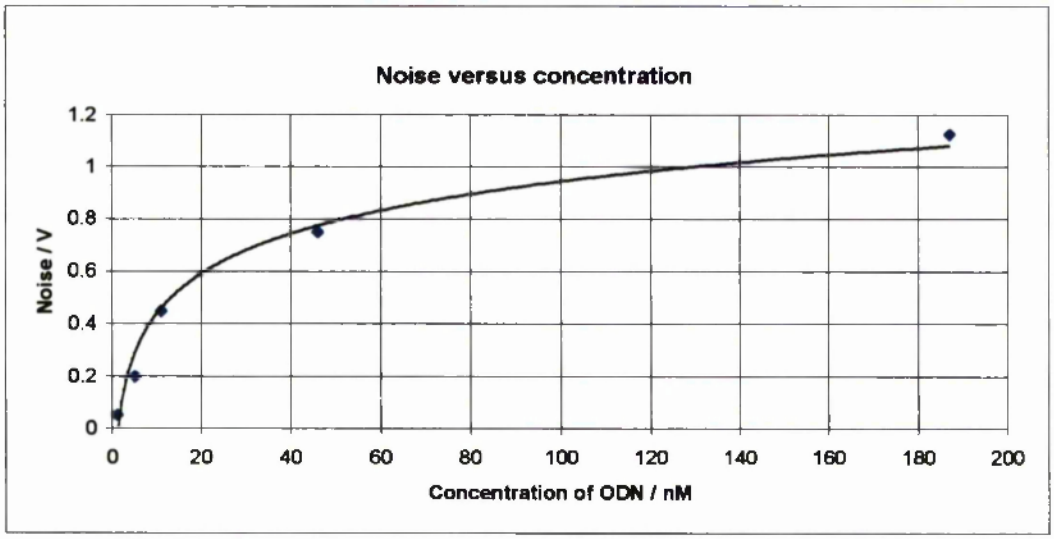

Figure 3.19: Representation of the S/N ratio versus the analytical signal. This plot indicates that the elastic scattering noise increases for higher concentrations of fluorophore.

3.5 Conclusions.

A FHD device was developed in a form that is suitable to fluorescence measurements, demonstrating its future applicability to either biological or chemical assays [53]. These devices consisted of low loss waveguides with deep and vertical channels. Their performance was assessed in the framework of low volume fluorescence-based assays, using the fluorophore Cy5. Solutions of the fluorophore were excited with a He-Ne laser and analytical measurements were made with either a PMT or a CCD camera. An optical characterisation of FHD glass was carried out reaching the conclusion that FHD glass fulfilled the requirements of fluorescence bioassays in terms of autofluorescence, scattering, and adsorption of the fluorophore. Devices featuring chambers with different

volumes (between 200 and 600 pL) and different optical configurations (in-line and orthogonal waveguides) were fabricated. These devices determined that the optimal fluorescence configuration consisted of an orthogonal set-up using a chamber of 500 μm long. In this optimal arrangement, the experimental detection limit was determined as ca. 20 pM (equivalent to 10 zeptomoles or ca. 6000 molecules) of Cy5 [53]. This detection limit was compared with other optical techniques and materials, and was found to be very competitive. The factors that limit the signal resolution were also characterised in terms of autofluorescence, and scattering from the FHD glasses (scattering from the sample molecules and detector noise). The applicability of the device to the miniaturisation of bioassays was illustrated by analytical measurements on fluorescently-labelled oligodeoxynucleotides, as might be appropriate for a "Lab-on-a-Chip" platform.

An intrinsic advantage of the technology is that it can be integrated within a suitable fabrication protocol, such that optical chips can be produced simultaneously with an associated microfluidics circuitry. This capability was enhanced by the elaboration of additional techniques described in Chapter 2. The flexibility of the technology will enable a variety of configurations to be conceived and implemented, with the prospect of using the techniques for Lab-on-a-Chip technologies. A further possibility is the use of silane chemistries to immobilise biomolecules *in situ*, in order to fabricate miniaturised biosensors where the high surface to volume ratios will enhance analytical capabilities. Finally, it should be emphasised that although, in this research project, optical connections were made using free-space optics, the compatibility of FHD glass with optical fibres makes low loss pigtailing possible[2].

3.6 References.

1 Kawachi M., IEE Proc.-Optoelectron., Vol. 143, No. 5, 1996.

2 Jones C.A., Cooper K.,IEE Proc.-Optoelectron., Vol. 143,No. 5, 1996.

3 Kawachi M., Opt. Quantum Electron., 22, 391, 1990.

4 Puyol M., del Valle M., Garces I., Villuendas F., Dominguez C., Alonso J., Anal. Chem., Vol. 71, pp. 5037-5044, 1999.

5 Plowman T.E., Reichert W.M., Biosensors & Bioelectronics, Vol. 11, N. 1/2, pp. 149-160, 1996.

6 Effenhauser C. S.; Bruin G. J. M.; Paulus, A., Ehrat M., Anal. Chem., 1997, Vol. 69, pp. 3451-57.

7 Vo-Dinh T., Alarie J.P., Isola N., Landis D., Wintenberg A. L., Ericson M. N., Anal. Chem., 1999, Vol. 71, 358-63.

8 Thompson W.R., Cai M., Ho M.K., Pemberton J.E., Langmuir, Vol.13, No.8, pp.2291-2302, 1997.

9 Mukherjeeroy M., Kurihara M., Penn L.S., Journal Of Adhesion Science And Technology, Vol.9, No.7, pp.953-969, 1995.

10 Turner T.E., Karube I., Wilson G., Biosensors, London: Oxford University Press, 1998.

11 Hall E. A. H., Biosensors, Cambridge University, Open University Press, 1990.

12 Boisdé G., Harmer A., Chemical and Biochemical Sensing with Optical Fibers and Waveguides, Artech House Inc., 1996.

13 Wolfeis O. S., Fiber Optic Sensors and Biosensors, Vols. I and II, Boca Raton:CRC Press, 1991.

14 Blum L. J., and Coulet P. R., Biosensor: Principles and Applications, New York: Marcel Dekker, 1991.

15 DeRisi J.L., Iyer V.R., Brown P.O., Science, Vol.278, No.5338, pp.680-686, 1997.

16 Cheung V.G., Nature Genetics, Vol.18, No.3, pp.225-230, 1998.

17 Petric A., Jacobson A.F., Barrio J.R., Bioorganic & Medicinal Chemistry Letters, Vol. 8., No. 12, pp. 1455-1460, 1998.

18 Werner T., Huber C., Heinl S., Kollmannsberger M., Daub J., Wolfbeis O.S., Fresenius Journal Of Analytical Chemistry, Vol. 359, No.2, pp. 150-154, 1997.

19 Aich S., Basu S., Photochemistry and Photobiology, Vol.70, No. 4, pp. 602-606, 1999.

20 Balandin A.A., Lopaev D.V., Klopovskii K.S., Popov N.A., Rakhimov A.T., Rakhimova T.V., Plasma Physics Reports, Vol.25, No.11, pp.893-904, 1999.

21 Ohyama T., Maruo Y.Y., Tanaka T., Hayashi T., Sensors And Actuators B-Chemical, Vol.59, No.1, pp.16-20, 1999.

22 Razek T.M.A., Miller M.J., Hassan S.S.M., Arnold M.A., Talanta, Vol.50, No.3, pp.491-498, 1999.

23 Zander C., Sauer M., Drexhage K.H., Ko D.S., Schulz A., Wolfrum J., Brand L., Eggeling C., Seidel C.A.M., Appl. Phys. B., 63, pp. 517-523, 1996.

24 Roberts W.L., Pharmacotherapy, Vol.19, No.12, pp.1467-1468, 1999.

25 Pin S.S., Kariv I., Graciani N.R., Oldenburg K.R., Analytical Biochemistry, Vol.275, No.2, pp.156-161, 1999.

26 Nikiforov T.T., Jeong S., Analytical Biochemistry, Vol.275, No.2, pp.248-253, 1999.

27 Sauer M., Arden-Jacob J., Drexhage K.H., Gobel F., Lieberwirth U., Muhlegger K., Muller R., Wolfrum J., Zander C., Bioimaging, 6, pp. 14-24, 1998

28 Broach J.R., Thorner J. Nature Suppl., 384, pp. 14-16, 1996.

29 Fodor S., Nature, 364, pp. 555-556, 1993.

30 Lubbers D. W., and Opitz N., Naturdorsch Z., Vol. 30C, pp. 532-533, 1975.

31 Brown P.O., Botstein D., Nature Genetics Supplement, 21, pp. 33-37, 1999.

32 Wolfbeis O.S., Klimant I., Werner T., Huber C., Kosch U., Krause C., Neurauter G., Durkop A., Sensors And Actuators B-Chemical, Vol.51, No.1-3, pp.17-24, 1998.

33 Koch S., Wolf H., Danapel C., Feller K.A., Biosensors & Bioelectronics, Vol.14, No.10-11, pp.779-784, 2000.

34 Skladal P., Deng A.P., Kolar V., Analytica Chimica Acta, Vol.399, No.1-2, pp.29-36, 1999.

35 Papkovsky D.B., ORiordan T.C., Guilbault G.G., Anal. Chem., Vol.71, No.8, pp.1568-1573, 1999.

36 Mallat E., Barzen C., Klotz A., Brecht A., Ganglitz G., Barcelo D., Environmental Science & Technology, Vol.33, No.6, pp.965- 971, 1999.

37 Kroger D., Katerkamp A., Renneberg R., Cammann K. Biosensors & Bioelectronics, Vol.13, No.10, pp.1141-1147, 1998.

38 Dubendorfer J., Kunz R.E., Applied Optics, Vol.37, No.10, pp.1890-1894, 1998.

39 Marks R.S., Bassis E., Bychenko A., Levine M.M., Optical Engineering, Vol.36, No.12, pp.3258-3264, 1997.

40 Farrell C.D., Rowell F.J., Cumming R.H., Analytical Proceedings, Vol.32, No.6, pp.205-206, 1995.

41 Maeda Y., Smith B.L., Agre P., Knepper M.A., Journal Of Clinical Investigation, Vol.95, No.1, pp.422- 428, 1995.

42 Yevick D., Glasner M., Optics Letters, Vol. 15, No. 3, pp. 174-176, 1990.

43 Chung Y., Dagli N., Thylen L., Electronics Letters, Vol.27, No. 23, pp. 2119-2121, 1991.

44 Masoudi H.M., Arnold J.M., IEEE Photonics Technology Letters, Vol.6, No.7, pp.848-850, 1994.

45 Daniel Ortega, PhD Thesis, University of Glasgow, 1998.

46 Yevick, D., Optical Quant. Electron., 26, pp. S185-s197, 1994.

47 Ruano J.M., Ortega D., Bonar J.R., Cooper J.M., Aitchison J.S., CLEO Europe 98 Proc., 198, 1998.

48 Klekamp A., Kersten P., Rehm W., Journal of Lightwave Technology, Vol 14, N. 12, 1996.

49 Bonar J.R., PhD Thesis, Glasgow University, 1995.

50 Vincent Benoit, University of Glasgow, Personal Communication.

51 Ross D.A., Dimas N., Particle & particle systems characterization, Vol.10, No.2, pp.62-69, 1993.

52 Ingle J.D., Crouch S.R., Spectrochemical Analysis, Prentice Hall, ISBN: 013826876-2, 1988.

53 Ruano J.M., Benoit V., Aitchison J.S., Cooper J.M., Anal.Chem., Vol.72, pp. 1093-1097, 2000.

Chapter 4: OPTICAL TREATMENT OF THE SIGNAL FOR ARRAY SENSORS IN FHD GLASS.

4.1 Introduction.

Integrated optics for the 1550 nm telecommunication wavelength were intensively studied in the early 90's [1,2,3,4,5]. This chapter, however, describes a variety of integrated optical circuit designs for wavelengths of 633 nm which aim to demonstrate the application of FHD technology to biosensing.

At the early stage of this research, it was found that there was no method to integrate different kinds of simple optical biosensing devices. This section therefore provides formulas, tables, and designs, where the interested researcher can find the dimensions of bends, tapered waveguides, power splitters, and filters. It also demonstrates that FHD based optical devices can be modelled using software, and subsequently fabricated to a high degree of predictability between the model and the device. To conclude this chapter, a planar array of FHD fluorescence sensors is described. This device illustrates that many of the concepts of integrated optics can be transferred across to the biosensing area. In this case, a 1x16 power splitter was used on a basic building block for an array sensor.

The dimensions of the integrated optical components were optimised using a commercial package based on a beam propagation method (2D BPM software,

Optiwave Corporation, Canada). A brief summary about this simulation technique was given in the previous chapter (see Section 3.3.1).

4.2 Tapered Waveguides for 633 nm in FHD glass.

For certain integrated optical functions, it was necessary to convert a beam guided by a channel waveguide into a collimated or focusing beam, guided by a slab waveguide. In fluorescence sensing, for example, it is necessary to expand the beam coupled in a narrow waveguide, in order to excite a wider analytical chamber (see Chapter 3). A tapered waveguide consists of a waveguide with different input and output widths (see Figure 4.1). To maintain an adiabatic operation in the electromagnetic field expansion process, it is necessary to make the change of width gradually. When the waveguide width is increased, new modes are allowed to develop in the waveguide. The adiabatic expansion allows a single input mode to evolve into the fundamental mode of the wider waveguide. If the waveguide width changes too rapidly, the input mode scatters into higher order modes supported by the wide output section. Long tapered waveguides will ensure adiabatic expansion and thus, low losses, however they can be excessively long.

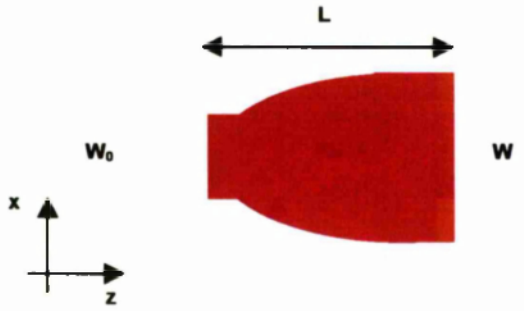

Figure 4.1: Schematic representation of a tapered waveguide consisting of a waveguide with different input and output widths.

This section explores, through a very simple approximation, the minimum distance required in a tapered waveguide in order to keep an adiabatic process.

Subsequently, this approximation was verified using the BPM software (see Chapter 3). The work carried out by Milton *et al.* [6] was particularly relevant to this section as it provided the starting point of the design device process. In this work, he deduced a formula that predicts the taper length (L) which keeps an adiabatic expansion for a given initial and final waveguide width (W_o and W respectively), accordingly:

$$L = \frac{n_{eff}}{2\alpha\lambda_o}(W^2 - W_o^2) \qquad \text{Equation 4.1}$$

Where α was a parameter that indicates the taper shape (equal to 1 for parabola), and λ_o was 633 nm. The value of the effective refractive index (n_{eff}) was between the refractive index of the cladding (n_{clad}) and the refractive index of the core (n_{core}). Due to the fact that n_{clad} and n_{core} were very similar, it was approximated that n_{eff} was equal to n_{clad}. For example, for an initial width of 5 μm and a final width of 15 μm (represented in Figure 4.2 by 5:15), the length given by Equation 4.1 was 230 μm. Ideal taper lengths were calculated for different ratios of widths, such as 5:20 (an initial width of 5 μm and a final of 20 μm), 5:25, 5:30, and 25:100.

These simulation assumes that most of the power in the waveguide is in the fundamental mode. The results obtained from the Equation 4.1 were confirmed using 2D BPM as follows. For each ratio, several simulations were performed with different lengths. A Gaussian electromagnetic field was introduced in the input waveguide. The software calculated, for each length, the power inside the boundaries at the end of the output waveguide. In all the cases, it was noted that below a minimum distance, high losses were observed. The results obtained from each ratio width were plotted in Figure 4.2. The ordinate X is the ratio between the simulated length and the calculated length. The abscissa Y was the power inside the boundaries at the end of the output waveguides. It was seen that all of the tapered waveguides had a transmission efficiency higher than 90% when the

length of the taper was at least that calculated with the Equation 4.1 or longer. Therefore, the formula used to calculate the length was a valid and simple way to design tapered waveguides.

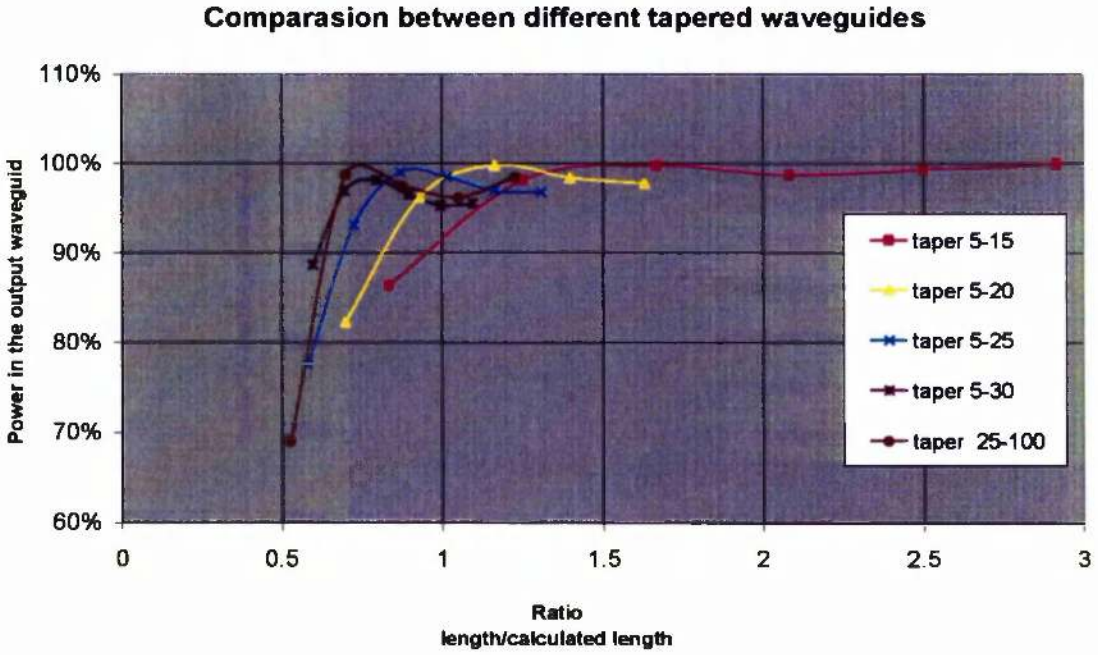

Figure 4.2: BPM analysis of the losses produced in tapered waveguides. The ordinate X axe is the ratio between the simulated length and the calculated length. Thus, a value of X equal to 2 means that the simulated length is the double length of the calculated value. The abscissa Y was the power inside the boundaries at the end of the output waveguides.

4.3 Bends in Waveguides for 633 nm in FHD glass.

A similar problem to that described in the previous section was further explored in order to design waveguide bends. When two waveguides, at different axes planes, need to be connected (see Figure 4.3.a), it is necessary to obtain the minimum distance that allows us to link both waveguides without significant loss of power. Kawachi [1] calculated experimentally the losses in FHD silica monomode waveguide at a wavelength of 1550 nm. This work revealed that in order to have bend losses less than 0.1 dB for 1550 nm it was necessary to keep a large radius

bend. For example, a refractive index difference of 0.25%, 0.45%, 0.75% needs a radius of 25 mm, 15 mm, 5 mm, respectively. A high refractive index difference produces high confinement which, in turn, allows for a smaller radius bend. In order to apply Kawachi's radius for a shorter wavelength (633 nm), monomode waveguiding was required. This reduced the bend losses to at least 0.1 dB because shorter wavelengths were more confined into the bend waveguide.

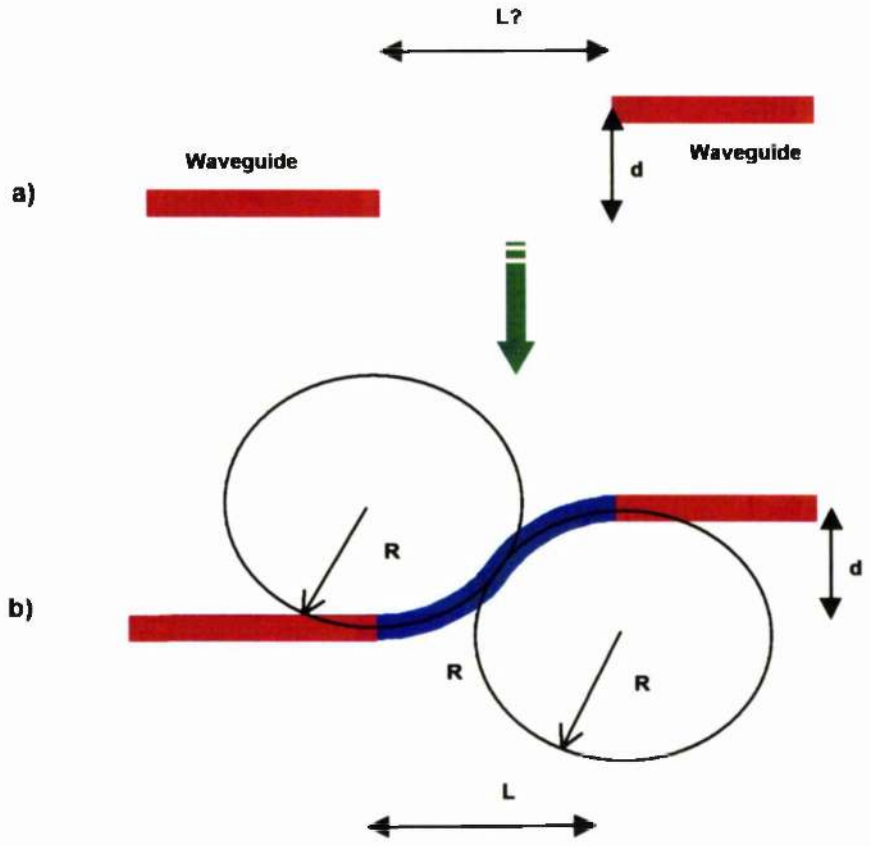

Figure 4.3: a) Schematic representation of the stated problem. b) Description of the solution to obtain the length of the bend. Two arcs were linked each other in order to connect both waveguides.

Two arcs were used to link both waveguides, using an S-bend (Figure 4.3). The arc radius of the S-bend must be chosen in agreement with the refractive index difference according Kawachi's paper [1]. Hence, with a known radius, there was

a unique length of the S-bend that gave us losses smaller than 0.1 dB. This length was calculated using geometrical formulas, and it was equal to:

$$L = \sqrt{4Rd - d^2} \qquad \text{Equation 4.2}$$

Where d was the distance between the waveguides and L the length of the S-bend arc. The Equation 4.2 has been plotted for three different refractive indexes in Figure 4.4. For example, a transversal distance between waveguides of 400 μm, "d" in Figure 4.3(a) and (b), with a 0.45% refractive index difference glass, requires a S-bend length of approximately 5000 μm to keep the radius as small as 15 mm (Kawachi's radius) and losses as low as 0.1 dB. Figure 4.4 was a very useful tool in order to obtain a set of design rules of low loss bends in monomode waveguides. Once the length was obtained by this graph, the two circumference arcs were substituted with cosine arcs. It has been shown that minimum bending losses were obtained with cosine shapes when compared with other S bends [7].

The devices fabricated during this research had bends which were designed by this method. It was qualitatively observed that such a waveguide did not produce scattering and resulted in high throughputs.

Another approach could have been used in order to define the bending losses. Assuming that only the fundamental mode is above the cutoff frequency it is possible to calculate the power loss for a monomode bend waveguide and a wavelength. Lee shows that the attenuation coefficient in a waveguide depends exponentially on the bending radius and that there is also a wavelength dependent pre-factor [8]. As an example, halving the wavelength, the radius, and a corresponding reduction in the width, the radiation loss increases by a factor of two.

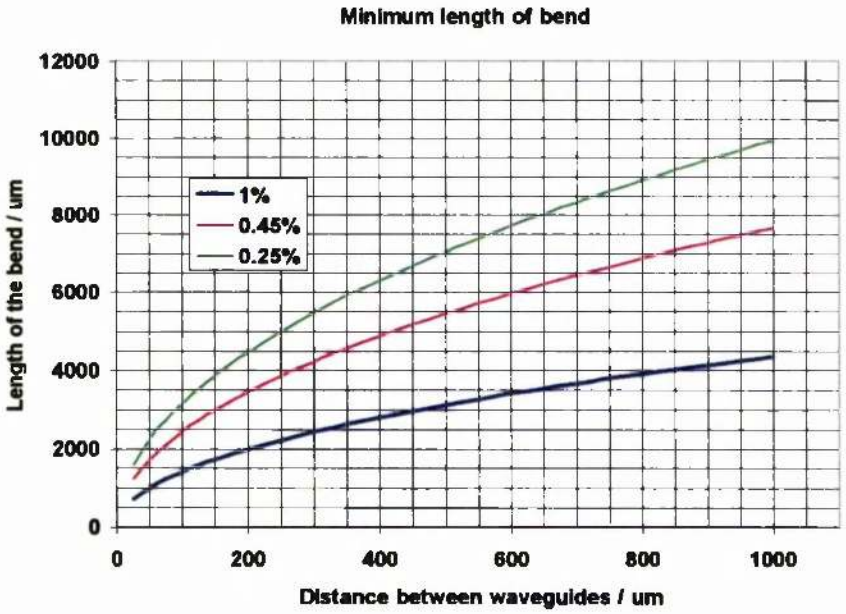

Figure 4.4: Plot of the Equation 4.2 for three different refractive indexes: The ordinate X is the distance between the waveguides, and the abscissa Y is the length of the link between them. For example, a distance between waveguides of 400 μm in a 0.45% refractive index difference glass, requires approximately 5000 μm to keep the radius bend as small as 15 mm and losses as low as 0.1 dB.

4.4 Integrated Optics Power Splitters for 633 nm.

There are several methods to produce an integrated beam splitter. Those studied in this section were based on: Y-branches, multimode interference (MMI), and directional couplers. Monomode guiding was an important issue in the design of power splitters. For example, optical couplers require monomode operation [4], and the Y-branch splitting ratio depends less on the input fibre alignment if monomode guiding is used [9]. The MMI splitter does not require monomode guiding, however monomode MMI's have bigger fabrication tolerances [10]. As it will be seen, monomode guiding for 633 nm implies that the acceptable fabrication errors were small.

4.4.1 Monomode Guiding Requirements.

Using the BPM software, Chapter 3, it was possible to obtain the accurate dimensions and refractive index difference required for 633 nm monomode operation. The input data for the mode solver was the cross section of the waveguide and the refractive index. This method calculates the propagation constant and the optical field profile of the waveguide modes [11]. A 0.25 % refractive index difference and waveguides of 4 μm width and 4 μm depth enabled monomode guiding. To damp fluctuations in the refractive index during FHD deposition and ensure a monomode waveguide, the width of the waveguides was chosen to be smaller that 3 μm. The depth of the waveguide remained 4 μm. The waveguide, thus, was light polarisation dependent, however this was not an important feature for the power splitters.

4.4.2 Fabrication issues of Power Splitters.

During the fabrication protocol, only the first five steps of the seven processes presented in Section 2.2 were necessary (see Page 41), because the microfluidic system was not required at this stage. To obtain the monomode core characteristics, it was necessary to make a slight variation in the flowmeters rates from the deposition explained in Section 2.2.2. The waveguides core recipe is described in Table 4.1 and gives a waveguide thickness of 4 μm. The prism coupling technique verified that it was a monomode glass [12]. The cladding layer was 14 μm-thick.

Warming stage:				
Initial turntable temperature: 150 ° C		Torch warming transversals		
		Number:	2	
		Oxygen:	2 l min^{-1}	
		Hydrogen:	5 l min^{-1}	
		Nitrogen:	3 l min^{-1}	
Deposition stage:				
Halides flows:		Torch flows:		
$SiCl_4$: 150 sccm		Number:	4	
$GeCl_4$: 23 sccm		Oxygen:	2 l min^{-1}	
BCl_3: 65 sccm		Hydrogen:	5 l min^{-1}	
Master: 676 sccm		Nitrogen:	3 l min^{-1}	
Sintering cycle:				
Initial Temperature	Increasing rate	Sintering time and temperature	Decreasing rate	Final Temperature
1050 °C	15 °C min^{-1}	2 hours at 1350 °C	-10 °C min^{-1}	750 °C
Sintering atmosphere:				
Helium: 0.7 l min^{-1}		Oxygen: 0.1 l min^{-1}		

Table 4.1: Deposition parameters of $SiO_2 - GeO_2$ for the fabrication of a monomode optical circuitry. Notice that the only variation with the core deposition of Chapter 2 was regarding the amount of Ge used.

4.4.3 Optical Set-up for Characterisation.

Once the devices were fabricated, they were tested using the system shown in Figure 4.5. The detector was a colour CCD camera (CoolSNAP, RS Photometrics). A narrow band excitation (633NB3.0) optical filter was used from Omega Optical (Glen Spectra, UK). Excitation light was provided by a 1.8 mW HeNe laser, λ=633 nm, and was coupled to the input waveguide using a 633 nm monomode fibre (Model FS-SN-3224, N.A. 0.12, 3M, USA). The light was coupled into the fibre by a x5 lens with a N.A. 0.12 (Nikon, UK). Light from the

output waveguides was collected on the CCD detector using microscope objective lens (N.A. 0.4, 16 mm, Ealing).

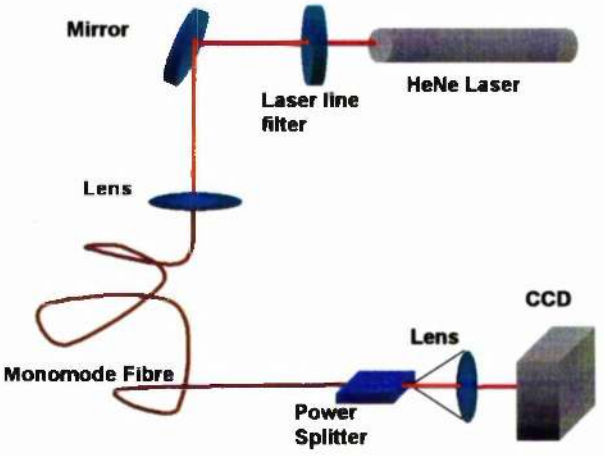

Figure 4.5: Set-up representation of configuration used to test the power splitters.

The images obtained using the CCD were stored in a computer (Optiplex, DELL) and subsequently analysed using an image processing software (IPLab for Windows, Scananalytics Inc., U.S.A). This software allowed us to obtain the profile of the beams.

4.4.4 Y-Branches Power Splitters for 633 nm in FHD glass.

4.4.4.1 Design stage.

The Y-branch was divided in two known structures: (i) a tapered waveguide, and (ii) two S-bend arcs, as shown Figure 4.6. As mentioned, monomode waveguiding minimised the variations of the splitting ratio versus the input fibre displacement. When multimode waveguides were required, a narrow "neck" should be introduced in the input waveguide to keep steady the splitting ratio [9], see Figure 4.6.

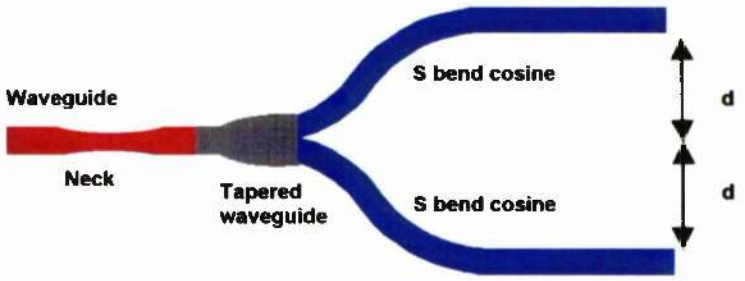

Figure 4.6: Schematic representation of a Y-branch. It was divided in three parts: a tapered waveguide and two S bend arcs.

4.4.4.2 Fabrication stage.

A set of Y-branches was fabricated to divide the light in 16 beams (see Figure 4.7). The width of the waveguides was 3 μm. The tapered waveguide initial width was 3 μm and the final width was 8 μm. The final 16 waveguides were separated by 125 μm to avoid coupling between each other. As mentioned, these dimensions provided monomode guiding and then, these Y-branches did not require a narrow waveguide neck. The total length of the 16 beam splitter was 25 mm.

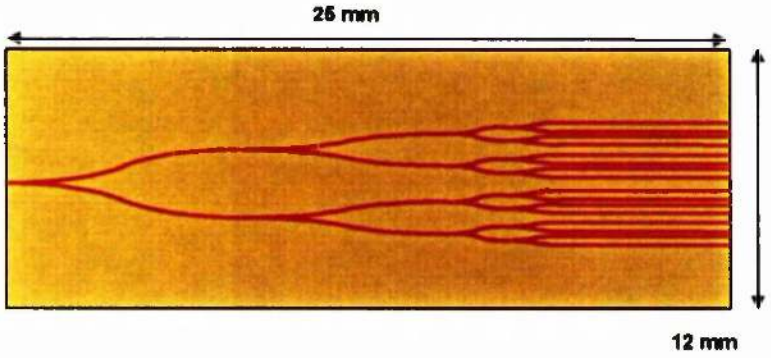

Figure 4.7: Schematic representation of the 1x16 splitter. The total length of the 16 beam splitter was 25 mm. The width of the waveguides was 3 μm. The tapered waveguide initial width was 3 μm and the final 8 μm. The final 16 waveguides were separated 125 μm to avoid coupling between each other.

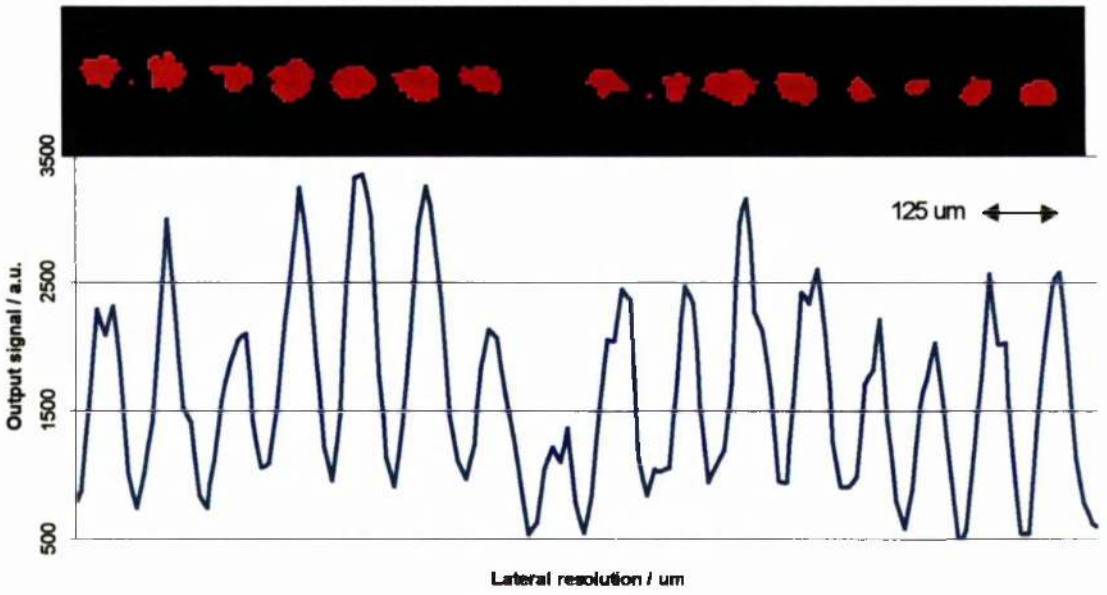

Figure 4.8: Analysis of the efficiency and uniformity of the Y-branches waveguides. Top shows a CCD image of these splitters and the bottom represents its profile.

4.4.4.3 Results.

Images of the output of the 1x16 beam splitter were obtained and treated using the optical set-up and the software explained in Section 4.4.3. Figure 4.8 demonstrates that it is feasible to use these devices for beam splitting techniques. However, due to fabrication defects, the power in the 16 outputs is not uniform. More work must be carried out to improve the uniformity. The difficulty to achieve a uniform photolithography and RIE process in all the Y-branches causes this lack of uniformity, and is a problem that could be overcome by detailed process development.

A possible solution could be the insertion of a truncated Y-branch (see Figure 4.9). This junction was designed to make the splitter less dependent of the quality of the fabrication process. This truncated profile will produce more losses in the Y-branch, although it would provide a more uniform power distribution [13].

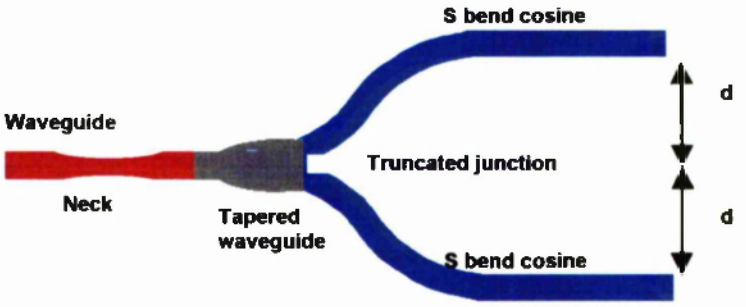

Figure 4.9: Schematic representation of the improved Y-branch design.

4.4.5 Multimode Interference (MMI) Splitters for 633 nm.

The main purpose of this section is to demonstrate the feasibility of fabrication of an MMI for operation at a wavelength of 633 nm, and to provide a valid design method for MMI through formulas and BPM simulations.

The operation of a MMI device is based on the self imaging principle [14]. Self-imaging is a property of multimode waveguides by which an input field profile is reproduced, in single or multiple images, at periodic intervals along the propagation direction. This property has been extensively used in telecommunications to increase the flexibility and reconfigurability of an optical network. Optical devices based on MMI effects have a large optical bandwidth, are polarisation insensitive, have compact size, and relatively good fabrication tolerances [15]. Phase diversity networks [16], Mach-Zehnder switches [17] and modulators [18], ring lasers [19], and power splitters [20] incorporate this multimode interference principle.

4.4.5.1 Design stage.

The central structure of an MMI device is a waveguide designed to support a large number of modes. To launch light into, and recover light from a multimode waveguide, a number of access waveguides are placed at the input and output.

Such devices are referred to as MxN MMI couplers, where N and M are the number of output and input waveguides respectively.

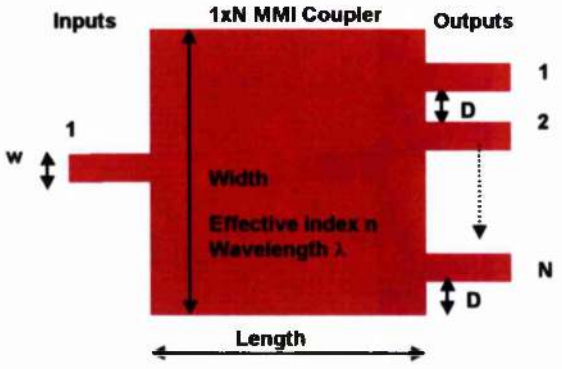

Figure 4.10: Geometrical design of a multimode interference (MMI) coupler based on symmetrical interference. Dimensions: width W=2(N·D+1), where D=w, and w represents the with of the waveguides, length $L=(1/N)\cdot nW^2/\lambda$ [22].

This research has focused in the 1×N power splitters for 633 nm. The analysis method followed in this work was based on two techniques. Firstly, a rough theoretical analysis, using the guided-mode propagation analysis (MPA) [21], was carried out. Secondly, the BPM method was employed. The MPA method has been reviewed in [15] and summarised in [22]. This last paper has been used here to begin the design of the MMI devices in silica. It must be pointed out that this theoretical analysis technique uses approximations based on the fact that strong guiding is taking place in the device. However, FHD silica waveguides do not fulfil this supposition, and consequently the device design must be refined using 2D BPM.

The formulas from MPA method were:

$$W = 2(N \cdot w + 1) \qquad \text{Equation 4.3}$$

$$L = (1/N) \cdot nW^2 / \lambda \qquad \text{Equation 4.4}$$

Where N was the number of images, w was the width of the waveguides, λ was the wavelength, n was the effective refractive index, W was the width of the MMI, and L its length. From Equation 4.3 it can be seen that the narrower the MMI width, the shorter the device required. It was desirable to produce a device where the MMI width was as narrow as the fabrication process could achieve. As mentioned, the waveguide width was established as 3 μm. The distance between the output waveguides was then defined with the same value, i.e. 3 μm, simply because this dimension was the smallest that was feasible to fabricate at a high yield through a photolithographic process. The total width depended on the number of waveguides and the width of the waveguides, as well as the separation between the output waveguides and the number.

Equation 4.4 was deduced from [22] and describes the length (L) for a strong guiding MMI. Therefore, with this approximated width and length, a simulation was carried out using 2D BPM software. The simulation gave the exact length required.

4.4.5.2 Fabrication stage.

It was necessary to verify experimentally the MMI designs. Their fabrication was the same as the one described in Section 4.4.2. Many MMI devices were fabricated with the same widths but for different waveguide lengths (see Figure 4.11). The optical set-up explained in Section 4.4.3 was used to obtain the images at the end of the MMI splitters. All the devices were excited with a monomode fibre, and the splitting images (1x4, 1x5, 1x7) were analysed following the method described in 4.4.3.

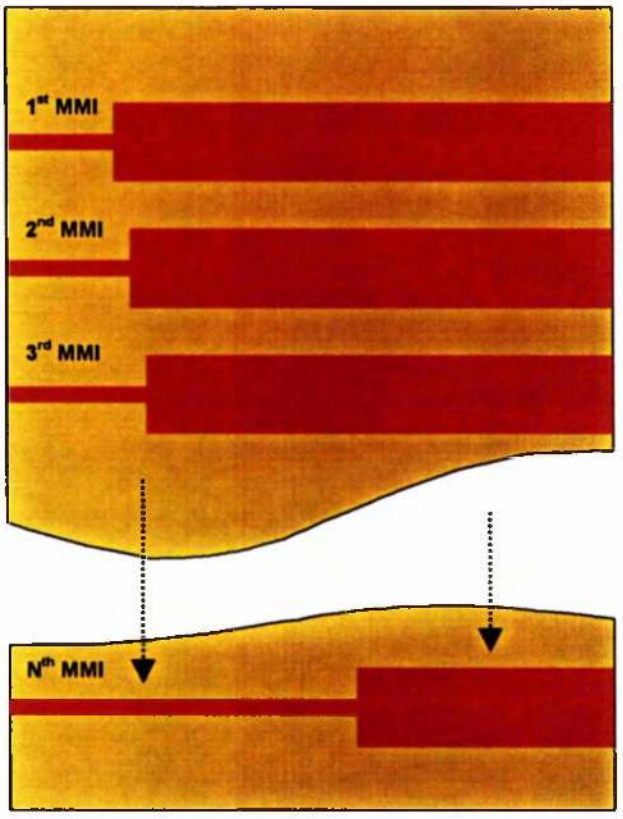

Figure 4.11: Schematic representation of the layout of MMI's. All the MMI devices were fabricated with the same width but with different lengths.

4.4.5.3 Results.

The results, as demonstrated in Figure 4.12, were encouraging as a proof of concept. A high uniformity was achieved, as well as good agreement with the design. This indicated that MMI splitters were not very sensitive to fabrication errors. However, the low intensity of the spots obtained with the CCD, and the low value of the peaks of the graphs in Figure 4.12 indicate that the losses were high. Despite of these values, for many applications, a balanced output is more important than the losses [15].

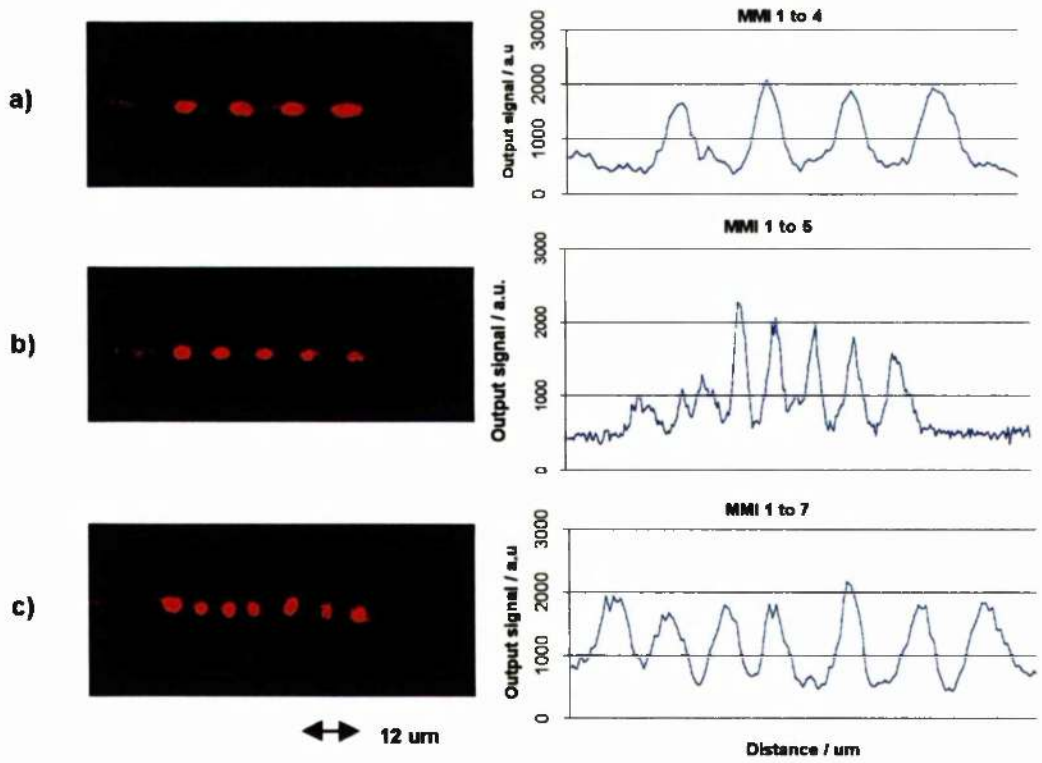

Figure 4.12: CCD images (left) and their profiles (right) from MMI splitters designed by MPA and BPM simulations and fabricated by FHD and RIE. a) 1x4; b) 1x5; c) 1x7.

4.4.6 Directional Coupler Splitters for 633 nm in FHD glass.

Directional couplers are important for many applications in optical communications and integrated optics [4,5]. In its simplest form, a directional coupler consists of two parallel dielectric waveguides in close proximity to each other [23,24]. Under suitable conditions (e.g. equal propagation constant) light launched into one of the waveguides can couple completely into the opposite guide. Nevertheless, once the light has crossed over into the second waveguide, the wave couples back into the first guide so that the power is exchanged continuously, along the length of the device.

Directional couplers can be used as power splitters. Since complete exchange of power was possible, any arbitrary power splitting ratio can, in principle, be

achieved by proper adjustment of the length of the directional coupler. They also can serve as wavelength filters (see Section 4.4.8).

To intuitively comprehend how a directional coupler works, it is useful to understand that a structure that consists of two single-mode waveguides placed near each other is no longer a single-mode device. This becomes obvious when considering the extreme case, namely that the two waveguides touch each other and fuse into one wider waveguide. More information about optical coupling can be found in the following sources [1,2].

4.4.6.1 Design stage.

2D BPM was used to obtain the correct length of a power splitter with 9 output waveguides for 633 nm. First, a structure of three identical waveguides 3 μm width, 3μm gap between them, and 0.25 % refractive index difference was simulated. The three single-mode waveguides were identical and parallel in the coupling region, and bend away from each other gradually at both ends. From that simulation, it was observed that after 456 μm, the power was the same in the three waveguides (see Figure 4.13).

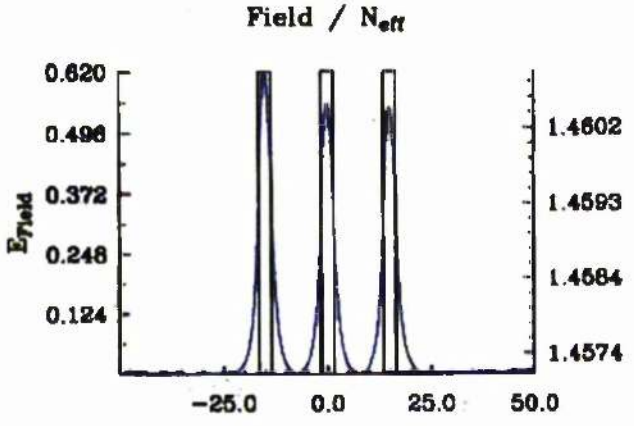

Figure 4.13: BPM result of a 3 beam directional coupler splitter. This coupling was achieved when the light wave travels 456 μm.

Subsequently, a more complex structure was simulated, where the power was split into 9 beams (see Figure 4.14). This structure consisted of a set of 4 beam directional couplers. It should be noted that S-bends were also included in the device.

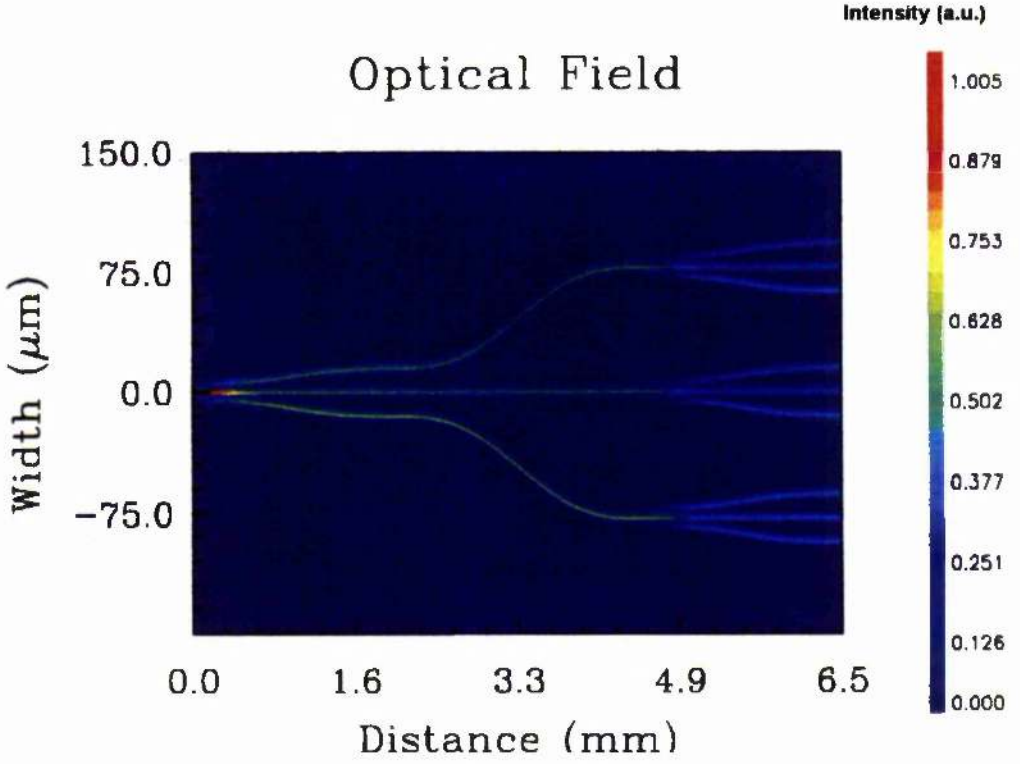

Figure 4.14: BPM result of a 9 beam directional coupler splitter. This structure consisted of a set of 4 beam directional couplers in parallel linked by bend waveguides. The scale of colours in the right indicates the intensity of the propagated beam. This figure shows that the intensity was well confined into the waveguides.

4.4.6.2 Fabrication.

Following the design results, a 9 beam splitter device was fabricated using the same process as the one described in Section 4.4.2. It should be pointed out that this method is phase dependent and the device is heavily subjected to fabrication tolerances.

4.4.6.3 Results.

Images of the outputs were obtained and treated using the optical set-up and the software explained in Section 4.4.3. Figure 4.15 was the CCD image of the 9 output waveguides. This image shows that the intensity was well confined into the waveguides and their bends. The fabricated device did not exhibit either high uniformity or symmetry due to fabrication defects affecting randomly the distribution of the power. On the contrary, the peak values of this device were the highest among the fabricated power splitters.

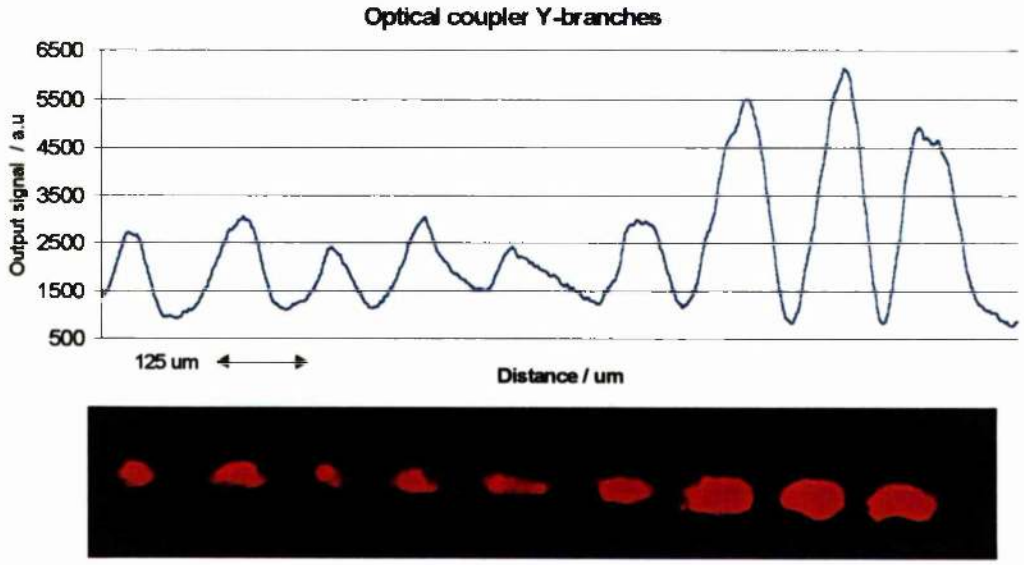

Figure 4.15: CCD image of the 9 output waveguides from an optical coupler splitter.

4.4.7 Comparison of Optical Power Splitters for 633 nm in FHD glass.

The information collected from the experimental results obtained from the power splitters, has been summarised in Table 4.2. From each device, the "peak" and the "valley" values of the measured intensity have been extracted. The term "minimum" in Table 4.2 was the average of the valley values, whilst the "maximum" was the average of the peak values. In order to obtain a referenced intensity value among the devices, the "maximum" was divided by the "minimum"

and it was named "ratio". The standard deviation of the "maximum" value was called SD. Unfortunately, it was not possible to obtain an accurate measurement of the total losses because the unavailability of precise nanopositioners during the analytical experiments.

By analysing the "ratio", it was possible to establish a comparison in terms of power efficiency. The lowest losses were obtained in the optical coupling device and in the MMI with 4 outputs. It is possible that the coupling effect was the most efficient mechanism of splitting the power in a waveguide. On the other hand, if the SD was compared, the most balanced splitting mechanism was the MMI and the worst was the optical coupling. This result agreed with work previously published [15], where it was demonstrated that optical coupling uniformity was more sensitive to fabrication tolerances than the MMI mechanism. The Y-branch splitters were straightforward devices to design and fabricate. Their performance was not very high because they were sensitive to fabrication processes and it was difficult to achieve reproducible results among all the Y-branches contained on a 1x16 splitter.

It must be taken into account that many of the problems related here come from the fact that monomode guiding was employed. This requires very small dimension features, which makes the device more susceptible to fabrication errors. However, MMI splitters do not require this monomode condition, therefore, this could provide a route of interesting future work in order to develop MMI with multimode waveguides.

DEVICES	Minimum (a.u.)	Maximum (a.u.)	Ratio	SD	T	S	U	C
Y-Branch	777	2543	3.27	552	high	High	Low	Bad
Coupler splitter	1065	3638	3.42	1449	Medium	High	Low	Bad
MMI8	890	2179	2.45	375	Low	Low	High	Good
MMI7	624	1835	2.94	158				
MMI5	594	1933	3.25	253				
MMI4	461	1873	4.07	147				

Table 4.2: Summary of the main characteristics of different power splitters fabricated on FHD. T, Throughput. S, Sensitive to fabrication errors. U, Uniformity. C, Compactness.

4.4.8 Band Pass Filters for 633 nm based on Optical Couplers.

As previously mentioned, a directional coupler can be also used as a filter. The periodicity of the power exchange depends on the coupler dimensions, the refractive index, and more importantly on the wavelength. If we excite an optical coupler (3 μm waveguide widths and 3 μm gap between them) with a 633 nm wavelength, the result will be similar to the one simulated using 2D BPM and represented in Figure 4.16. The 633 nm field is periodically transferred from one waveguide to the other. In the same way, power in a wavelength of 670 nm (the excitation wavelength of the fluorophore Cy5) is exchanged more rapidly between the waveguides. Therefore, the optical coupler excited with both wavelengths will be travelling along both waveguides.

There will be a distance in the coupler along which, the 670 nm power was transferred to the parallel waveguide, whilst the 633 nm power stays in the initial waveguide (see Figure 4.17). The distance that gives a maximum of the field in one wavelength and a minimum in the other can be used as a filter. This distance was calculated using 2D BPM for the optical coupler already described, and it was equal to 11061 μm.

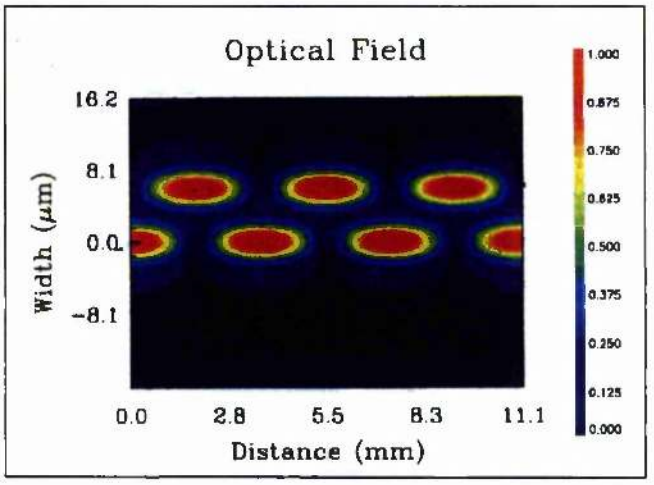

Figure 4.16: Result obtained from 2D BPM when an optical coupler (3 μm waveguide widths and 3 μm gap between them) was excited with a 633 nm wavelength.

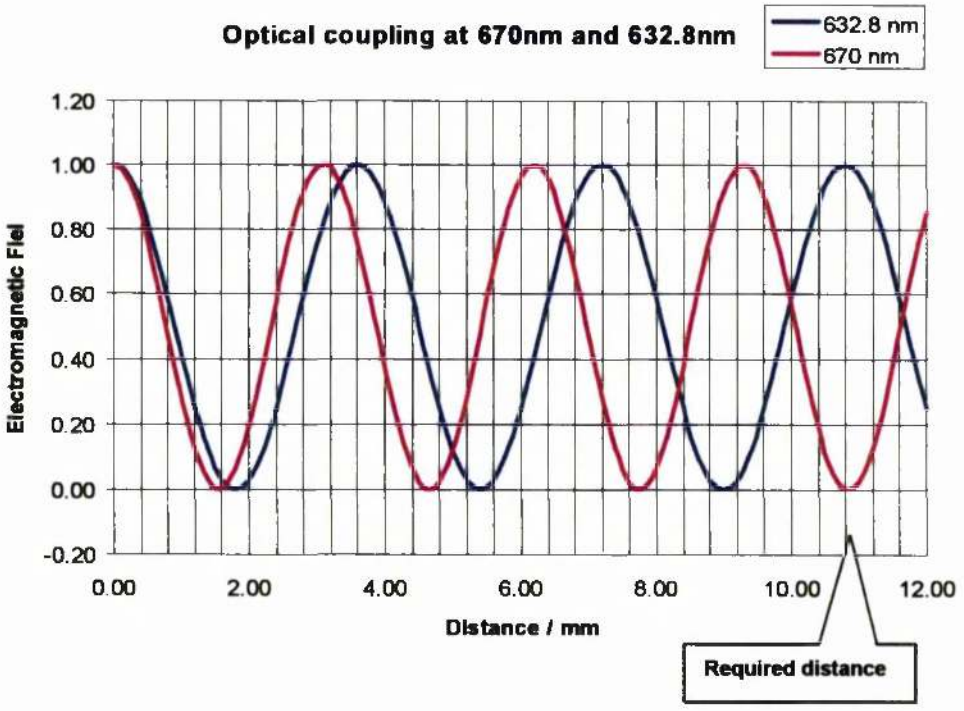

Figure 4.17: 2D BPM simulation of the optical coupler excited with both wavelengths travelling along both waveguides. There is a distance in the coupler where, the 670 nm power was transferred to the parallel waveguide, whilst the 633 nm power stays in the initial waveguide. The distance that gives a maximum of the field in one wavelength and a minimum in the other can be used as a filter.

Several simulations for different wavelengths were run with this optical coupler (two waveguides of 11061 μm-length, 3 μm-width and a gap of 3μm). Figure 4.18 represents the transmitted power in one of the waveguides using a wavelength range from 600 nm to 700 nm. An attenuation of 18 dB can be achieved.

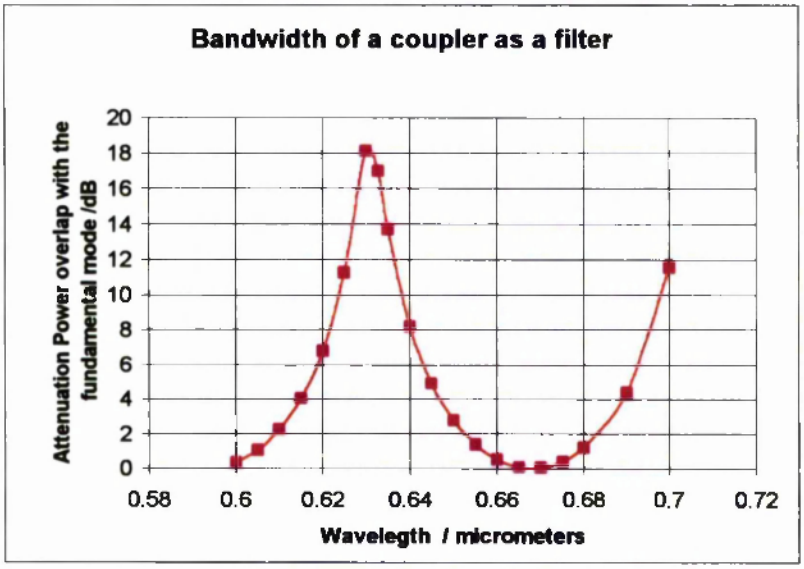

Figure 4.18: Representation of the transmitted power in one of the waveguides using a wavelength range from 600 nm to 700 nm. An attenuation of 18 dB can be achieved.

4.5 Picolitre Volume Planar Arrays for Lab-on-a-Chip.

The planar nature of FHD glass facilitates a straightforward arraying of sensors. The work presented in this section, further developed this technology as an array based biochip. Integrated optic elements developed in previous section such as, tapered and bend waveguides, and Y-branches have been employed to enhance the features of an optical FHD sensor. This improvement allowed us to perform simultaneously 16 fluorescence measurements.

In the past ten years, the use of combinatorial chemistry [25,26] in the pharmaceutical and agrochemical industries has driven a need for being able to perform many sensitive assays in parallel, and thereby deliver a high throughput

screening technology. There were a number of systems that necessitated measurements to be made in parallel, often with a degree of redundancy, including those for the determination of DNA hybridisation [27, 28, 29, 30], or for olfactory measurements in optical "noses" [31]. Within the framework of drug discovery, this frequently involves the implementation of fluorescence based measurements (determining the presence of a fluorophore as a label in a ligand-binding assay). In this context, our previous work described in Chapter 3 demonstrated that FHD sensors can be integrated with microfluidic capillaries, to deliver fluorescently labelled cyanine-5 oligonucleotides to single (individual) chambers [32].

This section starts by explaining the fabrication protocol of an array of planar FHD silica devices of ultra-low volume chambers (85 pL). Glasses were deposited and patterned using methods, which were essentially the same as those described for single chambers and fluidic channels (See Chapter 2). This work demonstrates that FHD technology leads itself to high throughput systems.

4.5.1 Fabrication Protocol of an Array Sensor in FHD.

The seven stage fabrication protocol presented in Section 2.2 was used to fabricate this array. The fabrication procedure was practically the same, except there were some variations in the optical circuitry components that are explained bellow. The differences reside in the fact that monomode operation was required to incorporate the Y-brach beam splitters needed to divide the beam into 16, allowing us to illuminate 16 analytical chambers simultaneously.

Each of the seven fabrication steps are described in the following points:

1. Thermal oxidation of a silicon wafer to achieve 16 μm of SiO_2.

2. Deposition of a layer of 4 μm of $SiO_2 - GeO_2$ glass by FHD technique (0.25% refractive index difference).

3. Photolithography step used to transfer the waveguides pattern onto the photoresist using S1828 photoresist on top of 75 nm of NiCr.

4. Reactive ion etching (RIE) of the $SiO_2 - GeO_2$ glass to obtain the optical circuitry 5 μm depth.

5. The deposition of a layer of 14 μm of $SiO_2 - P_2O_5$ by FHD technique (cladding of the waveguides).

6. A photolithographic step to transfer the micro-channel patterns onto the photoresist using AZ4562 photoresist on top of 150 nm of NiCr

7. RIE of chambers and channels in order to accomplish a microfluidic circuitry reaching a depth of 28 μm.

The first five processes correspond to the fabrication of the Y-branches used in Section 4.4.4. The resulting waveguide had 0.25% refractive index difference between core and cladding, 3 μm width and 4 μm depth. Regarding the microfluidic circuitry, a layout consisting of 16 analytical chambers was etched in the glass following the instructions in Section 2.2.7.

4.5.2 Description of the Experimental Assays Performed in the 4x4 Array.

4.5.2.1 Reagents.

Reagent grade H_2O_2, H_2SO_4, chlorobenzene, diethyl ether and acetone were from Aldrich, Gillingham, UK. AZ4562 and S1828 photoresists were from Shipley, UK. Metals, including Cr and Ni were from Goodfellows, Cambridge, UK. Aqueous solutions of Cy5 (Amersham, UK) with concentrations ranging 1.5 μM to 24 μM were prepared by successive dilutions in reverse osmosis water.

4.5.2.2 4x4 Array layout.

The layout of the chip is shown schematically in Figure 4.19. In addition to the buried waveguides, the chip comprised an array of 16 micro-chambers 30 μm wide, 100μm long, and 28 μm deep, yielding sub-nanolitre volume structure of ca. 84 pL. Each titre-chamber device featured one input waveguide (for the fluorescence excitation) and one output waveguide. For such chambers, there was the possibility of being able to collect the emission as a footprint image, using a CCD. The overall size of the chip was 2.5 cm x 1.25 cm. Previous experiments, as well as simulations with BPM software (Optiwave Corporation -Canada-), led to the design and fabrication of rectangular shaped micro-analytical chambers (see Section 3.3).

The waveguides that followed the Y-Branches, were 4 μm deep and had a taper-shaped width in order to improve the collection and dispersion efficiency at the titre chamber interface [33]. The input waveguides had widths that varied between 3 μm and 10 μm, the output waveguides were 20 μm (starting width) to 9 μm (final width). A set of monomode waveguides were fabricated within the optical chip, in order to characterise the levels of both autofluorescence and the losses within the FHD glass for 633 nm.

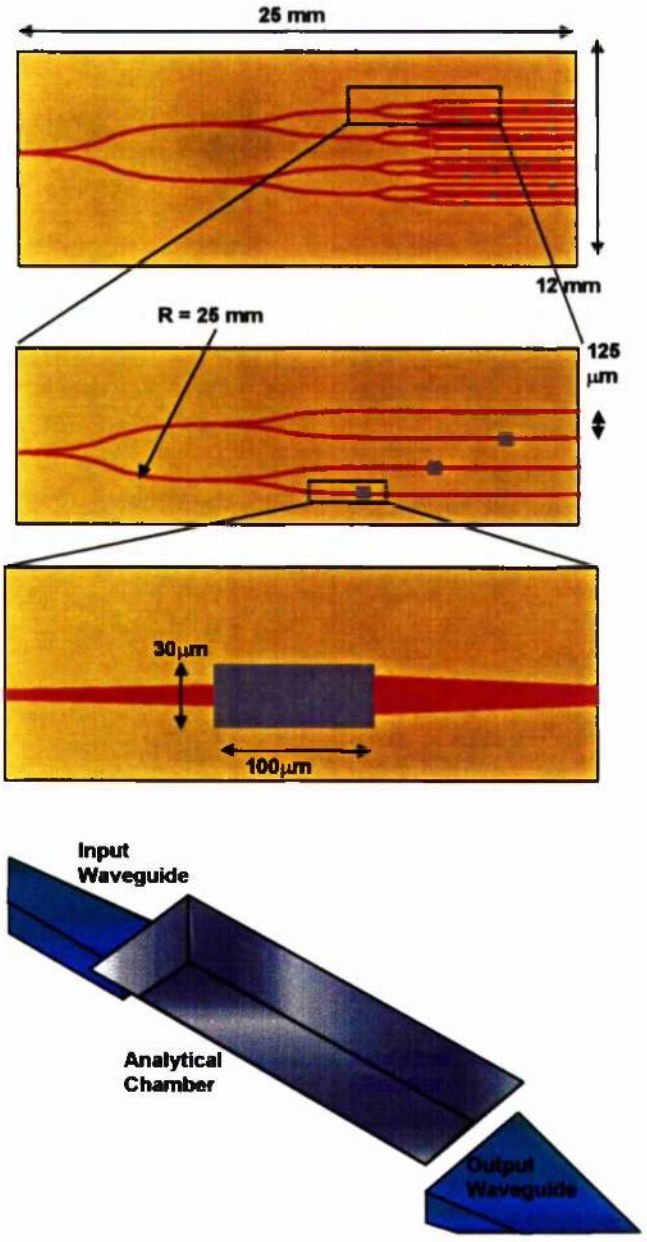

Figure 4.19: Schematic representation of the array. The chip comprised an array of 16 micro-chamber 30 µm wide, 100 µm long, and 28 µm deep. The overall size of the chip was 2.5 cm x 1.25 cm. Each titre-chamber device featured one input waveguide (for the fluorescence excitation) and one output waveguide.

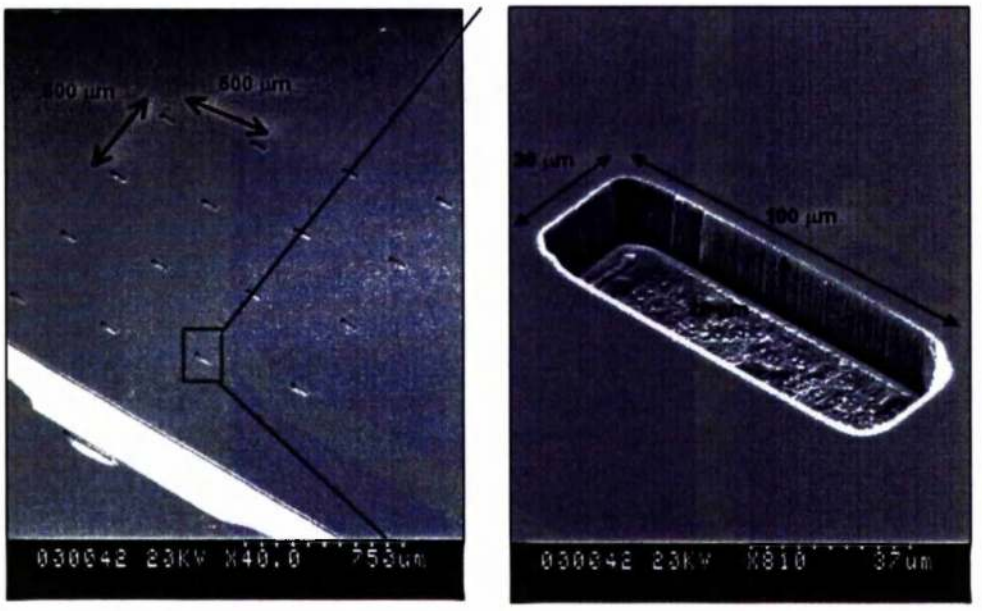

Figure 4.20: Left) SEM picture of the 16 chamber array (4x4); Right) SEM picture of an individual chamber 30 µm wide, 100 µm long, and 28 µm deep, yielding sub-nanolitre volume structure of ca. 84 pL.

4.5.2.3 Experimental Setup used to test the 4x4 array.

The fluorescence emissions taking place in the analytical chambers were analysed using the configuration described in Figure 4.21. This set-up excited the fluorophore using the input waveguide and collected the output signal from above the chambers. This configuration allowed us to obtain a footprint across the array. The detector was a colour CCD camera (CoolSNAP, RS Photometrics). Optical filters were from Omega Optical (Glen Spectra, UK) and comprised a narrow band excitation (633NB3.0) filter and one emission (670DF40) filter. Excitation light was provided by a 1.8 mW HeNe laser, λ=633 nm, and was coupled to the input waveguide using free space optics (i.e. a x 5 lens with an N.A. 0.12 , Nikon, UK). Fluorescence emission light from the chambers was collected on the CCD detector using microscope objective lens (N.A. 0.4, 16 mm, Ealing). A silicon photodetector (Anritsu ML910B) was used to measure the light coming out from the output waveguide. The light was collected using a x 10 lens with a N.A. 0.30, Nikon, UK.

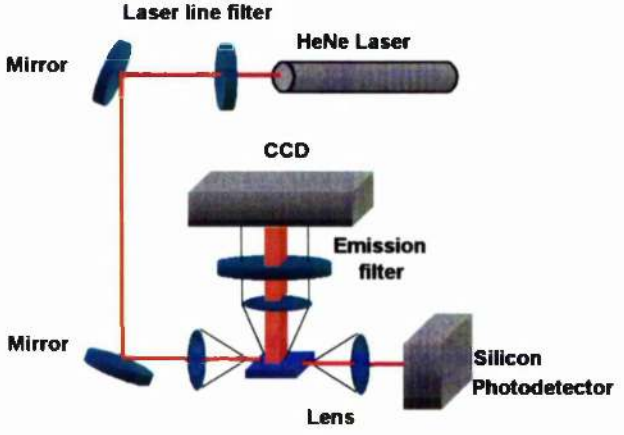

Figure 4.21: Setup representation of the on-top configuration, this arrangement allowed us to obtain a footprint across the array.

The images obtained using the CCD were stored in a computer (Optiplex, DELL) and subsequently analysed using an image processing software (IPLab for Windows, Scananalytics, Inc., U.S.A). This software allowed us to obtain the fluorescence profile of the beams.

4.5.2.4 Procedure for Fluorescence Measurements.

Prior to use, the devices were cleaned in Pirhana solution (90 % of H_2SO_4 / 10% of H_2O_2). In addition to removing any dirt, this cleaning routine increased the hydrophilicity of the glass surface, which facilitated the subsequent filling of the channels and chamber by capillary action. In order to eliminate evaporation, an overlayer of either PDMS, or glass was bonded onto the device (see Chapter 2)

Upon injection of a droplet of analyte into the reservoir, an increase in the power measured from the in-line output waveguide was observed, indicating that the chamber was filled.

In order to allow for a complete signal and noise analysis to be carried out, the blank (Bk) level was measured in each optical configuration, by filling the analytical chamber with water. The total signal (sum of the blank signal and analytical signal, S) was then measured for increasing concentration of the analyte.

The dark (Dk) current and associated noise of the detectors were also measured in the conditions of the analysis.

Fluorescence was collected directly within the chamber from the top, using a waveguide for the excitation. The washing procedure employed between measurements was satisfactory to ensure that no significant memory effects took place, due adsorption of the sample molecules onto the walls of the channels and chamber, as was demonstrated in Section 3.4.5.1.

4.5.3 Results Obtained from the Array.

4.5.3.1 Optical Waveguiding Performance.

The in-line waveguides fabricated within the optical chip were used to measure the losses within the FHD glass for 633 nm. The optical set-up and procedure were previously explained in Section 3.4.3.4. Transmission and insertion losses were measured as 4-dB for a waveguide of 1 cm long at 633 nm. This loss included those produced in the mis-alignment of the beam into the monomode waveguide. It should be mentioned that nanometer precision alignment was difficult to achieve by hand manipulation. The scattering observed was higher. The level of losses observed at the monomode waveguides was higher than in the multimode guiding (0.5 dB cm^{-1}, see Section 3.4.5.3). This could be due to the fact that fabrication defect dimensions in both types of waveguides were the same. However, the monomode waveguide was smaller and, therefore, the same defects produce more losses than in a multimode waveguide.

4.5.3.2 Fluorescence Measurements.

Fluorescence results for aqueous solutions of Cy5 were experimentally determined. Figure 4.22.(a) shows a top image of the 16-chamber array filled with 2 fmol of the fluorophore Cy5. This data was processed and expressed as analytical signals in each of the chambers (Figure 4.22.b and c). As is apparent in Figure 4.22, no high

excitation uniformity was achieved. The same reasons for this inconsistency are proposed as were described for the beam splitter in the precious section.

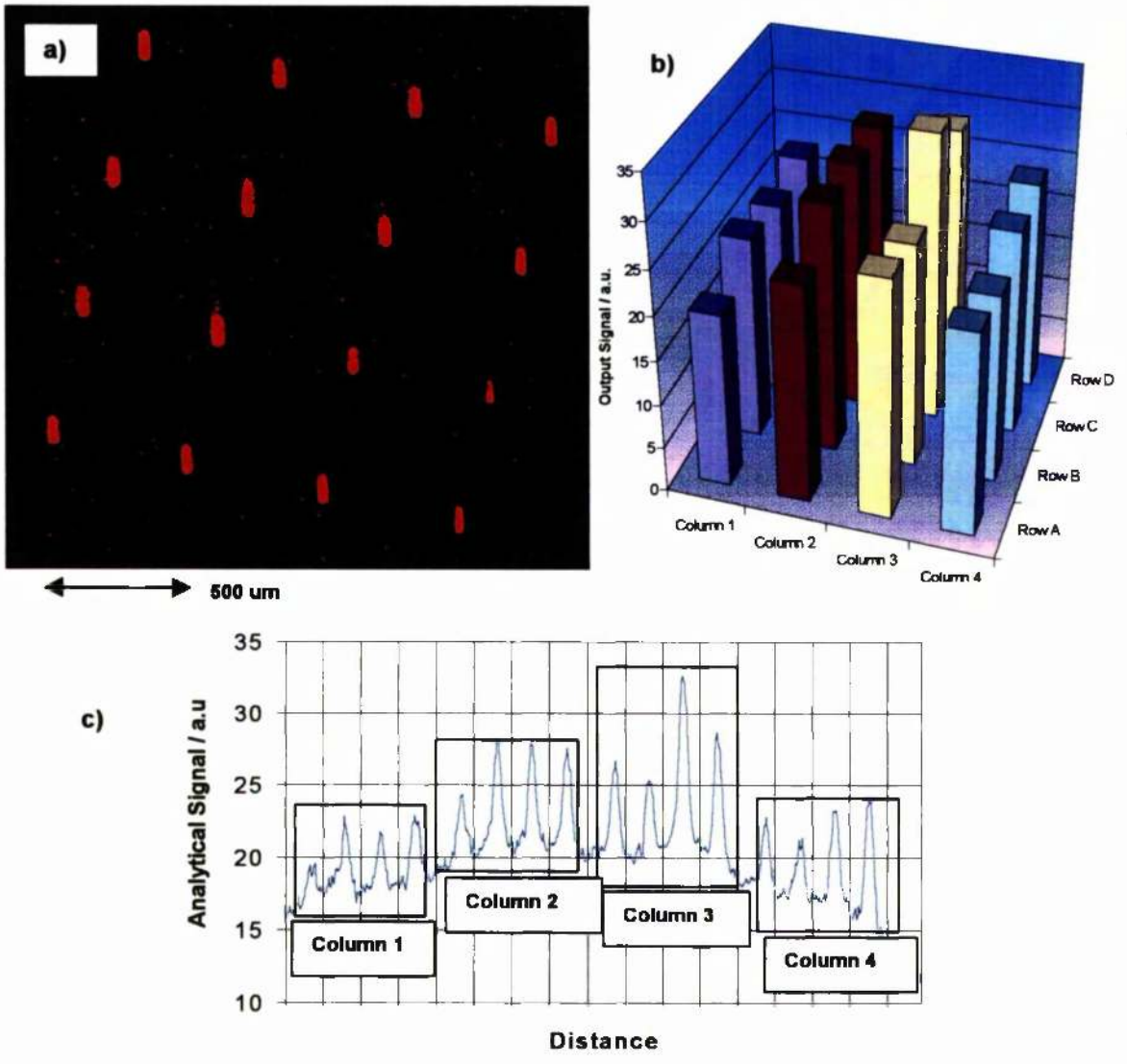

Figure 4.22: a) CCD image shows a top view of the 16-chamber array filled with aqueous solutions of Cy5 (24 μM); b) this graph shows the output signal collected in every single chamber; (c) this data was processed and expressed in analytical signal.

The analytical figures of merit for this optical set-up were obtained with a concentration of Cy5 in water of 24 μM, consequently the amount of Cy5 was 2

fmoles. Values of 9.14 for signal – noise ratio and 0.96 for signal – background were obtained from the averages of the 16 analytical and blank signals. These values were the expected ones for this concentration and optical configuration (orthogonal fluorescence collection).

4.6 Conclusions.

Two other important areas concerning the use of FHD integrated optical structures and analytical devices in biotechnology were demonstrated, namely: the use of integrated optics for 633 nm for the production of an array technology; and the simultaneous measurement, in a picolitre volume, of the "footprint" across the array using a CCD camera.

Optical functions for 633 nm were designed and fabricated, such as bends, tapered waveguides, Y-branches, MMI or optical couplers. Their performance verified the strong relationship between the design and fabrication processes.

Not all the optical functions were integrated with a sensor. Nevertheless, a demonstration of this optical treatment for analytical devices in bio-chemical sensing was achieved when a 16-beam splitter by Y-Branches was integrated with 16 analytical chambers. A fluorescence experiment, using this device, confirmed how versatile the FHD technique is. This allowed us to perform simultaneously 16 fluorescence measurements.

4.7 References.

1 Kawachi M., Opt. Quantum Electron., Vol. 22, 391, 1990.

2 Kawachi M., IEE Proc.-Optoelectron., Vol. 143,N. 5, 1996.

3 Tang C.K., Kewell A.K., Reed G.T., Rickman A.G., Namavar F., IEE Proc. Optoelectronics, Vol. 143, N. 5, pp. 3125-315, 1996.

4 Rasmussen T., Bjarklev A., Applied Optics, Vol.33, No.15, pp. 3231-3236, 1994.

5 Li Y. P., Henry C.H., IEE Proceedings-Optoelectronics, Vol. 143, No. 5, pp. 263-280, 1996.

6 Milton A.F., Burns W.K., IEEE-Journal of Quantum Electronics, Vol.QE-13, No. 10, pp. 828-35, 1977.

7 Koai K.T., Liu P.L., Journal Of Lightwave Technology, Vol.7, No. 7, pp. 1016-1022, 1989.

8 Lee D.L., Electromagnetic principles of integrated optics, Ed. John Wiley & Sons Inc., 1986.

9 Klekamp A., Kersten P., Rehm W., Journal of Lightwave Technology, Vol 14, N. 12, 1996.

10 Bocang Qiu, University of Glasgow, Personal Communication.

11 Daniel Ortega, PhD Thesis, University of Glasgow, 1998.

12 R. Ulrich, R. Torgue, Applied Optics, Vol. 12, No. 12., 1973.

13 HanBin L., ReiShin C., WayScen w., IEEE photonics technology letters, Vol.6, No.7, pp.825-827, 1994.

14 Bryngdahl O., J. Opt. Soc. Amer., Vol. 63, N. 4, pp. 416-419, 1973.

15 Soldano L.B., Pennings E.C.M., J. Lightwave Technol., Vol. 13, N. 4, pp. 615-627, 1995.

16 Soldano L.B., Smit M.K., de Vreede A.H., Van Uffelen J.W.M., Verbeek B.H., Van Bennekom P., de Krom W.H.C., Van Etten W., Proc. European Conf. Opt. Commun (ECOC), Paris, France, pp. 96-99, Sept. 1991.

17 Bachmann M., Smit M. K., Soldano L.B. Besse P.A., Gini E., and Melchior H., in Proc. Conf. Opt. Fiber Commun. (OFC), San Jose, CA, pp. 32-33, 1993.

18 Zucker J.E., Jones K.L., Chiu T.H., and Brown-Goebeler K., J. Lightwave Technol., Vol. 10, N. 2, pp. 1926-1930, 1992.

19 Van Roijen R., Pennings E.C.M., Van Stralen M.J.N., Van Dongen T., Verbeek, B.H. and Van Der Heijden, J.M.M., Appl. Phys. Lett., Vol. 64, N. 14, pp. 1753-1755, 1994.

20 Heaton J.M., Jenkins R.M., Wight D. R., Parker J.T., Birbeck J.C.H., and Hilton K.P., Appl. Phys. Lett., Vol. 61, N. 15, pp. 1754-1756, 1992.

21 Soldano L., Bachmann M., Besse P., Smit M., Melchior H., Proc. ECIO'93, Neuchatel, paper 14-10, 1993.

22 Besse P.A., Bachmann M., Melchior H., Soldano L.B., Smit M.K., J. Lightwave Technol., Vol. 12, N. 6, pp. 1004-1009, 1994.

23 Marcuse D., Theory of dielectric optical waveguides, Academic Press, New York, 2nd Edn., 1991.

24 Marz R., Integarted optics: design and modeling, Artech House, Boston, 1994.

25 Kirkpatrick D.L., Watson S., Ulhaq S., Combinatorial Chemistry & High Throughput Screening, Vol.2, No.4, pp. 211-221, 1999.

26 Henry C., Chemical & Engineering News, Vol.77, No.37, p.9, 1999.

27 DeRisi J.L., Iyer V.R., Brown P.O., Science, Vol.278, No. 5338, pp. 680-686, 1997.

28 Cheung V.G., Nature Genetics, Vol.18, No.3, pp. 225-230, 1998.

29 Duggan D.J., Bittner M., Chen Y.D., Meltzer P., Trent J.M., Nature Genetics, Vol.21, No.SS, pp. 10-14, 1999.

30 Bowtell D., Nature Genetics, Vol.21, No.2, p.241, 1999.

31 Jurs P.C., Johnson S.R., Engelhardt H.L., Sutter J.M., Dickinson T.A., Walt D.R., White J., Kauer J.S., Abstracts of papers of the American Chemical Society, Vol.214, No.Pt1, pp.50-ANYL, 1999.

32 Ruano J.M., Benoit V., Aitchison J.S., Cooper J.M., Anal.Chem., Vol.72, pp. 1093-1097, 2000.

33 Ruano J. M., Ortega D., Bonar J. R., Cooper J. M., Aitchison J. S., CLEO Europe 98 Proc., 198, 1998.

Chapter 5: DEVELOPMENT OF LAB-ON-A-CHIP FUNCTIONS ON FHD DEVICES

5.1 Introduction.

As already demonstrated, FHD offers the potential for monolithic integration of miniaturised optical sensors, providing an easy and cheap implementation of batch fabrication processes. Due to the compact nature of the sensor, it is more robust and reliable at extremes temperatures, or when exposed to mechanical vibrations. This chapter describes the further development of the fabrication of complex structures based on the processes described in Chapter 2. Further adapting these techniques, we were able to enhance the functionality of a FHD based sensor. This section demonstrates that it is possible to integrate micro-pumping function and nanocolumns for liquid chromatography.

The chapter starts by describing the fabrication processes needed to produce a separating system on FHD glass for liquid chromatography. This system results in such small structures (channels of 2 μm width), that can exploit the limited rates of mobile-phase mass transfer in liquid chromatography. In the future, this will enable us to develop liquid chromatography without the difficult and unreliable use of column materials [1]. Even more important is the novel fact that monolithic integration of a liquid chromatography system can be fabricated within a FHD based analytical system. Subsequently, research to pump liquids in a FHD optical

device is explained, enabling for first time, the movement, or mixing of the sample inside an FHD biosensing device. The movement of liquids was carried out by syringes applying pressure differences along the micro-channels, although as the chambers are constructed from silica based materials, in principle, there is no reason why electromagnetic pumping can not be supported (e.g. electro-osmosis).

This set of enhancements, together with the achievements of previous chapter, has moved the FHD technology into applications in Micro Total Analysis Systems (μTAS) [2,3] or Lab-on-a-Chip systems [4, 5, 6, 7, 8].

5.2 Nanocolumns Fabrication for Liquid Chromatography in FHD glass.

This work was motivated by the fabrication of nanocolumns for liquid chromatography on quartz reported by Bing *et al.* [9]. According to Bing, these columns have a number of advantages including that (i) they are easily filled; (ii) their loading capacity is extremely small; (iii) gradient elution with positive displacement is difficult, and (iv) the optical path length used for detection is very short. This leads to the question as to whether there were other unexplored methods of producing these columns on a substrate where analytical functions can also be carried out. This section, therefore, addresses the basic design and fabrication issues associated with producing liquid chromatography columns *in situ* on FHD silica on silicon. The advantage of this approach is not only that a separation element can be tightly coupled into a μTAS device as Bing stated [9], but also that it can be monolithically integrated with other analytical operations on the same substrate, such as a fluorescence sensor.

5.2.1 Liquid Chromatography Theory.

Chromatography involves the separation of compounds, and occurs due to differences in the equilibrium distribution of the sample components between two non-miscible phases. There are three basic components of a chromatograph: an

injection system, a separating element, and a detector system. One of the non-miscible phases is a moving or mobile phase, and the other was a stationary phase (often an adsorbent material such as silica). The mixture moves along the separating system (often a tube), then elongates, and finally starts to separate. The further the solvent front moves, the more individual compounds spread out and separate. The velocity of migration along the tube is a function of equilibrium distribution. The components with properties favouring the stationary phase migrate slower than those that have properties favouring the mobile phase. Separation then results from different velocities of migration as a consequence of differences in equilibrium distributions. Fortunately, components separate faster by dilution than they broaden. Subsequently, when the tube is dried and scanned with a detector, a chromatogram can be obtained.

Chromatographic methods can be classified according to the type of mobile phase selected. Gas chromatography encompasses those methods in which the mobile phase is a gas, whilst liquid chromatography, involves a mobile phase which is a liquid. The conventional liquid chromatography is performed in columns packed with particles. This technique has been extensively used for more than 50 years. The functions of these particles were threefold: i) to support the stationary phase; ii) to provide a large interfacial boundary between the stationary and mobile phase for analyte partitioning; and iii) to form a homogeneous network of channels for the convective transport of the mobile phase through the column [9]. These functions are most easily achieved in porous particles, however stagnant pools of mobile phase accumulate in the pore network limiting mass transfer [10]. Ocvirk *et al.* [11] miniaturised the chromatograph system by packing micromachined rectangular capillaries in silica with particles. They found it difficult to achieve uniformity in the packing of particles through twisted channels and corners. Thus, one main goal has been to address liquid chromatography without the use of particles [12]. Despite the fact that in the 1970's, open tubular columns had already been described, they had never become popular in liquid chromatography. The equivalent of open tubular columns in a microfabricated format was a semi-

rectangular open channels etched in silicon or quartz [13]. In 1998, Bing *et al.* [9] fabricated this structures by deep reactive ion etching (DRIE). They fulfilled the requirement of etched channels widths of 2 μm or less, necessary to deal with limited rates of mobile-phase mass transfer in liquid chromatography [14]. More information about liquid chromatography can be found elsewhere [15,16,17].

5.2.2 Nanocolumns Fabrication Process.

The work described in this thesis has already demonstrated that both injection and detection elements in liquid chromatography can be integrated in a FHD substrate. To integrate a complete liquid chromatographic microsystem in FHD, it would be necessary to fabricate a separating element. This section describes the process used to fabricate this separating component, although it has not been tested analytically. The fabrication protocol involved the use of the photolithographic process previously developed on a FHD silica substrate, and explained in Section 2.2.3. This was followed by the reactive ion etching (RIE) described in Section 2.2.4.

5.2.2.1 Mask fabrication and Materials.

In order to transfer the desirable column pattern onto FHD silica, a photolithographic mask must be written. The layout of the mask was designed using CATS™ software. The pattern consists of sets of arrays of squares, separated from each other by different distances (10 μm, 5μm, 2 μm, 1 μm). This layout provides a wide dimensional range of structures, in order to determine if the combination of photolithographic and RIE process can reach the desirable 2 μm channels width [14]. A Leica 5 electron beam writer (Leica, Cambridge, UK) was used to write a 2.5 inch x 2.5 inch ferric mask plate. The photoresist was S1828 from Shipley. Metals, including Cr and Ni, were from Goodfellows, Cambridge, UK.

5.2.2.2 Photolithography and RIE of the columns.

Before the photolithographic process, 10μm of SiO_2 doped with P_2O_5 was deposited according to Section 2.2.5 on top of 16μm of thermal oxidised silica (see Section 2.2.1). Following this step, the photolithographic process was carried out on this sample in order to deposit a bilayer mask consisting of 75 nm of NiCr, and 2.8 μm of S1828 photoresist. It should be noted that thicker resist (i.e. S4562) was avoided because its high viscosity limits the transfer of small patterns by a photolithographic process. Three RIE runs of 30 minutes of the process described in Section 2.2.4 were performed. The results are shown in the following section.

5.2.2.3 Analyse techniques of RIE.

A DekTak surface profiler was used to measure the mask's thickness prior to, and after etching. A Talystep measurement was also used to confirm the results. A Hitachi S-800 scanning electron microscope was used to examine and verify the quality of the etch profiles of the samples.

5.2.3 Results and Conclusions.

After an analysis of the etch depth and profile of the etched structures, it was concluded that the requirement for channels of 2 μm width have been realised. The two smallest square columns successfully transferred by these techniques were: (i) 1 μm width and 8 μm depth separated each other by 2 μm (see Figure 5.1) and (ii) 10 μm width, 8 μm depth and 2 μm between columns (see Figure 5.2). Figure 5.1 and Figure 5.2 show a high degree of uniformity with regard to support distribution, regularity of support particles, congruity of channels, and absolute channel width. Careful examination of the SEM pictures in Figure 5.2 shows that there was heterogeneity in the etching pattern of the walls of the monolithic structures. The surface roughness, seen in Figure 5.2, increases the surface area, and thus, the chromatography phase ratio. However, rough surfaces can also trap liquid and create polls of stagnant mobile phase. The fact that these pools were only a few thousands angstroms deep (~100 nm), means that diffusive transport

distances were too small to seriously impact band spreading in all cases except for very large molecules with very low rates of diffusion. It is likely that the benefits of increased surface area obtained from rough surface outweigh stagnant mobile-phase mass-transfer functions [9].

In order to perform liquid chromatography, a sealing process must used to seal the channels and allow the liquid to be pumped through the columns. The bonding techniques explained in Section 2.3 (anodic bonding, FHD soot and PDMS) enable pumping by applying vacuum. If the pumping is to be by electrokinetic forces, the anodic bonding process must be excluded (the metallic "wetting" material would cause a short-circuit, see Section 2.3.1). Otherwise, the other two bonding techniques, FHD soot (Section 2.3.2) and PDMS (Section 2.3.3), can be also employed and they are compatible with the application of voltages.

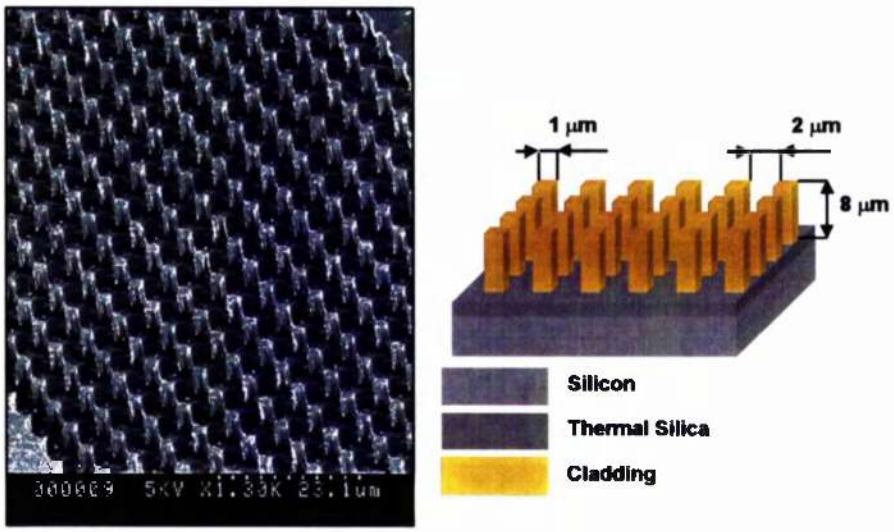

Figure 5.1: SEM picture and its schematic representation of an array of columns etched on FHD glass. The geometry of the column was 1μm width, 8 μm height and 2 μm between columns.

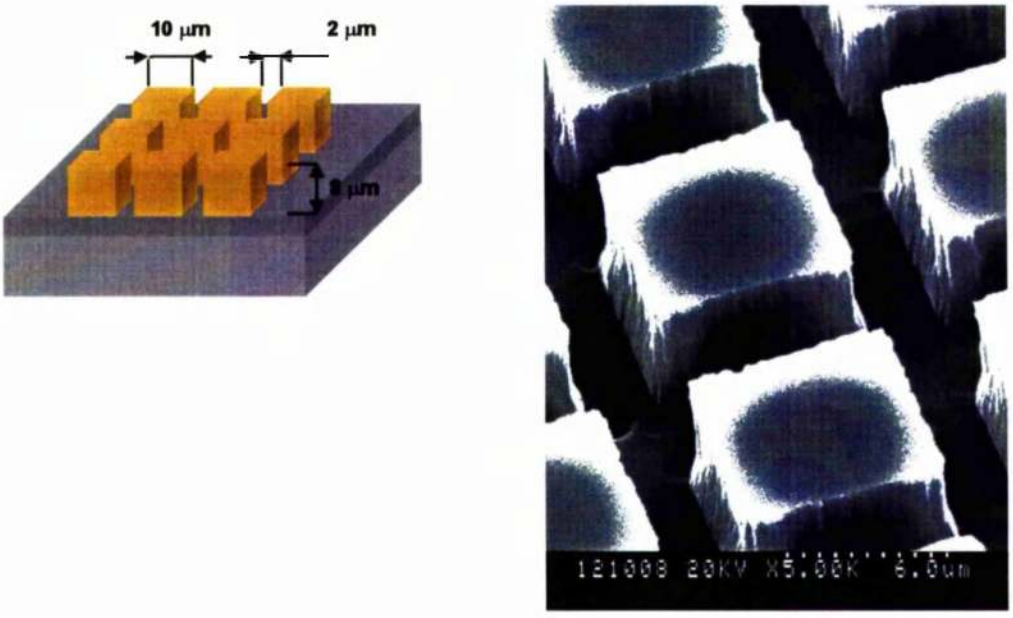

Figure 5.2: SEM pictures of the columns and its schematic representation of an array of columns etched on FHD glass. The geometry of the column was 10 μm width, 8 μm height and 2 μm between columns.

In order to illustrate the broad applicability of these methods, some other structures were fabricated. Array of holes ranging from 2 μm width and 8 μm deep (see Figure 5.3.a), to 20 μm width and 24 deep separated by walls of 3 μm width (Figure 5.3.b) were fabricated, along with walls from 1 μm width and 8 μm deep (Figure 5.3.c). For example, the array of holes could be used for the development of DNA microarrays [18, 19].

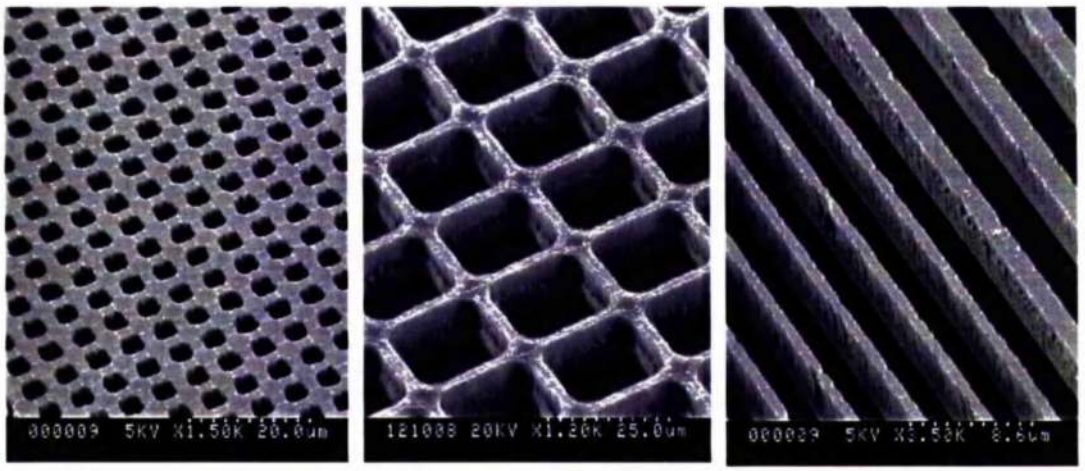

a b c

Figure 5.3: Other structures fabricated to demonstrate how complex structures the RIE technique developed in this research can be accomplished. a) Array of holes from 2 μm width and 8 μm deep. b) Array of holes from 20 μm width and 24 μm deep separated by walls of 3 μm width. c) Walls ranging from 1 μm to 5 μm width and 8 μm deep.

5.3 Micropumping in FHD glass.

Bonding and sealing of FHD microstructures was carried out using a polymer called poly(dimethylsiloxane), PDMS (Section 2.3.3). This involved sealing the PDMS irreversibly to samples of FHD glass. Apart from a strong seal, it was also necessary to establish the fluidic connections that allow us to transport liquids from a macro-scale reservoir (i.e. syringe), to a micro-scale reservoir etched into the surface of the FHD glass. This section describes the method developed to fabricate a pumping microsystem on a FHD sensor. The fluorescence sensor tested in the previous chapter was used as a platform to achieve this.

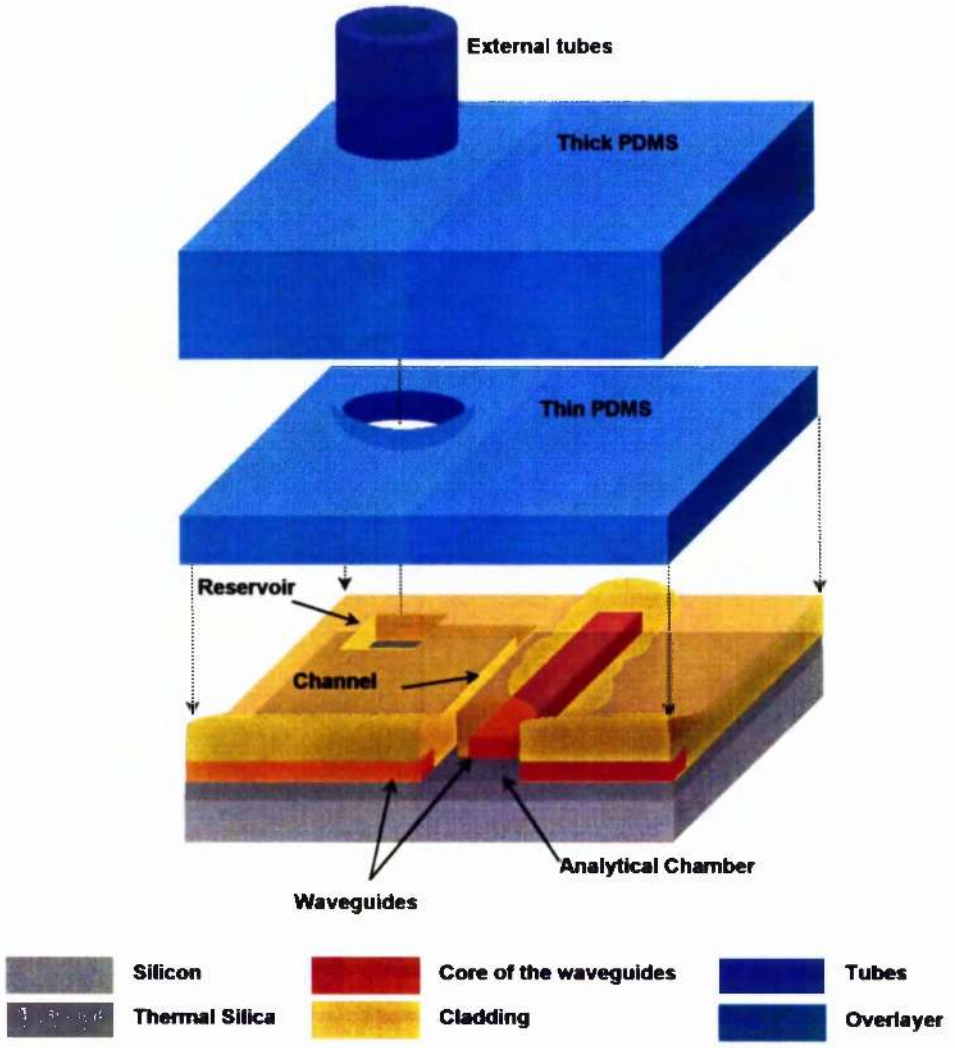

Figure 5.4: Schematic representation of a microfluidic system made on FHD glass with PDMS. Two PDMS pieces of different thickness are cured (3 mm and 6 mm). On one hand, the thinner layer works as a sealing layer of channels and its thinness enabled to seal uneven surfaces. On the other hand, the thicker one facilitates the connection of tubes to the reservoirs. Both layers have holes that connect the reservoir of the FHD device to the outside world.

5.3.1 Steps to Fabricate a Pumping System on a FHD Device.

The fabrication of the pumping system involved three main steps: moulding, sealing, and fluidic interconnections. The first, moulding, produces two PDMS pieces of different thicknesses (3 mm and 6 mm approximately). The thinner layer deformed and sealed uneven surfaces, whilst the thicker layer facilitated the connections of tubes to the reservoirs, since it was more robust. The second step

involved a modification of the properties of the three surfaces (namely the FHD sensor, thin and thick PDMS layer) to perform the subsequent bonding processes (thin PDMS to FHD glass, and thick to thin PDMS, see Figure 5.4). In the third and final step, the microfluidic system in the device was connected to an external macro-fluidic circuitry, consisting of commercial tubes and standard syringes. The syringes acted like pumps.

5.3.1.1 Moulding reservoirs in the PDMS layers.

Both the thin and thick layer of PDMS had to include holes that connected the etched reservoirs in the FHD device to the external macro-fluidic circuitry (see Figure 5.4). These holes had to be defined through the two PDMS layers by placing posts onto the substrate during the curing process. They also had to be aligned with the reservoirs of the FHD device, and thus, it was necessary to introduce a new photolithographic step that modified the curing process described in Section 2.3.3.1. The layer of sputtered gold (used to facilitate the removal of the PDMS) was printed with the help of a polymer by photolithography. This process copied the channel circuitry pattern that was previously etched on the FHD device onto the gold surface (see Figure 5.5). Most importantly, it also transfers the reservoir positions that will enable the post to be fixed in the correct locations (see step 4th in Figure 5.5).

A 10:1 mixture of PDMS pre-polymer and curing agent (Sylgard 184, Dow Corning, Midland, MI) was thoroughly stirred and poured onto a gold surface with the glued posts. The mixture was settled for 5 hours to remove the bubbles formed in the previous stirring stage. This process can be enhanced by degassing the sample under vacuum. A cure process was then performed for 15 minutes at 90 °C and ending with the removal of the PDMS from the gold surface. This process was repeated twice to obtain two layers of different thickness (3 mm and 6 mm approximately).

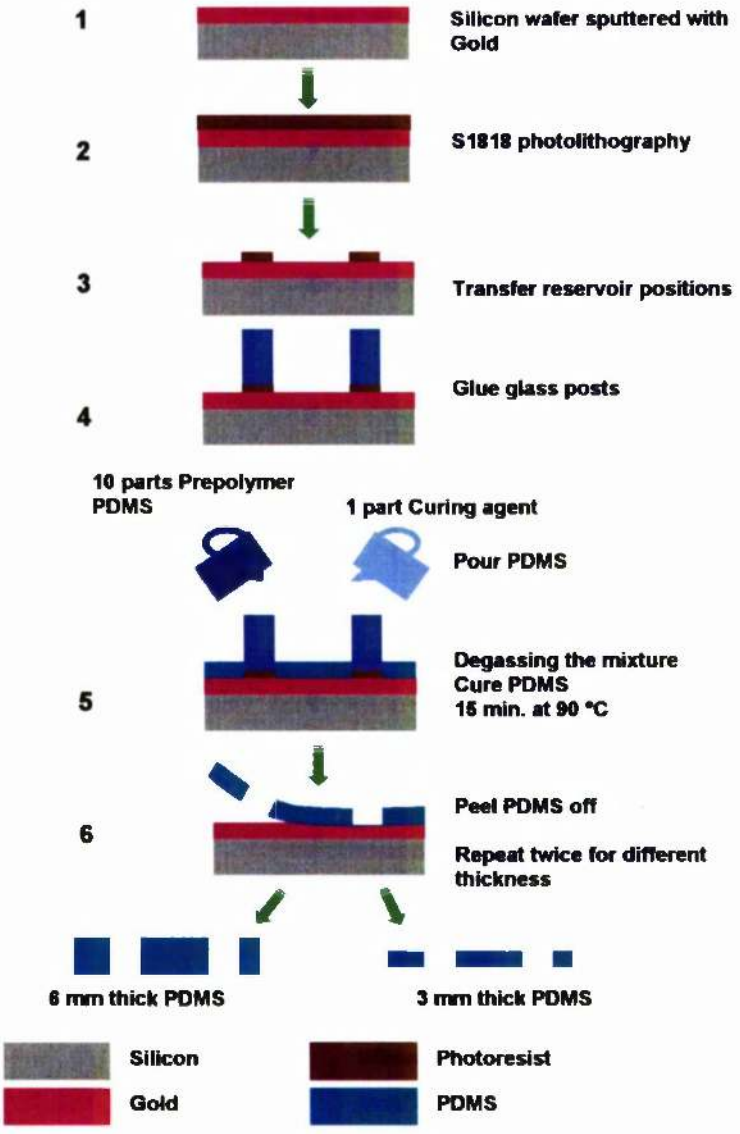

Figure 5.5: Scheme describing the fabrication of the two PDMS layers. The layer of sputtered gold (75 nm) was deposited, with the help of a photoresist polymer, by photolithography. This copies on the gold surface, the channel circuitry pattern that was previously etched on the FHD device. Most importantly, the process transfers the reservoir positions that will place the post in the right locations. Consequently, a 10:1 mixture of PDMS pre-polymer and curing agent was thoroughly stirred and poured onto a gold surface with the glued posts. Once the mixture was degassed, a cure process was performed for 15 minutes at 90 °C. The curing process was ended with the removal of the PDMS from the gold surface. This process was repeated twice to obtain two layers of different thickness (3 mm and 6 mm approximately).

5.3.1.2 Sealing of the two PDMS layers to the FHD device.

The FHD device was first cleaned in heptane, and then the device and the PDMS layers were rinsed in ethanol and exposed in 20 sccm oxygen plasma flow for 1 minute, 100 W and 13 mT using an Oxford PlasmaTechnology RIE80 machine. Immediately after removal from the oxygen plasma, the thin PDMS substrate and the FHD device were brought into contact. Without delay, the thick PDMS layer was also bonded to the thin PDMS layer. The dimensions of the reservoir were large enough (1 mm square) to make the alignment of the layers with the naked eye. This process created an irreversible seal of channels and left the device ready for the fluidic connections (see Figure 5.6).

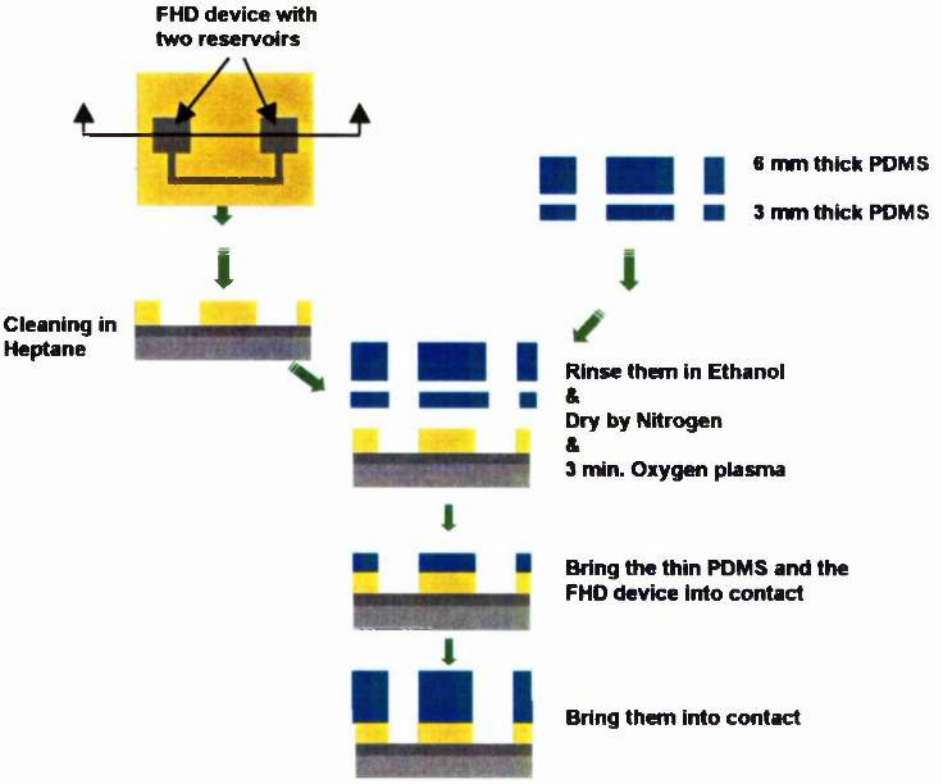

Figure 5.6: Representation of the bonding process of the three layers (FHD device and the thin and thick PDMS pieces). Immediately after removal from the oxygen plasma, the thin PDMS substrate and the FHD device are brought into contact. This process creates an irreversible seal of channels and leaves the device ready for the fluidic connections.

It should be pointed out that this arrangement of PDMS layers offered the possibility of adding an extra microfluidic circuit between the two PDMS layers. This can be carried out following the procedure explained elsewhere [20].

5.3.1.3 External fluidic connections.

This step can be incorporated as part of the packaging process of a sensor fabricated in FHD glass. The device was connected to "the macroscopic fluidic world" by plastic tubes, syringes and pipettes. The syringes were used to provide the necessary pump forces to move the liquid along the channels. The tubes were directly plugged into the hole previously moulded in the PDMS over-layers. The diameter of the holes was 0.5 mm smaller than that of the tubes. This difference in diameter, together with the elastic properties of the PDMS, enabled a strong "plugged" connection. Once the connections were established, the entire device was placed on top of a microscope slide, and an extra layer of PDMS was poured and cured onto the whole surface of the device (see Figure 5.7). This last curing process sealed completely the connections and encapsulated the device (see Figure 5.8). These pipes, in turn, could be connected to a syringe or to a pipette. The PDMS was not only used as a sealing material, it was also used to provide robustness to the device. It should be pointed out that, the versatile nature of PDMS offers many different possibilities with a variety of excellent features.

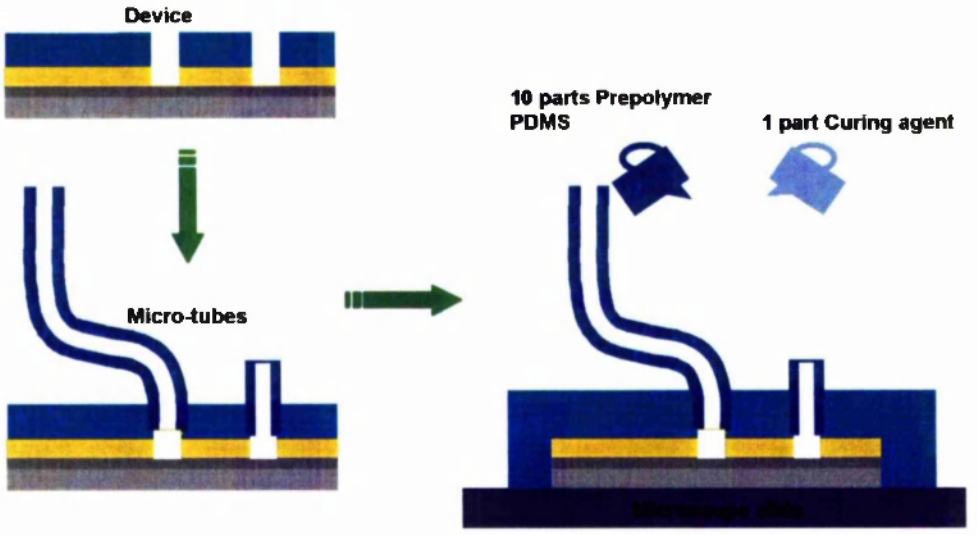

Figure 5.7: Schematic protocol of the packaging and connection of the devices with the external world. The tubes were directly plugged into the hole previously moulded in the PDMS over-layers (bottom left). Once the connections were established, the entire device was place on top of a microscope slide and an extra layer of PDMS was poured and cured onto the whole surface of the device. This last curing process seals the connections and encapsulates the device.

5.3.2 Results and Conclusions.

Liquid was transported from one reservoir to another, along the capillary channels etched on FHD, and sealed by PDMS following the indications given in the right side of Figure 5.8. Pressure was applied via a syringe, connected to one reservoir, which moved the liquid from the syringe to the pipette plugged at the end of the second reservoir.

As was mentioned in Chapter 2, the oxidation of PDMS and FHD glass, performed in the bonding process, produced an ionised layer on the walls of the channels. It would be feasible to perform electro-kinetic movement of particles inside such a capillary made on FHD and sealed by PDMS. To date, this was the simplest sealing technique developed to accomplish capillary electrophoresis in a FHD device.

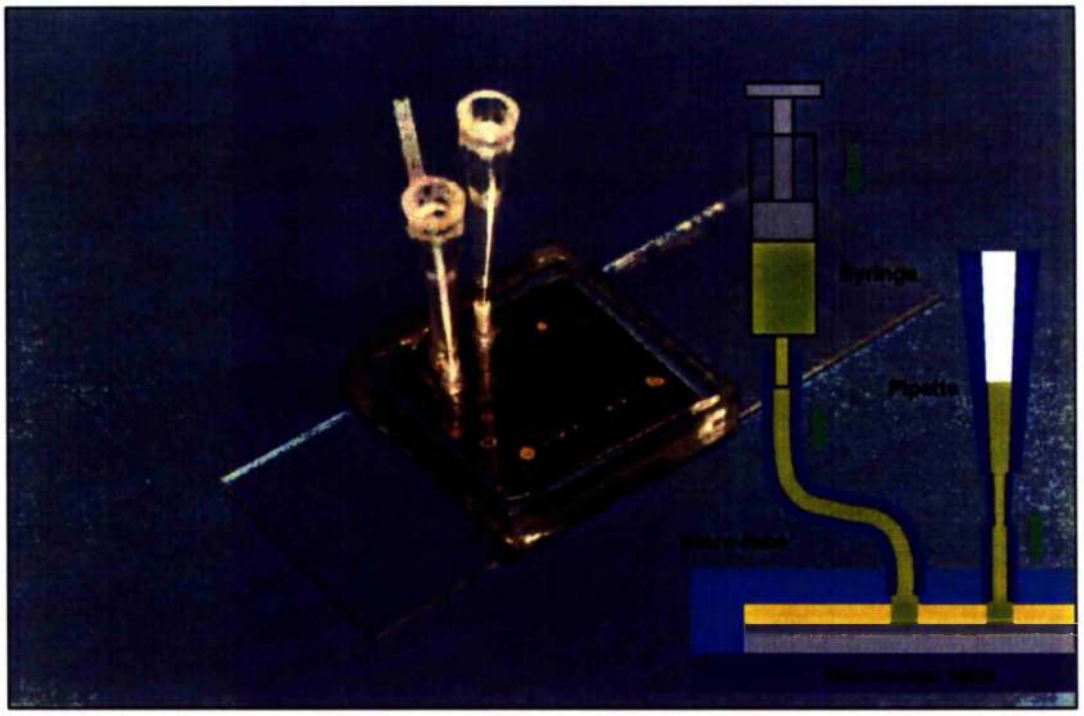

Figure 5.8: Picture of the fluorescence sensor device made in FHD and its schematic representation in the right handside. This device was successfully tested in Chapter 3. The tubes were directly plugged into the hole previously moulded in the PDMS over-layers. These pipes, in turn, can be connected to a syringe or to a pipette. Once the connections were established, the entire device was placed on top of a microscope slide, and more prepolymer was poured and cured onto the whole surface of the device. This last curing process seals the connections and encapsulates the device. The PDMS was not only used as a sealing material, it was also used to provide a robust encapsulated device.

5.4 Conclusions.

The work undertaken in this chapter involved the pumping liquids in a FHD optical device. The movement of liquids was carried out by applying pressure differences along the micro-channels. It would be also feasible to apply the forces by capillary electrophoresis. Subsequently, a separating system of a liquid chromatography system was fabricated in FHD. This separating system achieved such small structures than it may enable the limited rates of mobile-phase mass transfer in liquid chromatography. This separating system, in combination with the microfluidic system developed previously, has the potential to enable the creation

of a liquid chromatography system with a monolithically integrated sensor obtaining an analytical system on FHD glass.

5.5 References.

1 Nota G., Marrino G., Buonocore V., Ballio A., J. Chromatography, Vol. 46, pp. 103-106, 1970.

2 Manz A., Graber N., and Widmer H.M., Sensors and Actuators, Vol. 62, pp. 978-994, 1990.

3 Van den Berg A., Berfeld, μTAS'96 Conference, 17-22 Nov, pp. 9-15, 1996.

4 Pethig R., Burt J. P. H., Parton A., Rizvi N., Talary M. S., Tame J. A., J. Micromechanics and Microengineering, No.8, pp. 57-63, 1998.

5 Effenhauser C. S., Bruin G. J. M., Paulus A., Ehrat M., Anal. Chem., Vol. 69, pp. 3451-57, 1997.

6 Schober A., Schlingloff G., Thamm A., Kiel H. J., Tomandl D., Gebinoga M., Doring M., Kohler T., Bruno A. E., Barnard S., Rouilly M., Walder A., Berger J., Ehrat M., Anal. Chem., Vol. 69, pp. 507-13, 1997.

7 Bratten C. D. T., Cobbold P. H., Cooper J. M., Anal. Chem., Vol. 70, pp. 1164-70, 1998.

8 Dempsey E., Diamond D., Smyth M. R., Urban G., Jobst G., Moser I., Verpoorte E. M. J., Manz A., Widmer H. M., Rabenstein K., Freaney R., Anal. Chim. Acta, Vol. 346, 341-49, 1997.

9 Bing H., Tait N., Regnier F., Anal. Chem., Vol. 70, pp. 4974-4984, 1998.

10 Giddings J.C., Unified Separation Science; John Wiley & Sons: New York, 1991.

11 Ocvirk G., Verpoote E., Manz A., Grasserbauer M., Widmer H.M., Anal. Methods Instrum., Vol. 22, pp.1-9, 1995.

12 Tennikova T.B., Svec F., J. Chromatogr. A, 669, pp. 279-288, 1993.

13 Moore A. W., Jacobson S.C., Ramsey J.M, Anal. Chem., Vol.67, pp. 4184-4189, 1995.

14 Knox J.H., J. Chromatography Sci., Vol. 18, pp. 453-461, 1980.

15 Kirkland J.J., Modern practice of liquid chromatography, Wiley-Interscience, 1971.

16 Giddings J.C., Dynamics of Chromatography, Arnold E. (London) and Dekker M. (New York), 1965.

17 Done J.N., Knox J.H., Loheac J., Applications of high speed liquid chromatography, Wiley, London, 1974.

18 DeRisi J.L., Iyer V.R., Brown P.O., Science, Vol.278, No.5338, pp.680-686, 1997.

19 Cheung V.G., Nature Genetics, Vol.18, No.3, pp.225-230, 1998.

20 Duffy C.D., McDonald J.C., Schueller J.A., Whitesides G.M., Anal. Chem., Vol. 70, N. 23, pp 4974-4984, 1998.

Chapter 6: CONCLUSIONS AND FUTURE WORK

6.1 Conclusions.

This PhD has demonstrated that the FHD technique is a flexible, adaptable, and fruitful method to fabricate total analytical systems, such as those used in Lab-on-a-Chip technology. This has been illustrated through a multitude of points, such as: the high sensitivity results achieved for fluorescence detection, the low detection volume used, the large number of functions integrated, as well as the properties of silica as a perfect substrate for immobilisation.

Protocols for the FHD technology have been developed, which were employed to produce different platforms for biological or chemical assays. These FHD platforms were fabricated and assessed in the framework of low volume fluorescence-based assays. Their experimental detection limit was determined as 20 pM (equivalent to 10 zeptomoles or ca. 6000 molecules) of Cy5 fluorophore. The applicability of the devices to the miniaturisation of bioassays was illustrated by analytical measurements on fluorescently-labelled oligodeoxynucleotides, as might be appropriate for a genomics platform.

Optical structures and analytical devices in biotechnology have been combined. A demonstration of this optical treatment was achieved when a 1x16 splitter was produced by Y-branches and was integrated with 16 analytical chambers, enabling us to perform 16 fluorescence measurements simultaneously, using a CCD.

Furthermore, this work was the first demonstration of successfully pumping liquids into a FHD based optical biosensor device. These optical devices comprised low loss waveguides (0.5 dB cm^{-1}) with deep, smooth vertical channels (up to 40 μm). The channels were sealed using PDMS polymer and the movement of the liquids was made possible along the channels by applying pressure differences.

Other goals were achieved, including: fabricating a separating system of liquid chromatography device in FHD; developing hybrid techniques for fibre positioning; creating bonding processes for FHD by anodic or fuse bonding; and improving the etching process for glass doped with rare earth.

6.2 Future work.

As discussed above, this project was based on the exploration of new optical biosensing applications using FHD technology. Future work in this field would offer many other possibilities worth implementing, some leading to laboratory-on-a-chip technologies. The following subsections describe some potential directions worth exploring for the application of FHD technology in biosensing.

6.2.1 Sacrificial Layers.

An interesting route, which has not been addressed in this thesis, would be the development of a sacrificial layer for FHD glass, in the same fashion as polysilicon is used in micromachining. Such a material could be used as "forms" and "spacers" to make desired shapes, which could later be removed. This would allow moving parts, such as cantilevers, channels, and membranes to be formed in FHD glass, some of which are more appropriate for physical sensors, or actuators. In addition, chemical sensors could also take advantage of these new features in the form of micro-pumps. An appropriate starting point could be based on the fact that "phosphosilicate glass etches much faster in HF than thermally grown or undoped oxides", as described by Howe [1] and Kovacs [2].

6.2.2 Development of a Capillary Electrophoresis System.

The combination of an FHD based sensor and a microfluidic circuitry promises a very sensitive and compact capillary electrophoresis system. The FHD structure, which was sealed using PDMS, could have been used for capillary electrophoresis if platinum wires were integrated into the device. Similarly, chips that are more compact can be created if the platinum electrodes are deposited on the surface of the device. This idea is based on my own research in this area, and on the work performed by Duffy [3] and Effenhauser [4], who performed a capillary electrophoresis system on similar materials. Figure 6.1 shows this alternative design, intended to produce a more compact system with the electrodes evaporated, or sputtered on the surroundings of the etched reservoir. The platform used in this design would be the same as that used for the fluorescence measurements in Chapter 3.

In this new system, the liquid must be in contact with the electrodes deposited on the etched reservoirs. However, a high directional metal deposition may cover the bottom and the top surfaces of the reservoir exclusively. The walls are not covered, therefore, the bottom surface would be isolated from the rest of the device. Two steps are required to solve this deposition problem: the hole opened in the PDMS must be larger than the reservoir size, and the deposited metallic area must cover the area near to the reservoir and not covered by PDMS. Hence, the electrical contact between the liquid and the platinum would be established by the metal covering the top surface of the device.

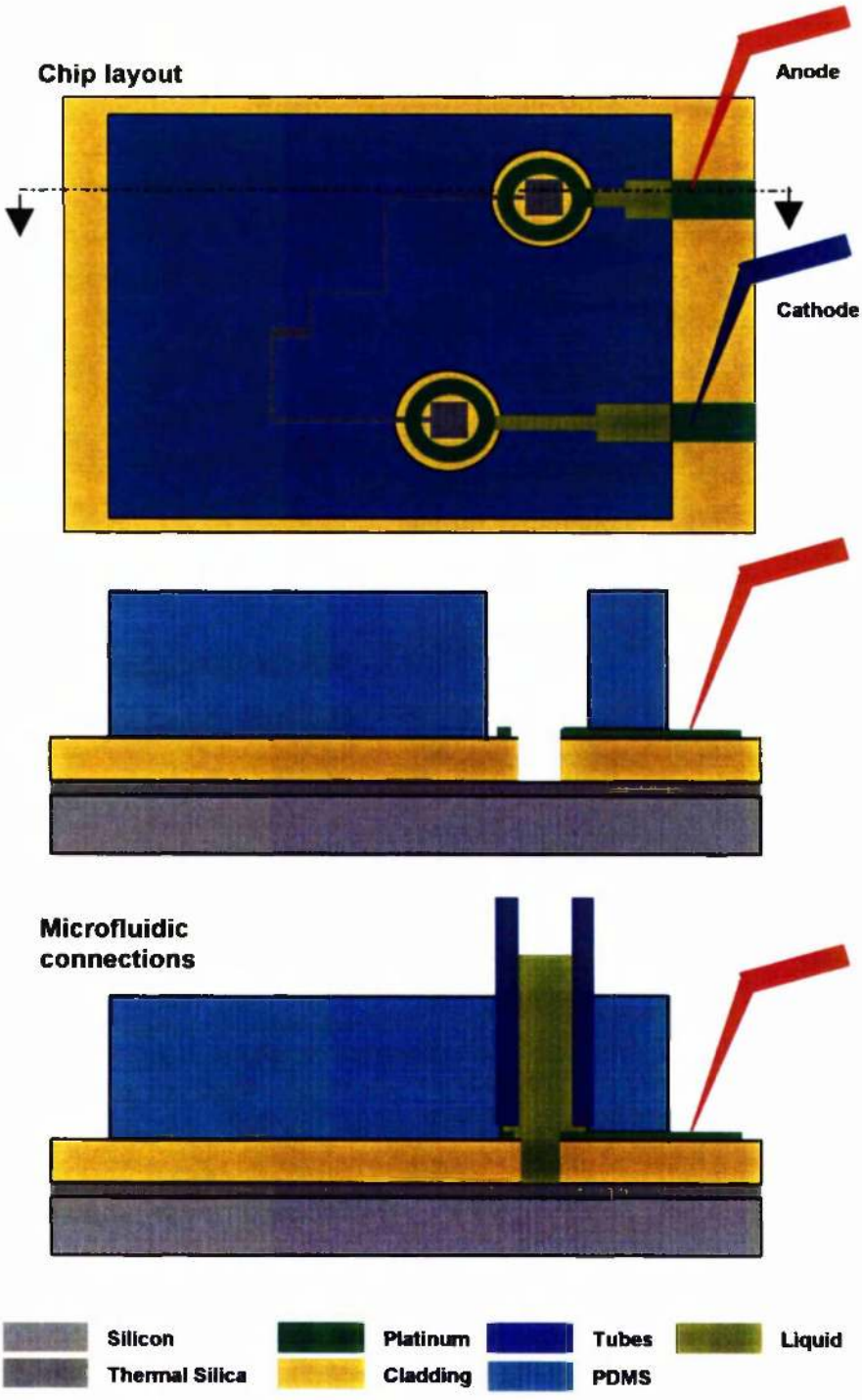

Figure 6.1: Schematic representation of a possible design to perform a compact capillary electrophoresis system with electrodes evaporated or sputtered on the surroundings of the etched reservoir.

6.2.3 Liquid Chromatography.

Further research could be based on the use of the etched nanocolumns 10 μm width, 8 μm depth and 2 μm between columns (see Section 5.2). These etched nanocolumns are equipped with channels, which when sealed using the PDMS technique described in Section 5.3, allow the liquids to be pumped through the microfluidic system. The liquids are subsequently separated and analysed in the analytical chamber. As described in Figure 6.2, the chip layout would be very similar to the device fabricated and described in Chapter 3, with the exception that the integrated separating system would consist of square columns.

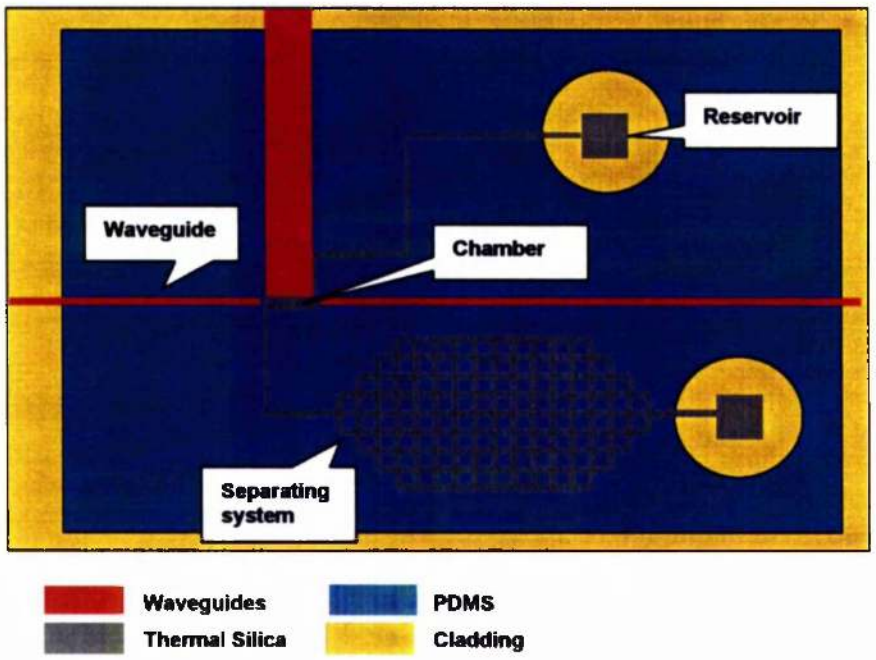

Figure 6.2: Schematic representation of a future integrated liquid chromatography in FHD glass.

6.2.4 Fibre Clamping for FHD passive Pigtailing.

This section describes a future process to position fibres in-line with FHD waveguides. This pigtailing prototype is based on the fibre positioner explained in appendix B, and its fabrication would start with the fibre placed in the V-groove and topped with a Pyrex™. The clamped fibre would be, then, actively aligned to the FHD waveguide by commercial nano-positioners (see Figure 6.3.a) and both

devices (V-groove chip and FHD optical device) would be glued together by an epoxy or ultraviolet glue (see Figure 6.3.b). Once the devices are properly sealed, they could be encapsulated by PDMS (see Figure 6.3.c). Moreover, if the fibre fits with high precision in the V-groove, it becomes feasible to manually plug and unplug the fibre into the FHD device. The V-groove size should enable a horizontal, but not lateral or vertical movement (see Figure 6.3.a). The versatility of this technique would come from the fact that these fibres would not be fixed or glued, and movement of the fibres along the V-grooves would be possible.

One important issue is how the thermal expansion of the glue, and / or PDMS, affects the optical coupling. The glue used must be chosen carefully in order to fabricate a temperature insensitive pigtail.

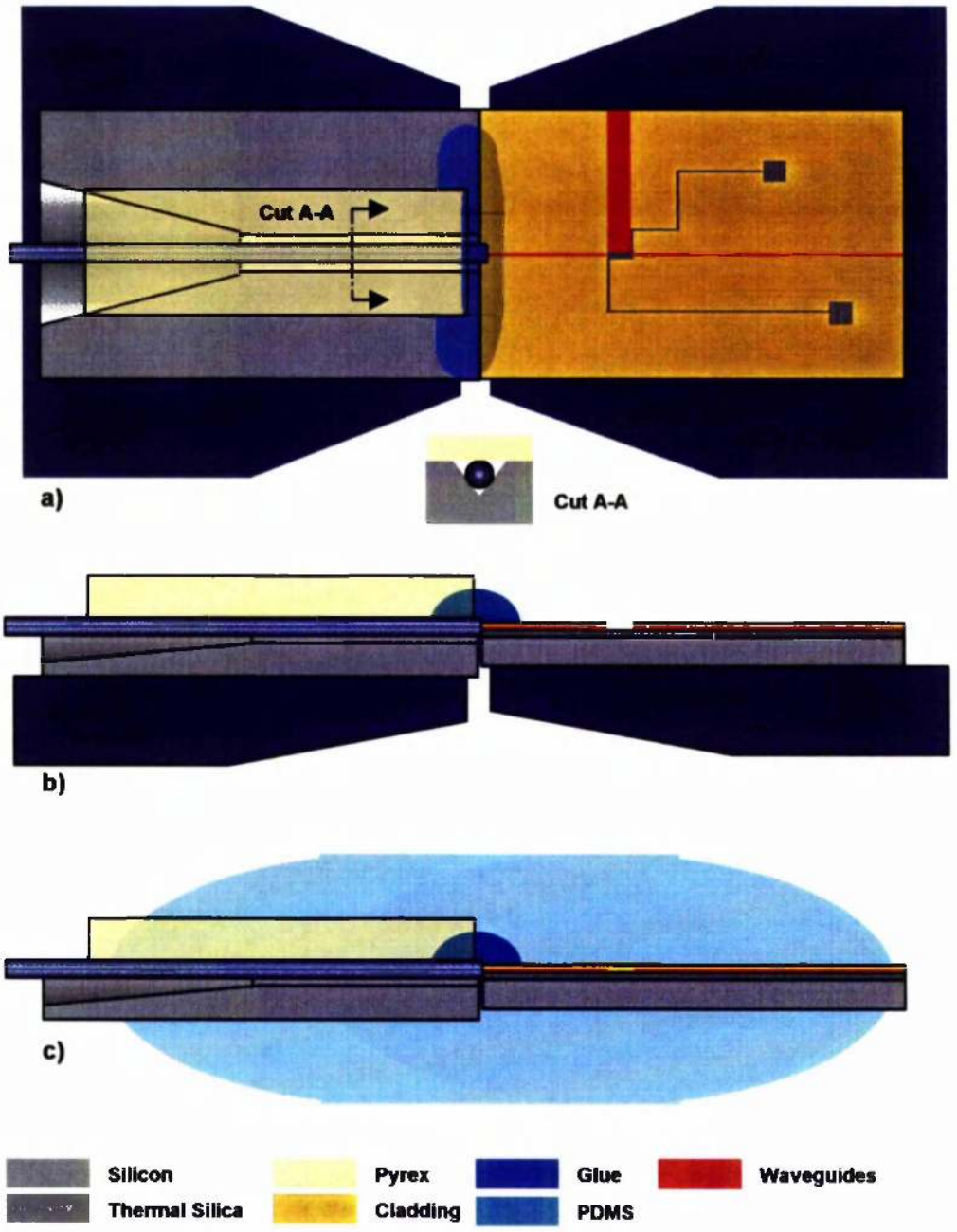

Figure 6.3: The fabricated prototypes would consist of V-grooves in silicon, with an optical fibre fixed by a cover slide anodically bonded. (a) The V-groove covered with Pyrex™ glass can provide the robustness necessary to place the fibre that will be actively aligned to the FHD waveguide by commercial nano-positioners. Subsequently, (b) both devices (V-groove chip and FHD optical device) would be glued together by an epoxy or ultraviolet glue. Once the devices are properly glued, (c) they could be encapsulated by PDMS. The fibre could be manually plug and unplug fibre into the FHD device. The V-groove size must enable a horizontal movement but not a vertical one movement (see cut A-A).

6.2.5 DNA Array Analysis.

An array of 16 analytical chambers was fabricated in FHD glass as described in 4.5.1. An excitation beam was divided by integrated Y-branches, and the fluorescence collection was imaged onto a CCD camera placed above the chip (see Section 4.5). As an alternative experiment, one could collect the fluorescence from perpendicular waveguides, as was done in the single device in Chapter 3. My own experiment is illustrated in Figure 6.4. From this trial, the low refractive index difference (0.21%) did not allow the confinement of fluorescence into the output waveguides. Therefore, to collect light using this method, a higher refractive index contrast should be used, involving non-monomode guiding in the splitters, which can be compensated by multimode Y-branches with waveguide necks, or by MMI splitters (see Section 4.4.4 and 4.4.5 respectively).

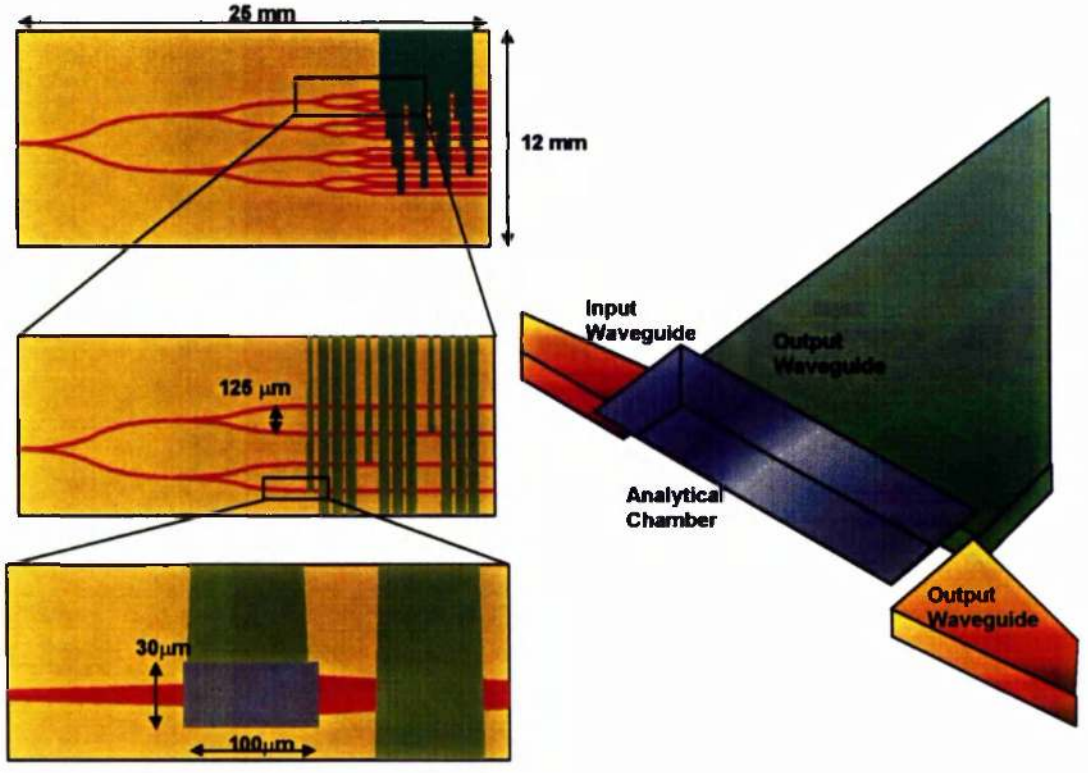

Figure 6.4: Schematic representation of a future DNA array analysis.

In Figure 6.4, the input waveguides cross a perpendicular waveguide of 100 μm width affecting the excitation of the subsequent chamber. In addition to this problem, the design has the restriction that no channels can be etched on its surface, due to the lack of space used either by input or output waveguides. Thus, this DNA array needs enhancement by the use of a bonded PDMS overlayer, with previously moulded channels. These channels will join the analytical chambers to each other.

6.2.6 Stack Technology for DNA Array Analysis: the 3D Biochip.

Following the approach described by Verpoorte [5], and Jo [6] it might be possible to link their idea with FHD glass and obtain a possible 3-dimentional DNA array biochip. It would involve stacking devices and layers of PDMS one over the other, and would be similar in construction to the ones presented earlier and schematically represented in Figure 6.4. The PDMS layer would work as a glue sealing the pile of devices. The fluorescence collection would be achieved by collecting light coming from the orthogonal waveguides, by using a high numerical aperture lens and a CCD. All the chambers would be communicated in the same vertical column by holes in the PDMS and silicon back etch (see Figure 6.5).

To overcome the problem of alignment of the different multiple fluidic modules, alignment holes for stacking should be perforated (by etching). These holes would go through each module and a metallic or glass post introduced to perform a passive alignment of the devices.

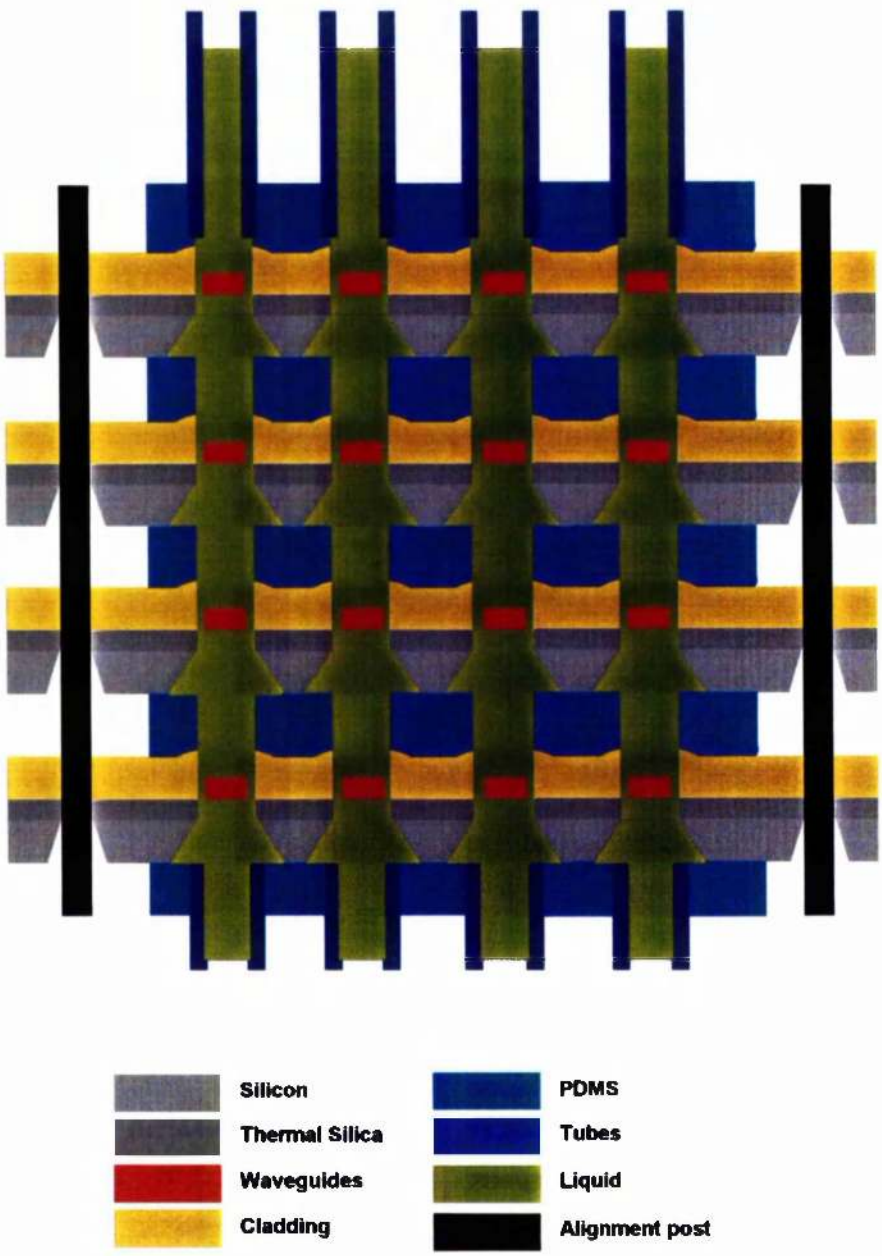

Figure 6.5: Schematic representation of the future 3D Biochip for DNA array analysis based on Stack technology.

6.2.7 Cell Screening.

Throughout this research, a collaboration was established between a company called New Dimension Research & Instrument, Inc. (USA), and Glasgow University, Department of Electrical Engineering. The aim of this collaboration was to use FHD devices for cell screening, leading to the discovery of new drugs.

The methods used by this company were twofold: i) to excite a fluorophore using a laser to scan the bottom of 96 or 384 well plate and ii) to collect the fluorescence signal from the bottom of this plate. However, the problem they encountered was they did not have a high throughput platform, which meant that they could not analyse high numbers of wells when different drugs were added. A FHD device would be a suitable platform to perform these two tasks.

This company is planing to test some FHD devices fabricated as part of this PhD research. The FHD devices were designed specifically for this purpose and the size of the chambers was constructed larger in order to contain 50-100 cells. For details concerning the fabrication protocols, the reader must refer to Section 2.2. Before sending the FHD devices to New Dimension Research & Instrument, they were tested by a top fluorescence collection (see Section 4.5.2.3). The measurement process is explained in Section 4.5.2.4. In Figure 6.6, a SEM picture depicts a successful fluorophore excitation by the input waveguide.

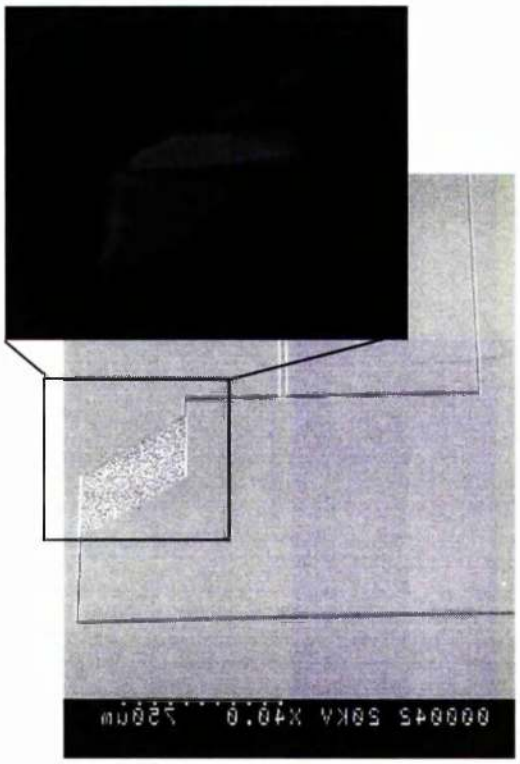

Figure 6.6: SEM picture of the device fabricated specifically for cell screening. The top figure shows that a fluorophore placed in the chamber was successfully excited by the light coming out from the input waveguide.

6.2.8 Bulk Micromachined Channels on FHD.

The idea of etching and sealing channels in FHD without the use of an extra overlayer can be done following Boer's guidelines [7]. The starting point is a silicon substrate with a layer of FHD silica on top of thermally oxidised silica. The silicon below the silica is used to perforate the channels, but prior to this, the silica must be selectively etched away in order to expose the silicon. Following this, an anisotropic silicon etch (e.g. KOH) is carried out on the silicon with the silica acting as a mask. Rather than run a new deposition to seal the trench, simply re-flowing the cladding to collide the trench will suffice to seal the channel (see Figure 6.7).

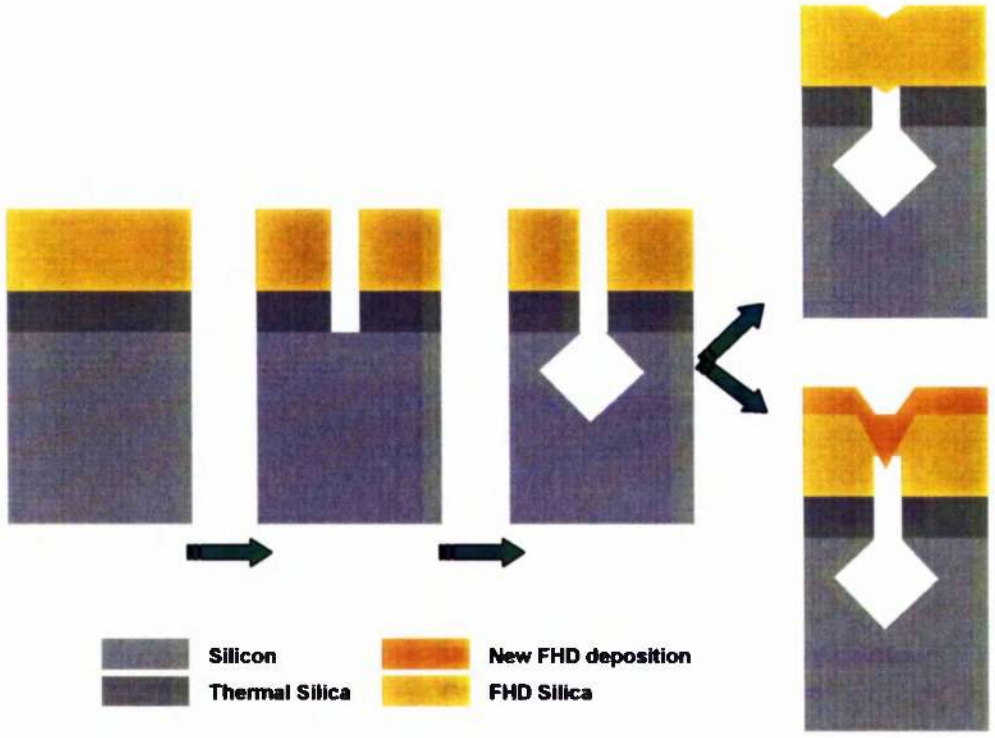

Figure 6.7: Schematic representation of the fabrication of bulk micromachined channels. The last step could consist on a simply reflow.

6.2.9 Anodic Bonding by FHD Sodium Glass.

By doping FHD glass with sodium using and aerosol technique [8,9], a new approach was tested to develop anodic bonding replacing the Pyrex™ glass with this new material. Unfortunately, the attempts were unsuccessful. This method would have given the opportunity to bond FHD silica to silicon without a metallic layer. One could argue that some ions in FHD glass were interfering with the creation of the necessary ion flow, as no current decay was observed, and no electrostatic bond was created. Future work could focus on reaching the right dopant concentrations of ions.

In order to fabricate sodium doped FHD glass, the following procedure was utilised: the sodium was dissolved until saturation in an aqueous solution, and was then nebulised employing an extra port in the FHD torch. A PVC pneumatic atomiser swept the sodium into the reaction zone using zero grade nitrogen as the carrier gas. The flame in the torch was used to expel the evaporated water, leaving

behind a submicron particle of sodium that was oxidised and directly incorporated in to the partially fused core layer. One run was performed to obtain 8 μm of glass, and its parameters are outlined in Table 6.1.

Warming stage:				
Initial turntable temperature: 150 ° C		Torch warming transversals		
		Number:	4	
		Oxygen:	2 l min^{-1}	
		Hydrogen:	5 l min^{-1}	
		Nitrogen:	3 l min^{-1}	
Deposition stage:				
Halides flows:		Torch flows:		
$SiCl_4$: 120 sccm		Number of transversals :	8	
PCl_3: 190 sccm		Oxygen:	6 l min^{-1}	
$POCl_3$: 450 sccm		Hydrogen:	4 l min^{-1}	
Master: 90 sccm		Nitrogen:	3 l min^{-1}	
NaCl concentration: 1 M				
Sintering cycle:				
Initial Temperature	Increasing rate	Sintering time and temperature	Decreasing rate	Final Temperature
850 °C	20 °C min^{-1}	15 min at 1375 °C	-15 °C min^{-1}	850 °C
Sintering atmosphere:				
Helium: 0.1 l min^{-1}		Oxygen: 0.1 l min^{-1}		

Table 6.1: Deposition parameters of sodium silica for the fabrication of sample that could substitute Pyrex™ glass in the anodic bonding process. This process was divided in warming stage, deposition stage and sintering cycle.

6.2.10 Conclusions of the Future Work.

From all the future ideas, above presented, future FHD researches should be encouraged to examine especially the following options:

Bulk micromachined channels on FHD glass (Section 6.2.8): The main advantage resides on the fact that it is a straightforward protocol and it may provide fruitful results.

Development of a capillary electrophoresis system (Section 6.2.2): This is a more elaborate future task, but it would be worthy because it could provide a platform with the best compromise between integration and sensitivity.

Sacrificial layers for FHD glass (Section 6.2.1): This task would involve many iterative attempts with different materials and conditions, but if successful, it would give many more possibilities for bio-chemical and physical sensors. Such realisation would offer a versatile approach where moveable parts and integrated optics could be fabricated on the same substrate. This combination would yield a variety of possibilities, such as: moveable mirrors, scanning mirrors for raster displays, optical switches, modulators, etc.

6.3 References.

1 Howe R.T., Journal of Vacuum Science and Technology B, Vol. 6, No. 6, pp. 1809-1813, 1998.

2 Kovacs G.T.A., Micromachined Transducers Sourcebook, McGraw-Hill, 1998.

3 Duffy C.D., McDonald J.C., Schueller J.A., Whitesides G.M., Anal. Chem., Vol. 70, N. 23, pp 4974-4984, 1998.

4 Effenhauser C. S., Bruin G. J. M., Paulus A.; Ehrat M., Anal. Chem., Vol. 69, pp. 3451-57, 1997.

5 Verporrte E.M.J., Van der Schoot B.H., Jeanneret S., Manz A., Widmer H.M., de Rooij N.F., J. Micromech. Microeng., Vol. 4, pp. 246-256, 1994.

6 Jo B.H., Van Lerberghe L.M., Motsegood K.M., Beebe D.J., Journal Of Microelectromechanical Systems, Vol.9, No.1, pp.76-81, 2000.

7 De Boer M.J., Tjerkstra R.W., Berenschot J.W., Jansen H.V., Burger C.J., Gardeniers J.G.E., Elwenspoek M., vandenBerg A. Journal Of Microelectromechanical Systems, Vol.9, No.1, pp.94-103, 2000.

8 Bonar J. R., PhD Thesis, University of Glasgow, 1995.

9 Vermelho M, PhD Thesis, University of Glasgow, 1999.

Appendix A: Anodic Bonding Instrumentation.

This appendix includes the design schemes of both the ceramic clamp and the ammeter protection circuit used in the anodic bonding instrumentation.

A.1 Clamp Dimensions.

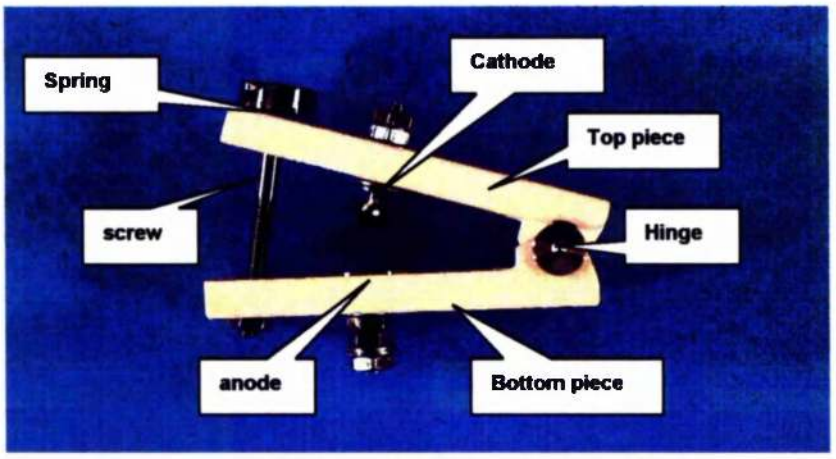

Figure A1.1: Picture of the ceramic clamp.

The following diagrams show the dimensions of the different parts of the clamp depicted in Figure A1.1.

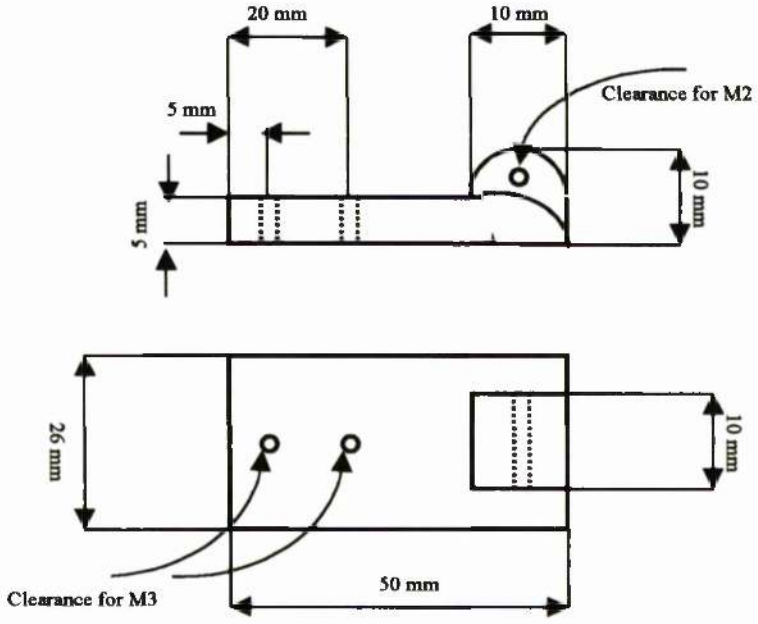

Figure A1.2: Drawing of the bottom piece of the clamp. Material: a machinable ceramic called Macor.

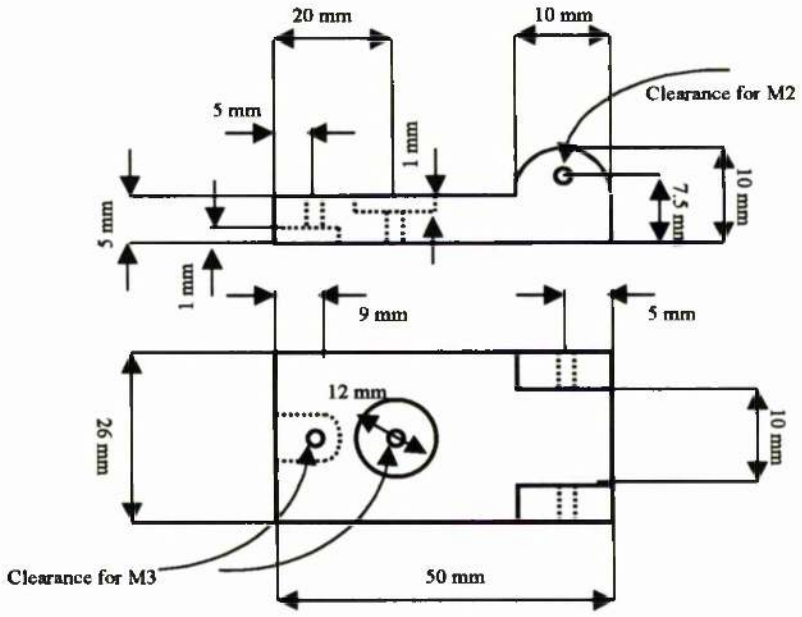

Figure A1.3: Drawing of the top piece of the clamp. Material: a machinable ceramic called Macor.

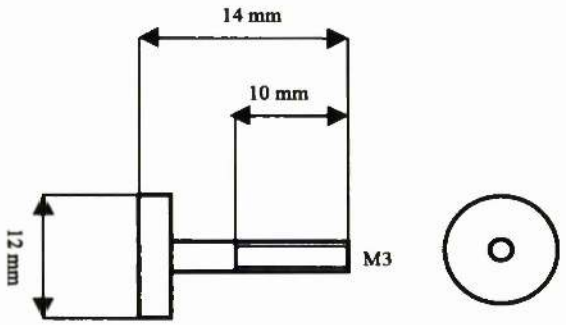

ITEM 1

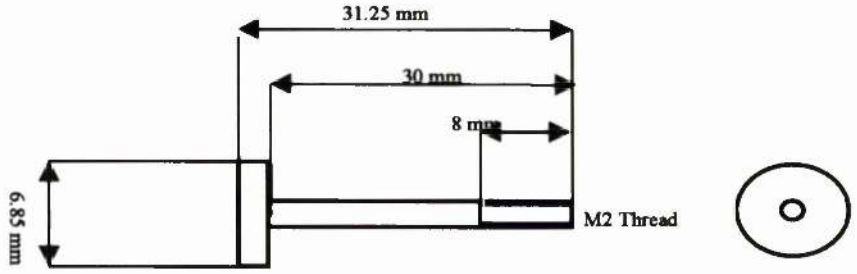

ITEM 2

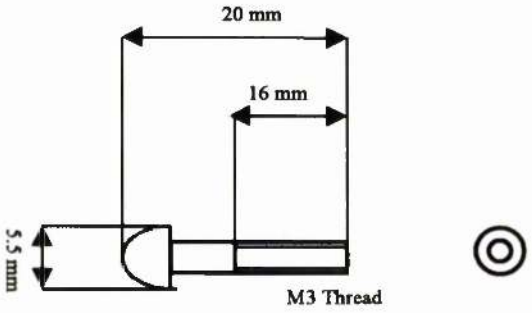

ITEM 3

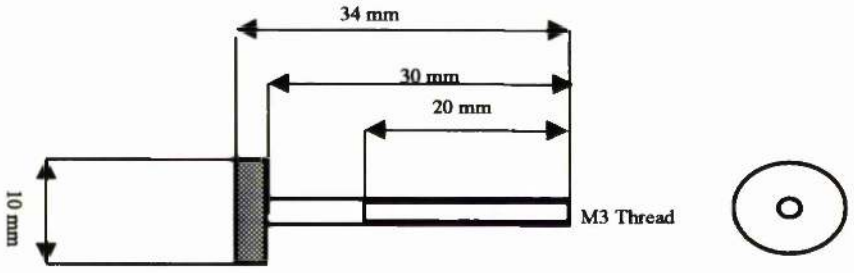

ITEM 4

Figure A1.4: Drawing of the stainless steel pieces. Item 1 corresponds to the bottom electrode. Item 2 is the screw that work as a hinge for the clamp. Item 3 is the ball electrode. Item 4 is a screw used to close the clamp.

A.2 Protection Circuit for the Ammeter and the Power Supply.

The tasks of the circuit developed in the anodic bonding instrumentation were twofold: (i) to protect the ammeter from short-circuits created in the clamp and (ii) to produce a minimum current flow in the power supply (Figure A1.5).

The ammeter protection circuit works as follows: when the maximum current allowed in the ammeter goes through the clamp, the resistor in series with the ammeter will create a voltage that will make the diodes conduct, protecting the ammeter.

The power supply used needed a minimum load, therefore, it was necessary to place in parallel five high-power resistors (100Ω and 24W) in order to keep the necessary minimum current flow.

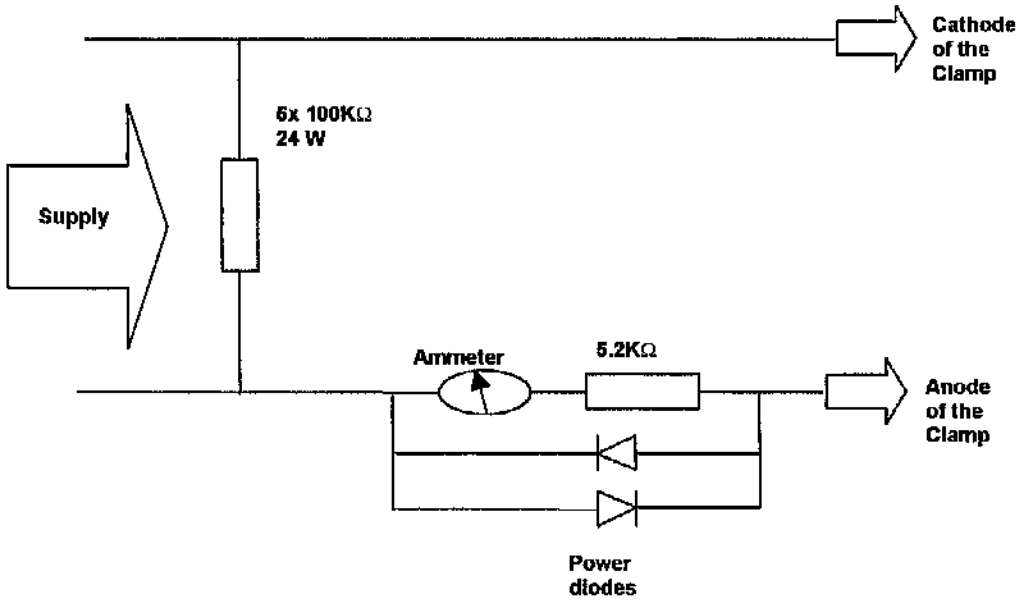

Figure A1.5: Circuit scheme to protect the ammeter and the power supply.

Appendix B: Fibre Optic Positioning for FHD Optical Devices by Hybrid Micromachined Techniques.

In an early stage of this work, some devices were fabricated as prototypes using hybrid integration. The fabricated prototypes consisted of V-grooves in silicon, with two optical fibres separated by a gap and topped by a cover slide (see Figure B2.1). The cover-slide was bound onto the silicon by an anodic bond (see Section 2.3.1 and Figure B2.3). Their purpose was to provide a versatile microsystem to study the influence of different parameters, such as, chamber dimensions, or different optical configurations in the fluorescence collection efficiency (see Chapter 3). These experiments offered a clear idea about fluorescence emitted by a fluorophore in an aqueous solution [1]. It is the author's opinion that this hybrid device can be a valid platform to align fibres in-line with FHD waveguides (fibre pigtailing), as it will be described in Section 6.2.4. This microsystem was successfully used to transfer photolithographic patterns onto fibre surfaces.

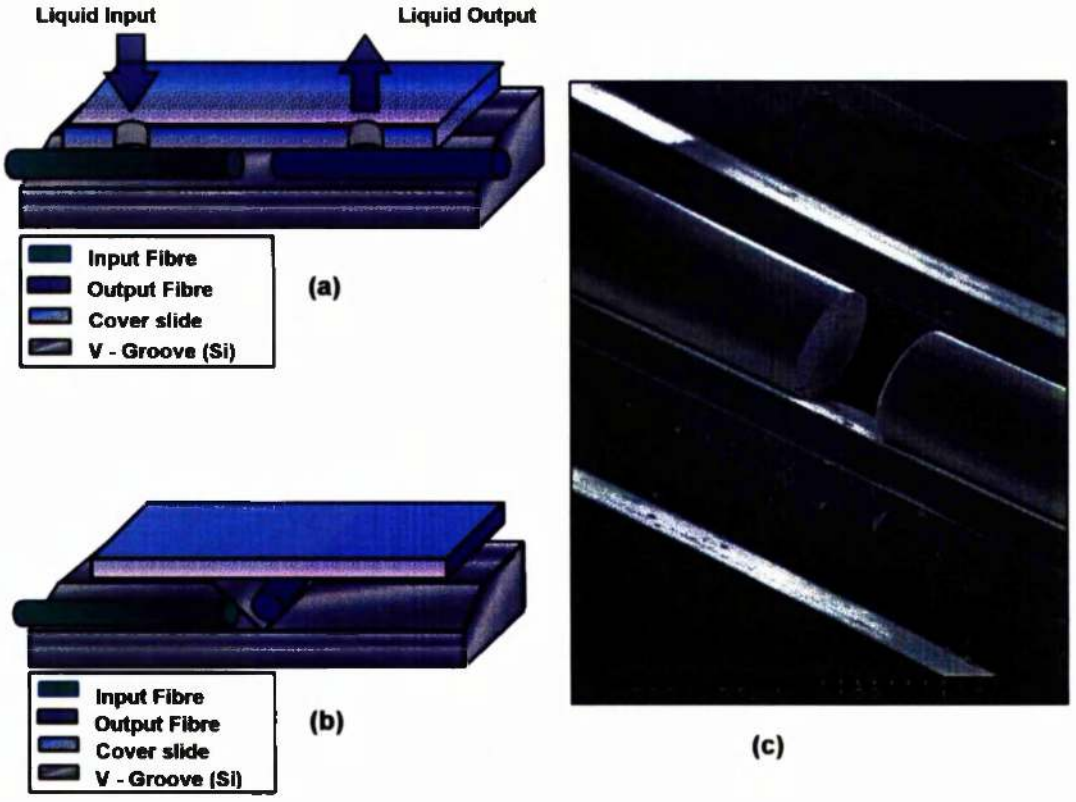

Figure B2.1: (a) Schematic representation of V-grooves in silicon to position two on-line fibres, in order to create a gap to place the analyte; (b) Schematic representation of V-grooves in silicon to position two perpendicular fibres, and to create a gap to place the analyte; (c) SEM picture of V-grooves in silicon to position two on-line fibres (Picture courtesy of Dr. Mike Jubber).

B.1 Fabrication Method of a Micromachined Fibre Optic Positioner.

The fabrication process was based on an anisotropic wet etch using KOH [2]. The process is outlined in Figure B2.2 and started with the deposition of 600 nm of low stress Si_3N_4 on both sides, of a silicon wafer (orientation 100). Edinburgh University laboratories manufactured this process by a low-pressure chemical vapour deposition (LPCVD). After a standard S1818 photolithographic process [3], the substrate was immerse in HF to wet etch the Si_3N_4, which served as mask in the subsequent KOH wet etch. This etch produced a silicon etching rate of 70 $\mu m\ hr^{-1}$ at ~ 80 °C and 45 weight percent. The etching depth of the V-groove was 243 μm. This depth enabled us to position the optical fibre (125 μm diameter)

vertically fixed by the anodically bonded glass slide and the V-groove (see Figure B2.3), while horizontal movement of the fibre along the V-grooves was possible. The fibres were placed using a microscope and a set of micro-blocks.

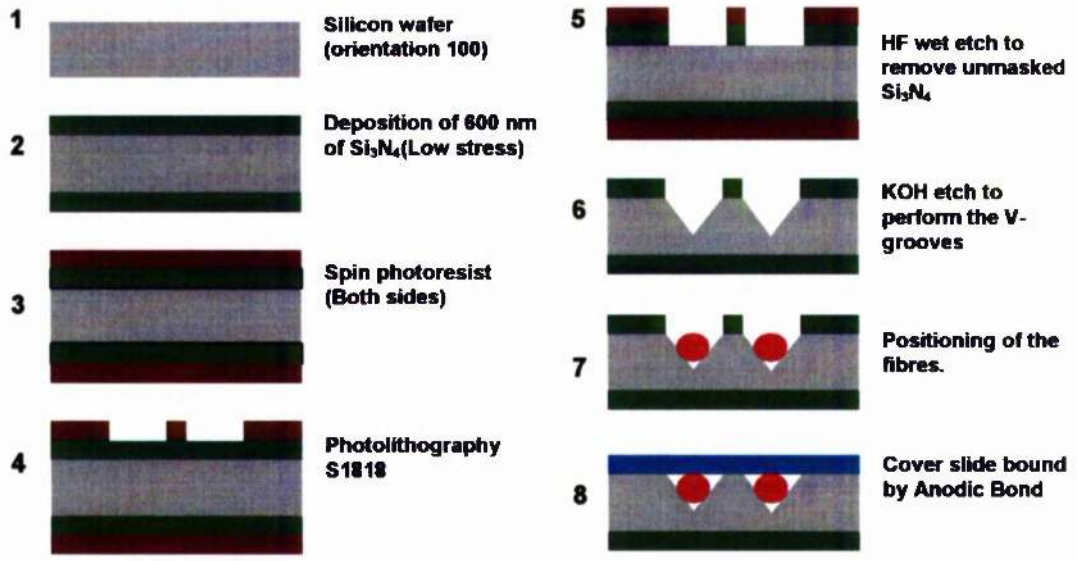

Figure B2.2: Fabrication procedure for a prototype consisting on V-Groves in silicon and fibres on them. The V-groove is topped by a cover by anodic bonding.

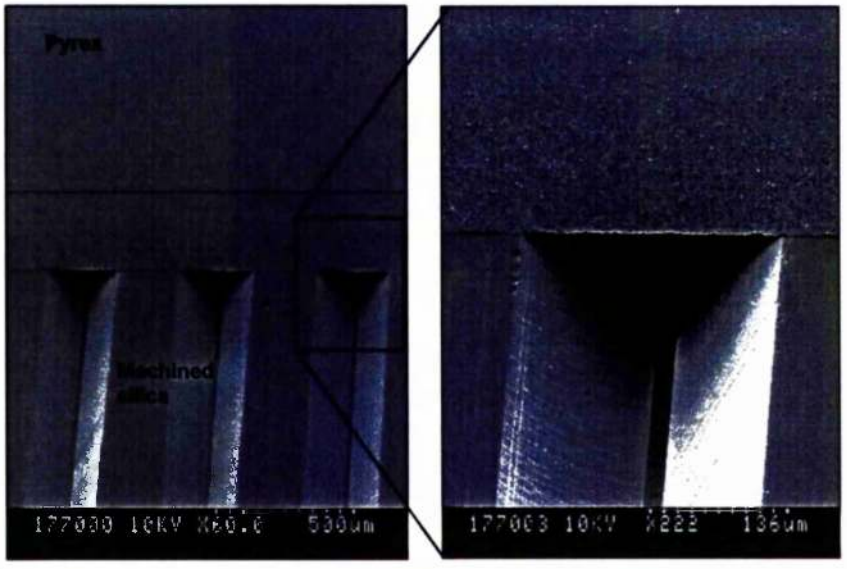

Figure B2.3: Anodic bonding between Pyrex and micromachined silicon by KOH.

B.2 Transfer of Photolithographic Patterns onto Fibre Surfaces using the Fibre Positioner.

V-grooves for fibre positioning enables the transferring of photolithographic patterns onto fibre surfaces. Once the fibre is adhered into the V-groove, any step described in Section 2.2, can be easily applied, such as RIE, thermal oxidation, FHD, photolithography, metal evaporation, etc. It was possible, for example, to perform all the necessary steps for photolithography including, spinning, resistive evaporation and wet etching of nichrome. In order to validate the photolithographic process on fibres, the reactive ion etching (RIE) described in 2.2.6, was carried out. Figure B2.5 shows a SEM picture of a fibre with several holes etched on it.

The fabrication protocol is outlined in Figure B2.4. The etching depth was 15 μm, deep enough to reach the core of the fibre (multimode with 100 μm diameter core). This depth could allow us to direct light in contact with the analyte (See Figure B2.5). This photolithographic process followed by a high-density (inductively coupled) plasma source can produce deeper holes to fabricate very uncomplicated mass-producible optical sensors.

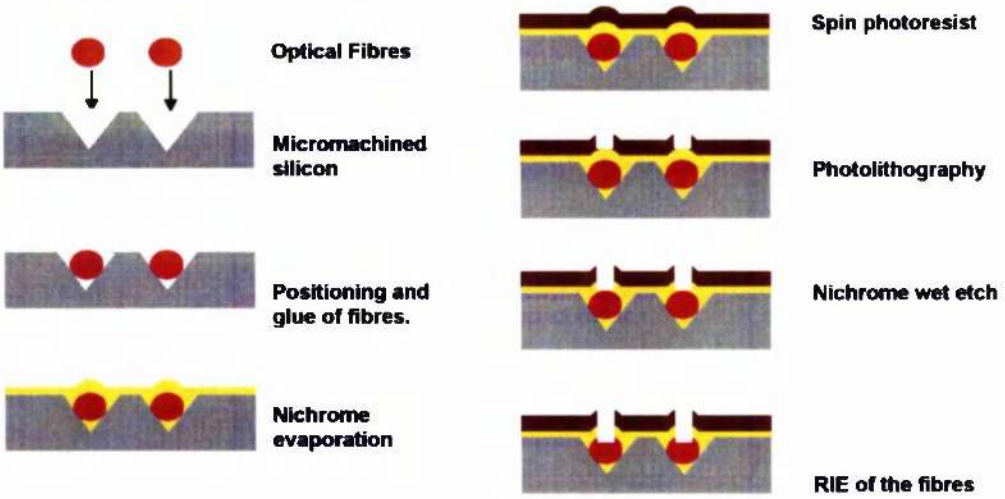

Figure B2.4: Fabrication protocol for the etching of holes on optical fibres. The device is treated like a monolithic substrate. Once the fibre is glued onto the V-groove, it is possible to perform all the necessary steps for photolithography including, spinning, evaporation of nichrome to perform the RIE process. The etching depth is 15 μm.

Figure B2.5: SEM images of etched chambers on fibres by photolithography and RIE. The reached depth was 15 μm.

B.3 References.

1 Ruano J. M., Ortega D., Bonar J. R., McLaughlin A. J., Jubber M. G., Cooper J. M., Aitchison J. S., MNE 98 Conference, 1998.

2 Kendall D.L., Journal Of Vacuum Science & Technology A-Vacuum Surfaces And Films, Vol.8, No.4, pp. 3598-3605, 1990.

3 Bargon J., Methods and Materials in Microelectronic Technology (IBM Research Symposia Series), Plenum Pub Corp; ISBN: 0306418037, October 1984.

Appendix C: Reactive Ion Etching of Erbium Doped Waveguides for Sensing Purposes.

To conclude, this appendix describes an interesting fabrication target for future research. The work is based on the integration onto a common silicon substrate of 'active' silica waveguides (doped with erbium, Er^{3+}) with passive components. This research has led to the filing of a patent application [1].

In recent years the role of erbium doped silica fibre has become important because of its emission at 1.55 μm, the low-loss telecommunications window. In addition, the pump bands at 980 and 1480 nm allow semiconductor lasers to be used as pump sources [2]. Rare earth materials have been also used as solid state electrolytes for gas sensing, CO_2 [3], O_2 [4], galvanic cell for H_2 sensors [5], or rare earth semiconductors for NO_2 sensing [6]. Recently, new advances have made possible the transfer of rare earth doped structures to optical sensing, especially for temperature sensors [7, 8], gyroscopes [9] and CO sensors [10].

The production of rare earth integrated lasing and amplifier structures requires a homogeneous distribution of dopant (reduce ion-ion interactions) and a minimisation of the background propagation losses. An aerosol technique for rare earth doping based in FHD solves the first requirement. However, it is difficult to

find an adequate etching process of waveguides to minimise the losses. This resides in the fact that high doping is required due to the limited gain length of rare earth doped waveguides. The non-volatile nature of this dopant creates high surface roughness producing high loss waveguides.

Some etching techniques, which result in a low degree of surface roughness, are available, such as, ion beam milling etches ion doped silica based waveguides with a low degree of surface roughness. However, these techniques provide low etching rates and suffer from poor sidewall angles (<90°) due to the nature of the system. This results in asymmetric waveguides and thus a high degree of polarisation sensitivity. Therefore, the main objective of this study was to develop an optimised CHF_3 and O_2 RIE process, which has a low surface roughness, acceptable glass etching rates, and at the same, produces time vertical sidewalls. Hence, orthogonal design technique was used to associate the function and results of different input parameters for this process. This technique examined how a selection of RIE parameters (etchant gas, pressure, and forward RF power) influenced the RIE characteristics of rare earth planar silica waveguides.

C.1 Fabrication of the Samples.

An orthogonal design process demands the preparation of several rare earth doped samples. The following two subsections describe the preparation process of these samples consisting of an aerosol technique and a photolithography step.

C.1.1 Aerosol Doping.

Once a 16 μm-thick SiO_2 layer is thermally grown on the silicon wafer (see Section 2.2.1), aerosol doping [11] is used to fabricate phosphosilicate waveguides formed by FHD (see Section 1.6). The dopant is incorporated homogeneously, reducing ion - ion interaction [12]. The only variation in the FHD system is the incorporation of an extra port on the torch for the aerosol inlet. To atomise the solution a PVC pneumatic atomiser is employed using zero grade N_2 gas which

also transported the aerosol droplets to the torch. The parameters of the deposition of the core of the doped waveguides are summarised in Table C3.1.

Warming stage:				
Initial turntable temperature: 150 ° C		Torch warming transversals		
		Number:	4	
		Oxygen:	2 l min^{-1}	
		Hydrogen:	5 l min^{-1}	
		Nitrogen:	3 l min^{-1}	
Deposition stage:				
Halides flows:		Torch flows:		
$SiCl_4$: 150 sccm*		Number of transversals :	6	
PCl_3: 180 sccm		Oxygen:	2 l min^{-1}	
$POCl_3$: 480 sccm		Hydrogen:	4 l min^{-1}	
Master: 40 sccm		Nitrogen:	3 l min^{-1}	
Er^{3+} Concentration: 0.02M				
Sintering cycle:				
Initial Temperature	Increasing rate	Sintering time and temperature	Decreasing rate	Final Temperature
850 °C	20 °C min^{-1}	15 min at 925 °C	-15 °C min^{-1}	850 °C
Sintering atmosphere:				
Helium: 0.7 l min^{-1}		Oxygen: 0.1 l min^{-1}		

Table C3.1: Deposition parameters to fabricate rare-earth waveguides by FHD. This process is divided in warming stage, deposition stage and sintering cycle. * sccm: standard cubic centimetre gas flow per minute.

The rare earth concentration depends on the strength of the solution and the transport gas flow rate. The torch was designed to avoid the possibility of gravitational settling and hence, condensation of the rare earth. The low-density soot is then fully sintered to produce a low loss doped silica waveguide.

The wafer was highly doped (SiO_2: P_2O_5: Er - 78.31:21.13:0.56 wt% respectively) due to the limited gain length available on planar structures [13,14,15]. The thickness measured by a prism coupling technique is found to be 7 μm. The wafer

was subsequently diced up by a diamond saw to provide samples (10mm × 10 mm) for process characterisation.

C.1.2 Mask Patterning.

It is clear from previous work that metallic masks are preferable to photoresist for RIE of FHD glass because the quality of the sidewalls. Therefore, the same photolithographic process as that used in Section 2.2.3 was employed. A resistive evaporator was used to coat samples with 75 nm of nichrome, which is subsequently patterned using Shipley S1828 photoresist, and post-baked at 120 °C prior to the etch formation of the nichrome. Samples were also prepared which used photoresist only as the dry etch mask. The analyses of the etching results are accomplished using the same techniques explained in Section 2.2.4.1.

C.2 Experiment Description.

The straightforward way to achieve a high glass etch rate is to increase the RF power since the etching is more assisted by ions due to the increasing of their speed. However, at the same time, the roughness will be very high. Due to the characteristics of RIE process a structured and rigorous approach is required to fine tune the etch process. A technique of orthogonal design based upon Taguchi techniques [16,17] was used. An advantage of this technique is that an experiment with four factors at three level settings would require 81 experiments to investigate the full parameter spare (full factorial design), whereas this Taguchi design only required nine experiments. The application of this technique did not allow us to statistically examine the interactions between factors, however it gave a good indication of the main effects of each individual parameter to understand the etching process. The following sections will describe the design of the orthogonal experiments to improve the rare earth etching process.

C.2.1 Selection of Investigated Factors and their Range.

There must be a basic knowledge of the main influential factors in the process. This came from a prior working knowledge of the process from previous experiments. The main factors are CHF_3 flow rate, O_2 flow rate, etch pressure and RF power. Once these parameters were identified, it was important to know the range over which factors can be varied. It is important that the experimental range was neither too narrow, thus making the effects of the factors insignificant, nor too broad. In general, it is acceptable to have a maximum and minimum level with a equally spaced mid-point in between. The factor levels used are illustrated in Table C3.2.

Level Settings	CHF_3 Flow Rate (sccm)	O_2 Flow Rate (sccm)	Etch Pressure (mtorr)	RF Power (W)
1	5	0	20	50
2	25	5	60	120
3	45	10	100	190

Table C3.2: Input Parameters and Level Settings used in then optimisation of CHF_3 / O_2 RIE process of rare earth doped glass.

C.2.2 Process Development.

When the parameters and their ranges were known, it was necessary to design an orthogonal table consisting of a left hand column and a top row, with various numbers at the intersections of each column and row. This table denoted by $L_9 3^4$ applies to four input parameters, each of which can be varied over three level settings. Nine experimental runs are required to complete the table (see Table C3.3). This table satisfies the conditions of orthogonality.

Input Parameters				
Run	CHF_3 Flow	O_2 Flow	Etch Pressure	RF Power
1	1	1	1	1
2	1	2	2	2
3	1	3	3	3
4	2	1	2	3
5	2	2	3	1
6	2	3	1	2
7	3	1	3	2
8	3	2	1	3
9	3	3	2	1

Table C3.3: Orthogonal table designated $L_9 3^4$, for 4 factors, 3 level settings and 9 runs

The Table C3.4 illustrates the actual experiments to be carried out in order to characterise the process. Also shown in Table C3.4 are two additional experiments 3' and 8'. These experiments are included to investigate random variation within the process arising from sample variation, operator effects, machine anomalies, etc.

Input Parameters								
Run	CHF3 (sccm)		O2 (sccm)		Pressure (mT)		RF Power (W)	
	Level	Value	Level	Value	Level	Value	Level	Value
1	1	5	1	0	1	20	1	50
2	1	5	2	5	2	60	2	120
3	1	5	3	10	3	100	3	190
4	2	25	1	0	2	60	3	190
5	2	25	2	5	3	100	1	50
6	2	25	3	10	1	20	2	120
7	3	45	1	0	3	100	2	120
8	3	45	2	5	1	20	3	190
9	3	45	3	10	2	60	1	50
6'	2	25	3	10	1	20	2	120
8'	3	45	2	5	1	20	3	190

Table C3.4: Orthogonal table designated $L_9 3^4$, for 4 factors, 3 level settings and 9 runs used in then optimisation of CHF_3 / O_2 RIE process. Two additional experiments, 6' and 8', are added to analyse random effect in the experiments.

C.3 Results and Discussion.

C.3.1 Experiment Results.

The output functions of interest in our research are the etch rate and the roughness. The results for each of the nine experiments required by the $L_9 3^4$ matrix are listed in Table C3.5; plus, two extra experiments (6' and 8').

	Input Parameters								Output Functions			
Run	CHF_3 (sccm)		O_2 (sccm)		Pressure (mT)		RF Power (W)		Etching rate ($\mu m\ hr^{-1}$)		Roughness (nm)	
1	**1**	5	**1**	0	**1**	20	**1**	50	E1=	1.85	R1=	13.30
2	1	5	**2**	5	**2**	60	**2**	120	E2=	5.42	R2=	56.80
3	**1**	5	**3**	10	**3**	100	**3**	190	E3=	13.11	R3=	147.40
4	**2**	25	**1**	0	**2**	60	**3**	190	E4=	7.62	R4=	137.90
5	**2**	25	**2**	5	**3**	100	**1**	50	E5=	1.84	R5=	11.80
6	**2**	25	**3**	10	**1**	20	**2**	120	E6=	3.02	R6=	19.00
7	**3**	45	**1**	0	**3**	100	**2**	120	E7=	4.68	R7=	61.20
8	**3**	45	**2**	5	**1**	20	**3**	190	E8=	6.02	R8=	19.00
9	**3**	45	**3**	10	**2**	60	**1**	50	E9=	3.00	R9=	40.00
6'	**2**	25	**3**	10	**1**	20	**2**	120	E6'=	2.9	R6'=	18.00
8'	**3**	45	**2**	5	**1**	20	**3**	190	E8'=	5.9	R8'=	17

Table C3.5: The Orthogonal Experimental results for Rare Earth Etching rate and Roughness. The numbers in bold in the input parameters are the setting levels.

SEM pictures of three of these runs, 3, 8,6 are shown in Figure C3.1. It is noticed that the 6th run has no redeposition and acceptable etch rate (3.02 $\mu m\ hr^{-1}$).

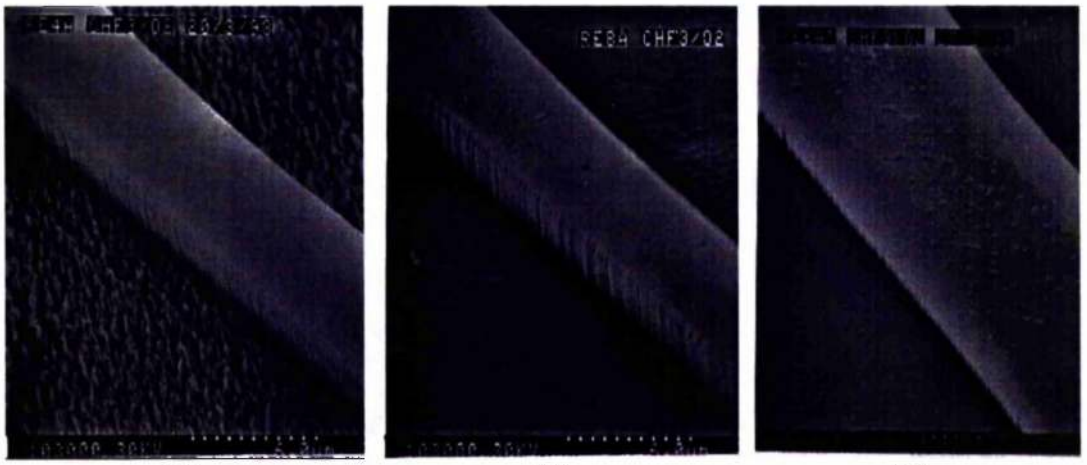

Figure C3.1: SEM pictures of erbium doped phosphosilicate waveguides etched in different conditions. (a) High roughness and very high etching rate (run number 3)(b) moderate amount of defects and high glass etching rate (run number 8); (c) null redeposition and moderate etching rate (run number 6).

C.3.2 Data Analysis.

A standard first order data analysis of the results is carried out to optimise and characterise the process. This study allowed the influence of each input factor on each output parameter to be understood. The analysis starts by calculating the output average for each level setting for each input parameter. Thus, the average etch rate for a CHF_3 flow of 5 sccm (runs 1,2, and 3) is given by the average of E1 (1.85 $\mu m\ hr^{-1}$), E2 (5.42 $\mu m\ hr^{-1}$) and E3 (13.11$\mu m\ hr^{-1}$). This is denoted as E_{C1}, and is 6.79 $\mu m\ hr^{-1}$. Similarly, the average etch rate for a CHF_3 flow setting 2, of 25 sccm, is given by the average of the etching rates of experiments 4,5 and 6 and is 4.16 $\mu m\ hr^{-1}$. The average etch rate for CHF_3 flow level setting 3 is E_{C3} = 4.57 $\mu m\ hr^{-1}$. Note that for each level setting, the orthogonal property of the matrix randomises the settings for O_2 flow, pressure and power, so that the effect of each of these parameters tends to be minimised. Continuing in the same vein, the output function averages for each input parameter level is calculated for the etching rate and roughness. This is done and is shown in Table C3.6 and Table C3.7 respectively. The simplified approach to quantify the effect of each input parameter on the output function is to calculate the difference between the

maximum and minimum values for each set of output function averages (ΔE, ΔR). The etching rate difference for CHF_3 flow, ΔEC, is EC1-EC2, or 2.63 μm hr^{-1}. Similarly, the etching rate difference for pressure is given by EPr3 - EPr1, or 2.91 μm hr^{-1}.

Glass Etching rate (μm hr^{-1})

Level	Related to CHF_3	Related to O_2	Related to pressure	Related to Power
1	E_{C1}= 6.79	E_{O1}= 4.72	E_{Pr1}= 3.63	E_{Po1}= 2.23
2	E_{C2}= 4.16	E_{O2}= 4.43	E_{Pr2}= 5.35	E_{Po2}= 4.37
3	E_{C3}= 4.57	E_{O3}= 6.38	E_{Pr3}= 6.54	E_{Po3}= 8.92
	ΔE_C= 2.63	ΔE_O= 1.95	ΔE_{Pr}= 2.91	ΔE_{Po}= 6.69

Table C3.6: First order data analysis of the output results for glasses etching rate. The output function average for each level setting for each input parameter is determined. For instance, the etching rate average for CHF_3 flow of 5 sccm (runs 1,2, and 3) is given by the average of E1, E2 and E3. This is denoted as E_{C1}, and is 6.79 μm hr^{-1}. The value denoted by ΔE indicates the difference between the maximum and the minimum averages. Grey shading cells are those optimal values for highest etching rate. Light blue shading values have the biggest influence in the etching rate.

C.3.3 Glass Etching Rate Analysis.

Table C3.6 provides a guide to obtaining a process, which would yield the highest etching rate. By comparing the four differences for etching rate, it was possible to quantify the relative effect of each input on etching rate over the level setting range chosen for that parameter. It is clear that the RF power has a strongest influence on the etching rate (highest ΔE, blue cell in Table C3.6). This is the expected result since the effect of power on etching is well known. It was also noticed that the maximum etching rate for each input parameter occurred at the smallest CHF_3 flow, greatest O_2 flow, highest pressure and highest power (Grey cells called E_{C1}, E_{O3}, E_{Pr3}, E_{Po3} in Table C3.6). The process is optimised for a maximum etching rate at these level settings. This recipe, represented by level settings 1,3,3 and 3 is one of the experiments included in the original L9 orthogonal matrix (see Table C3.4) and the etching rate is the highest 13.11 μm hr^{-1} (see Table C3.5 and Figure C3.1.a).

Further information is gleaned from the orthogonal matrix by plotting the level average as a function of level setting. This is shown in Figure C3.2. It is observed that power, pressure, and flows have a uniform trend and being the power the strongest factor for the etching rate.

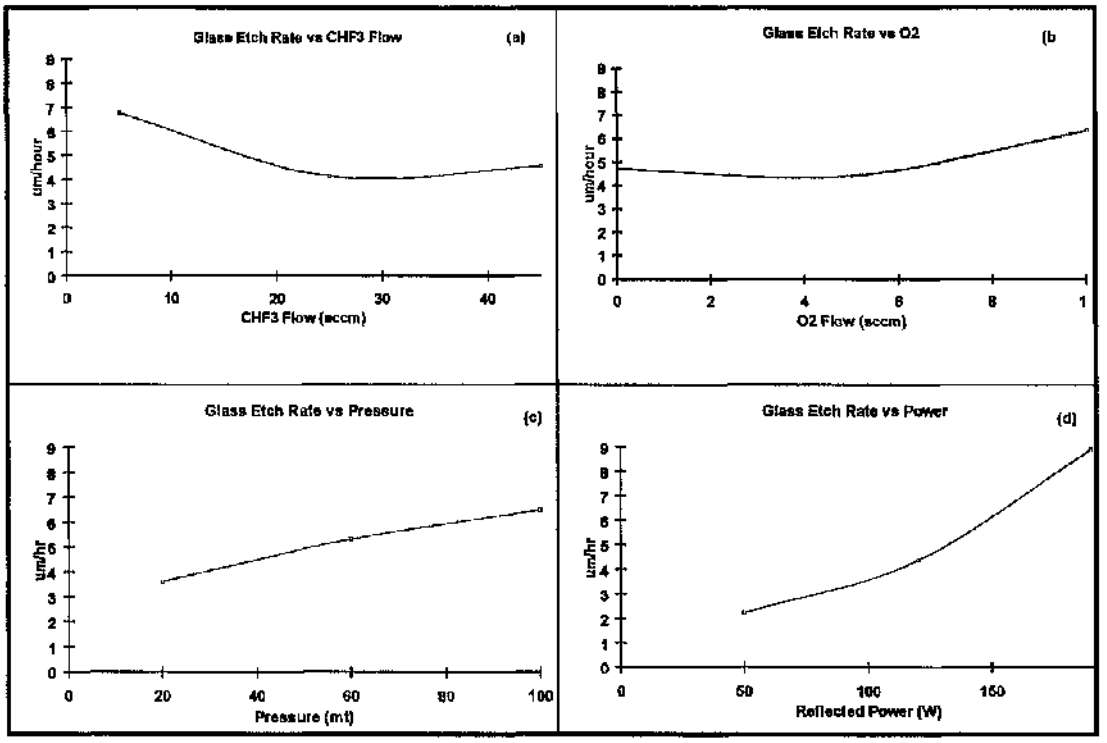

Figure C3.2: Graph analysis of the parameters for the etching rate function. This is obtained by plotting the results given in Table C3.6 for etching rate.

C.3.4 Roughness Analysis.

Similarly, it is determined a process that would yield the lowest roughness. It was found that power and pressure are the input parameters that strongly affect the roughness function (high ΔE, blue cells in Table C3.7). Notice in Table C3.7 that the minimum roughness for each input parameter occurred at the greatest CHF_3 flow, medium O_2 flow, smallest pressure and smallest power (Grey cells called E_{C3}, E_{O2}, E_{Pr1}, E_{Po1} in Table C3.7). The process was optimised for minimum redeposition at these level settings. This recipe, represented by level setting 3,2,1 and 1 is not one of the experiments included in the original L9 orthogonal matrix (see Table C3.4) but this recipe is not carried out due to the low glass etching rate.

However, the closest experiment included is run 6 (see Figure C3.1.c) and this is the one that performs etching without redeposition and acceptable etching rates.

Roughness (nm)

Level	Related to CHF_3	Related to 0_2	Related to pressure	Related to Power
1	R_{C1}= 72.50	R_{O1}= 70.80	R_{Pr1}= 17.10	R_{Po1}= 21.70
2	R_{C2}= 56.23	R_{O2}= 29.20	R_{Pr2}= 78.23	R_{Po2}= 45.67
3	R_{C3}= 40.07	R_{O3}= 68.80	R_{Pr3}= 73.47	R_{Po3}= 101.43
	ΔR_C= 32.43	ΔR_0= 41.60	ΔR_{Pr}= 61.13	ΔR_{Po}= 79.73

Table C3.7: First order data analysis of the output results for roughness. The output function average for each level setting for each input parameter is determined. For instance, the roughness average for CHF_3 flow of 5 sccm (runs 1,2, and 3) is given by the average of R1, R2 and R3. This is denoted as R_{C1}, and is 72.50 nm. The value denoted by ΔR indicates the difference between the maximum and the minimum averages. Grey shading cells are those optimal values for lowest roughness. Light blue shading values have the biggest influence in the roughness.

Further information was gleaned from the orthogonal matrix by plotting the level average as a function of level setting. This is shown in Figure C3.3. It was observed that except for the 0_2 flow, the rest of the parameters (power, pressure, and CHF_3 flow) have a uniform trend.

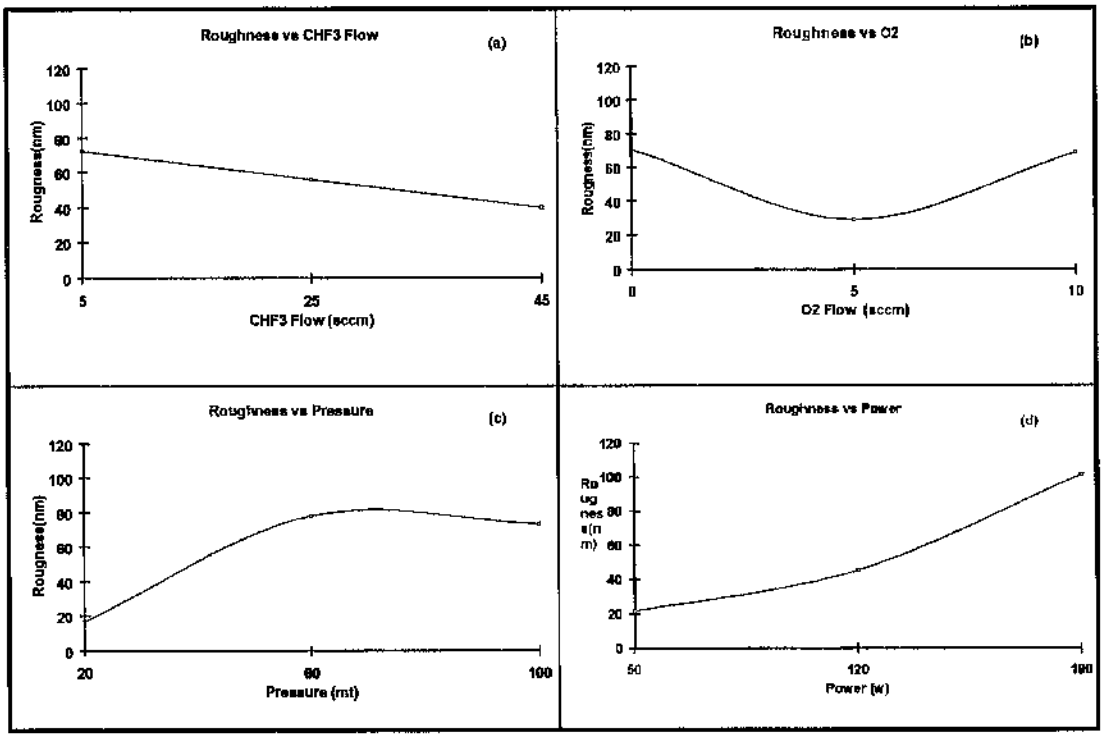

Figure C3.3: Graph analysis of the parameters for the etching rate function. This is obtained by plotting the results given in Table C3.7 for etching rate.

C.3.5 Glass Etching Rate Analysis & Roughness Analysis.

The 6th run (25 sccm of CHF_3, 10 sccm of O_2, 20 mT of Pressure and 120 W of RF Power) gave a recipe that has no redeposition and acceptable etch rate (3.02 μm hr^{-1}). However, it was tolerable to have more redeposition in order to gain a larger etch rate. Hence, it was necessary discover a process that has a higher glass etching rate and low surface roughness at the same time. From the nine experiments, the following recipes would be chosen for both outputs on an individual manner, as summarised in Table C3.8.

Conditions	CHF_3 (sccm)	O_2 (sccm)	Pressure (mT)	RF Power (W)
Maximise etching rate:	1	3	3	3
Minimise roughness:	3	2	1	1

Table C3.8: Optimal recipes for a maximum etch rate and a minimum roughness.

It was necessary to choose the proper setting levels from this table that balanced the process with high etch rate and smooth etching. The most influent parameter for the etching rate function is the power. However, the pressure and the power factors have the strongest effect over the roughness. The power was at the highest level (level 3, 190 W) because a high etching rate is an indispensable requirement. Conversely, this level affected negatively in the roughness, then the following choices should optimise the roughness output. For the following pressure factor, it is the author's opinion, that this is the crucial parameter. This factor did not have a large effect on the etching rate, however it is an essential factor for low roughness. The lowest pressure level was chosen (level 1, 20 mT) because it would decrease the resident time of the removed material. This high vacuum would avoid the redeposition. Concerning the O_2 flow, it had a small influence in etching rate. Nevertheless, it can be seen that the middle level 2 (5 sccm) is the best one for roughness, consequently this level is chosen. The already chosen values are 190 W (level 3), 20 mT (level 1) and 5 sccm of Oxygen (level 2). Regarding the CHF_3 flow, the decision is not straight forward because this gas has the opposite effect on the etching rate and in the roughness. The Figure C3.3.a shows that the highest flow would reduce the roughness (run number 8, see picture in Figure C3.1.b) and the Figure C3.2.a suggests that a low CHF_3 flow would give high etching rate. A low CHF_3 run in combination with low pressure and high power is not in the initial list of runs. Therefore, this new combination of parameters was tested. The results show in Table C3.9 demonstrated that higher CHF_3 flow provides higher etch rate, 6 $\mu m\ hr^{-1}$ versus 3 $\mu m\ hr^{-1}$. This is a contradictory result when compared with the first analysis done of the previous nine experiments because interference between the pressure and flow parameters did not occur. An etching process at low pressure demanded as much as possible etchant gas flow to obtain an acceptable etching rate. The resident time of this gas would be low due to the high vacuum existing in the chamber. Consequently, not only the resident time of the etchant gas would be low, the etched material resident time too. This would produce clean surfaces and smooth walls but a low etch rate. Therefore, because the low pressure, the highest etchant gas flow is chosen (25 sccm).

	Input Parameters								Output Functions			
Run	CHF_3 (sccm)		O_2 (sccm)		Pressure (mT)		RF Power (W)		Etching rate ($\mu m\ hr^{-1}$)		Roughness (nm)	
Low CHF3	2	25	1	5	1	20	1	190	El=	3.6	Rl=	18.30
High CHF3	3	45	2	5	1	20	3	190	Eh=	6.02	Rh=	19.00

Table C3.9: Comparison of two runs (the first one is not included in the original 9 runs) These results are obtained in medium O_2 flow, low pressure, high power conditions and with different CHF_3 flows.

C.3.6 Conclusions of Rare Earth Doped Waveguides.

The run with high CHF_3, medium 0_2, low pressure, and high power is found as the best compromise between etch rate and roughness. On the other hand it is found a recipe with no redeposition and acceptable etch rate. Therefore two procedures are obtained:

Maximised compromise between the etching rate and the roughness: 45 sccm of CHF_3, 5 sccm of O_2, 20 mT of Pressure, and 190 W of RF Power. This gives 6.02 $\mu m\ hr^{-1}$ and very low redeposition (see Figure C3.1.b).

Acceptable etching rates and no redeposition: 25 sccm of CHF_3, 10 sccm of O_2, 20 mT of Pressure and 120 W of RF Power. This gives 3.02 $\mu m\ hr^{-1}$ no redeposition (see Figure C3.1.c).

Both recipes also produced excellent sidewall angles (~90°) which is of importance to the degree of polarisation. The consequently decrease in scattering losses of the channel waveguides due to the removal of surface roughness will lead to more efficient parameters for a myriad of devices. This work geared up the integration of active optical microstructures. In the future, this work could allow the integration of an optical amplifier on FHD for infrared wavelengths. It has not been possible yet to establish a direct application of this technique for biosensing purposes. There is not interest yet among analytical chemistry community to

analyse bio-compounds using these wavelengths due to the intrinsic auto-fluorescence of these tissues at this wavelength. Nevertheless, it should be take into account the recent progresses of CO sensing by rare earth [10]. On the other hand, this rare earth etch procedure can have important consequences in the telecommunication field. In particular, for erbium-doped amplifiers and lasers which provide operation in the 1550 nm telecomm window.

C.4 References.

1 Ruano J.M., McLaughlin A.J., Bonar J.R., Jubber M.G., Marques P.V.S., Wilkinson. C.D.W., Aitchison J.S., "A reactive ion etching process", 9907302.5, 31st March 1999.

2 France P.W., Optical Fibre Lasers and Amplifiers, Blackie Publishers, 1991.

3 Sugai T., Matsuzawa T., Sensors and Actuators B-Chemical, Vol.13, No. 1-3, pp. 480-482, 1993.

4 Loong C.K., Thiyagarajan P., Richardson J.W., Ozawa M., Suzuki S., Journal of catalysis, Vol. 171, No. 2, pp. 498-505, 1997.

5 Schumutzier H.J., Sanhage K.H., Nava J.C., Journal of the American Ceramic Society, Vol. 79, No. 6, pp. 1575-1584, 1996.

6 Imanaka N., Hirota Y., Adachi G.Y., Journal of the Electrochemical Society, Vol. 142, No. 6, pp. 1950-1951, 1995.

7 Mitchell I.R., Farrel P.M., Baxter G.W., Collins S.F., Grattan K.T.V., Sun T., Review of Scientific Instruments, Vol. 71, No. 1, pp 100-103, 2000.

8 Dos Santos P. V., deAraujo M.T., GouveiaNeto A.S., Sombra A.S.B., IEEE Journal of Quantum Electronics, Vol. 35, No. 3, pp. 395-399, 1999.

9 Potter B.G., Sinclair M. B., Journal of Electroceramics, Vol. 2, No. 4, pp. 295-308, 1998.

10 Krier A., Gao H., Sherstnev V., Yakovlev Y., Electronics Letters, Vol. 35, No. 19, pp. 1665-1667, 1999.

11 Bonar J.R., Bebbington J.A., Aitchison J.S., Maxwell G.D, Ainslie B.J., Electron. Lett., 31, 99, 1995.

12 Hattori K., Kitagawa T., Oguma M., Okazaki H, Ohmori Y., Journal of Applied Physics, Vol.80, No.9, pp.5301-5308, 1996.

13 Yan Y.C., Faber A.J., deWaal H., Kik P.G., Polman A., Applied Physics Letters, Vol.71, No.20, pp.2922-2924, 1997.

14 Ghosh R.N., Shmulovich J., Kane C.F., Debarros M. R. X., Nykolak G., Bruce A.J., Becker P.C., Ieee Photonics Technology Letters, Vol.8, No.4, pp.518-520, 1996.

15 Hattori K., Kitagawa T., Oguma M., Ohmori Y., Horiguchi M., Electronics Letters, 30, pp. 856-857, 1994.

16 Yin G.Z., Jillie D.W., Solid State Technology, Vol.30, No.5, pp.127-132, 1987.

17 Jenkins M.W., Mocella M.T., Allen K.D., Sawin H.H, Solid State Technology, Vol.29, No.4, pp.175-182, 1986.

Appendix D: Photo-multiplier Tube Signai Amplifier Circuit.

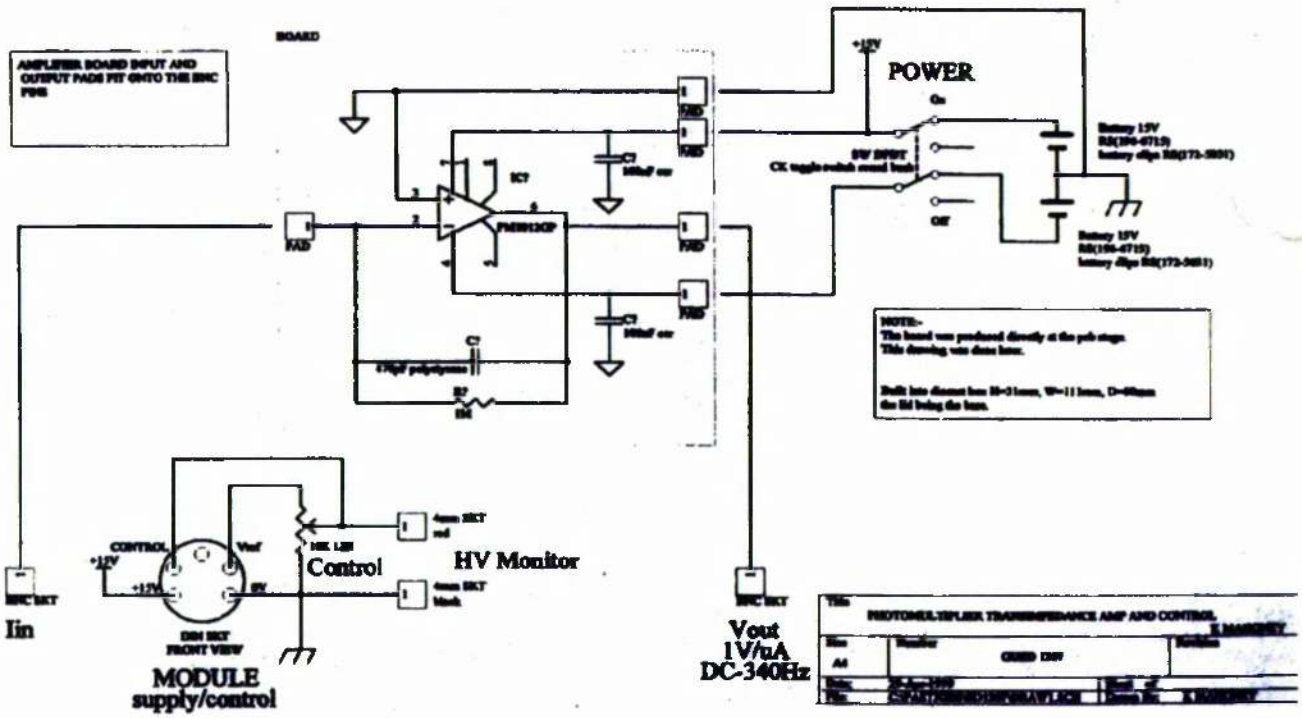

Figure D4.1: This circuit converts the intensity into a voltage (1 V μA^{-1}). There is also a filter treatment of the signal. The circuit is fed by two batteries of 15 V.